NASA Conference Publication 2082

Flight Mechanics/Estimation Theory Symposium October 1978

Sponsored by
Systems Development and Analysis Branch
Mission Support Computing and Analysis Division
Goddard Space Flight Center
Greenbelt, Maryland

National Aeronautics and
Space Administration
Goddard Space Flight Center
Greenbelt, Maryland 20771

April 1979

NASA Conference Publication 2082

Flight Mechanics/Estimation Theory Symposium

October 1978

Sponsored by
Systems Development and Analysis Branch
Mission Support Computing and Analysis Division
Goddard Space Flight Center
Greenbelt, Maryland

National Aeronautics and
Space Administration

April 1979

EDITOR'S NOTE

The papers presented herein have been derived primarily from speakers' summaries of talks presented at the Flight Mechanics/Estimation Theory Symposium held October 18 and 19, 1978 at Goddard Space Flight Center. For the sake of completeness, abstracts are included of those talks for which summaries were unavailable at press time. Papers included in this document are presented basically as received from the authors with a minimum of editing.

CONTENTS

CONTENTS (Continued)

ONBOARD IMAGE PROCESSING

Donald R. Martin and Alfred S. Samulon

TRW Defense and Space Systems Group

ABSTRACT

This paper considers the possibility of onboard geometric correction of Thematic Mapper type imagery to make possible image registration. Typically, image registration is performed by processing raw image data on the ground. The geometric distortion (e.g., due to variation in spacecraft location and viewing angle) is estimated by using a Kalman filter updated by correlating the received data with a small reference subimage, which has known location. Onboard image processing dictates minimizing the complexity of the distortion estimation while offering the advantages of a real-time environment. In keeping with this, the distortion estimation can be replaced by information obtained from the Global Positioning System and from advanced star trackers. Although not as accurate as the conventional ground control point technique, this approach is capable of achieving subpixel registration. Appropriate attitude commands can be used in conjunction with image processing to achieve exact overlap of image frames. The paper investigates the magnitude of the various distortion contributions, the accuracy with which they can be measured in real-time, and approaches to onboard correction.

The Thematic Mapper scans a succession (16 at a time) of lines on the earth, each of which is 185 kilometers long. This is accomplished by optically focusing the light from the scene and sweeping it across a row of small individual photodetectors. The scanning action is continuously repeated with the spacecraft motion causing successive scans to lie a fixed distance from each other.

A user of images produced by Thematic Mapper is likely to be interested in some particular kind of geologic, agricultural, urban, or other feature of the scenes being analyzed. In performing this analysis, it is frequently desirable that two images of the same scene be registered; that is, each physical part of the scene is in the same location on the two images so that the picture elements (pixels) of the two images can be aligned. Such precision is not easy to attain, mainly because of varying distortions and viewing conditions from one image to the next. (See Figure 1.)

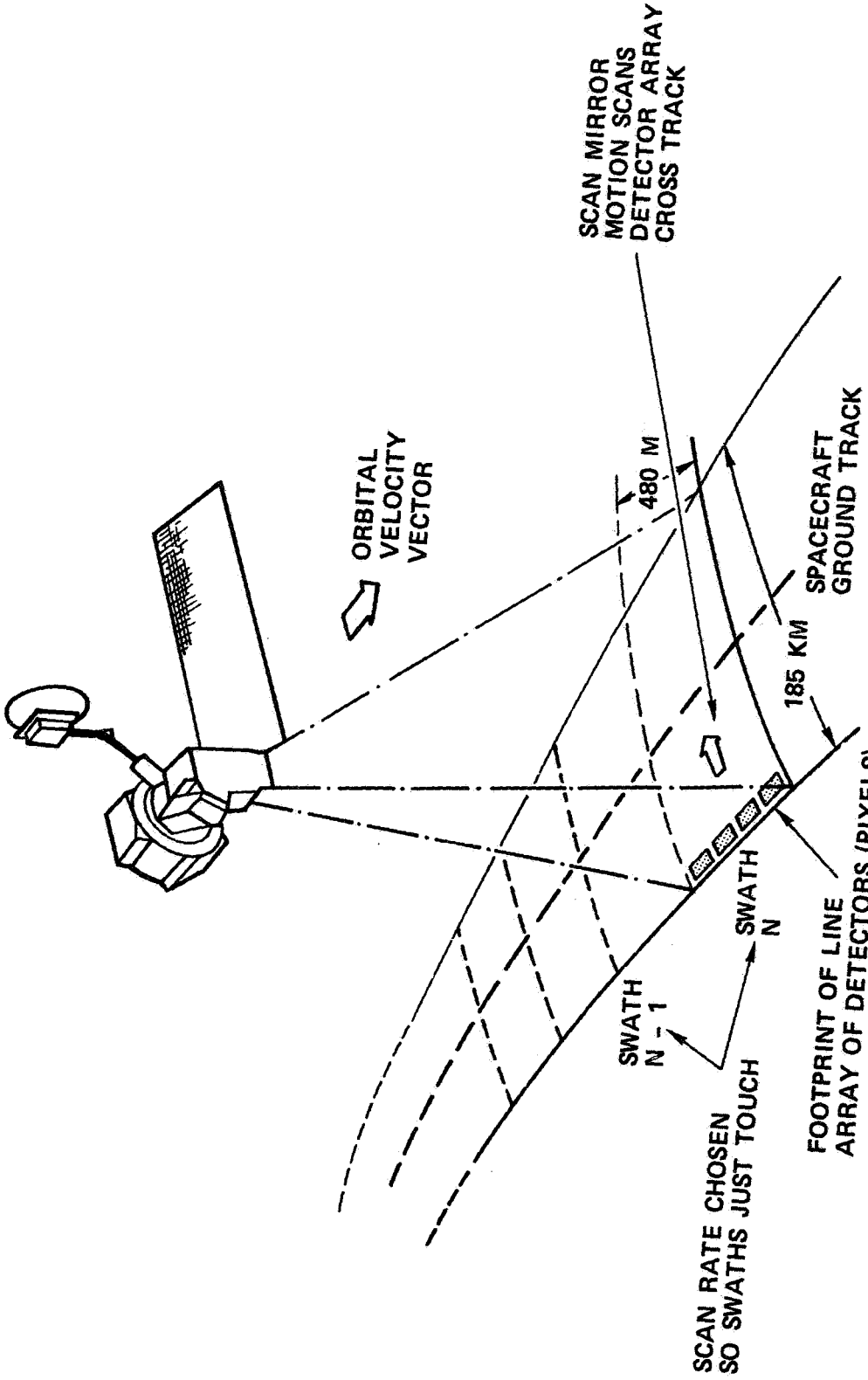

Figure 1. Multispectral Scanning Sensor Geometry

Registration is accomplished by estimating the sources of distortion and performing geometric correction to compensate for the distortion. The ultimate registration error is therefore primarily determined by the accuracy of the distortion estimation, not by its actual magnitude. The levels of registration differ by the amount of processing required. Isodistance requires constant interpixel distances and parallel scan lines in images of the same region. However, different images of the same region have an unknown relative displacement which is generally not an integer number of pixels. Absolute location of pixels specifies the relative displacement of different images and must be an integer number of pixels. Exact overlap of image frames require the same distortion information as absolute location registration; however it requires that the geometric correction produce image frames with exactly corresponding pixel locations. Map projection includes the previous levels of registration in addition to correcting the distortion caused by factors not associated with the satellite (e.g., earth curvature and rotation). (See Figure 2.)

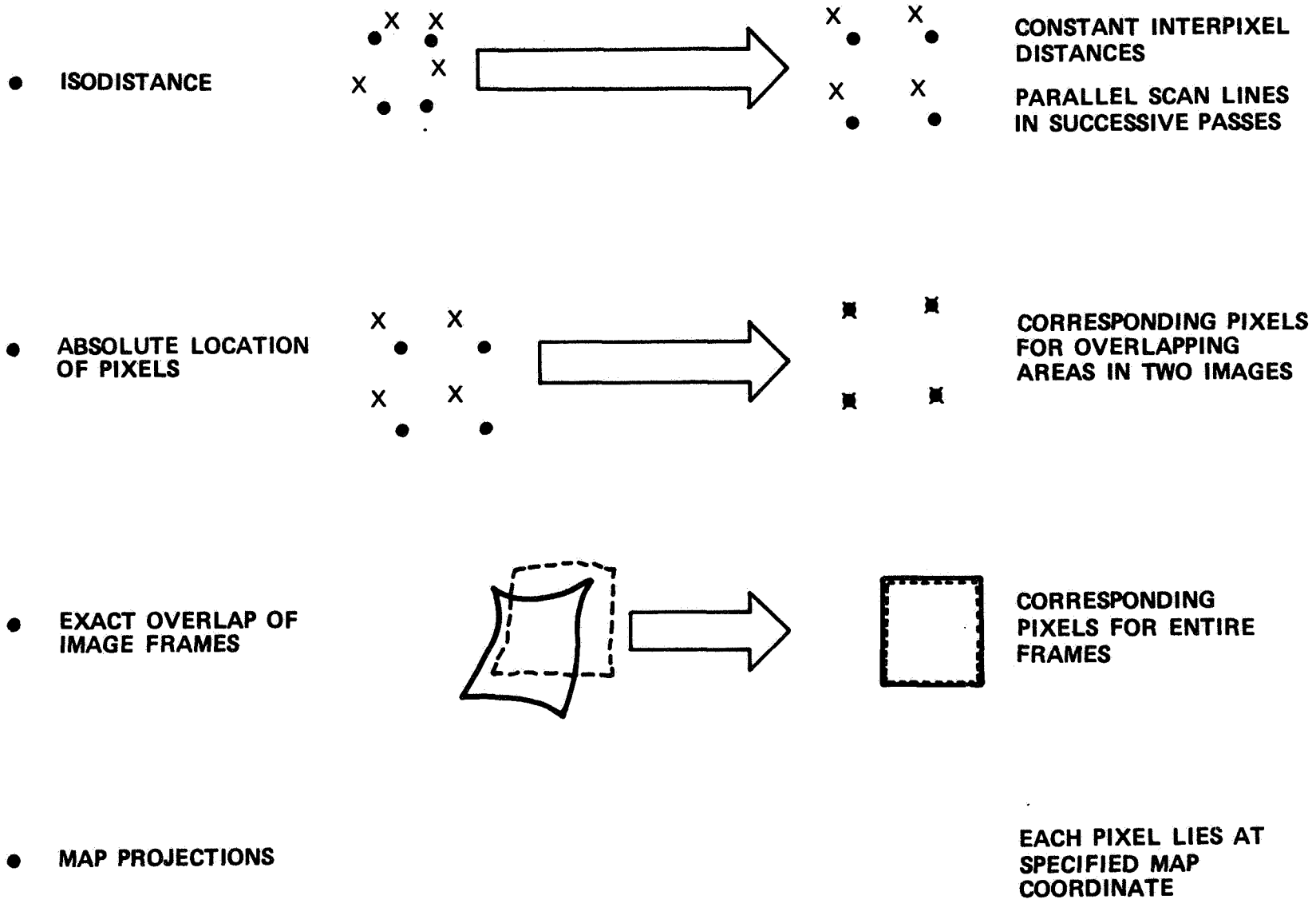

Figure 2. Registration Levels

The location of the spacecraft with respect to the ground at a given time of day can vary significantly for different passes over a region. Pixels compared at the same time of day for subsequent passes, with no knowledge of spacecraft location, can cause significant offset in pixel location. Absolute location registration requires that this offset be known and corrected and is essential if different images of the same region are to be compared. (See Figure 3.)

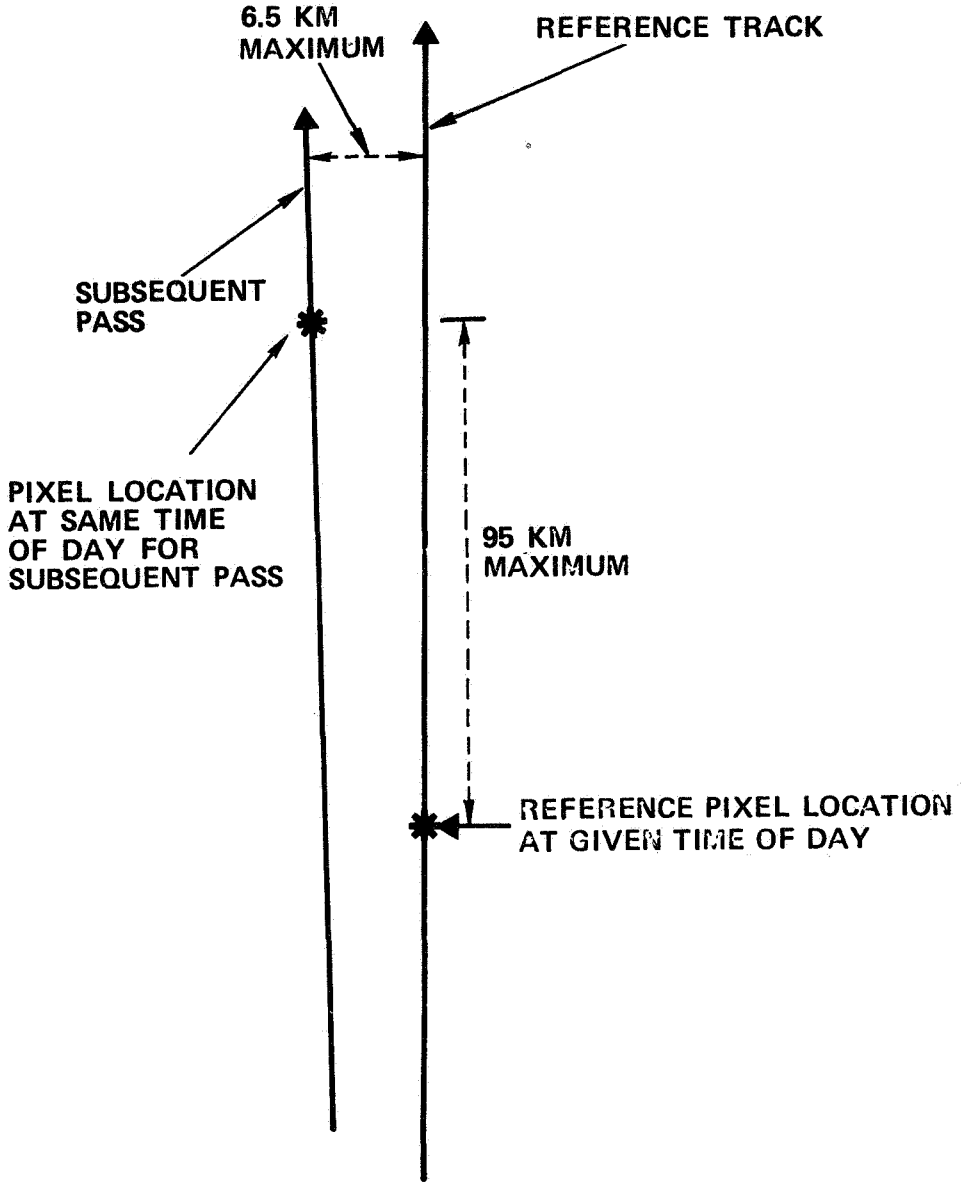

Figure 3. Absolute Location Ephemeris Distortion

Variation in the spacecraft altitude for different passes over a region affects pixel spacing in the cross track direction for both isodistance and absolute registration. Except for the effect of variation in the orbital velocity, the difference in the spacecraft's along track and cross track position has no impact on isodistance distortion. The altitude and orbital velocity of the spacecraft changes very little in comparison to the cross track drift for different passes over a region. Consequently, isodistance distortion caused by ephemeris variation is far smaller than the corresponding absolute distortion. (See Figure 4.)

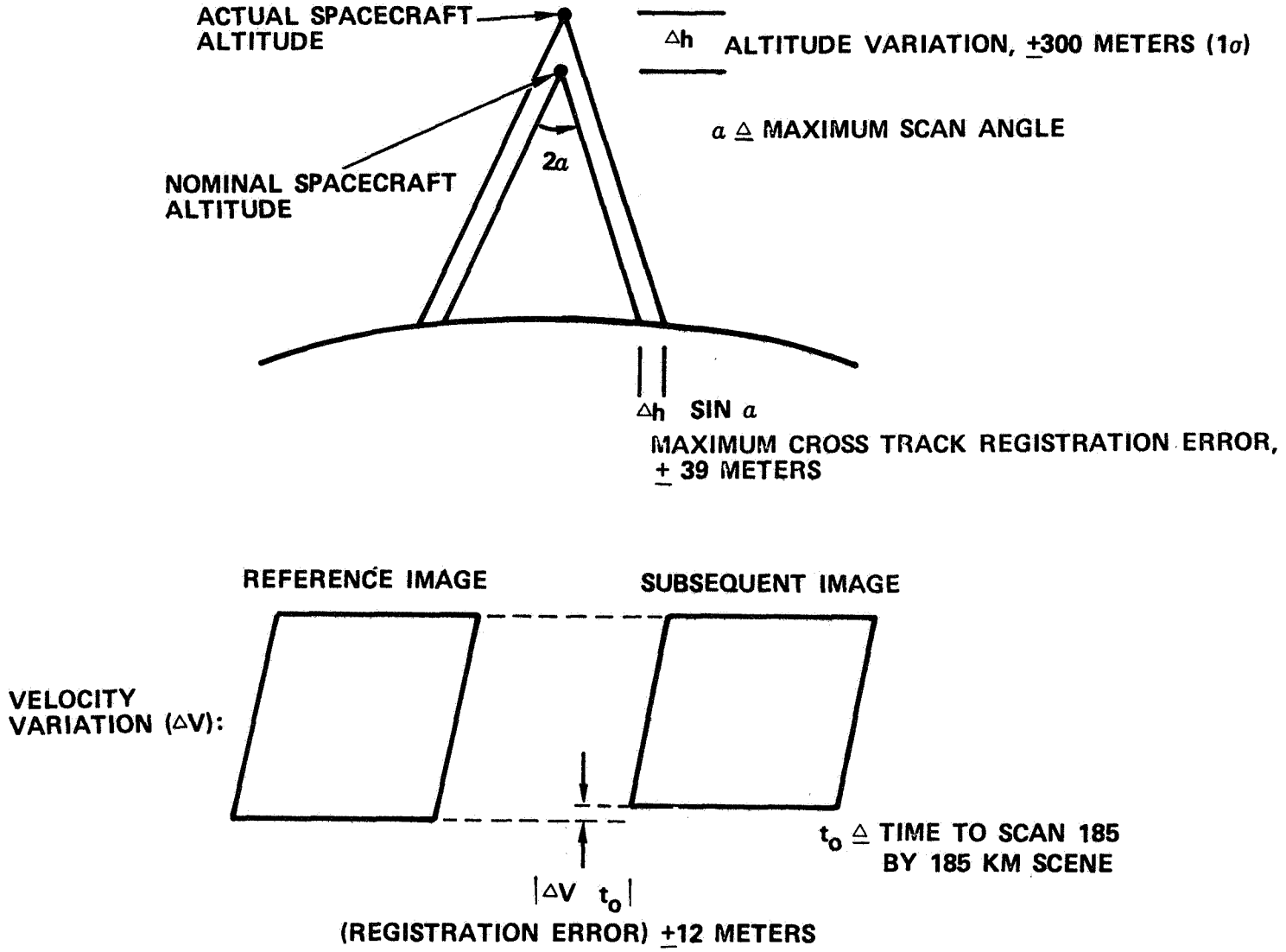

Figure 4. Isodistance Ephemeris Distortion

The scanning motion of the Thematic Mapper must be precisely the same on subsequent passes over a region if no distortion is to be introduced. Variation in the active scan duration (i.e., scan velocity) will cause stretching (or compression) of the pixel spacing within a scan line. Variation in the scan period will cause the spacing between scan lines to be different for subsequent images of a region, causing different images of the same region to have a different number of scan lines. (See Figure 5.)

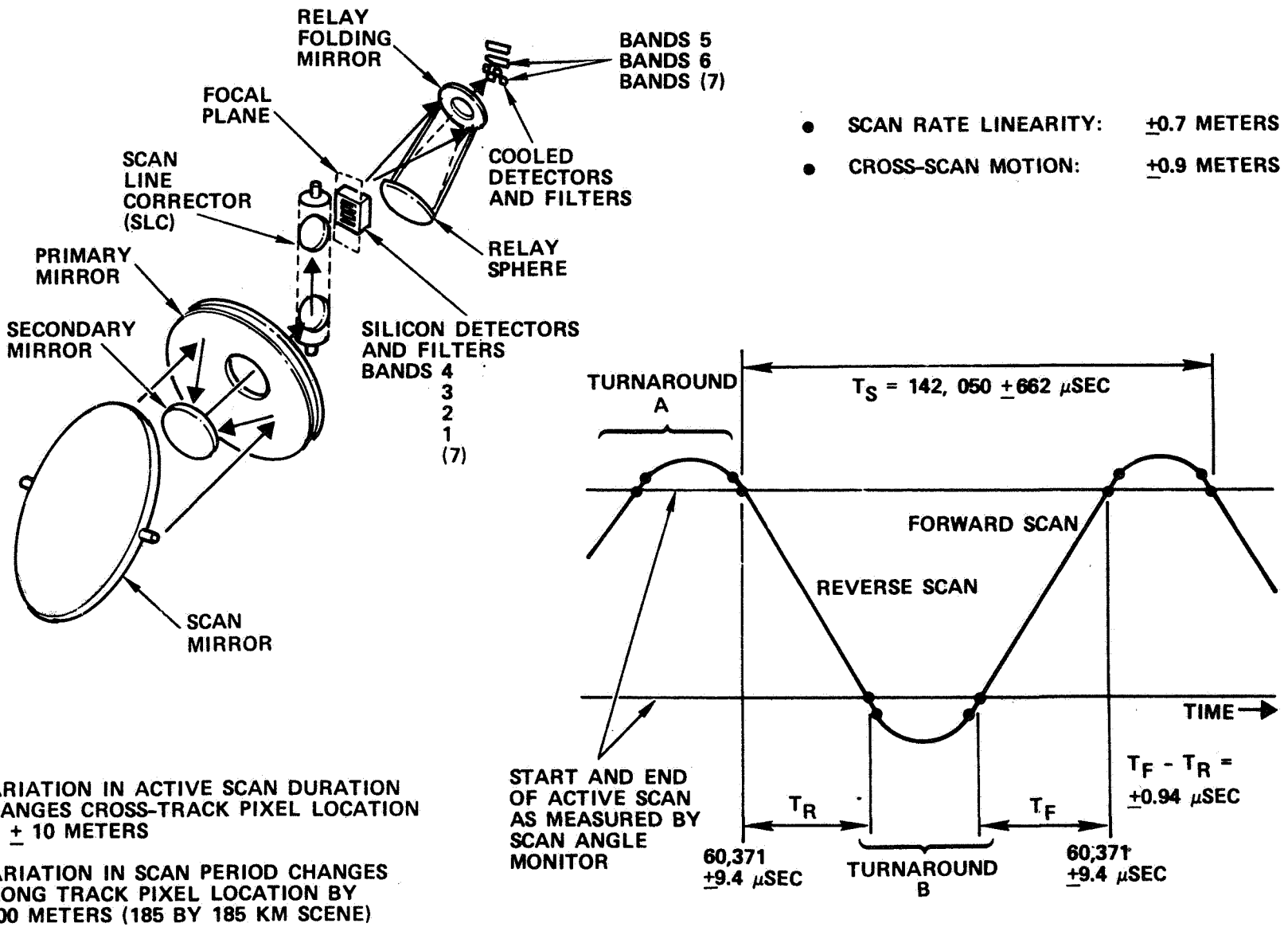

Figure 5. Thematic Mapper Scan Distortion

The spacecraft is assumed to be in an earth-pointing attitude mode. Variation in the absolute attitude of the spacecraft with respect to a previous pass will cause an absolute location registration error proportional to this attitude variation. Such variation is limited by the accuracy of the star tracker. Isodistance registration requires a stable attitude reference during the scene, but is relatively unaffected by the absolute accuracy of this reference. Consequently, isodistance registration is primarily determined by the gyro drift in the stellar-inertial attitude reference system. (See Figure 6.)

- EFFECT ON SCAN LINE

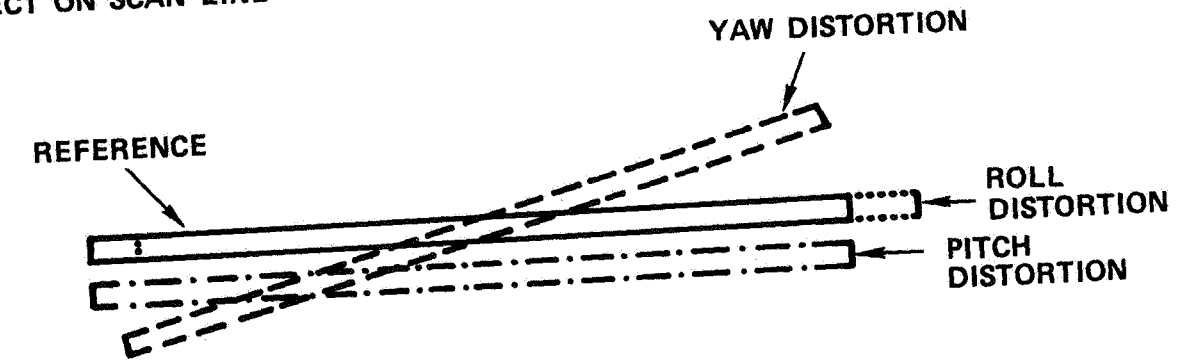

- EFFECT ON REGISTRATION

POINTING STABILITY
± 0.0006 DEGREE

POINTING ACCURACY
±0.0027 DEGREE

ISODISTANCE DISTORTION: ±7.7 METERS (ALONG)
±6.3 METERS (CROSS)

ABSOLUTE DISTORTION: ±33 METERS (ALONG AND CROSS)

Figure 6. Attitude Distortion

For the reasons previously cited, the attitude of the Thematic Mapper must be held constant (with respect to the earth-pointing frame of reference) to prevent distortion. However, the coordinate axes of the Thematic Mapper are not the same as those of the Attitude Control System. The difference between these sets of axes exhibits both long term drift and a short term sinusoidal variation at the orbital frequency due to thermal effects. The relative alignment of the Thematic Mapper and the Attitude Control System must be determined and the appropriate geometric correction performed. (See Figure 7.)

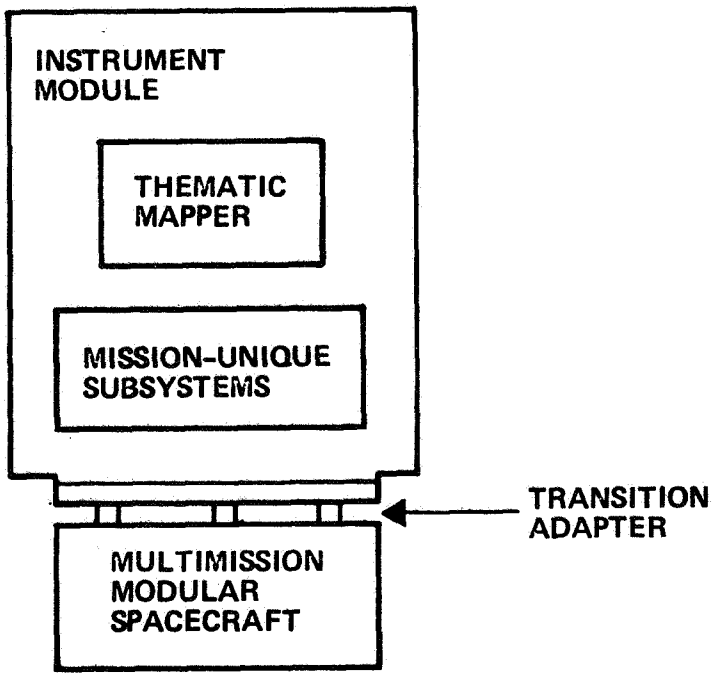

- MUST KNOW ATTITUDE OF THEMATIC MAPPER RELATIVE TO MMS ATTITUDE REFERENCE
- ALIGNMENT CONSISTS OF SLOWLY VARYING BIAS COMPONENT AND APPROXIMATELY SINUSOIDAL THERMAL COMPONENT
- ABSOLUTE DISTORTION: ±34 METERS (ALONG AND CROSS)
- ISODISTANCE DISTORTION: ±4.4 METERS (ALONG)
  ±1.0 METERS (CROSS)

Figure 7. Alignment Distortion

The technique usually employed to estimate distortion on the ground uses ground control points which consist of 32 by 32 pixel subimages with known location. The received imagery is correlated with the ground control point to determine the proper position of one pixel. A dynamic model is used for the distortion, with the correlation information serving as observations of the distortion process. By using Kalman filtering, the distortion at each pixel in the image can be estimated and corrected. Variations in the scan duration occur at a higher frequency than can be measured by ground control points; consequently, scan distortion must be measured by the Scan Angle Monitor. (See Figure 8.)

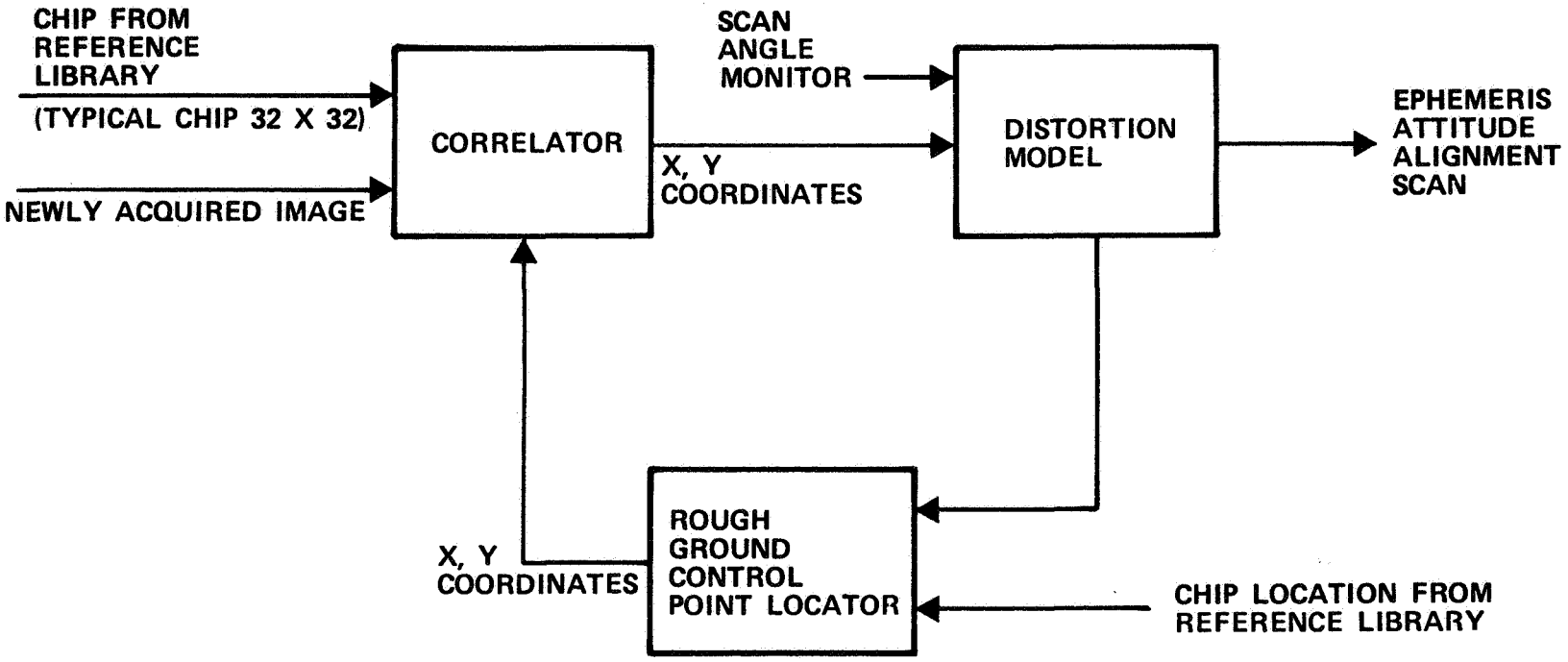

- VALUE: VIRTUALLY ELIMINATES DISTORTIONS THAT CHANGE SLOWLY COMPARED TO GCP FREQUENCY
- ASSUMPTIONS: GCP HAS FIXED APPEARANCE
- COST: MEMORY, COMPLEXITY

Figure 8. Use of Ground Control Points

The location and velocity of the spacecraft can be determined to ±5 meters and ±0.3 meters per second (one-sigma), respectively, by using the Global Positioning System. The isodistance registration error depends on the velocity uncertainty over the duration of a scene (approximately 30 seconds). The GPS velocity uncertainty has less impact on pixel spacing over the scene duration than does the GPS location uncertainty. The attitude of the spacecraft is determined by the attitude control system. The absolute attitude accuracy is consequently limited by the stellar-inertial attitude reference, which is assumed to use a star tracker of advanced design. The isodistance attitude error is determined by the stability of the spacecraft's attitude during a scene, not by its absolute pointing accuracy. Alignment can be calibrated every few days from the ground using ground control points. Isodistance registration requires the scan lines to be parallel for different images of a region; as a result the alignment error due to yaw is the same for both absolute and isodistance registration. Scan distortion must be estimated from the Scan Angle Monitor information. Because of the high frequency content of the scan distortion, it also has the same impact on isodistance and absolute registration. (See Figure 9.)

DISTORTION SOURCE	ESTIMATION TECHNIQUE	ONE-SIGMA ERROR (EACH AXIS)	
		ABSOLUTE (METERS)	ISODISTANCE (METERS)
EPHEMERIS	GLOBAL POSITIONING SYSTEM	5	1
SCAN	SCAN ANGLE MONITOR	1.6	1.6
ATTITUDE	STELLAR-INERTIAL REFERENCED ATTITUDE CONTROL SYSTEM	10	3.3
ALIGNMENT	PERIODIC CALIBRATION FROM GROUND	5	5
RSS		12.4	6.3

Figure 9. Distortion Estimation Without GCPS

The onboard real-time environment dictates that processing and data storage be kept as small as possible. However, in order for the processing to be useful, it must meet certain minimum requirements in terms of registration accuracy. Absolute registration accuracy in the 0.5 to 0.3 pixel range can be achieved without the use of ground control points. Isodistance registration accuracy of 0.2 pixel is also achievable. Improvement in absolute registration accuracy to less than 0.2 pixel (one-sigma) can be obtained with the use of ground control points; however, this requires a very sophisticated distortion model in addition to the large number of ground control points. Processing considerations therefore indicate that ground control points be avoided if acceptable registration performance is achieved without them. (See Figure 10.)

- PROCESSING COMPLEXITY
  - WITH GCP'S
    - KALMAN FILTER (~20 STATES)
    - GCP CORRELATION
    - SCAN ANGLE MONITOR READOUT
  - WITHOUT GCP'S
    - SCAN ANGLE MONITOR READOUT
    - GPS
    - ADVANCED STAR TRACKER
- DATA STORAGE REQUIREMENTS
  - WITH GCP'S
    - AT LEAST SEVERAL SCANS
    - POSSIBLY SEVERAL ENTIRE IMAGES (INCREASED ACCURACY)
    - CONTROL POINT LIBRARY
  - WITHOUT GCP'S
    - FEW SCANS AT MOST
- PERFORMANCE

  GCP'S IMPROVE REGISTRATION

Figure 10. Tradeoffs in Distortion Measurement

Ephemeris adjustment is employed infrequently because of limitations in the propellant capacity. Large cross track drifts can be corrected by performing ephemeris adjustment once every 16 days. Because of the response time of the attitude control system, attitude commands can be used at most only a few times per orbit. This is sufficient to minimize the data storage requirement by maintaining the scan lines to be roughly parallel to the reference scan. Also, by pointing cross track, attitude commands can facilitate the exact overlap of image frames. The remaining geometric correction is performed by resampling the pixel intensities to achieve the desired output matrix. Resampling consists of locating the position of a desired pixel in the scanned image and interpolating to determine its intensity. (See Figure 11.)

- EPHEMERIS ADJUSTMENT
  - COMPENSATE FOR CROSS TRACK DRIFT
- ATTITUDE COMMANDS
  - COMPENSATE FOR ALIGNMENT ERRORS
  - EXACT FRAME OVERLAP
- RESAMPLING
  - COMPENSATE FOR SCANNER ERRORS
  - COMPENSATE FOR EPHEMERIS
  - COMPENSATE FOR ATTITUDE CONTROL ERRORS

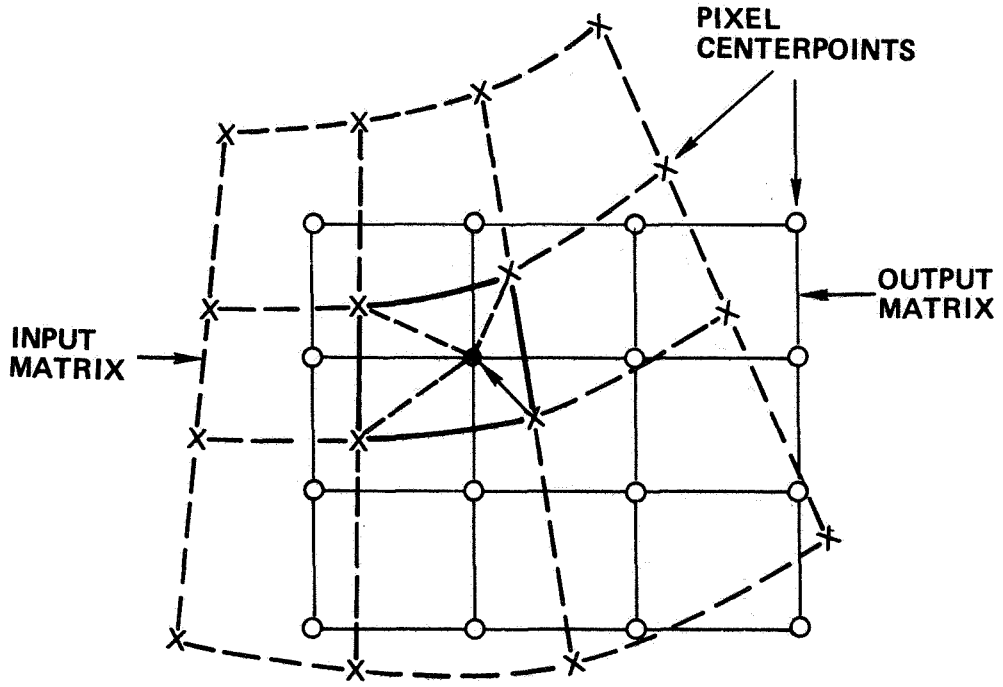

Figure 11. Geometric Correction Techniques

The image registration functions are specified in the block diagram. The correction determination box accepts scan duration and ephemeris information from the Thematic Mapper and GPS receiver, respectively. Alignment information is periodically furnished to this box from the ground. The correction determination box uses this information to determine attitude commands and resampling parameters, and the appropriate header information giving the location of a given image frame is also calculated. The resampling box accepts the correction parameters and performs the appropriate resampling and data formatting of the radiometrically corrected data. The resampling box should consist of custom-designed hardware because of the speed with which the processing must be performed. (See Figure 12.)

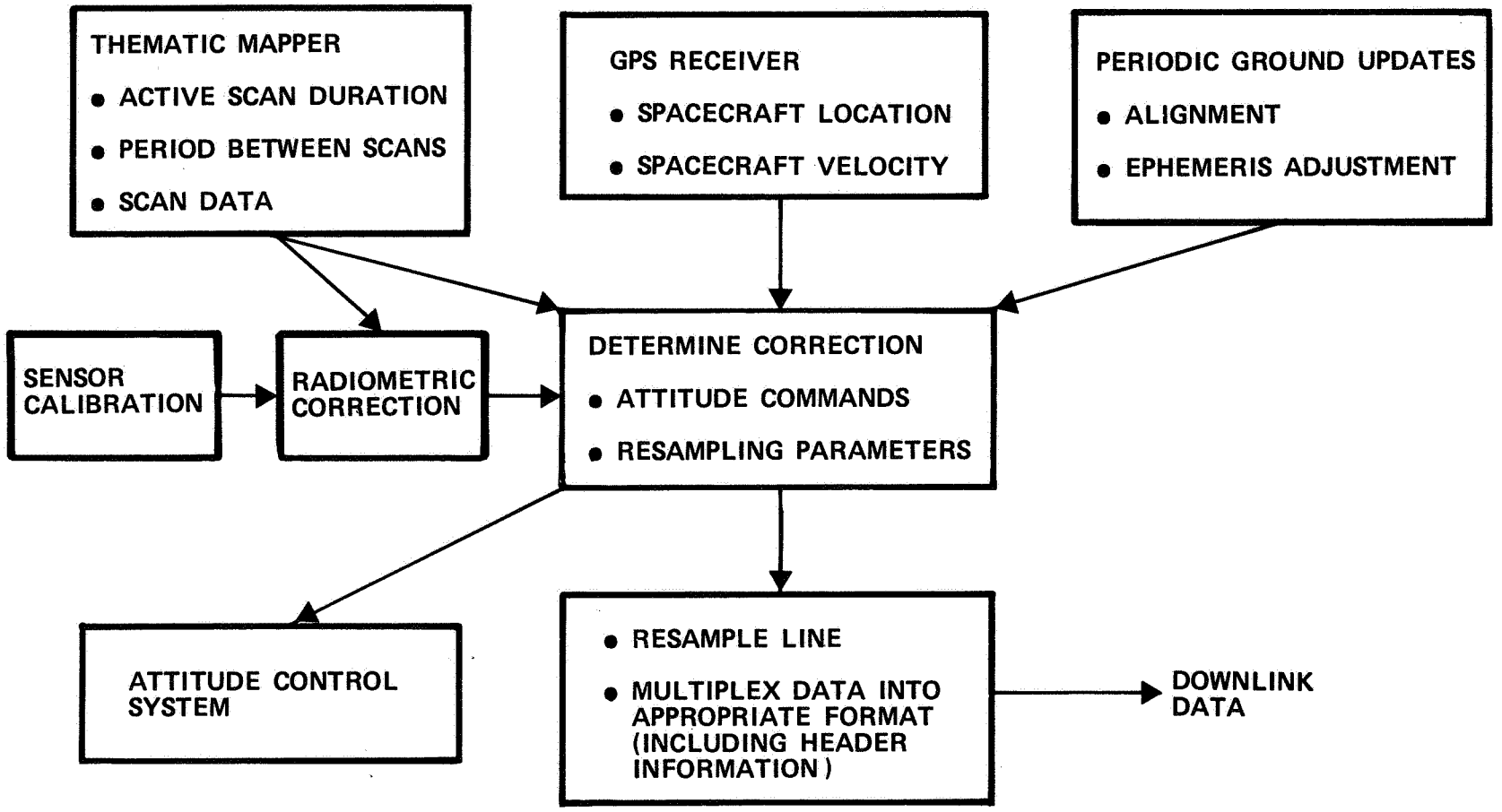

Figure 12. Onboard Processing Functional Block Diagram

REAL-TIME ONBOARD GEOMETRIC IMAGE CORRECTION

Walter Discenza and Georges Frippel

General Electric Space Division

ABSTRACT

This paper describes a system to perform real time onboard geometric correction of Landsat D resolution satellite imagery. System requirements, algorithms, sensors, and other hardware components are defined. Feasibility of implementing the correction process is demonstrated using Kalman filter techniques to incorporate information from onboard ephemeris (GPS), attitude control (MACS) and ground control points. Random access sensor systems, such as Charge Injected Devices (CID) and Charge Coupled Devices (CCD), are used to obtain pixel values at desired ground locations, thus greatly reducing the data processing requirements.

Real-Time Onboard Geometric Image Correction

by

Walter Discenza and Georges Frippel
General Electric Space Division

The results presented are from a study that is currently in progress to extend and further develop an alternate approach to performing geometric image correction and registration using a technique conceived in a previous study performed by GE (Ref. 1) (See Figure 1).

A brief overview of the need for geometric image compensation is provided followed by an explanation of the alternate approach. A discussion of possible implementation approaches for this new concept is provided followed by the development of a conceptual design based on current Landsat-D requirements (for baseline purposes only) (See Figure 2).

For the purposes of this presentation, we classify geometric image distortions as deterministic or non-deterministic (See Figure 3). The deterministic errors are assumed to be known apriori and removed by appropriate processing. Only the non-deterministic or time varying errors related to such items as alignments variation, ephemeris uncertainty, attitude control pointing errors, sensor distortion or warping and mapping projections transformations must be identified and compensated as the data becomes available. The magnitude of these effects can vary over wide ranges such as the ephemeris determination using GPS (10 meters) to the uncertainty from the standard ground tracking system (256 meters). Even with such improvements, the anticipated achievable accuracy is still several hundred meters and the required performance less than 10 meters. Investigation and previous experience have indicated that by using ground control point (GCP) correlation the desired accuracy can be achieved.

The Landsat-C and proposed Landsat-D geometric image correction and registration approaches both utilize resampling and interpolation to perform the correction function (See Figure 5). A real-time operating environment eliminates or severely restricts the ability to use resampling techniques. The proposed alternate approach ("Smart Sensor") uses an over-sampled two-dimensional image plane and a Kalman filter-driven direct readout controller to eliminate the need for interpolation and resampling. The level of over-sampling is selected to provide an acceptable level of error using the nearest neighbor approach.

The differences between the approaches currently in use and the "Smart Sensor" can be vividly seen by considering an example where the center of the output pixel is not on the input or measurement data grid (See Figure 4). To obtain the value of the output pixel, a horizontal interpolation must first be performed to construct several values along the output grid line on which the desired pixel lies. These constructed points

are then used to perform an interpolation in the vertical direction to obtain the desired value. In the "Smart Sensor" approach, the high density of sub-pixel detector elements coupled with the correction coefficients derived from the Kalman filter allows the value at the desired point to be read out directly. Improvements in the achievable signal-to-noise ratio can be obtained by utilizing the output of several detectors centered about the desired point.

Several trade off studies were conducted to establish a preferred approach (See Figure 6 and 7). The "push broom" (MLA) or a long cross track image plane that is moved along the ground track by the spacecraft velocity was found to be preferred to a "whisk broom" (Thematic mapper) approach, since it eliminates the errors associated with mirror scan repeatibility (7 meters RMS),potentially one of the largest Landsat-D error sources, and is not S/N or sampling rate constrained.

The "push broom" approach may be implemented using either a one (linear) or two (matrix) dimensional array of detectors (See Figure 8). The matrix approach was determined to be superior, since it eliminates the need for large buffer memories, significantly reduces the amount of software processing required to construct a pixel, and is not oversample or sub-pixel limited along-track by maximum sample rate signal-to-noise considerations. Re-set residuals can be eliminated by using double correlated reads, however, this increases the sampling rate by a factor of two. The main area of concern is whether fabrication technology will be available to allow the manufacturing of such large scale detector arrays.

These detector arrays can be implemented using photo diodes, charge coupled devices (CCD) or charge injection devices (CID) (See Figure 9). Although there are many similarities, the CID appears to offer the most direct or easiest implementation. The photo-diodes require additional circuitry to provide a select read capability which effectively produces a 100 micrometer spacing. In addition, the use of a buffer memory is necessary to provide a non-destruct multiple detector per pixel read capability. The CCD can be operated in a time delay integration mode to improve the S/N but this effectively converts the two dimensional array into a single dimension. Thus, this feature cannot be utilized in the current configuration. Investigations have indicated that it might be possible to operate a CCD in the Random access non-destruct read mode but this capability is yet to be fully demonstrated.

The "Smart Sensor" approach appears to be compatible with real-time onboard implementation (See Figure 10). The recursive nature of the Kalman filter sample controller minimizes to quantity of data which must be stored. The question as to the number and frequency of the ground control points required to provide acceptable imaging errors when a new swath is started is yet to be investigated. Trade offs between the number of filter states and the number and frequency of ground control points must be investigated.

The upper part of the block diagram is essentially a top level representation of the multi-mission attitude control system (MMACS).

Evaluating whether GCP correlation errors can be integrated into the MMACS is no trivial task. The first cut approach would probably be to operate these two recursive filter in a semi-independent mode while making the output states of each filter available for use in the other. The primary benefit of improving overall attitude control system pointing performance appears to be associated with auxiliary experiments and not geometric image correction of the primary sensor.

The geometric correction matrix will be based on the Landsat-D configuration without the two states associated with the scan mechanism. Based on previous experience, the size of the GCP reference image has been chosen to be 32 x 32 30 Meter Pixels. Due to the accuracy required, the output of the detectors will probably have to undergo radiometric correction to issue proper GCP selection.

Landsat-D requirements were used to develop an application example in order to insure that a complete set of realistic and consistent specification which reflect current thinking were available. This example is intended to characterize the main features of the approach and highlight some of its salient characteristics (See Figure 11). To meet the specified requirements and provide direct read-out of a scan line, approximately a 6000 by 20 pixel array would be required to provide the ground swatch coverage necessary to account for the maximum errors along-track. An 8 x 8 array of detectors per pixel is required to meet the arbitrary error budget allocations indicated. The values were selected to provide a maximum uncertainty in the recursive filter since its characteristic and convergence properties are not yet defined. The array size or focal plane size appears to be the limiting item for this configuration.

Several sub-studies or analyses were conducted to provide parameteric data on key design parameters (See Figure 12). The required number of detector cells to obtain a desired accuracy using the nearest neighbor approach is based on a uniform distribution RMS error allocation. The Geometric Correction Matrix (GCM) error contribution to cross track error is the result of comparing the actual value with the estimated value for 30 and 90 grid points while varying the time intervals between GCM updates. The signal-to-noise ratio for the CID read out approaches considered, assumed a simplified signal-noise model consisting of the number of carriers due to photons, dark current and amplifier noise. The two extremes were investigated consisting of one set of read out electronics shared among 11 CID chips and one set of electronics per CID chip. The actual design implemented will probably lie somewhere between these two extremes. The depth of the detector array for yaw attitude error is derived from straightforward geometric considerations.

Present technology indicates that a CID chip will contain at least 1000 x 1000 detector cells (See Figure 13). The depth of 1000 cells is more than adequate to account for the worst case variations along track. The main challenge lies in the cross-track layout since for the specified configuration 48,000 detectors or 48 chips are required. The CID chip has

inherently a non-conducting border which prevents the detectors on adjacent chips from being directly abutted. There are several approaches which can be used to circumvent this problem. One way is to use a front to back staggered layout as indicated. This approach produces a fixed known along track displacement error which is deterministic. Based on the arbitrary error allocation of one (1) meter for pixel precision placement, an oversample factor of 8 is required. This oversample factor leads to an image plane size of 48 cm.

There are several approaches available for reducing the size of the required image plane (See Figure 14). If a re-evaluation of the error budget indicates that the recursive filter uncertainty can be limited to 3.67 meters then 2.0 meters could be allocated to pixel placement precision. This 2 meter requirement reduces the oversampling factor to 4, thus cutting the image plane size in half. Alternately, if the error budget were increased to 4.64 meters RMS or the multiple pass pixel to pixel registration requirement eliminated, the required performance could be achieved with an oversampling factor of 4. Other parameters which are directly proportional to the required number of detectors or image plane size are the swath width and pixel size or resolution. Thus, reducing the swath width to 90 KM or increasing the pixel size to 60 x 60 meters or some combination of these two parameters could be used to reduce the required image plane to approximately 20 cm.

The tasks remaining to be investigated include the definition of the recursive filter, the accuracy achievable and required computational capability associated with a specific design, the required number and spacing of GCP points to minimize data loss while the filter is converging to its steady state value (See Figure 15).

Acknowledgements:

This work is being prepared in support of National Aeronautics and Space Administration, Goddard Space Flight Center Contract NAS 5-23412, Amendment 133.

The authors would like to gratefully acknowledge the support of A.J. Fuchs, Contract Administrator and the contributions and assistance of E. Beyer who was the major technical contributor for Task One.

Reference:

Investigations of a Space Data Technology Facility (SDTF) for Spacelab Report #77SDS4267 December 1977. J.D. Welch.

REAL TIME ON-BOARD GEOMETRIC IMAGE CORRECTION

GENERAL ELECTRIC COMPANY - SPACE DIVISION
PHILADELPHIA, PENNSYLVANIA 19101

Figure 1

- REQUIREMENTS
- "SMART SENSOR" CONCEPT
- IMPLEMENTATION APPROACH
- CONCEPTUAL DESIGN
- SUMMARY AND CONCLUSIONS

Figure 2

- SOURCES
  - VIEWING GEOMETRY (NON-SYSTEMATIC)

ALIGNMENT	- 206.4 METERS
EPHEMERIS	- 10 TO 256 METERS
ATTITUDE CONTROL	- 175.2 METERS

  - SENSOR
  - MAPPING
- LANDSAT D REQUIREMENTS
  - GEODETIC:
    0.5 PIXEL (90%) - 9.12 METERS (RMS)
  - REGISTRATION
    0.3 PIXEL (90%) - 6.08 METERS (RMS)
  - OPERATIONAL
    $6.08/\sqrt{2}$ - 4.3 METERS (RMS)

GROUND CONTROL POINT CORRELATION IS REQUIRED

Figure 3

- CURRENT (LANDSAT C)
  - TWO DIMENSIONAL POLYNOMIAL CONSTRUCTION
  - RE-SAMPLING AND INTERPOLATION
- LANDSAT-D
  - GEOMETRIC CORRECTION MATRIX GENERATED FROM A 17 STATE KALMAN FILTER
  - RE-SAMPLING AND INTERPOLATION
- "SMART SENSOR"
  - OVER-SAMPLED TWO DIMENSIONAL IMAGE PLANE
  - KALMAN FILTER-DRIVEN DIRECT READOUT CONTROLLER

"SMART SENSOR" APPROACH ELIMINATES RE-SAMPLING

Figure 4

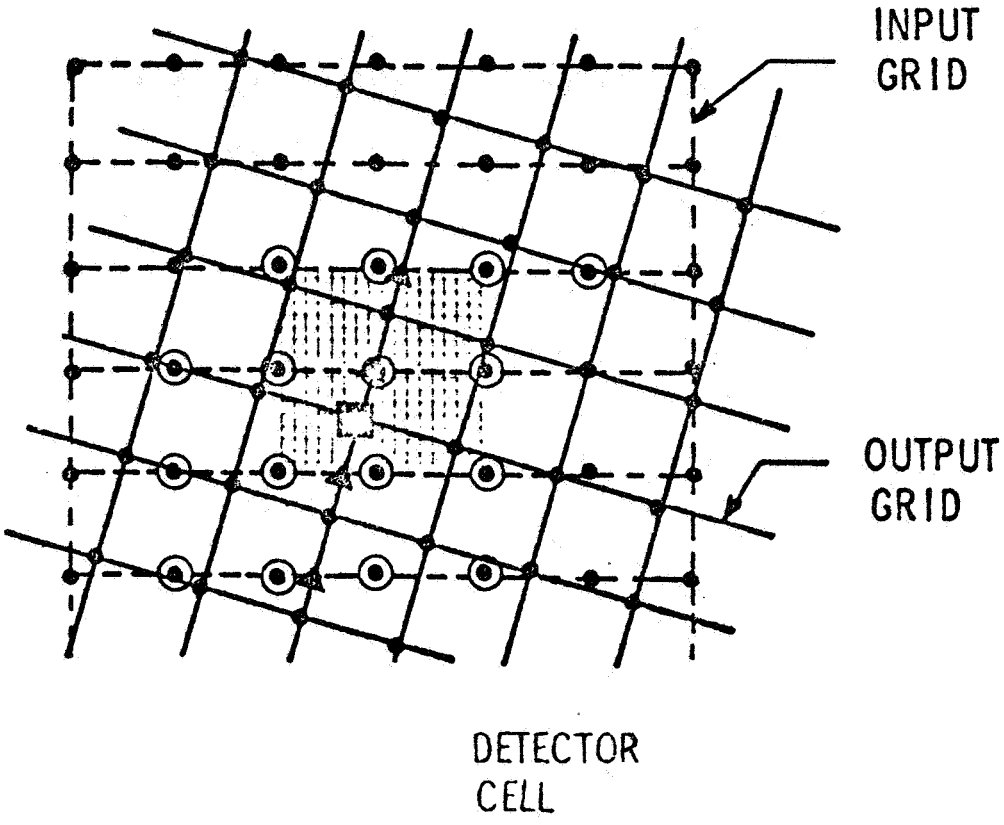

Figure 5

- SCANNING MECHANISMS AND CONFIGURATION
  - WHISK BROOM VS PUSH BROOM
  - LINEAR (WITH STORAGE) VS MATRIX
- TECHNOLOGIES
  - CCD
  - CID
  - PHOTODIODE

Figure 6

- WHISK-BROOM
  - SMALL IMAGE PLANE
  - SMALL NUMBER OF DETECTORS
  - RAPID SAMPLING (~10 μS/16 PIXELS)
  - MIRROR SCAN REPEATABILITY ERRORS (~7M RMS)

- PUSH-BROOM
  - LONG IMAGE PLANE
  - LARGE NUMBER OF DETECTORS
  - DETECTOR OUTPUT VARIATION (RADIOMETRIC CALIBRATION)
  - SLOW PARALLEL SAMPLING (~4 ms/PIXEL)
  - NO MOVING MECHANICAL ASSEMBLIES

PUSH BROOM ELIMINATES THE LARGEST SOURCES OF ERROR

Figure 7

- LINEAR ARRAY
  - LARGE MEMORY (120K BYTES)
  - ALL DETECTOR PROCESSING DONE IN THE COMPUTER (EXECUTION TIME)
  - SAMPLING AND READOUT LIMITED ALONG TRACK
  - RESET RESIDUALS
- TWO DIMENSIONAL ARRAY (MATRIX)
  - SLOW PARALLEL SAMPLING (~4 ms/PIXEL)
  - MAXIMUM OF 6K MEMORY REQUIRED
  - NO MEMORY REQUIRED WITH RANDOM ACCESS NON DESTRUCTIVE READ
  - IMPROVED S/N BY USING MULTIPLE DETECTORS PER PIXEL
  - VARIATION IN DETECTOR OUTPUT (RADIOMETRIC CALIBRATION)
  - DEPTH OF ARRAY DEPENDS ON OVERALL SYSTEM CONSIDERATIONS

A FABRICATION TECHNOLOGY VS A COMPLEX PROCESSING SOLUTION

Figure 8

- PHOTODIODES
- CHARGE COUPLED DEVICES (CCD)
- CHARGE INJECTION DEVICES (CID)
- SIMULARITIES
  - MULTIBAND CAPABILITY
  - RESPONSE IN 0.4 TO 1.1 MICRON RANGE
  - CONFIGURED IN A MATRIX LAYOUT
  - SUBJECT TO RESET NOISE, THERMAL OR DARK CURRENT, LEAKAGE CURRENT, PREAMPLIFIER NOISE, PATTERN NOISE AND CROSSTALK
- DIFFERENCES

DEVICE	DETECTOR SPACING		DETECTOR AND ADDRESSING CIRCUITRY	COMMENTS
	CURRENT	FUTURE		
PHOTODIODES	10-15	-	100	POOR RESOLUTION DUE TO LARGE SPACING REQUIRES BUFFERING AND MEMORY
CCD	20-30	10-15	SAME AS DETECTOR	INHERENTLY NOT RANDOM ACCESS, REQUIRES LARGE BUFFER MEMORY OR COMPLEX TECHNIQUES. TIME DELAY INTEGRATION NOT COMPATIBLE WITH MATRIX APPROACH
CID	20-30	10-15	SAME AS DETECTOR	INHERENT RANDOM ACCESS NON DESTRUCTIVE READ CAPABILITY

CID OFFERS EASIEST IMPLEMENTATION

Figure 9

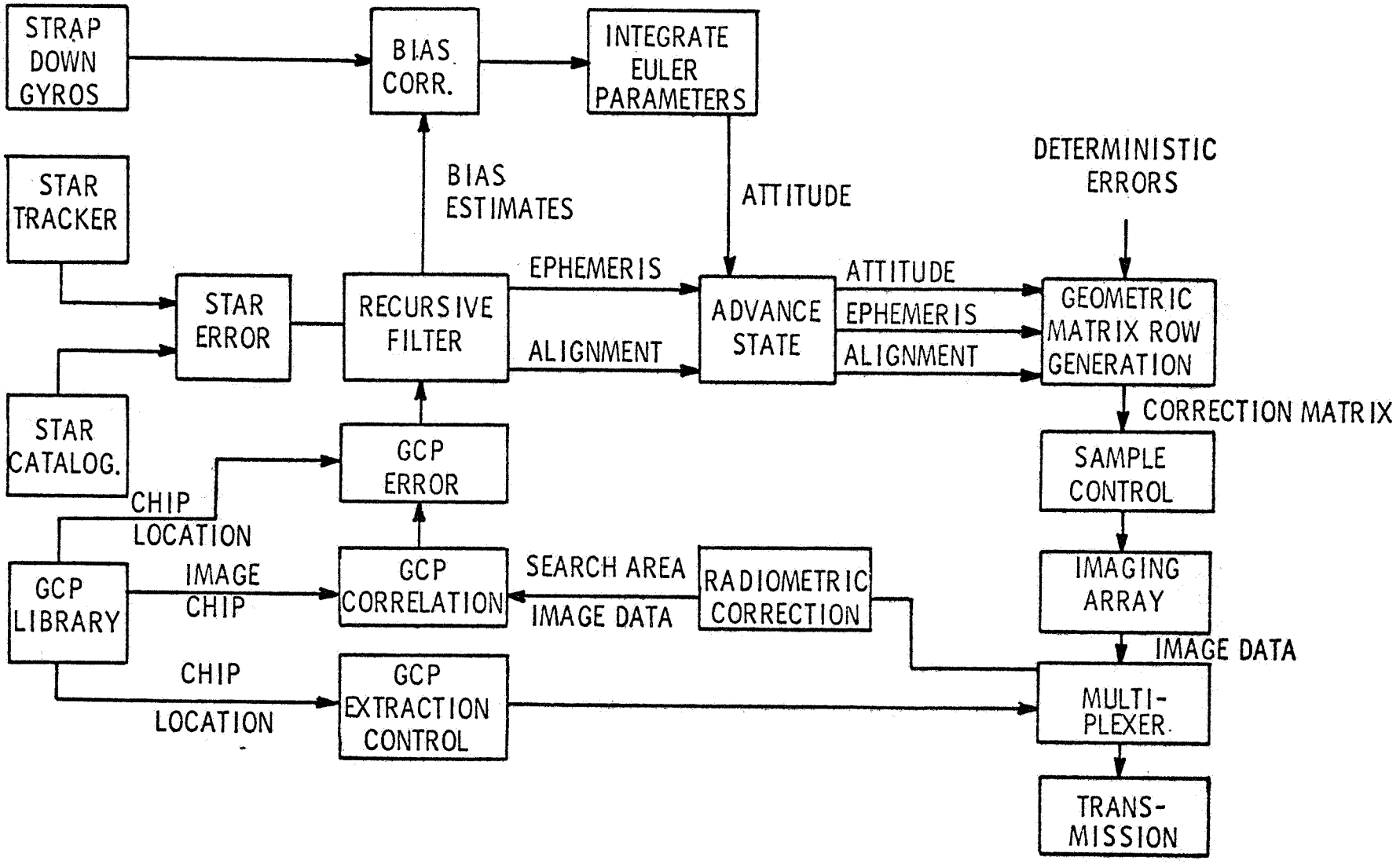
STRAP DOWN GYROS
BIAS CORR.
INTEGRATE EULER PARAMETERS
STAR TRACKER
BIAS ESTIMATES
ATTITUDE
DETERMINISTIC ERRORS
STAR ERROR
RECURSIVE FILTER
EPHEMERIS
ALIGNMENT
ADVANCE STATE
ATTITUDE
EPHEMERIS
ALIGNMENT
GEOMETRIC MATRIX ROW GENERATION
CORRECTION MATRIX
STAR CATALOG.
GCP ERROR
SAMPLE CONTROL
CHIP LOCATION
GCP LIBRARY
IMAGE CHIP
GCP CORRELATION
SEARCH AREA
IMAGE DATA
RADIOMETRIC CORRECTION
IMAGING ARRAY
IMAGE DATA
CHIP LOCATION
GCP EXTRACTION CONTROL
MULTI-PLEXER
TRANS-MISSION

Figure 10

- MISSION REQUIREMENTS
  - 708 KM ORBIT
  - 185 KM SWATH
  - 30 X 30 M PIXEL
  - MMS ATTITUDE CONTROL: 0.16 DEGREES YAW

- ERROR ALLOCATION (FIRST CUT)
  - PIXEL LOCATION PRECISION: 1.0 METER
  - CORRECTION MATRIX ERROR: 1.0 METER
  - KALMAN FILTER UNCERTAINTY: 4.06 METERS

- SENSOR CONFIGURATION
  - ~6000 X 20 PIXEL ARRAY
  - 8 X 8 DETECTORS PER PIXEL
  - 30 GRID POINT GEOMETRIC CORRECTION MATRIX WITH 3 SECONDS UPDATE
  - 32 X 32 PIXEL GCP CHIP WITH 38 PIXEL RADIUS OF UNCERTAINTY SEARCH AREA

ARRAY SIZE MAY BE A PROBLEM AT FOCAL PLANE

Figure 11

- REQUIRED NUMBER OF DETECTOR CELLS TO OBTAIN A DESIRED ACCURACY USING NEAREST NEIGHBOR APPROACH
  - 30 METER PIXEL
- GEOMETRIC CORRECTION MATRIX ERROR CONTRIBUTION TO CROSS TRACK ERROR
  - MODULAR ATTITUDE CONTROL
- SIGNAL TO NOISE RATIO FOR CID READOUT APPROACHES
  - RADIANCE 0.28 mw/CM^2
  - INTEGRATION TIME 4.5 ms
- DEPTH OF DETECTOR ARRAY FOR YAW ATTITUDE ERRORS
  - 185K METER IMAGE SWATH
  - 30 METER PIXEL

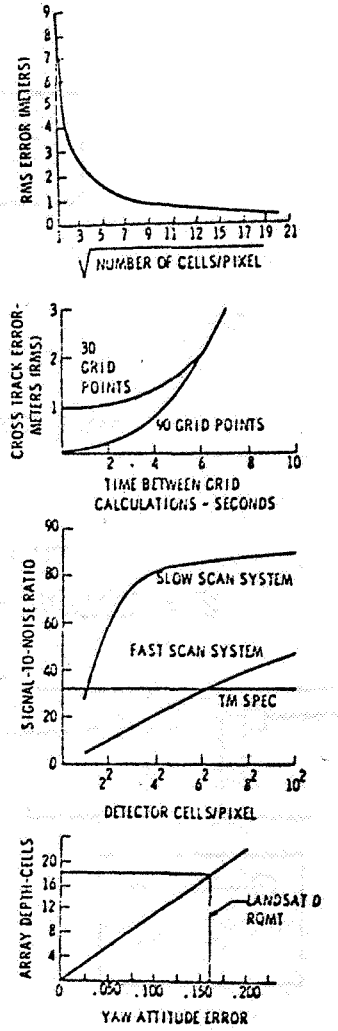

Figure 12

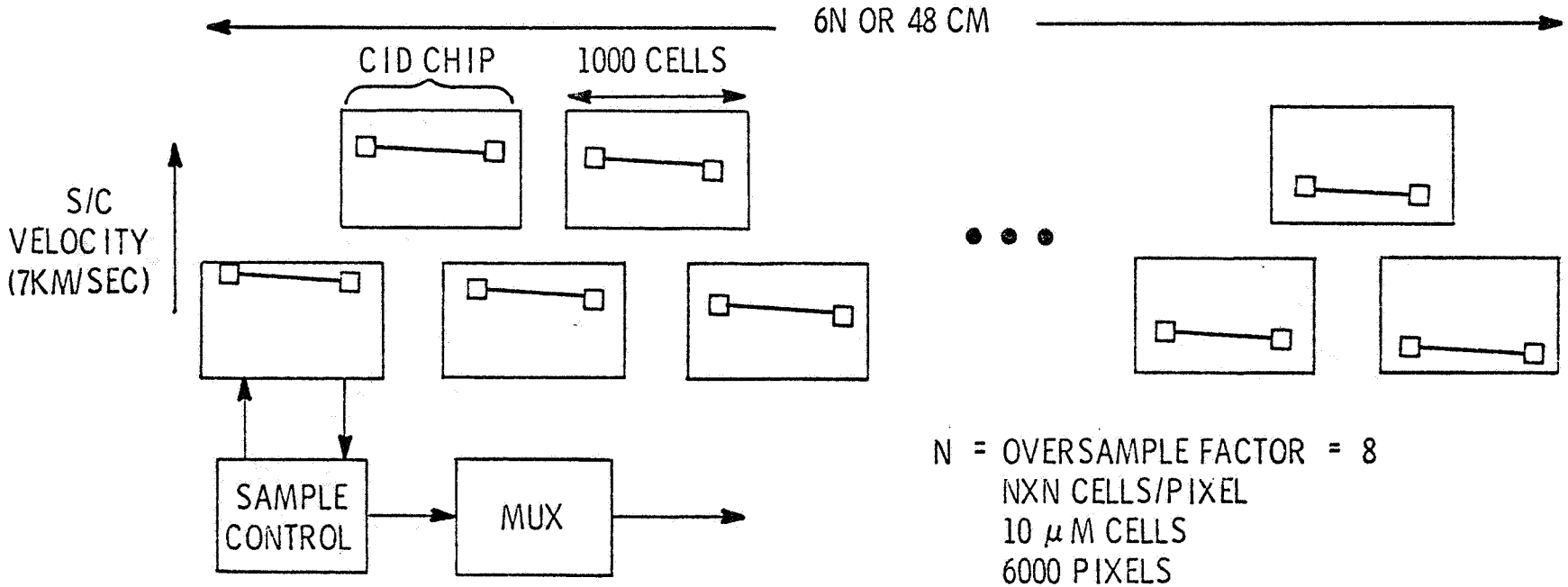

REDUCTION OF THE OVER SAMPLING FACTOR TO 4 MAKES THE REQUIRED IMAGE PLANE COMPATIBLE WITH MLA DESIGN

Figure 13

- REDUCE NUMBER OF ELEMENTS PER PIXEL
  - RE-ALLOCATE ERROR BUDGET (EX: KALMAN→3.67 M)
  - INCREASE ERROR BUDGET

- REDUCE NUMBER OF PIXELS
  - REDUCE SWATH WIDTH
  - REDUCE RESOLUTION

Figure 14

ANALYSES TO BE COMPLETED IN TASK 2

- ACHIEVABLE ACCURACY OF ERROR MODELING
- LOCATION AND FREQUENCY OF GROUND CONTROL POINT (GCP) UPDATES
- REQUIRED SIZE OF ON-BOARD GCP LIBRARY
- EFFECTS OF IMPROVING ATTITUDE CONTROL POINT ACCURACY AND JITTER
- OBSERVABILITY OF ATTITUDE, ALIGNMENT, AND EPHEMERIS
- EFFECTS OF IMPROVED EPHEMERIS ESTIMATES DERIVED FROM GLOBAL POSITIONING SATELLITE SYSTEM
- ON-BOARD COMPUTATIONAL REQUIREMENTS

Figure 15

SUMMARY AND CONCLUSIONS

- "SMART SENSOR" CONCEPT IS FEASIBLE AND OFFERS BENEFITS
- MAJOR CHALLENGE TO MEET LANDSAT-D REQUIREMENTS IS FOCAL PLANE SIZE
- 2-DIMENSIONAL PUSH-BROOM APPROACH IS PREFERRED
- CID YIELD SIMPLEST IMPLEMENTATION
- SEVERAL KEY ANSWERS NEEDED TO DETERMINE EFFECTIVENESS

Figure 16

A DIGITAL SCENE MATCHING TECHNIQUE FOR GEOMETRIC IMAGE CORRECTION AND AUTONOMOUS NAVIGATION

Glenn E. Tisdale
Westinghouse Systems Development Division

Bernard Peavey
NASA – Goddard Space Flight Center

ABSTRACT

A technique will be described for precise registration of two images of the same area, taken under different conditions. The images may differ in scale, orientation, or aspect angle, they may have limited distortion, or they may be obtained from different sensors, or from maps. The technique, called AUTO-MATCH, involves digital preprocessing of the images to extract edge contours, followed by a correlation of corresponding edge end points. The availability of an array of endpoints makes possible subpixel registration accuracy.

The technique is being applied to a system for assessment of geometric image quality (GIQAS), to be installed at NASA-Goddard later this year. This system will measure the registration vectors over an array of window pairs from Landsat images, so as to determine the distortion between them. Similar measurements could be used to infer relative positioning of the spacecraft. The GIQAS system accuracy is specified at 0.2 pixels.

The technique has also been considered for updating the inertial navigation systems of missiles or aircraft. Scene matching between an image obtained aboard the vehicle and a stored reference can eliminate the drift of an inertial platform. In order to demonstrate this capability in real time, Westinghouse has assembled a laboratory demonstration of AUTO-MATCH, which will be described.

INTRODUCTION

A digital scene matching technique will be described which performs precise registration between images under a variety of conditions. This capability can be used for geometric image correction, or for autonomous navigation of a vehicle with respect to terrain signatures. The technique involves two steps. First, the images are digitally preprocessed to extract edges. This is performed on a line-by-line basis in the images to achieve megapixel per second throughput rates. The edge end-points and its polarity (location of light and dark sides) are obtained, with a bandwidth compression of one or more orders of magnitude achieved. Second, edge end-points are compared between images. An algorithm is available which can perform registration between images independent of relative orientation, and of position and scale over wide ranges. Accuracy is possible to as low as 0.1 pixel depending on the available scene detail.

Details of the digital image processor will be described first, followed by a description of the registration operation. Application of the technique to the NASA GIQAS system (Geometric Image Quality Assessment System) will then be considered, as well as the problem of autonomous vehicle navigation.

DIGITAL IMAGE PREPROCESSOR

Image registration operations are accomplished by a hybrid digital image processor, consisting of a special-purpose preprocessor (to extract key image data) followed by a programmable general-purpose processor (to extract registration vectors). The function of the preprocessor is to extract the features required for registration computations from the gray level image samples. These features are straight-line contours of density gradient. In effect, the preprocessor produces a line drawing of the image. At the same time, the data bandwidth is reduced by one or two orders of magnitude, depending on the selected thresholds for minimum gradient detection and line length. In addition, the preprocessor routinely extracts statistics associated with a uniform matrix of image areas.

Operation of the preprocessor is on a line-by-line basis with respect to the input image. Therefore, video data may be handled directly. Furthermore, storage requirements in the preprocessor are limited to single lines of data only. The preprocessor comprises a series of shift registers. Data flow through the line extraction portion of the preprocessor is shown in Figure 1.

We will demonstrate the individual preprocessor operations with the use of Landsat images 1703-17590 (Reel 2) and 1739-17575 (Reel 2) representing location N 36 deg, W 120 deg (near Fresno, California) on June 26, 1974, and August 1, 1974, respectively. Portions of these images (MSS Band 4) are displayed in Figure 2. In particular, we will concern ourselves with the windows A and A', measuring 125 x 125 pixels in size. Gray level density values for these two areas are shown by Figure 3. The numbers represent the density to the nearest of 16 levels. Numbers above 9 are indicated with an overprinted "/". Large numbers represent dark areas.

Before preprocessing the images for line extraction, spatial filtering operations may be performed on the gray level data for purposes of noise smoothing or equalization of resolution in both dimensions.

To generate the straight-line contours (subsets) of the image, it is first necessary to compute the two-dimensional gradient (derivative) at each image point. This is done with a four-pixel window, which scans across the image in a raster format. The gradient direction (0 to 360 degrees) is quantized to one of 16 discrete directions. To suppress the areas of negligible gradient activity (containing no significant contour or edge information), a threshold is applied to the gradient amplitude. Gradients with amplitudes less than the threshold are set at 0. A display of gradient directions for windows A and A' in Figure 2 is shown in Figure 4. The numbers indicate direction from light to dark, (1 is from left to right). Numbers above 9 are overprinted with a "/".

After gradient thresholding, the edges are generally still too wide for subset generation. Therefore, a gradient thinning operation is performed that basically "skeletonizes" wide edges.

The algorithm uses a raster scanning window containing a gradient cell, X, and four of its nearest neighbors. The neighbors with colinear gradient directions are compared to X. The largest gradient amplitude is then retained. This procedure is repeated sequentially for each gradient point in the image. The maximized gradient display for images A and A' is shown by Figure 5. Compare this with Figure 4.

Edge generation is accomplished by "growing" a line formed by adjacent parallel gradients. As before, a 5-cell scanning window is employed. The new data point is labeled cell X. Its four neighbors are examined to find those containing a parallel (within a tolerance) gradient direction. If one is found, then the neighbor is dropped as a line endpoint, and X becomes the new endpoint. Neighbors that are colinear to the gradient of X are excluded to prevent false lines from forming.

The edges derived from images A and A' are shown in the graphical plots in Figure 6. They are numbered consecutively according to their lowest position on the plots. The polarity (location of light and dark sides) for each edge is coded by the presence or absence of stars at both ends. In general, the absence of the star indicates a change from light to dark in the clockwise direction, for an axis of rotation about the uppermost endpoint. For horizontal edges, the axis of rotation is placed at the right end of the subset.

A second preprocessor function is the collection of statistics over a matrix of square image areas. The measurements amount to a textural analysis of thewindows. They include histograms of gray density, gradient amplitude and direction, and subset length. Average values for gray density and gradient amplitude are also computed.

INITIAL ACQUISITION

The Westinghouse AUTO-MATCH techniques can achieve registration between two line-by-line scanned images of the same area totally independent of relative orientation and independent of position and scale over reasonable ranges. The registration output includes a measure of image similarity between the images, their relative scale and orientation, and the transformation of points between images. These steps are carried out in the sequence shown in Figure 7.

With reference to Figure 7, video signals from both images are digitized and preprocessed to extract image density contours or edges, as described earlier. The edges are defined by their endpoints. Features are formed from the edges that consist of the geometric relationships between pairs of edges and provide properties that are invariant, regardless of relative position, orientation, or scale. For example, these properties can include the relative angles between edges. These features are compared between images, with the initial result being a measure of similarity associated with the registration, as well as a measure of their relative orientation and scale. When the similarity match has been accomplished, endpoints on the corresponding contours in the images can be related. In particular, the center point of one image can be located on the second image.

The computations associated with a pair of subsets are listed in Figure 8. Edges AB and CD in image A correspond to A'B' and C'D' in image 8. A geometric feature is formed between the pairs by connecting endpoints A and C and A' and C'. The angles between the subsets and the connecting lines, γ_1, γ_2, and γ'_1 and γ'_2 will be equal if figures ABDC and A'B'D'C' are similar. Furthermore, their values are invariant with translation, scale, and orientation of these figures in the plane. Accordingly, these angles are the first elements in the geometric features used to achieve automatic acquisition. Along with these angles, the features also include the orientation, ϕ, ϕ', of the connecting lines relative to a reference axis in the image, and the lengths, S and S', of the connecting lines. They also include the edge endpoints.

Initial acquisition is obtained by matching pairs of features between the images with respect to γ, and by clustering the results with respect to relative orientation and relative scale. If the two images are identical except for translation, rotation, and scale, all the features will cluster at a point. If they have relative distortion, the cluster will be dispersed. The amount of acceptable distortion is controlled by an adjustable threshold.

The center of the cluster provides values for the relative orientation and scale of the two images. These values may be used to determine a transformation between the x and y coordinates for the two images. Since corresponding features contain endpoint coordinates, each pair can be used to calculate the nominal coordinates of translation, x_0, y_0, between the images.

These are again clustered to obtain an average over the images, and to eliminate anomalies caused by symmetrical figures such as rectangles. The cluster center in the x_o, y_o plane is used with the ϕ, S values to complete the final transformation from any point in image B to the corresponding point in image A.

Where correction for image warp is desired registration is carried out on a matrix of windows having sufficient density to accommodate the warp function.

PRECISION REGISTRATION

In the event that relative orientation and scale between the images are known, as is often the case, a much simpler computation is possible. In this alternate computation, a search is made in one image for a companion to the endpoint found in the other. The search is carried out over a window corresponding in size to the positional uncertainties between matching endpoints.

Either registration process differs from conventional point-by-point image correlation in several ways. First, only points of high information density (endpoints) are used in the computations; so, the processing load is greatly reduced. Second, since the positions of the endpoints are individually available, the average offset between the image pairs can be estimated directly. Finally, since density values are not used, multispectral or multisensor registration can be accomplished.

Registration operations that assume a prior knowledge of orientation and scale will be demonstrated on the pair of Landsat images in Figure 2. Preprocessor outputs for windows A and A' are given in Figure 6. The results obtained by stepping A against A' by 20 pixels in each direction are shown by Figures 9, 10, and 11. The match index contour of Figure 9 represents the number of matching endpoints at each location, divided by the number available for matching at the same location. Although it is similar to a correlation coefficient, it is used only for the approximate location of the match point. The precise location of the match point is obtained from the zero crossing point for the Δx and Δy contours of Figures 10 and 11. Each point on these contours is obtained from the average offset for the matching endpoints in the x and y directions. A transition from negative to positive values is obtained, somewhat like a discriminator characteristic.

Determination of the accuracy of the registration operation is based on the assumption that the uncertainty in the position of an endpoint, relative to its true position, is random. The uncertainty includes noise and quantization effects, and the characteristics of the preprocessor algorithm. If the average uncertainty is k' pixels, then the error for a window pair with n matching endpoints will be $k'/\sqrt{n}$. In a test with 40 pairs of Landsat images, it was found that the average error was less than 0.2 pixels, and the value for k for the Landsat images is approximately 2 pixels.

GEOMETRIC IMAGE QUALITY ASSESSMENT SYSTEM (GIQAS)

The AUTO-MATCH technique is being applied to a system for assessment of geometric image quality, to be installed at NASA-Goddard later this year. The system will measure the registration vectors over an array of window pairs from LANDSAT images, so as to determine the distortion between them. A block diagram of the system, which will serve as one component of the Image Processing Facility (IPF), is shown by Figure 12. A real-time demonstration of registration performance, using a special-purpose preprocessor, is shown by Figure 13. The preprocessor is on the table at left. This unit provides data throughput rates up to 2.0 megapixels per second. Registration operations are carried out in the militarized minicomputer at center.

AUTONOMOUS NAVIGATION

The AUTO-MATCH technique could be used for precise autonomous navigation of spacecraft or aircraft in the manner shown by Figure 14. AUTO-MATCH makes use of a sensor on-board the vehicle, and provides update information to the vehicle navigation system. Reference data is obtained from previously sensed images or from ground operations. In either case, storage or transmission of the reference data can be accomplished with compressed bandwidth by first preprocessing the images.

Westinghouse completed a feasibility study of the navigation update capability of AUTO-MATCH for the Air Force Avionics Laboratories in 1977. (Final Report AFAL-TR-77-88). A side-looking radar was proposed for the on-board sensor. In order to simplify reference data base preparation, USGS airphotos were used without modification. As a result of this choice, edge polarization data could not be used, since the relative contrast at the edges in radar and airphotos differs. Samples of the images used in the study are given in Figure 15. Four image pairs were correctly registered from these samples, in spite of heavy shadowing in the radar image. Differences in orientation and scale between samples were removed by simple computations applied only to the preprocessed edges, based upon estimated values for these parameters. The estimated values would normally be obtained from the navigation system.

Performance statistics were obtained from a series of 58 radar/airphoto pairs covering mountainous and rural terrain, urban areas, and land-water combinations. For single image pairs, correct acquisition was obtained in about 90% of the samples. Fix reliability can be greatly improved by the use of the windows in redundant combinations. Fractional pixel position accuracy was also demonstrated on this same image set.

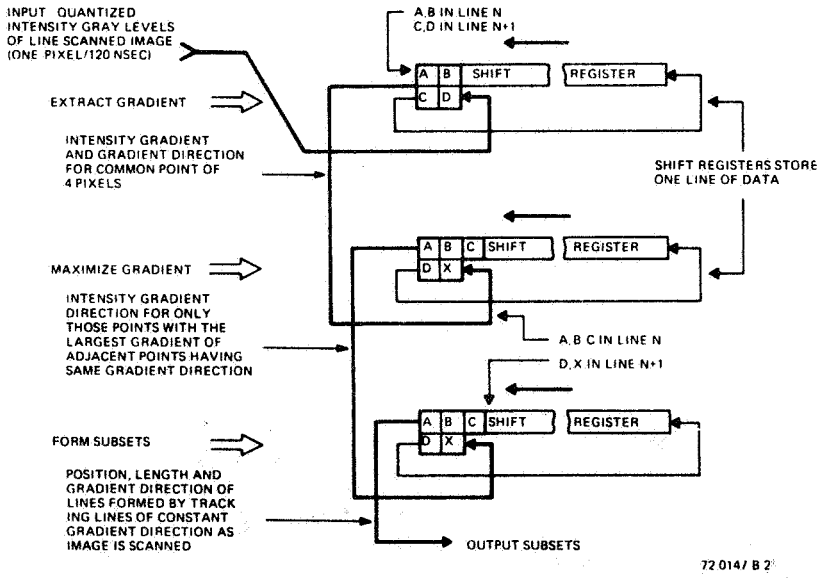

Figure 1. Flow of Data Through the Preprocessor

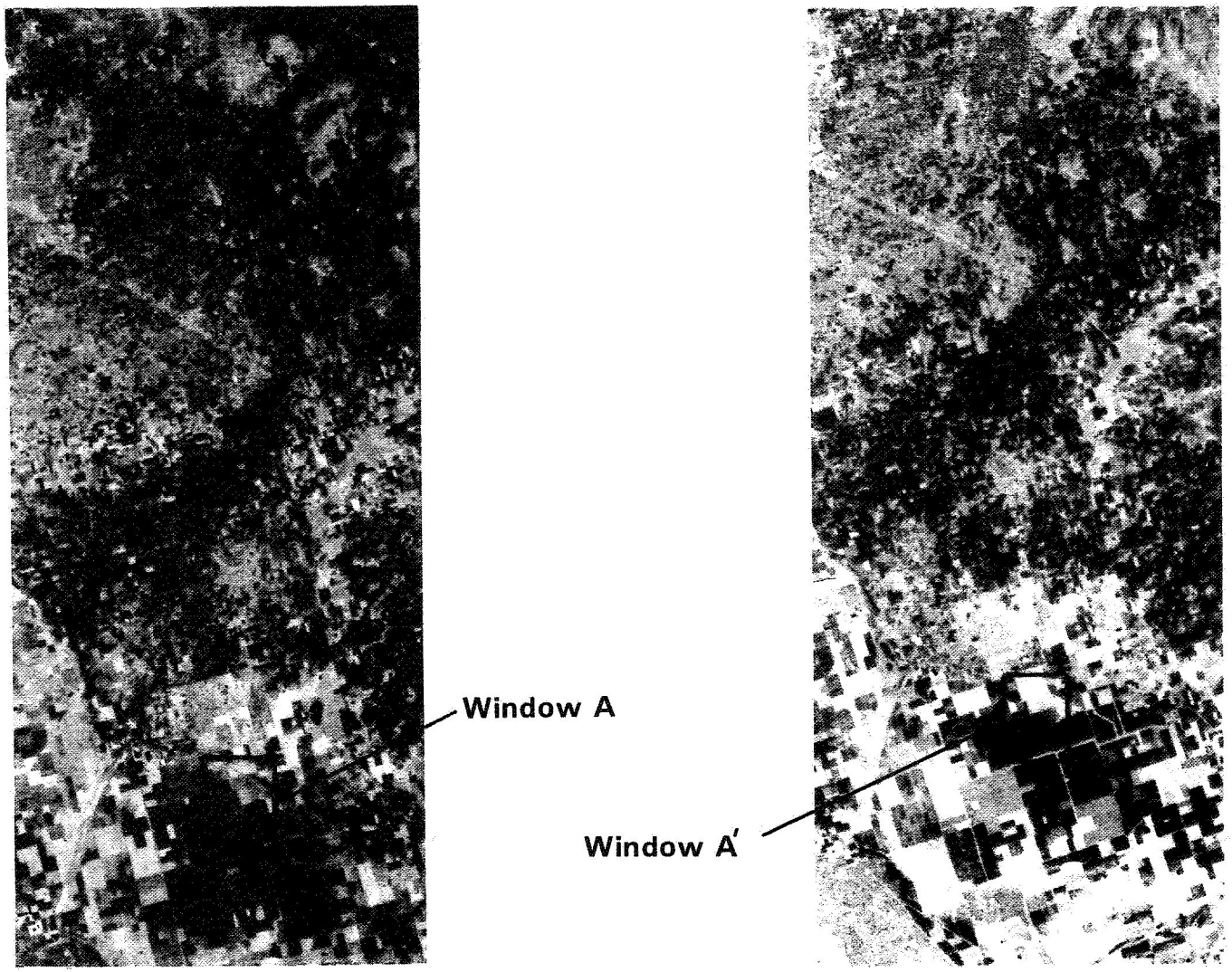

Figure 2. Portions of LANDSAT Images - (a) 1703-17590 and (b) 1739-17575 in the Vicinity of Fresno, California for June 26, 1974, and August 1, 1974, Respectively

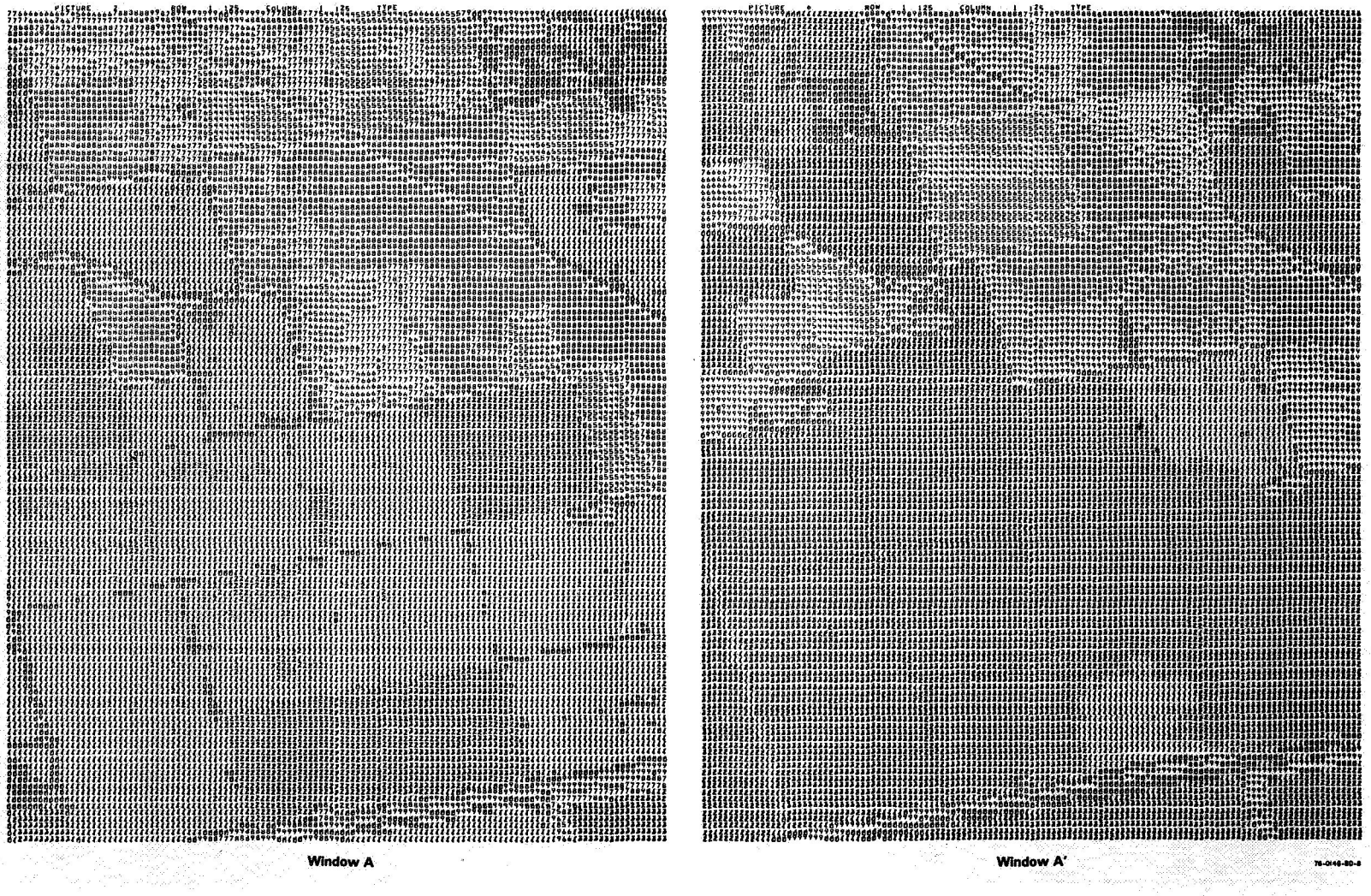

Figure 3. Gray Level Density Values for Windows A and A' in Figure 2

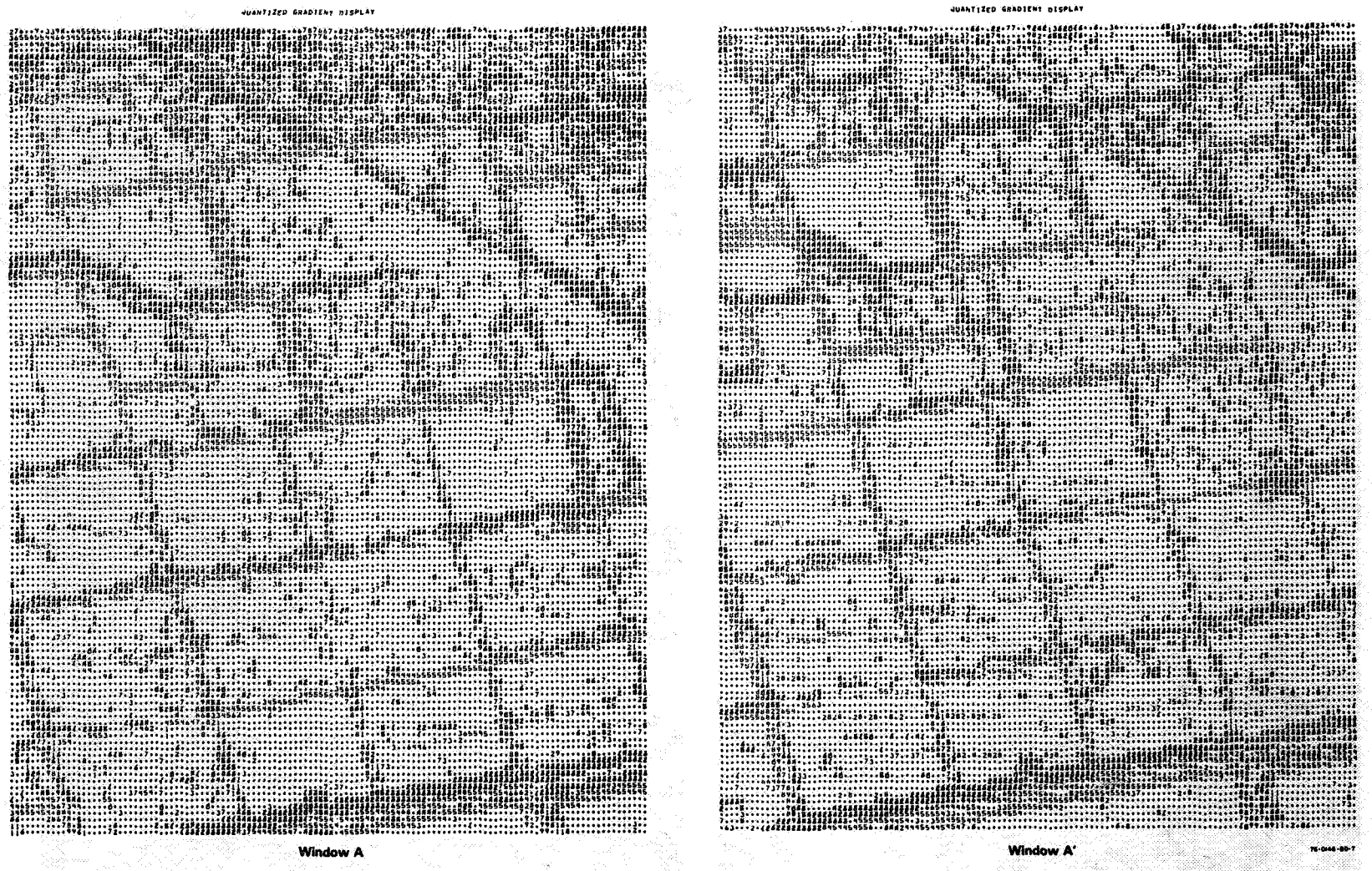

Figure 4. Gradient Directions for the Windows in Figure 2

Figure 5. Maximized Gradients for the Windows in Figure 3.

Figure 6. Line Contours (Subsets) for the Windows in Figure 2

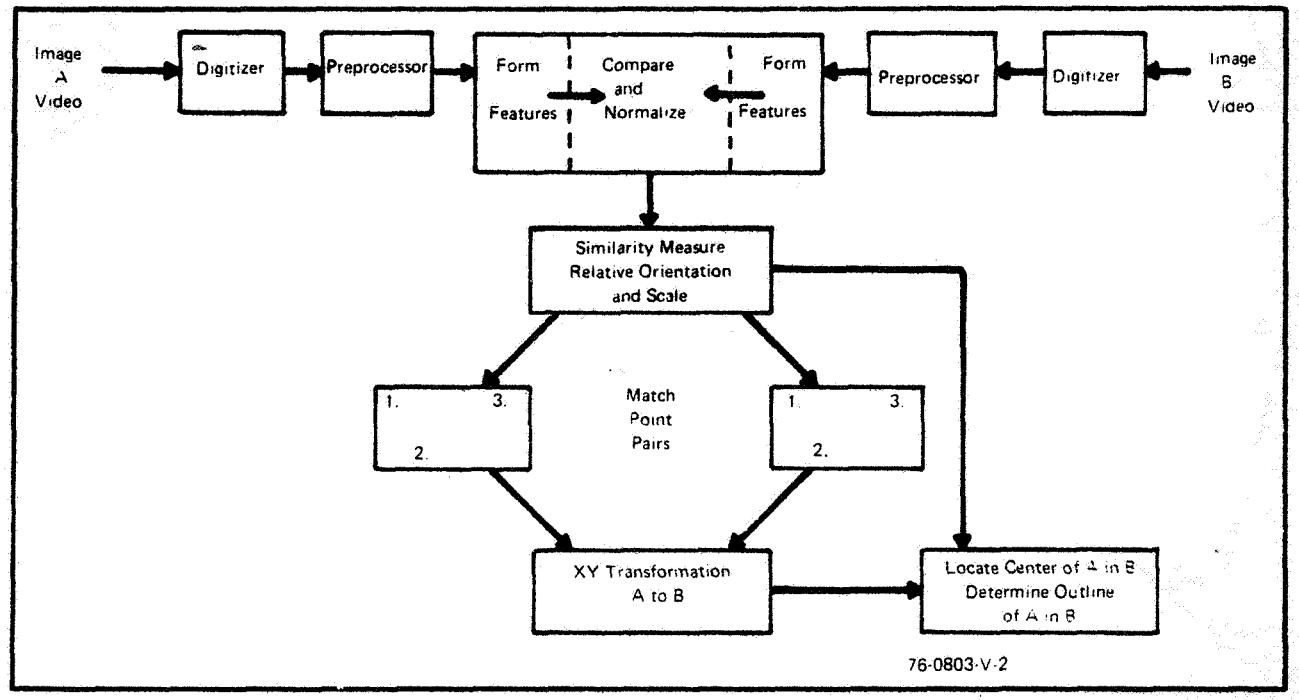

Figure 7. Registration Steps for Initial Acquisition

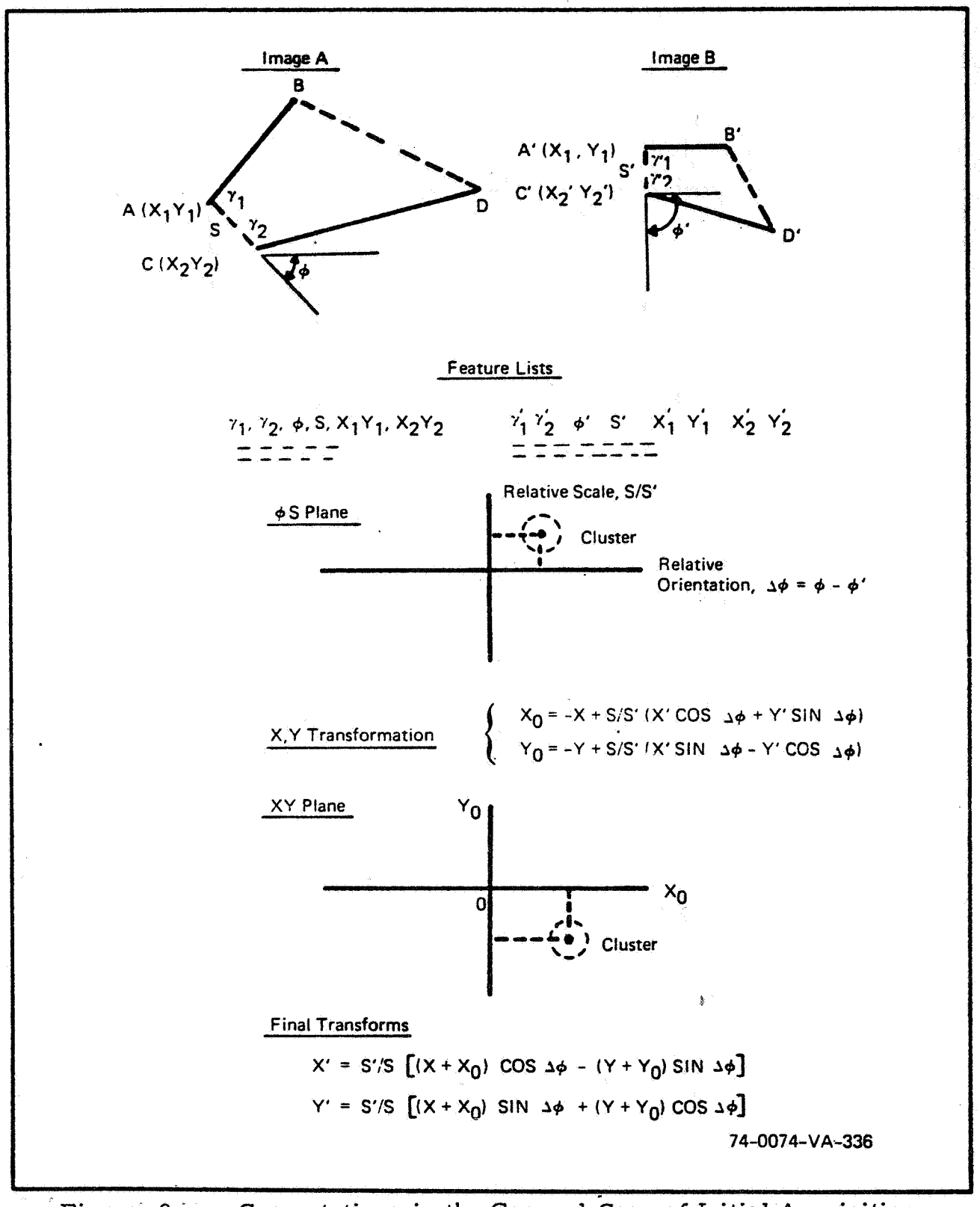

Figure 8. Computations in the General Case of Initial Acquisition between Images with Uncertainty of Position, Orientation, and Scale

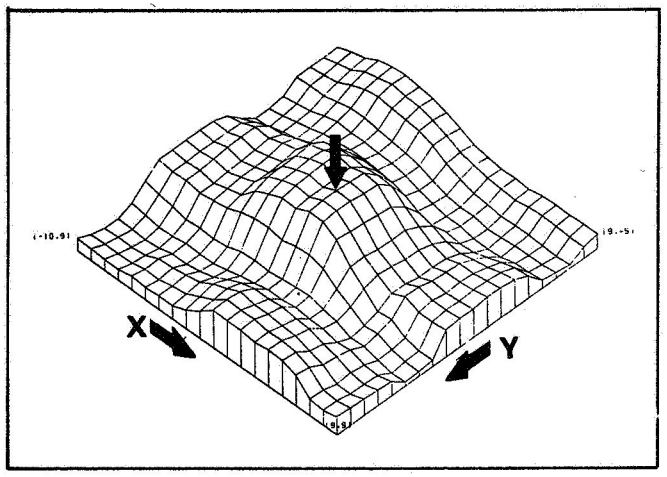

Figure 9 . Match Index Contour Obtained by Stepping Images A and A' of Figure 2

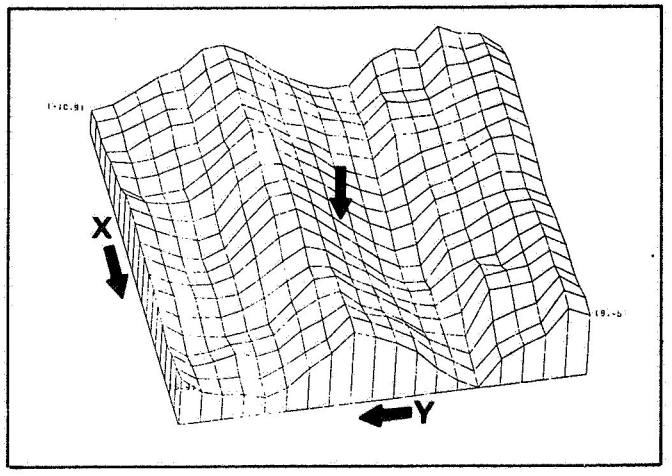

Figure 11. The ΔY Contour for Figure 9

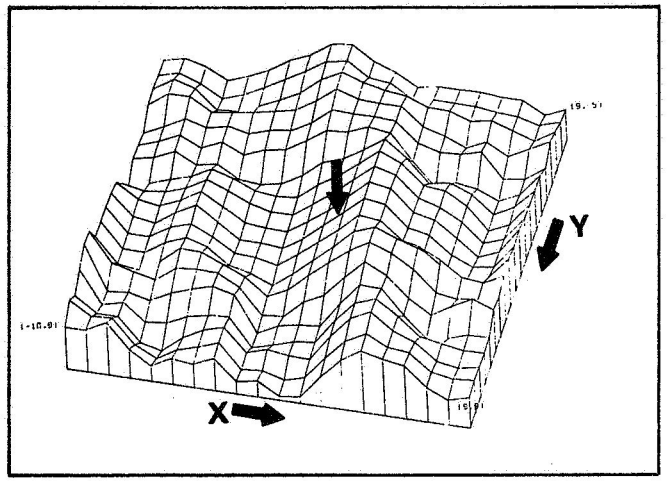

Figure 10. The ΔX Contour for Figure 9

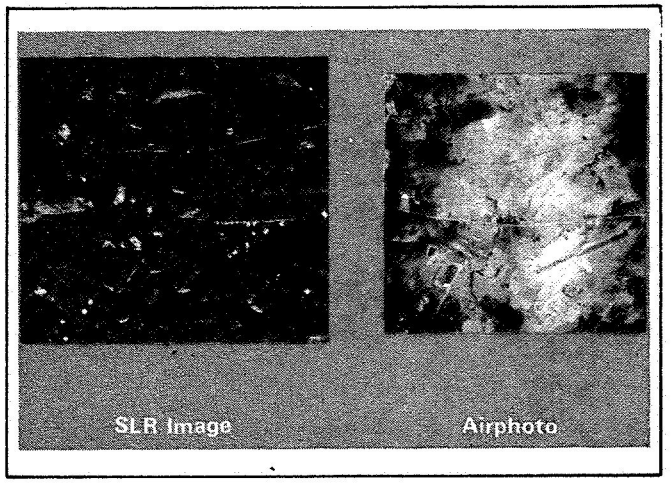

Figure 15. Images of the San Luis Obispo, CA, Area

Relationship of Hardware Components for Geometric Image Quality Assessment System

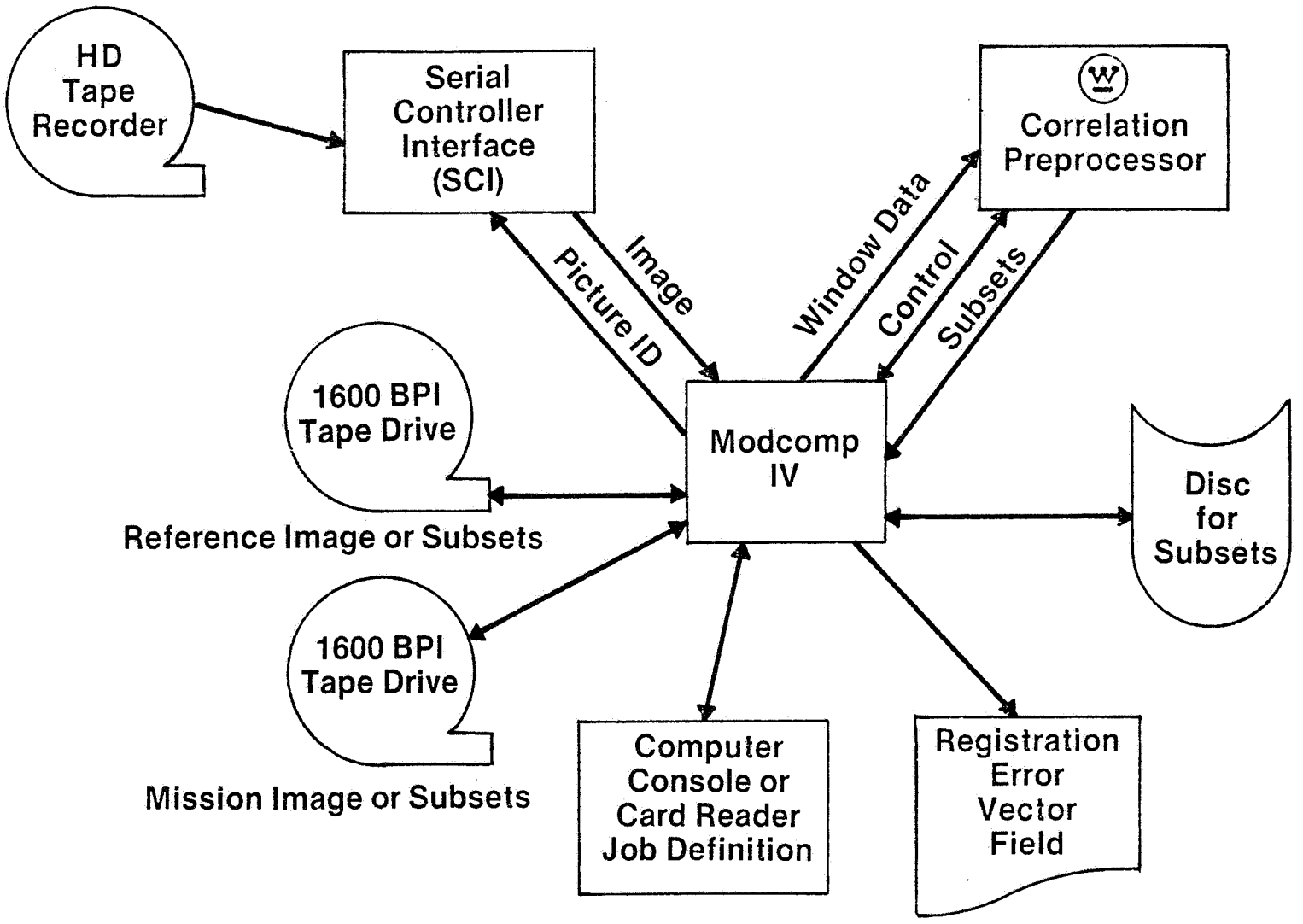

Figure 12.

78-0300-VB-6

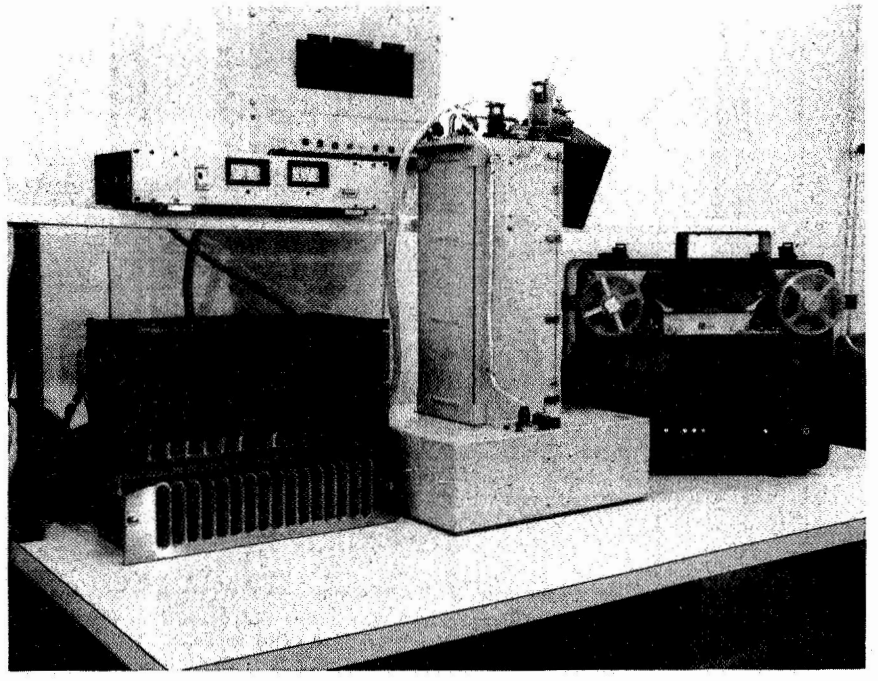

Figure 13. AUTO-MATCH Demonstration in the Westinghouse Image Processing Laboratory

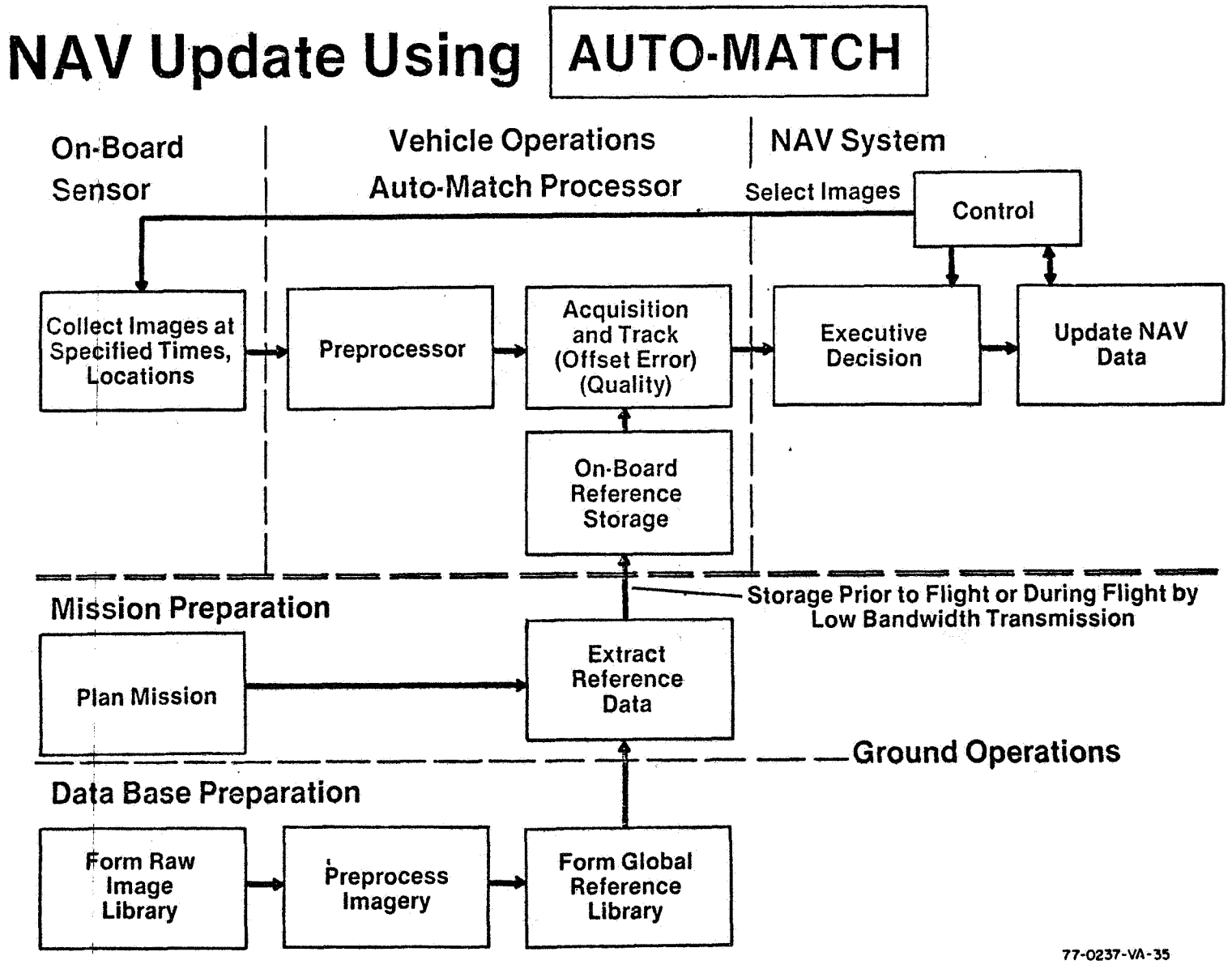
NAV Update Using AUTO-MATCH
On-Board Sensor
Vehicle Operations
Auto-Match Processor
NAV System
Select Images
Control
Collect Images at Specified Times, Locations
Preprocessor
Acquisition and Track (Offset Error) (Quality)
Executive Decision
Update NAV Data
On-Board Reference Storage
Storage Prior to Flight or During Flight by Low Bandwidth Transmission
Mission Preparation
Plan Mission
Extract Reference Data
Ground Operations
Data Base Preparation
Form Raw Image Library
Preprocess Imagery
Form Global Reference Library
77-0237-VA-35

Figure 14.

ORBIT/ATTITUDE ESTIMATION WITH LANDSAT LANDMARK DATA

D. L. Hall and S. Waligora

Computer Sciences Corporation

ABSTRACT

Several studies involving the use of Landsat Landmark data for orbit/attitude and camera bias estimation have been performed. The preliminary results of these investigations are presented. Three basic areas of work are covered. First, the Goddard Trajectory Determination System (GTDS) error analysis capability was used to perform error analysis studies. This provided preliminary guidelines for subsequent work with actual data. A number of questions were addressed including parameter observability and sensitivity, effects on the solve-for parameter errors of data span, density and distribution and a priori covariance weighting. The second area of investigation was the use of the GTDS differential correction (DC) capability with actual landmark data. The rms line and element observation residuals were studied as a function of the solve-for parameter set, a priori covariance weighting, force model, attitude model and data characteristics. Sample results are presented. Finally, verification and preliminary system evaluation of the Landsat NAVPAK system for sequential (extended Kalman Filter) estimation of orbit, attitude and camera bias parameters is given.

SECTION 1 - INTRODUCTION

1.1 OVERVIEW

Landmark data obtained from Earth pictures taken by onboard spacecraft cameras can be used to: provide a means of autonomous navigation (References 1 and 2); aid in on-the-ground orbit and attitude determination (References 3 and 4), and aid in the geographical and geometrical registration of the Earth pictures for scientific users (Reference 4 and 5).

An important series of satellites that provides Earth pictures is the Landsat series. This paper describes two research (non-operational) software systems which have been developed to test the feasibility of orbit and attitude estimation using Landsat (Landsat-1 and -2) landmark data. The software development was performed by the authors and other staff members of the Computer Sciences Corporation (CSC) for the Goddard Space Flight Center (GSFC). Contained in this paper is an overview of the software systems (Section 2), summary of the mathematical models (Section 3), and some initial numerical results (Section 4). The remainder of this section reviews the Landsat picture data used by the two software systems, and summarizes the numerical results.

1.2 LANDSAT PICTURE DATA

The Landsat-1 and -2 spacecraft are Earth-stabilized with a low altitude (900 km), near polar (inclination 99 degrees), Sun-synchronous orbit. Their primary function is to take continuous pictures of the Earth. Hence, they are provided with an attitude control system that keeps them triaxially stable, i.e., the platform is (nominally) maintained in a horizontal position with respect to local vertical and faces forward (in the direction of the velocity). The spacecraft are equipped with a multispectral scanner (MSS), which enables them to take continuous scans 185 km wide, which are blocked to 185x185 km images on the ground. Scans over roughly 25 seconds yield the 185x185 images in

several spectral bands. The pictures are transmitted to the Earth as two-dimensional arrays of gray levels with picture coordinates consisting of line and element integers. Data from the return beam vidicon (RBV) camera system on Landsat-1 and -2, which also provides Earth pictures, is not used by the software systems discussed in this paper. Details of the Landsat configuration are given in Reference 6 and shown schematically in Figures 1-1 and 1-2. Figure 1-2 indicates the Landsat-1 and -2 ground coverage pattern. Picture data obtained by the MSS consist of intensity measurements in a two-dimensional grid. There are integer pairs (line and element) that specify a location within the grid. Each quantized location is called a pixel and has the dimensions (on the ground) of 79 meters in elevation (latitude) and 56 meters in azimuth (longitude). The identification that a picture coordinate pair is associated with the known geodetic coordinates of a point on Earth constitutes a single landmark observation. The creation of landmark observations is discussed in Section 2.1.3.

1.3 SUMMARY OF RESULTS

Initial numerical results of using Landsat-1 and -2 landmark data for S/C orbit/attitude estimation were obtained using two software systems. The Landsat NAVPAK system allows sequential orbit/attitude estimation using an extended Kalman filter (EKF). The Research and Development Goddard Trajectory Determination System (R&D GTDS) was modified to allow batch differential correction (DC) orbit/attitude estimation using Landsat data. The data set used to obtain preliminary numerical results is discussed in Section 4 and consists of 106 landmark observations over a five-minute Landsat pass.

Several numerical experiments were performed using both the EKF and DC. Effects studied included the choice of solve-for parameters, the influence of the a priori covariance matrix, the use of wheel rate data to aid attitude modeling and force model effects. The basic results are summarized below.

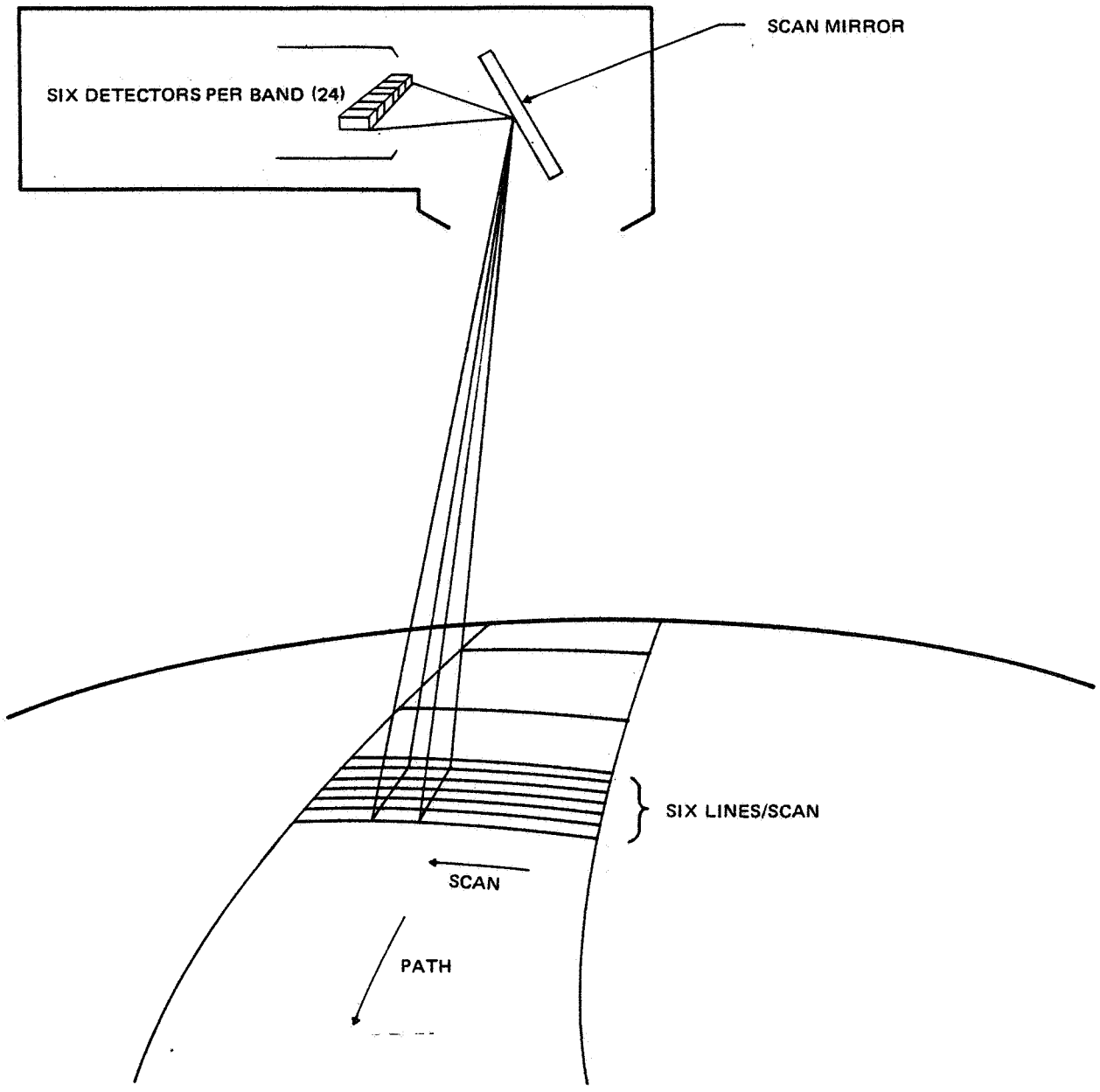

Figure 1-1. Landsat 1 and 2 Multispectral Scanner Coverage

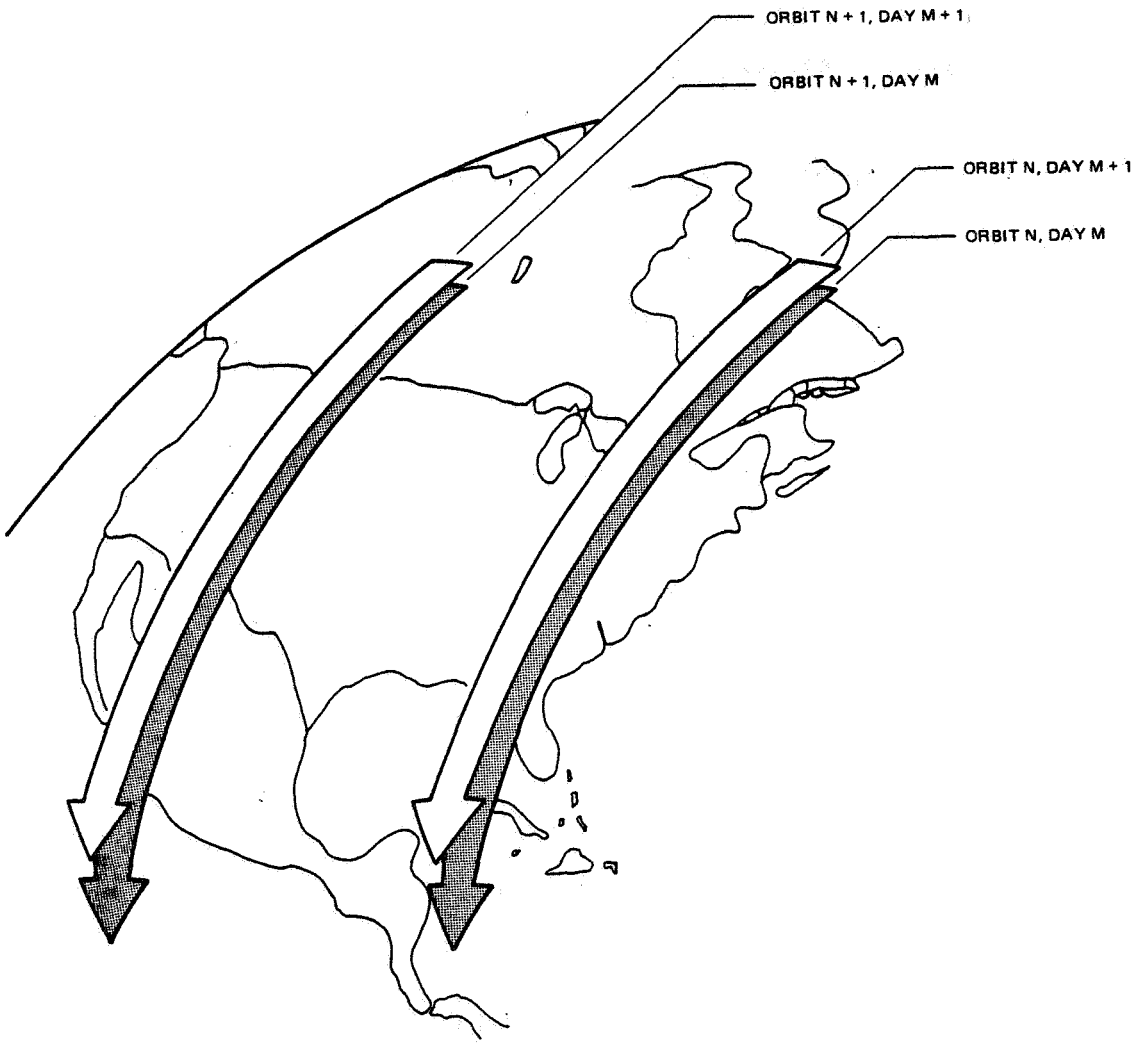

Figure 1-2. Landsat 1 and 2 MMS Ground Coverage Pattern

Batch (DC) Orbit/Attitude Estimation Results

In the following results, the residuals are computed based on a converged differential correction solution. Parameters which are not estimated are set to a priori values annotated on the Landsat image associated with the start of the data set.

- The S/C orbital parameters and several coefficients of an attitude time series model can be estimated using batch processing of Landsat landmark data. For a five-minute data span rms residuals of 7.3 pixels and 9.2 pixels can be obtained for scan angle and elevation angles, respectively.
- The use of wheel rate data for attitude modeling significantly improves the fit, resulting in residuals of 2.7 and 3.6 pixels for scan and elevation angle when solving for S/C state and three attitude coefficients as above.
- The choice of a priori covariance matrix (particularly the ratio of the S/C state covariance to the attitude covariance) influences the final observation residuals by a factor of about 40% when varied over several orders of magnitude range.
- Camera biases are indistinguishable from constant attitude coefficients when solved for using a five-minute data span.
- The force model consisting of the two body gravitational attraction of the Earth, J_2 nonspherical gravitational effect and drag model is completely adequate over a five-minute data span. More complicated models including higher order nonspherical geopotential terms, lunar/solar third-body effects, and solar radiation pressure affect the rms residuals by less than 0.01 pixel.

Sequential (EKF) Orbit/Attitude Estimation Results

In the following results, the residuals are obtained after one pass of the EKF through the data set. The final values of the solve-for parameters are propagated back through the observation set to compute observation residuals.

- The NAVPAK EKF was able to estimate S/C orbit and constant attitude parameters using landmark data. For a five-minute data span, rms residuals of 14.7 pixels and 11.9 pixels can be obtained for scan angle and elevation angles, respectively.
- Wheel rate data provided a slight decrease of residuals for a continuous (without gaps) data set. A significant improvement was obtained with wheel rate data when the landmark data contained at least one gap. Hence the wheel rate data had a stabilizing effect.
- Variation of the a priori covariance matrix (the relative weighting between S/C orbit and attitude covariances) caused a variation of about 20% in the overall observation residuals.
- The EKF was unable to realistically estimate multiple coefficients for each component of attitude (roll, pitch and yaw).
- The camera biases were indistinguishable from constant attitude coefficients.

SECTION 2 - SOFTWARE SYSTEM OVERVIEW

There are two research software systems described in this paper. The first is the Landsat NAVPAK (Navigation Package) system which provides for data preprocessing, Landsat image display and manipulation, observation creation, and orbit/attitude estimation using Landsat data via an extended Kalman filter. The second system is a portion of the Research and Development Goddard Trajectory Determination System (R&D GTDS) which has the capability to perform orbit/attitude estimation using Landsat data via a batch least squares or differential correction (DC) approach. The basic features of these systems are described in this section.

2.1 LANDSAT NAVPAK

The Landsat NAVPAK is a menu driven, interactive software (FORTRAN) system which has been implemented on a PDP 11/70 computer operating under the RSX-11D system. Reference 7 gives details of the mathematics, software and user instructions for NAVPAK. There are four basic functions performed by NAVPAK including data preprocessing, Landsat image display and manipulation, observation creation, and orbit/attitude estimation via an extended Kalman filter. Each of these functions is described below.

2.1.1 Data Preprocessing

The input data to the NAVPAK System are Landsat imagery received from Computer Compatible Tapes (CCTs), momentum wheel rate data from preprocessed data tapes, and user-specified estimation parameters. Another possible input is a R&D GTDS simulated observations tape, which can be used to verify the operation of the estimator. The data preprocessing function of NAVPAK provides for a manipulation of the input data to make it usable for the NAVPAK estimation and observation creation functions. The data preprocessing consists of the following.

Firstly, one or more single band Full Scene Images (FSIs) is reconstructed from a set of CCTs. Four CCTs are required to produce one image for each spectral band. This process is performed for each usable scene in a pass of Landsat imagery.

Secondly, on the IBM S/360-95 a raw wheel rate tape is converted to a PDP-11/70 compatible tape and the low frequency components of attitude (yaw, roll, and pitch) are determined. The tape is then moved to the PDP-11/70, where a file containing spacecraft body rates is created by removing the low frequencies, as described in Section 3.2.

For observation creation described in Section 2.1.3, Landmark reference chips and Super Search Areas are required. A reference chip is a 16 x 16 pixel area in a Landsat picture, which is centered on a landmark of known geodetic coordinates. Hence, the operator displays a Landsat picture (Section 2.1.2) and manually locates a position whose geodetic coordinates are known from, say, a reference map. The reference point is usually an easily recognizable feature, such as a road intersection, which has been accurately surveyed. The data preprocessor allows the user to extract a chip and store it on a file along with an identifying name and number and associated geodetic coordinates. The creation of a chip library is a one time only NAVPAK function.

Once a chip library exists, it is necessary to create a set of Super Search Areas (SSAs) to process a current pass of data. These SSAs are 100 x 100 pixel areas which are expected to contain areas which correspond to reference chips. Thus, for observation creation, each observation to be generated requires a SSA from the current pass of Landsat imagery and an associated reference chip (obtained from an original pass of Landsat data).

2.1.2 Image Display and Manipulation

The second NAVPAK function is Landsat image display and manipulation on an International Imaging System (I^2S) video device. A full 185km Landsat picture can be displayed on the I^2S by a reduced mode in which every sixth line and every eighth element are displayed. Also, portions of a picture can be displayed at full resolution (viz. every pixel displayed). In addition, any portion of a picture may be displayed at an expanded (zoomed) scale with a zoom ratio up to 64 to 1. The zoom is obtained by a two-dimensional cubic interpolation scheme.

The video device has a cursor (electronic cross-hair marker on the screen) which can be moved manually by a track-ball. The image display and manipulation function of NAVPAK provides for a read out of the picture coordinates (line and element numbers) corresponding to the location of the cursor. A standalone program is available to use these picture coordinates, along with an estimate of the spacecraft orbit and attitude to compute the geodetic coordinates associated with the cursor location. Finally, NAVPAK allows a user to automatically drive the cursor to the picture coordinates which correspond to a specified geodetic coordinate pair (φ, λ). This latter is done using the geodetic annotation on the Landsat picture instead of estimated orbit/attitude parameters.

2.1.3 Observation Creation

The third function performed by Landsat NAVPAK is observation creation. For a current pass of Landsat imagery, there exists a set of chips (in the chip library) which correspond to geodetic locations within the pass. The data preprocessor has been used to create SSAs corresponding to those chips. Each observation is created by correlating a SSA with its associated reference chip. This is done by an automatic direct correlation algorithm. This results in the association of picture and time (from a picture in the current pass) and the geodetic coordinates of the landmark. These observations are then stored in an observations file to be used by the estimator.

2.1.4 Orbit/Attitude Estimation

The fourth function performed by Landsat NAVPAK is spacecraft orbit/attitude estimation using an extended Kalman filter. This filter has the capability of solving for 24 parameters including 6 state parameters (geocentric inertial Cartesian position and velocity components), 15 attitude coefficients, and 3 spacecraft camera biases. Attitude modeling is obtained by solving for coefficients of fourth-degree time polynomials for the roll, pitch and yaw angles. In addition, an option exists to use integrated high frequency momentum wheel rate data to model the high frequency attitude motion. The force model for the spacecraft motion includes atmospheric drag using a modified Harris-Priester model, the two-body gravitational attraction of the Earth and the J_2 harmonic coefficient. Integration of the equations of motion are provided by a fourth-order Runge-Kutta method with modified Fehlberg coefficients. The transition matrix propagation is done by a Taylor series. Process noise is currently being implemented. The numerical results obtained in this study indicate that the force model is adequate for data spans not exceeding 10 minutes in length (i.e., a single pass over the United States).

A number of options exist for the operation of the filter and input and output. The data may be processed one point at a time with operator intervention at each point or an entire set of data processed. In addition, a data set may be processed iteratively such that the estimated parameters and covariance matrix for one iteration are propagated back to the first observation time to be used as a priori values for the succeeding iteration. Input data base management allows for control of the a priori solve-for parameters and covariance matrix, selection of force model terms, selection of solve-for parameters, control flags for fading memory, observation editing, process noise and use of wheel-rate data for attitude modeling. Output reports include initial conditions report, observation residuals output, end of iteration solve-for parameter and covariance matrix output. In addition the filter update history may be output. Details of the orbit/attitude mathematics are given in the next section.

2.2 R&D GTDS

The R&D GTDS is a very large (500k core) collection of FORTRAN subroutines to provide orbit/attitude determination, data simulation and error analysis for GSFC research. A number of data types are provided for, with state-of-the-art sophistication in spacecraft dynamic modeling and numerical techniques for orbit propagation. The fundamental mathematical specifications for this system are given by Reference 8. The system was enhanced to process Landsat landmark data (Reference 4). Specifically, orbit/attitude estimation can be done using Landsat landmark data by a batch weighted least-square method. The R&D GTDS does not have any capability for Landsat picture display and manipulation or observation creation (other than data simulation). For that reason, Landsat NAVPAK was used in this study to generate Landsat landmark observation data. Then, the R&D GTDS was used for orbit/attitude estimation for comparison with the sequential estimation by NAVPAK.

A number of numerical and force model options exist in the R&D GTDS. The spacecraft force model may be specified from simple two-body gravitational

force to a 21 × 21 geopotential expansion. In addition, several atmosphere models are available as well as lunar/solar third body gravitational forces and solar radiation pressure. The integration of the spacecraft differential equations of motion may be done by Runge-Kutta methods (up to 8th order) or Cowell methods (up to 12th order). Spacecraft orbit propagation may also be done by variation-of-parameters methods or general perturbations techniques such as the Brower-Lyddane method.

The observation model used in the R&D GTDS for Landsat data is identical to that used in NAVPAK, including the attitude model. In Section 4, comparisons are made between batch estimation using the R&D GTDS and sequential estimation using NAVPAK.

SECTION 3 - MATHEMATICAL MODELS

The observation and attitude models used in the R&D GTDS and Landsat NAVPAK systems are identical. As previously indicated, differences exist in the force model and numerical techniques used by each system for spacecraft orbit propagation. Also, the two systems use different estimation techniques. Both the estimation techniques and the spacecraft orbit propagation and numerical methods have all appeared in the literature. Hence, the detailed mathematics will not be presented here. On the other hand, the observation model and attitude models have not appeared in the literature. Thus, this section presents the Landsat observation model and attitude model.

3.1 OBSERVATION MODEL

The observation model in the R&D GTDS and Landsat NAVPAK is used to predict the observed picture coordinates (viz. the integer pair which specifies a location within the picture) as a function of an observation time t_s, a given satellite state vector $(\bar{r}_o, \dot{\bar{r}}_o)$ at some epoch time, t_o, the satellite attitude time polynomial coefficients ($R_o, R_1, \ldots, R_4$ for roll, Y_i for yaw and P_i for pitch), camera biases (α, β, γ) and the geodetic coordinates (ϕ, λ) of a point on Earth which corresponds to the location within the picture. Instead of the integer pair (ℓ, e) to specify locations within a picture, NAVPAK and the R&D GTDS models use an equivalent set of direction angles (ψ, ϵ). The transformation between (ℓ, e) and (ψ, ϵ) is developed in References 4 and 9. Slight modifications were made to the transformation constants to reflect experience with actual Landsat imagery. The observation time can be obtained from the time associated with the picture (scene) center, t_{ct} and the picture coordinates (ℓ, e) by the linear relation developed in Reference 4. The time system used in the NAVPAK and R&D GTDS processing of Landsat data is Universal Time Coordinated (UTC).

In order to predict the angles ψ and ϵ at a given time t, four basic coordinate systems are required.

Three of systems are shown in Figure 3-1, these are:

- (x, y, z)--The geocentric inertial Cartesian coordinate system in which all of the basic computations, such as the numerical integration of the spacecraft equation of motion, are performed. The origin is at the center of the Earth and the z axis is along the Earth's axis of rotation positive towards the north pole. The x axis points towards the vernal equinox while the y axis completes the right hand orthogonal system. The (x, y, z) system is fixed in inertial space. A discussion of geocentric inertial coordinate systems (there are several, all available in the R&D GTDS, such as true-of-data, mean-of-1950, etc.) can be found in Reference 8 or any standard celestial mechanics text such as Reference 10.

- (x', y', z')--The geocentric non-inertial cartesian coordinate system in which geodetic landmark coordinates (ϕ, λ) are measured. In this coordinate system the x' axis points towards the intersection between the Greenwich meridian and the Earth's equator. The z' axis lies along the Earth's axis of rotation and y' completes the right hand orthogonal set. This system rotates with the Earth (viz., it is fixed with respect to surface of the Earth).

- $(\hat{i}, \hat{j}, \hat{k})$--This is the instantaneous roll, pitch and yaw coordinate system. The $(\hat{i}, \hat{j}, \hat{k})$ system is a moving "orbital" reference frame defined such that,

$$\bar{I} = \bar{j} \times \bar{k}, \quad \bar{j} = \frac{\bar{r}_s \times \bar{v}_s}{|\bar{r}_s \times \bar{v}_s|}, \quad \bar{k} = \frac{\bar{r}_s}{|\bar{r}_s|} \tag{3-1}$$

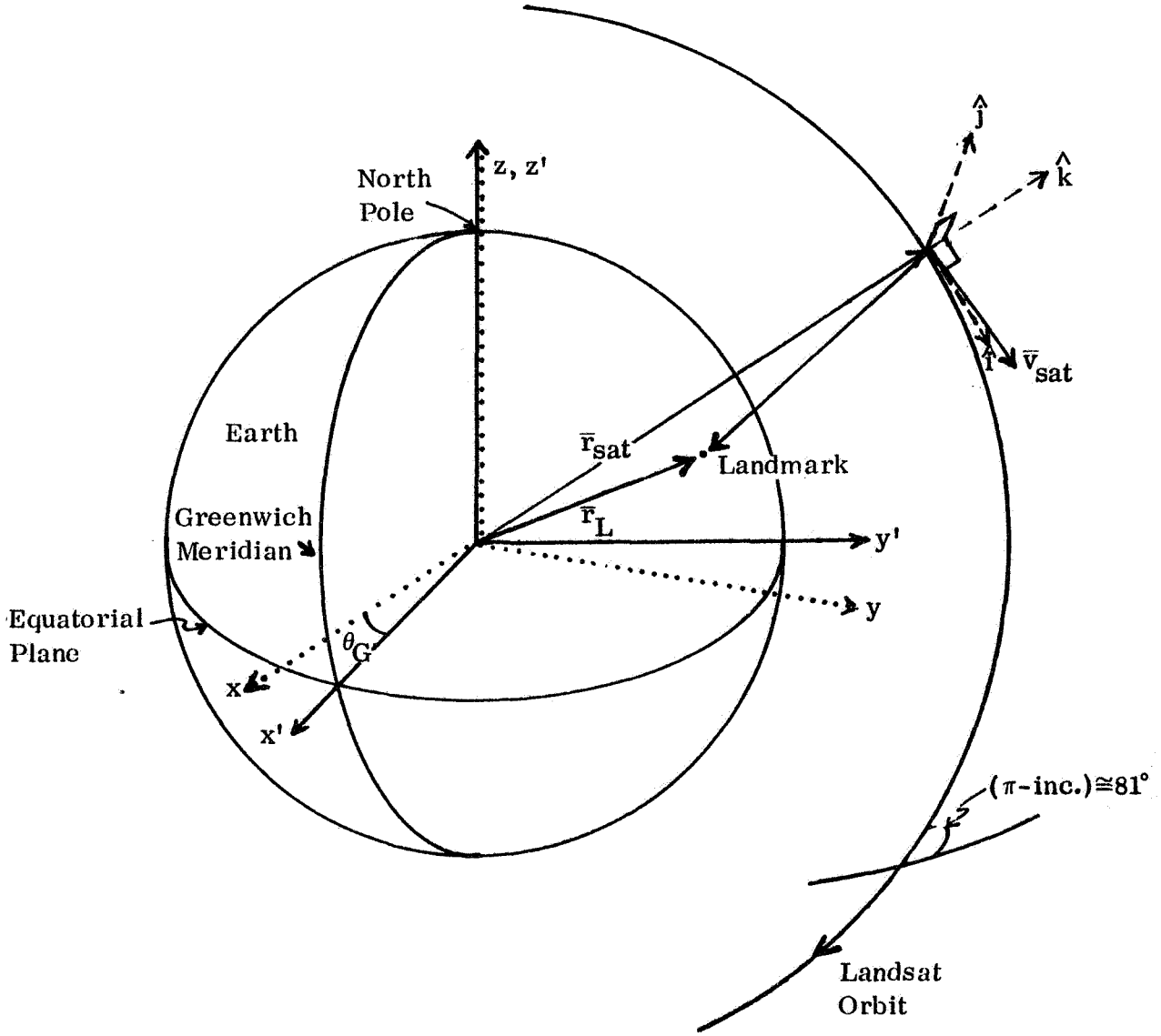

Figure 3-1. Landsat Orbit and Attitude Schematic

Note: A Landsat orbit and spacecraft nominal attitude are shown schematically relative to geocentric coordinates.

where $\bar{r}_s$ and $\bar{v}_s$ are the spacecraft position and velocity expressed in the (x, y, z) system. It is with respect to this system that the orientation of the spacecraft is measured.

The (x'', y'', z'') system represents the spacecraft body axis system. This coordinate system is centered at the spacecraft. The spacecraft is nominally aligned along the roll, pitch and yaw $(\hat{i}, \hat{j}, \hat{k})$ frame. However, the time dependent misalignment between the spacecraft body system and the $(\hat{i}, \hat{j}, \hat{k})$ frame is modeled by the attitude rotation matrix

$$S = \begin{pmatrix} \cos P \cos Y & \cos P \sin Y & -\sin P \\ -\cos R \sin Y + \sin R \sin P \cos Y & \cos R \cos Y + \sin R \sin P \sin Y & \sin R \cos P \\ \sin R \sin Y + \cos R \sin P \cos Y & -\sin R \cos Y + \cos R \sin P \sin Y & \cos R \cos P \end{pmatrix} \quad (3\text{-}2)$$

where R, P and Y are the time dependent roll, pitch and yaw angles discussed in Section 3.2.

Given the geodetic coordinates (geodetic latitude, ϕ, and longitude, λ) of a point on Earth the non-inertial geocentric cartesian coordinates (viz., the x', y', z') are found by the following transformation.

$$\bar{r}'_L = \begin{cases} s \cos \lambda \cos \varphi \\ s \sin \lambda \cos \varphi \\ s \sin \varphi \left(1 - E_e^2\right) \end{cases} \quad (3\text{-}3)$$

where the Earth's eccentricity, E_e, is

$$E_e^2 = 2 \cdot f - f^2 \quad (3\text{-}4)$$

where f is the flattening coefficient of the Earth ($f \approx 1/298.3$), and s is the distance from the landmark to the z' axis measured along $\bar{r}'_L$. This is

$$s = \frac{R_e}{\sqrt{1 - E_e^2 \sin^2 \varphi}} \tag{3-5}$$

with R_e the mean equatorial radius of the Earth. The Earth is represented as an ellipsoid, which has an x', y' plane circular cross section. Any plane which contains the z' axis intersects the ellipsoid to form an ellipse (meridian) of semimajor axis R_e and eccentricity E_e.

In order to represent $\bar{r}'_L$ in the geocentric inertial coordinate system (x, y, z) the following transformation is performed

$$\bar{r}_L = B(t)^{-1} \bar{r}'_L \tag{3-6}$$

where

$$B(t) = \begin{bmatrix} \cos[\theta_g(t)] & \sin[\theta_g(t)] & 0 \\ -\sin[\theta_g(t)] & \cos[\theta_g(t)] & 0 \\ 0 & 0 & 1 \end{bmatrix} \tag{3-7}$$

The angle $\theta_g(t)$ is the time dependent Greenwich hour angle. The NAVPAK and R&D GTDS use the true-of-date system. NAVPAK evaluates θ_g by Newcomb's expression which includes only precession effects, while the R&D GTDS evaluates θ_g to include both precession and nutation. The use of the two different methods for determining θ_g is of significance only when comparing the epoch S/C state vector components obtained by NAVPAK and R&D GTDS. The effect

on the observation residuals is negligible. In the R&D GTDS the evaluation of $\theta_g(t)$ is made by accessing a data file created from a Jet Propulsion Laboratory (JPL) computer tape (see Reference 8).

The spacecraft position vector, $\bar{r}_s$, at the observation time, t, is determined from the estimated value of the spacecraft position vector, $\bar{r}_{s_0}$ at an epoch time t_0. The method is to numerically integrate the second order differential equation of motion.

$$\frac{d^2\bar{r}_s}{dt^2} = F(\bar{r}_s, \dot{\bar{r}}_s, t) \qquad (3\text{-}8)$$

The R&D GTDS program has the options to perform this numerical integration by a variety of methods. The most accurate is a 12th order Cowell method. The Cowell method is discussed in Reference 11. The numerical integration of Equation (3-8) in NAVPAK is performed by a fourth-order Runge-Kutta method, using modified Fehlberg coefficients (Reference 12).

The total force, $\bar{F}$, on the satellite is modeled in NAVPAK to include atmospheric drag using a modified Harris-Priester model, two-body gravitational attraction of the Earth and the J_2 non-spherical gravitational effect. The R&D GTDS has options to include a (21x21) spherical harmonic geopotential model of the Earth's gravitation, lunar/solar third-body gravitational forces, atmospheric drag and solar radiation pressure. Having obtained $\bar{r}_L$ and $\bar{r}_s$, the inertial line-of-sight direction cosines $\bar{\ell}(\ell_x, \ell_y, \ell_z)$ from the spacecraft to the landmark are

$$\bar{\ell} = \frac{\bar{r}_L - \bar{r}_s}{|\bar{r}_L - \bar{r}_s|} \qquad (3\text{-}9)$$

This line-of-sight unit vector can be transformed into the yaw-pitch-roll $(\hat{i}, \hat{j}, \hat{k})$ frame by the transformation

$$\bar{\ell}_o = T\bar{\ell} \tag{3-10}$$

where

$$T = \begin{Bmatrix} j_{oy}k_{oz} - j_{oz}k_{oy} & j_{oz}k_{ox} - j_{ox}k_{oz} & j_{ox}k_{oy} - j_{oy}k_{ox} \\ \dfrac{y_s\dot{z}_s - z_s\dot{y}_s}{L} & \dfrac{z_s\dot{x}_s - x_s\dot{z}_s}{L} & \dfrac{x_s\dot{y}_s - y_s\dot{x}_s}{L} \\ \dfrac{x_s}{|r_s|} & \dfrac{y_s}{|r_s|} & \dfrac{z_s}{|r_s|} \end{Bmatrix} \tag{3-11}$$

where $|r_s| = \sqrt{x_s^2 + y_s^2 + z_s^2}$

L = angular momentum magnitude $(|\bar{r}_s \times \bar{v}_s|)$.

The transformation matrix T is simply the components of the $\hat{i}$, $\hat{j}$ and $\hat{k}$ given in Equation (3-1).

The line-of-sight unit vector may be expressed in the spacecraft body frame (x'', y'', z'') coordinate system by the rotation

$$\bar{\ell}'' = S\bar{\ell}_o = ST\bar{\ell} \tag{3-12}$$

The S matrix is the attitude rotation matrix given by Equation (3-2). The modeling of these angles as a function of time is discussed in Section 3.2 of this paper. The S matrix is the result of a yaw, pitch and roll sequence of rotations.

Finally, the selected observables, ϵ and ψ, must be related to the spacecraft body frame line-of-sight direction cosines, $\bar{\ell}''$. It can be seen that

$$\epsilon = \arctan\left(\ell''_y/\ell''_z\right)$$
$$\psi = \arcsin\left(\ell''_x\right) \tag{3-13}$$

provided ϵ is an azimuthal angle measured (in the y'' z'' plane) from the z'-axis, and ψ is an elevation angle from the z'' y'' plane measured toward the x''-axis. Figure 3-2 shows these angles. (The reference axes of Reference 9 are related to those of Figure 3-2 by $x' \longrightarrow x''$, $y'' \longrightarrow y''$, $z'' \longrightarrow -z''$).

Equations (3- 9), (3-12), and (3-13) represent the landmark observation model for any Earth-stabilized spacecraft in the absence of camera misalignments. If a misalignment exists, it may be represented by distinguishing the camera frame direction cosines $\bar{\ell}'''$ from the spacecraft frame direction cosines $\bar{\ell}''$, and relating them via a misalignment matrix corresponding to small rotations α, β, γ about the x'', y'', z'' axes, respectively

$$\begin{Bmatrix} \ell'''_x \\ \ell'''_y \\ \ell''_z \end{Bmatrix} = \begin{Bmatrix} 1 & \gamma & -\beta \\ -\gamma & 1 & \alpha \\ \beta & -\alpha & 1 \end{Bmatrix} \begin{Bmatrix} \ell''_x \\ \ell''_y \\ \ell''_z \end{Bmatrix} \tag{3-14}$$

or

$$\bar{\ell}''' = M\bar{\ell}'' \tag{3-15}$$

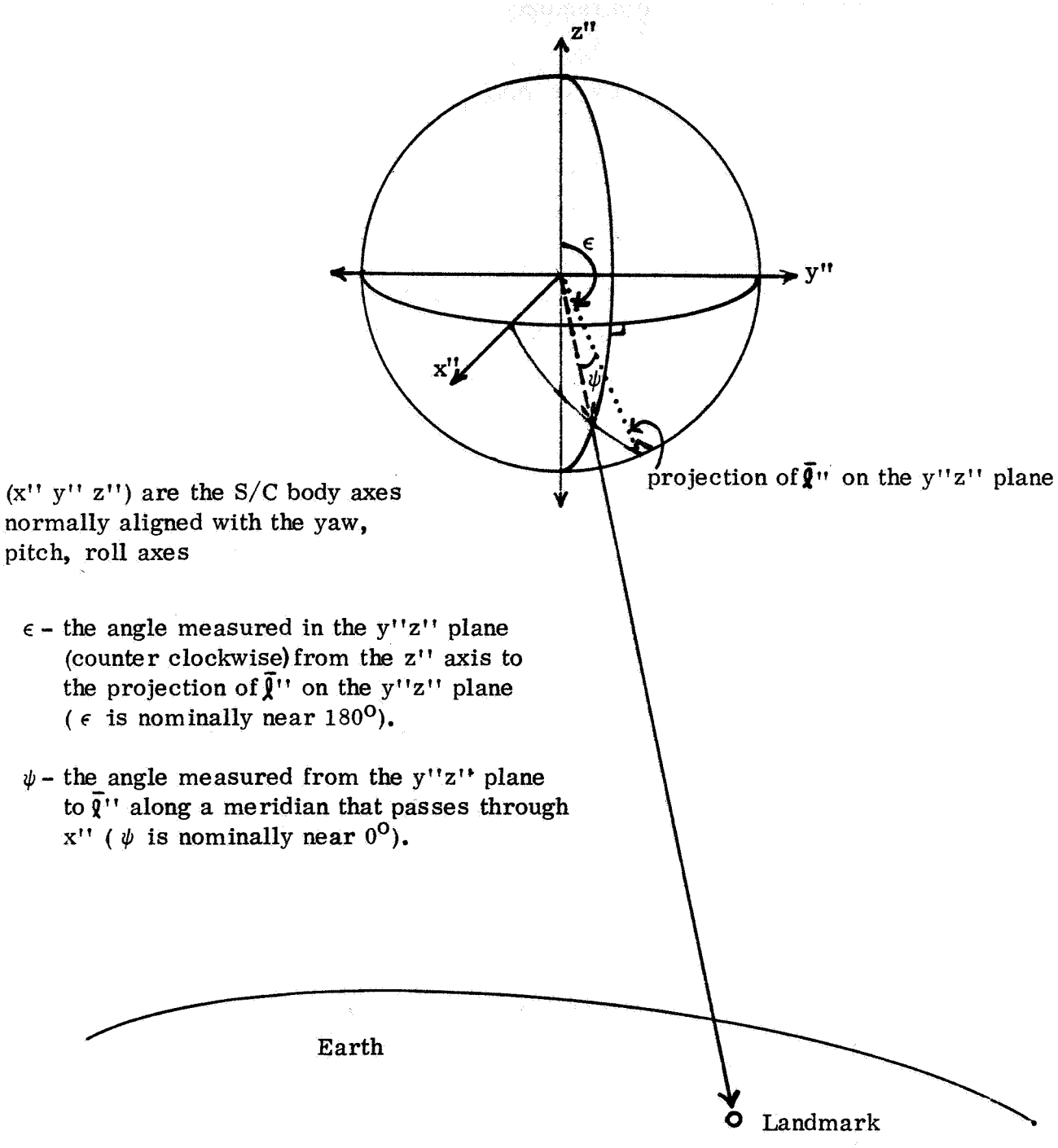

Figure 3-2. Observables for Landmark Model

where M , the misalignment matrix, is given by

$$M = \begin{pmatrix} 1 & \gamma & -\beta \\ -\gamma & 1 & \alpha \\ \beta & -\alpha & 1 \end{pmatrix} \tag{3-16}$$

The observation Equation (3-13) is then replaced with

$$\epsilon = \arctan\left(\ell'''_y / \ell'''_z\right)$$
$$\psi = \arcsin\left(\ell'''_x\right) \tag{3-17}$$

3.2 ATTITUDE PROPAGATION MODEL

The Landsat satellite is a triaxially stabilized spacecraft in which momentum flywheels are used in a feedback system to attempt to stabilize the spacecraft's attitude against the variety of torques acting to change its attitude. Definitions of the roll, pitch, and yaw axes about which the spacecraft is stabilized are given in Section 3.1. The environmental torques causing inertial motion of the attitude (Y, P, R) frame are the aerodynamic torque caused by the Earth's atmosphere; the gravity-gradient torque due to the small difference in gravitational attraction from one end of the spacecraft to the other; the magnetic torque due to the interaction of the spacecraft's magnetic field with the Earth's magnetic field; and solar radiation and solar wind pressure acting on the spacecraft. In addition to these environmental torques, the spacecraft is influenced by internal activities (equipment functioning) and controls exerted by the spacecraft's attitude control system (ACS).

The process of determining the spacecraft attitude by modeling the attitude equations of motion while simultaneously determining the orbital parameters of the spacecraft is computationally difficult. For that reason, the current

attitude model used in the Landsat NAVPAK system and the R&D GTDS uses a simplified formulation that obviates the need for the complete integration of the attitude differential equations of motion.

The use of the monitored speed (rpm) of the stabilizing momentum wheels to aid in the attitude determination of the Landsat satellite was originally suggested by E. Lefferts and discussed in Reference 13. The wheel rate data from Landsat consists of forward and reverse wheel rates for roll and wheel rates for pitch and yaw in revolutions per minute given every second. The roll wheel rates are subtracted (forward-reverse) to obtain a net roll wheel rate. The use of wheel rate data to monitor the rapid attitude variations of Landsat is based on three assumptions:

- All disturbances that generate attitude motion for a three-axis stabilized spacecraft such as Landsat can be classified into the two following types: (1) environmental disturbance torques, N, or (2) errors and noise, η , in the sensors and the onboard ACS.
- The three channels (roll, pitch, and yaw) of the ACS are linear, continuous, and uncoupled, such that they can be treated independently.
- The attitude and wheel rate response due to the torques $(a_N , \dot{a}_{W_N})$ is independent of the response due to the noise $(a_\eta , \dot{a}_{w_\eta})$.

Given these assumptions, the following equations are satisfied:

$$a(t) = a_N(t) + a_\eta(t) \qquad (3\text{-}18)$$

$$\dot{a}_W(t) = \dot{a}_{W_N}(t) + \dot{a}_{W_\eta}(t) \qquad (3\text{-}19)$$

where a is an attitude angle and $\dot{a}_W$ is the reaction wheel rate.

The environmental disturbance torques, N, are near-deterministic and near-periodic at the orbital frequency and its low multiples. Examination of Landsat wheel rate data shows a large oscillation at the orbital period, which is believed to be due almost entirely to N. The torque contribution should also produce sizable components (particularly in roll and yaw) that are nearly constant over the orbital period. The disturbances arising from the noise, η, are largely random and should occur in a higher frequency regime than the main contributions from the environmental torques.

The attitude rates, $\dot{a}_\eta$, are related to the wheel rates, $\dot{a}_{W_\eta}$, as

$$\dot{a}_\eta = \frac{-I_W}{I} \dot{a}_{W_\eta} \qquad (3\text{-}20)$$

where I_W is the moment of inertia of the reaction wheel and I is the moment of inertia of the spacecraft. This is valid because η produces, via the ACS, a wheel torque that drives both the reaction wheel and the spacecraft. The analogous equation for $\dot{a}_N$ and $\dot{a}_{W_N}$ is not correct, i.e.,

$$\dot{a}_N \neq \frac{-I_W}{I} \dot{a}_{W_N} \qquad (3\text{-}21)$$

This is because the environmental torques, N, act <u>directly</u> on the spacecraft but not on the reaction wheel. Therefore, integration of the raw wheel rate

data will not produce an accurate attitude history. However, filtering the raw wheel rates to remove a_{W_N}

$$\dot{a}_{W_\eta} = \dot{a}_W - \dot{a}_{W_N} \tag{3-22}$$

and integrating the $\dot{a}_\eta$ derived from $\dot{a}_{W_\eta}$ (note relationship between attitude rates and wheel rates in Equation (3-21)) should yield an accurate representation of a_η .

The attitude motion arising from the environmental torques, a_N , should be near-periodic in the mean orbital period, $\bar{\omega}_0$, such that

$$a_N \cong a_0 + a_1 t + a_2 \sin(\bar{\omega}_o t + a_3) \tag{3-23}$$

Over a fractional period, a_N should be represented by a series expansion of the above equation:

$$a_N \cong a_0 + a_1 t + a'_2 t^2 + a'_3 t^3 + \ldots \tag{3-24}$$

This representation of a_N is implemented in Landsat NAVPAK since data is processed only over a fraction of the orbital period. Both models (Equations 3-23 and 3-24) are implemented in the R&D GTDS.

The process of using wheel rate data for the representation of a_η requires that the low-frequency component of roll, pitch, and yaw wheel rate data be

removed. The low-frequency component is determined and removed by the following process:

1. The low frequency, $\bar{\omega}_0$, is input to a least squares program to fit the following trigonometric series to the raw wheel rate data:

$$\begin{aligned}\dot{a}_{W_N}(t) = {} & (A_1 + A_2 t) + (A_7 + A_8 t) \sin(\bar{\omega}_0 t) + (A_{13} + A_{14} t) \cos(\bar{\omega}_0 t) \\ & + (A_{19} + A_{20} t) \sin^2(\bar{\omega}_0 t) + (A_{24} + A_{25} t) \sin(\bar{\omega}_0 t) \cos(\bar{\omega}_0 t) \\ & + (A_{29} + A_{30} t) \sin^3(\bar{\omega}_0 t) + (A_{33} + A_{34} t) \sin^2(\bar{\omega}_0 t) \cos(\bar{\omega}_0 t)\end{aligned} \tag{3-25}$$

2. Using the coefficients (A_1 through A_{34}) obtained in Step 1, the Fourier series is evaluated at each wheel rate data point and subtracted to obtain a file of high-frequency wheel rate data.

$$\dot{a}_{W_\eta} = \dot{a}_W - \dot{a}_{W_N} \tag{3-26}$$

3. The high-frequency integrated wheel rates are then converted to body rates as follows:

$$\dot{a}_\eta = \frac{-I_W}{I} \, a_{W_\eta} \tag{3-27}$$

where I_W is the moment of inertia of the reaction wheel, and I is the moment of inertia of the spacecraft.

The low frequency, $\bar{\omega}_0$, contained in the wheel rate data is obtained through the maximum entropy method (MEM).

This MEM is a technique of performing a discrete Fourier analysis on data, subject to the constraint that the assumed ignorance (entropy) of data that are not given (data outside the given data interval) is a maximum. This is in contrast to the standard Fast Fourier Transform (FFT) in which implicit assumptions are made regarding data outside the given data span. The theory of the MEM is discussed in Reference 14 and the software used to perform in the spectral analysis is discussed in 15. Numerical experiments have shown that the MEM is superior to the FFT in its ability to extract low-frequency information from a given data set.

After a body rates file $(\dot{a}_\eta(t))$ has been created by the process described above, then the attitude model is specified by Equation (3-18) where $a_N(t)$ is approximated by Equation (3-24) and $a_\eta(t)$ is obtained from $\dot{a}_\eta(t)$ by a trapezoidal numerical integration. The coefficients of Equation (3-24) are either prespecified or estimated in the orbit/attitude determination process.

SECTION 4 - NUMERICAL RESULTS

Several numerical experiments have been performed with the Landsat NAVPAK and R&D GTDS using real landmark data. Prior to these experiments both software systems had been tested using simulated data. The numerical results must be considered as preliminary because of the limited data which was available. The data was generated using a single pass of Landsat-2 over the United States on April 15, 1977. There were 11 pictures available from New York to Florida. Landmark observations were created by the method discussed previously. The landmarks were selected at random throughout each picture with an attempt to cover the entire picture. United States Geological Survey maps (7-1/2 minute quadrangle size) were used to determine the geodetic coordinates of the landmarks. The data span and density were as follows: the first seven pictures of the pass (Time span 2 minutes, 50 seconds) contained 95 landmarks. The next two pictures were water scenes with no observable features providing a natural data gap of 1 minute and 12 seconds. The final two pictures contained 11 landmarks. The total data included 106 landmarks over a 4 minute, 46 second time span. For the same period wheel-rate data (R, P, Y) was available every second. The wheel-rate data was processed to obtain a high frequency body rate file by the previously indicated method.

4.1 R&D GTDS (BATCH DC) RESULTS

Several tests were made with the R&D GTDS using the landmark data. These tests included the effect of the choice of solve-for parameters, a priori convariance matrix, force model effects, and the use of wheel-rate data for attitude modeling. The results for each of these is discussed in this section.

4.1.1 Choice of Solve-For Parameters

The available solve-for parameters in the R&D GTDS landmark model include six spacecraft state vector components (either geocentric inertial Cartesian or classical orbital elements), the five coefficients for each attitude (R, P, Y)

time polynomial, and three camera biases (α, β, γ). Other possible solve-for parameters such as drag coefficient, harmonic coefficients in the Earth's geopotential model etc. are available. Only the first set of parameters (spacecraft state, attitude and camera biases) were used with the landmark data set. The data span is short enough so the other solve-for parameters cannot be realistically estimated.

It is well known that the addition of a solve-for parameter to a set of parameters to be estimated will decrease the residuals for a given data set. Thus, for example, estimating four parameters for a particular data set will result in smaller residuals than when only three of the parameters are estimated. This assumes that the parameters are observable (i.e., related to the observed quantities) and uncorrelated. Hence, using the complete solve-for set (spacecraft state, 15 attitude coefficients and camera biases) should produce the smallest residuals for the given data span. However, some of the parameters estimated in this manner are not particularly meaningful because of unobservability or high correlation among the solve-for parameters. The section addresses the question of how the choice of solve-for parameters affects the fit of the observational data.

The results for the full data span are shown in Table 4-1, which gives the rms residuals for the converged differential correction (DC) as a function of solve-for parameter set. The units of the residuals are pixels. When a parameter is not solved for, its value is specified as that which is annotated on the Landsat image file. This annotation contains values for the spacecraft state and constant attitude values, that is the first coefficient. The remaining attitude coefficients and camera biases were nominally set to zero when not solved for. In addition, the choice of a priori covariance matrix affected the final residuals. The covariance used was that determined by experiments described later in this section.

Several things are apparent from examining Table 4-1. First, the smallest residuals are obtained solving for the spacecraft state and 3 attitude coefficients (3 each for R, P, and Y). Slightly larger residuals are obtained when the spacecraft state and 2 attitude coefficients are solved for. The use of more than 3 attitude coefficients does not yield significantly smaller residuals. Of the three camera biases (α, β, γ), only the first one is observable over the data span used. Solving for the second or third (or both) camera biases does not produce smaller residuals than when they are not solved for. It is interesting to note that solving for the first camera bias gives the same rms residuals as solving for constant attitude coefficients. Indeed, over a short time span the camera bias coordinate rotation has the same effect as the attitude frame orientation. Over longer time spans the effects would be distinguishable. Results in Table 4-1 also compare the effect of solving for spacecraft state parameters compared to solving for attitude parameters.

4.1.2 A Priori Covariance Matrix

Numerical experiments in Reference 16 had suggested that the relative weighting between orbit and attitude parameters in the priori covariance weighting should produce large differences in the resulting observation residuals. For that reason, experiments were performed with the real landmark data in which the spacecraft state was solved for along with one coefficient each for roll, pitch and yaw. The relative weighting between spacecraft state parameters and the attitude parameters was varied widely. The results are listed in Table 4-2, which shows the observation residuals as a function of a priori covariance. The overall residuals changed by a factor of about 1.5 over the large change in a priori covariance. The covariances associated with run number 6 were used for all the remaining DC runs in this section including those in Table 4-1. Run 6 was chosen over run 2, even though run 2 yielded very slightly smaller residuals, because of the number of iterations required.

Table 4-1. Observation Residuals as a Function of Solve-for Parameters

Run No.	Solve-for Parameters	Observation Residuals (pixels)			No. of DC Iterations to Converge
		Scan (ϵ)	Elevation (ψ)	Total (rss)	
1	Spacecraft state only	14.0	10.2	17.3	7
2	State + α	12.3	9.4	15.5	10
3	State + β	14.1	10.2	17.4	7
4	State + γ	14.0	10.2	17.3	7
5	State + α,β	12.3	9.4	15.5	9
6	State + α, β, γ	12.3	9.4	15.5	10
7	State + β,γ	14.1	10.2	17.4	7
8	State + α,γ	12.3	9.4	15.5	9
9	State + 1 attitude coefficient	12.3	9.4	15.5	10
10	1 attitude coefficient only	16.9	12.1	20.8	3
11	State + 2 attitude coefficients	11.2	9.6	14.8	15
12	2 attitude coefficients only	17.6	12.3	21.5	3
13	State + 3 attitude coefficients	7.3	9.2	11.7	8
14	3 attitude coefficients only	11.0	11.9	16.2	3

Solve-for Parameters: Spacecraft state refers to six components ($x, y, z, \dot{x}, \dot{y}, \dot{z}$) of the spacecraft geocentric inertial state vector; (α, β, γ) are the camera misorientation biases; attitude coefficients are the coefficients of the time polynomial for roll, pitch, and yaw (i.e., two attitude coefficients means the first two coefficients for roll, pitch, and yaw for a total of six attitude parameters).

Observation Residuals: Units are pixels.

A Priori Covariances:

$$\sigma_x^2 = \sigma_y^2 = \sigma_z^2 = 25 \text{ km}^2$$

$$\sigma_{\dot{x}}^2 = \sigma_{\dot{y}}^2 = \sigma_{\dot{z}}^2 = .0025 \text{ km}^2/\text{sec}^2$$

$$\left.\begin{aligned} \sigma_0^2 &= 1 \text{ degree}^2 \\ \sigma_1^2 &= 1 \times 10^{-6} (\text{deg./sec})^2 \\ \sigma_2^2 &= 1 \times 10^{-12} (\text{deg./sec})^4 \end{aligned}\right\} \text{attitude coefficients}$$

Table 4-2. Observation Residuals as a Function of A Priori Covariance Matrix

Run No.	A Priori Covariance			Observation Residuals (pixels)		
	σ_x^2	$\sigma_{\dot{x}}^2$	σ_R^2	Scan (ϵ)	Elevation (ψ)	Total (rss)
1	1	1	1	21.8	10.2	24.1
2	25	0.25×10^{-4}	1	12.3	9.4	15.5
3	25	0.25×10^{-2}	1	12.3	9.4	15.5
4	0.25	0.25×10^{-6}	1	13.9	10.2	17.2
5	0.25×10^{-2}	0.25×10^{-8}	1	16.9	12.1	20.8
6	25×10^{2}	0.25×10^{-2}	1	12.3	9.2	15.4
7	25	0.25×10^{-4}	1×10^{-4}	14.3	12.1	18.7
8	25	0.24×10^{-4}	1×10^{-2}	12.7	9.7	16.0

Notes:

Units are kilometers^2, (kilometers^2/second^2) , and degrees^2.

Although Run No. 6 shows the smallest residuals, it required 14 iterations for the DC to converge. Run No. 2 shows comparable residuals but required only 10 iterations for convergence. Hence, Run No. 2 was selected as the a priori covariance for the remaining runs in this section.

Only a single component each for the position, velocity, and attitude covariance is shown. The position components σ_x, σ_y, σ_z are identical. Similarly for velocity and attitude.

4.1.3 Force Model Evaluation

The force model used in the Landsat NAVPAK system consists of the two-body Earth-satellite gravitational attraction with the added effects of J_2 non-spherical gravitational potential term and atmospheric drag. A question which can be easily answered via the R&D GTDS is whether this force model is adequate over typical data spans to be encountered (i.e., approximately 5 minutes). As previously indicated, the R&D GTDS has available force models including two-body Earth-satellite gravitational attraction, non-spherical Earth gravitational potential models including J_2 up to a 21 x 21 spherical harmonics, several atmospheric drag models, third body lunar/solar gravitational effects and solar radiation pressure.

Several R&D GTDS runs were made using various force model combinations with actual landmark data. The residuals were compared to observe the effect of different force models. In all these runs state and 1 attitude coefficient were solved-for using the complete data span and every landmark. The a priori covariance was the same as that of the runs given in Section 4.1.2. These runs show that the residuals are not significantly affected by the choice of force model. In fact, the rms residuals differed by less than 0.01 pixel regardless of force model. Thus, the force model used in Landsat NAVPAK is an adequate one.

4.1.4 Wheel-Rate Residuals

A lot of theoretical and software development has resulted from the contention that high frequency momentum wheel-rate data will aid in attitude modeling for Landsat (Reference 13). To test the contention a few runs were made using several solve-for parameter combinations with the 5-minute data span. In all cases, data density has been maintained as every landmark and the a priori covariances were those used in Section 4.1.2. The results presented in Table 4-3 compare the residuals for different choices of solve-for parameters.

Table 4-3. Effect of Wheel-Rate Data

Solve-for Parameters	Residuals (No Wheel-Rate Data)			Residuals (With Wheel-Rate Data)		
	Scan (ϵ)	Elevation (ψ)	Total (rss)	Scan (ϵ)	Elevation (ψ)	Total (rss)
Spacecraft state only	14.0	10.2	17.3	4.1	4.8	6.3
State + 1 attitude coefficient	12.3	9.4	15.5	3.1	3.6	4.8
State + 2 attitude coefficients	11.4	10.2	15.3	3.1	3.6	4.8
1 attitude coefficient only	21.5	12.8	25.0	18.5	9.1	20.6
2 attitude coefficients only	17.6	12.3	21.5	9.9	8.6	13.1
State + 3 attitude coefficients	7.3	9.3	11.8	2.7	3.6	4.5

Observation residuals are given as a function of solve-for parameters for the R&D GTDS DC. Two cases are shown. The left-hand results are without the use of wheel-rate data, while the right-hand results include wheel rate data. The units are pixels, and the a priori covariance matrix is the same as for Table 4-1. The data span is 5 minutes.

In all cases the wheel rate data decreased the observation residuals. Solving for S/C state and three attitude coefficients resulted in a total rss error of 4.5 pixels compared to the value of 11.8 without wheel rate data.

In addition to the overall residual decrease, the use of wheel rate data tended to stabilize the solution. Without wheel rate data, significant differences were obtained in the solve-for parameters when the three-minute and five-minute data spans were used. Specifically, the difference in magnitude of the S/C position vector between the five and three minute converged values was 11.4 km. The velocity vector magnitude changed by 0.021 km/sec. With wheel rate data, the changes were 2.9 km in position magnitude and 0.001 km/sec for velocity magnitude. Also, using wheel rate data the magnitude of the residuals stayed nearly the same using either a three minute or five minute data span. The implication here is that the use of wheel rate data stabilizes the solution so that less of a local fit phenomena is observed.

4.2 LANDSAT NAVPAK (SEQUENTIAL) RESULTS

A number of experiments were performed using the Landsat NAVPAK extended Kalman Filter (EKF) for orbit/attitude estimation with the landmark data set discussed previously. Three areas are addressed including the choice of solve-for parameters, the a priori covariance matrix and the use of wheel-rate data. Prior to presenting the numerical results it should be mentioned that the NAVPAK (EKF) was an untuned filter. There was no process noise applied in the filter and no decaying memory. Moreover all results presented are based on a single pass of the filter through the data set. It is expected that the implementation of all of these features (i.e., decaying memory, process noise and iterative filter) will enhance the preliminary results presented here.

The NAVPAK filter was tested using simulated data both with and without added noise. These simulated data experiments provided a useful preparation for the use of actual landmark data.

4.2.1 Choice of Solve-For Parameters

The effect of the choice of solve-for parameters for the NAVPAK EKF was investigated by trying a combination of parameter sets. The results are listed in Table 4-4 which gives the observation residuals (rms in pixel units) for several different solve-for parameter sets. A priori values of the parameters were obtained from the Landsat annotated images and the a priori covariance was selected based on results in Section 4.2.2. Two data spans are presented in Table 4-4. The three-minute span contains the data from the beginning of the Landsat pass up to the data gap. The five-minute span contains the entire data set discussed previously including the data gap. Observation residuals, used to compute the rms values in Table 4-4, were produced by propagating the final (last observation) EKF state vector back to the beginning of the data set and calculating residuals without further state corrections.

The smallest residuals are obtained by solving for the spacecraft state vector and one attitude coefficient each for roll, pitch and yaw. It is interesting to note that the rms residuals for the 3-minute span are usually smaller than the 5-minute span. This suggests a local fit situation in which the estimated parameters minimize the residuals but are not close enough to the true parameter values to exhibit the real noise level in the data.

Second and higher order attitude coefficients produced larger residuals than the first coefficient. Experiments with simulated data suggested that the filter closed down the a priori attitude covariance too rapidly to allow realistic estimation of these coefficients. The use of process noise may resolve this problem. Camera biases were not solved for. Experiments with simulated data indicated that the camera biases and attitude coefficient could not simultaneously be estimated realistically. This is caused by the fact that for a single observation the camera misalignment has an identical effect as a change in the constant attitude coefficients. The result was that solving for camera biases yielded

Table 4-4. Observation Residuals as a Function of Solve-for Parameters for NAVPAK

Run No.	Data Span (minutes)	Solve-for Parameters	Observation Residuals (pixels)		
			Scan (ϵ)	Elevation (ψ)	Total (rss)
1	5	Spacecraft state only	15.0	15.5	21.6
2	3	Spacecraft state only	7.9	15.2	17.1
3	5	State + 1 attitude coefficient	14.7	11.9	18.9
4	3	State + 1 attitude coefficient	7.2	10.1	12.4
5	5	1 attitude coefficient only	18.6	12.6	22.5
6	3	1 attitude coefficient only	19.4	12.9	23.3
7	5	2 attitude coefficients only	44.3	50.9	67.5
8	3	2 attitude coefficients only	44.3	50.9	67.5
9	5	State + 2 attitude coefficients	100.5	119.4	156.1
10	3	State + 2 attitude coefficients	10.4	14.2	17.6

Observation residuals are given as a function of the choice of solve-for parameters. Parameters not solved for are set to the Landsat picture annotation values. The residuals are computed using the final EKF state propagated through the data set. Two time spans are given: a 3-minute time span, which includes the data from the beginning of the pass to the data gap; and a 5-minute span, which includes the data gap and the data after the gap. The a priori covariance values are: $\sigma_x^2 = 1.0 \times 10^2$ km^2 ; $\sigma_{\dot{x}}^2 = 1.0 \times 10^{-2}$ (km^2/sec^2) ; and $\sigma_R^2 = 1.0 \times 10^{-5}$ deg^2.

identical results to solving for constant attitude biases. Again, the use of process noise may help this situation.

4.2.2 A Priori Covariance Effect

Table 4-5 shows the results of varying the a priori covariance matrix in the NAVPAK EKF. Observation residuals are given as a function of a priori covariance matrix for the case in which the spacecraft state and one attitude coefficient are solved for. The rms residuals change by about 20 percent with a wide variation in the absolute values of the a priori covariance as well as a large change in relative weighting between spacecraft orbital and attitude parameters. Run number 4 yielded the lowest residuals so these values for the a priori covariance were used in the rest of this section.

4.2.3 Wheel Rate Data Effects

The effect of wheel rate data using the Landsat NAVPAK system was investigated by performing the same computer runs as presented in Section 4.2.1 with the addition of wheel rate data for attitude modeling. The results are presented in Table 4-6, which gives the rms residuals for one pass through the data solving for various parameter combinations. The a priori covariances are the same as in Section 4.2.1. Comparison between Table 4-4 (without wheel rate data) and Table 4-6 (with wheel rate data) suggests several results. First, for the three-minute data span the wheel rate data does not provide significantly smaller residuals. Indeed for the case of solving for state plus one attitude coefficients the residuals are actually larger with wheel rate data. However, the 5-minute span does result in significantly smaller residuals using wheel rate data. The effect of the wheel rate data is to stabilize the attitude modeling over a data gap. A look at the residuals as a function of observation number indicated that the filter does not diverge (i.e., the solution degrading with propagation across the data gap) as much using wheel rate data as when wheel rate data is not used. The use of wheel rate data

also seems to allow for the realistic estimation of the second attitude coefficients. Such was not the case without wheel rate data.

Table 4-5. Observation Residuals as a Function of A Priori Covariance for NAVPAK

Run No.	A Priori Covariance			Observation Residuals (pixels)		
	σ_x^2	$\sigma_{\dot{x}}^2$	σ_R^2	Scan (ϵ)	Elevation (ψ)	Total (rss)
1	1.0×10^4	1.0×10^{-2}	1.0×10^{-3}	9.3	10.5	14.0
2	1.0×10^4	1.0	1.0×10^{-3}	9.1	10.5	13.9
3	1.0×10^6	1.0×10^2	1.0×10^{-3}	8.3	10.4	13.3
4	1.0×10^2	1.0×10^{-2}	1.0×10^{-5}	7.2	10.1	12.4
5	1.0×10^2	1.0×10^{-2}	1.0×10^{-1}	10.7	11.0	15.3

Observation residuals are given as a function of the a priori covariance. The units are km^2, (km^2/sec^2) , and $degrees^2$. The residuals are computed using the final EKF state, solving for the spacecraft state, and a constant attitude. The data span is 3 minutes.

Table 4-6. Effect of Wheel-Rate Data for NAVPAK

Solve-for Parameters	Data Span (minutes)	Observation Residuals (pixels) [With Wheel-Rate Data]		
		Scan (ϵ)	Elevation (ψ)	Total (rss)
Spacecraft state only	5	10.3	15.1	18.3
Spacecraft state only	3	10.9	15.3	18.8
State + 1 attitude coefficient	5	12.2	9.2	15.3
State + 1 attitude coefficient	3	10.6	9.4	14.2
1 attitude coefficient only	5	27.9	12.2	30.4
1 attitude coefficient only	3	24.4	10.6	26.6
2 attitude coefficients only	5	34.2	53.0	63.1
2 attitude coefficients only	3	34.2	53.0	63.1
State + 2 attitude coefficients	5	25.3	60.8	65.8
State + 2 attitude coefficients	3	12.5	9.5	15.7

The observation residuals are shown as a function of solve-for parameters for NAVPAK. The covariance matrix is the same as in Table 4-4.

REFERENCES

1. Computer Sciences Corporation, CSC/TM-75/6146, Landmark Observation Model for Earth Stabilized Satellites, P. S. Desai and H. Siddalingaiah, September 1975

2. --, CSC/TM-75/6147, Autonomous Navigation for TIROS-N and NIMBUS-6, P. S. Desai and H. Siddalingaiah, December 1975

3. --, CSC/SD-75/6058, GTDS Landmark Data Modeling, J. Fein, P. S. Desai and S. Wei, September 1975

4. --, CSC/SD-76/6054, Enhancements to the GTDS R&D Landmark and Picture Earth-Edge Data Capabilities, J. Fein, P. S. Desai, H. E. Stull, and F. L. Markley, September 1976

5. --, CSC/TM-77/6012, NAVPAK Design for Landsat and Kalman Filter Applications, E. M. O'Neill and H. E. Stull, January 1977

6. Goddard Doc. #76SDS4258 Landsat Data Users Handbook, September 2, 1976

7. Computer Sciences Corporation, CSC/SD-78/6173, Landsat NAVPAK System Description and User's Guide, S. R. Waligora, December 1978

8. National Aeronautics and Space Administration, Goddard Space Flight Center, S-582-76-77, Mathematical Theory of the Goddard Trajectory Determination System, edited by J. O. Cappellari, C. E. Velez, and A. J. Fuchs, April 1976

9. R. H. Caron and K. W. Simon, "Attitude Time-Series Estimator for Rectification of Spaceborne Imagery", Journal of Spacecraft and Rockets, vol. 12, #1, pp. 27-32

10. P. R. Escobal, Methods of Orbit Determination, 1965, John Wiley & Sons, Inc., New York

11. P. Henrici, Discrete Variable Methods in Ordinary Differential Equations, 1962, John Wiley & Sons, New York

12. D. G. Hull and D. G. Bettis, "Optimal Runge-Kutta Methods" (paper AA 575-080, presented at the AAS/AIAA Astrodynamics Conference, Nassau, Bahamas, July 1975)

REFERENCES

13. Computer Sciences Corporation, CSC/TM-77/6115, Evaluation of Wheel Rate Data for Landsat Attitude Modeling, J. Fein, April 1977

14. J. G. Ables, "Maximum Entropy Spectral Analysis", Astronomy and Astrophysics Supplement, vol. 15, 1974, pp. 383-389

15. Computer Sciences Corporation, CSC/TM-77/6297, Maximum Entropy Spectral Analysis, D. L. Hall, November 1977

16. --, CSC/TM-78/6108, Error Analysis Structures on Orbit/Attitude Determination Using Landsat-1 and -2 Landmark Data, N. V. Kumar and D. L. Hall, December 1978

MULTIPLE SCENE ATTITUDE ESTIMATOR PERFORMANCE FOR LANDSAT-1

Samuel S. Rifman, A. T. Monuki and C. P. Shortwell

TRW Defense and Space Systems Group

ABSTRACT

Initial results are presented to demonstrate the performance of a linear sequential estimator (Kalman Filter) used to estimate a LANDSAT-1 spacecraft attitude time series defined for four scenes. Previous work has shown that a similar estimator valid for one scene could facilitate precision geometric correction (rectification) and multitemporal registration to pixel (or better) accuracies. With the revised estimator a GCP poor scene – a scene with no usable geodetic control points (GCPs) – can be rectified to higher accuracies than otherwise, based on the use of GCPs in adjacent scenes. Attitude estimation errors have been determined by the use of GCPs located in the GCP-poor test scene, but which are not used to update the Kalman filter. Initial results achieved to date indicate that errors of <500m (rms) can be attained for the GCP-poor scenes. Operational factors are related to various scenarios.

1. INTRODUCTION

Since the launch of LANDSAT-1, much effort has been devoted to the development of digital methods for the geometric and radiometric correction of multispectral scanner (MSS) data collected by the LANDSAT series of spacecraft. As early as 1973 (References 1-3), examples of MSS data corrected to sub pixel accuracies by all digital methods were generated and reported on in the literature. Subsequent advances included scene/scene registration to sub pixel accuracies of multitemporal data (References 4,5).

A particularly successful technique employed to reduce the data processing load and yet achieve high accuracy entails the novel use of a linear sequential estimator (Kalman filter) for estimation of the satellite attitude state vector (Reference 6). Results have been previously reported regarding the evaluation by various methods of the estimator's accuracy for precision registration of full scene LANDSAT MSS data (Reference 4,5) and rectification of single scene data (References 1-3, 7).

In the previously referenced work, a given scene was corrected using knowledge of the spacecraft position, attitude and the sensor scan mechanism. For a given site* the locations of features within the imagery, referred to as contro points, were employed to refine estimates of the spacecraft attitude state vector defined for the same site. Registration was accomplished by means of essentially the same procedure, but with two small modifications: (a) measurement uncertainties were made much smaller than in the case of rectification (effectively giving less weight to a priori data); and (b) control points were used even if their precise geodetic locations on the earth's surface were unknown.

While it often is sufficient to employ a site specific estimator for rectification/registration purposes, the technique is dependent upon the availability of control points for the site in question. In some cases of interest, the subject site may have few or no usable geodetic control points (GCPs) the locations of which on the earth's surface are known to high accuracy. Examples of such cases include sites remote from civilization, sites containing featureless terrain, sites with poorly defined land/water interfaces, or sites which have not been surveyed to establish geodetic control.

*A site refers to a framed MSS scene approximately 185 km on a side.

In this paper, we report on the results of a technique which can increase the geometric correction and absolute location accuracy of such GCP poor sites when nearby sites do have adequate geodetic control. The technique is based essentially upon an extended definition of the attitude time series of the satellite, to encompass N sequential scenes in the direction of satellite motion.

It is not the purpose of this paper to present the details of the algorithm and design for the extended attitude estimator, per se. Rather it is the objective herein to present initial performance results of the estimator, and to identify certain features of the estimator's performance which may be of general interest.

2. PERFORMANCE EVALUATION METHOD

Based on available data for the LANDSAT attitude control system and attitude measurement system (Reference 8), as well as experience derived from previous work with the single scene estimator (References 6 and 7), it was decided to configure an initial series of tests involving four sequential LANDSAT scenes. Table 1 lists the scenes employed for this purpose, derived from path 16 of the Worldwide Reference System. There were 20 geodetic control points (GCPs) available per each scene, and the GCPs were approximately uniformly distributed within each scene.

The evaluation procedure proceded in two steps. First, for a given scenario, the m scenes (one, two or three in number) which were GCP poor were identified. The GCPs from the GCP poor scenes were not used to update the attitude estimator (they are, in fact, the statistical control points of Reference 7). Estimation errors were computed at the GCPs of the GCP poor sites, based upon updates of the estimator by means of GCP location data in the GCP rich sites (4-m in number).

The second step of the evaluation procedure reported on herein entailed calculation of the estimation errors at the GCPs of the GCP poor sites based only on a priori SIAT data recorded on the Computer Compatible Tapes purchased from the EROS Data Center.* The SIAT data includes attitude, altitude and sub-point position of the satellite for approximately 10 points in time spanning each 185Km x 185Km framed scene.

A relative comparison of the estimation errors obtained from the two steps of evaluation was the basis for determination of the improvement in attitude estimation accuracy achieved with the multiple scene attitude estimator, in contrast to performance achievable without the use of any GCPs from the site in question. This evaluation was undertaken for various scenarios of GCP rich/GCP poor scenes. Table 2 lists the various scenarios evaluated herein.

Upon commencing the evaluations, it was determined that the SIAT attitude data for successive scenes was discontinuous. Figure 1 shows the roll data for a sequence of scenes obtained directly from a NASA-produced Bulk Image Anno-

*SIAT data for a number of scenes is contained on a Bulk Image Annotation Tape (BIAT). The scene CCTs employed for the initial evaluations were obtained before SIAT data was recorded on CCTs. Thus, it was necessary in this study to employ the NASA BIAT tape data, which subsumes the currently provided SIAT data.

TABLE 1. LANDSAT-1 Scenes Employed for Multiscene Analysis

Scene Number	Scene ID Number	Row Number	Number of GCPs Available
1	1080-15183	31	20
2	1080-15185	32	20
3	1080-15192	33	20
4	1080-15194	34	20

TABLE 2. Scenarios Used for Performance Evaluation

Scenario Number	Scene ID Number 1080-15183	1080-15185	1080-15192	1080-15194
1	1	0	1	*
2	1	0	*	1
3	1	*	0	1
4	1	0	1	1
5	1	1	0	1
6	1	0	*	*
7	1	*	0	*
8	1	*	*	0
9	1	1	0	*
10	1	1	*	0
11	1	1	1	0

*: Scene not utilized
0: GCP poor scene
1: GCP rich scene

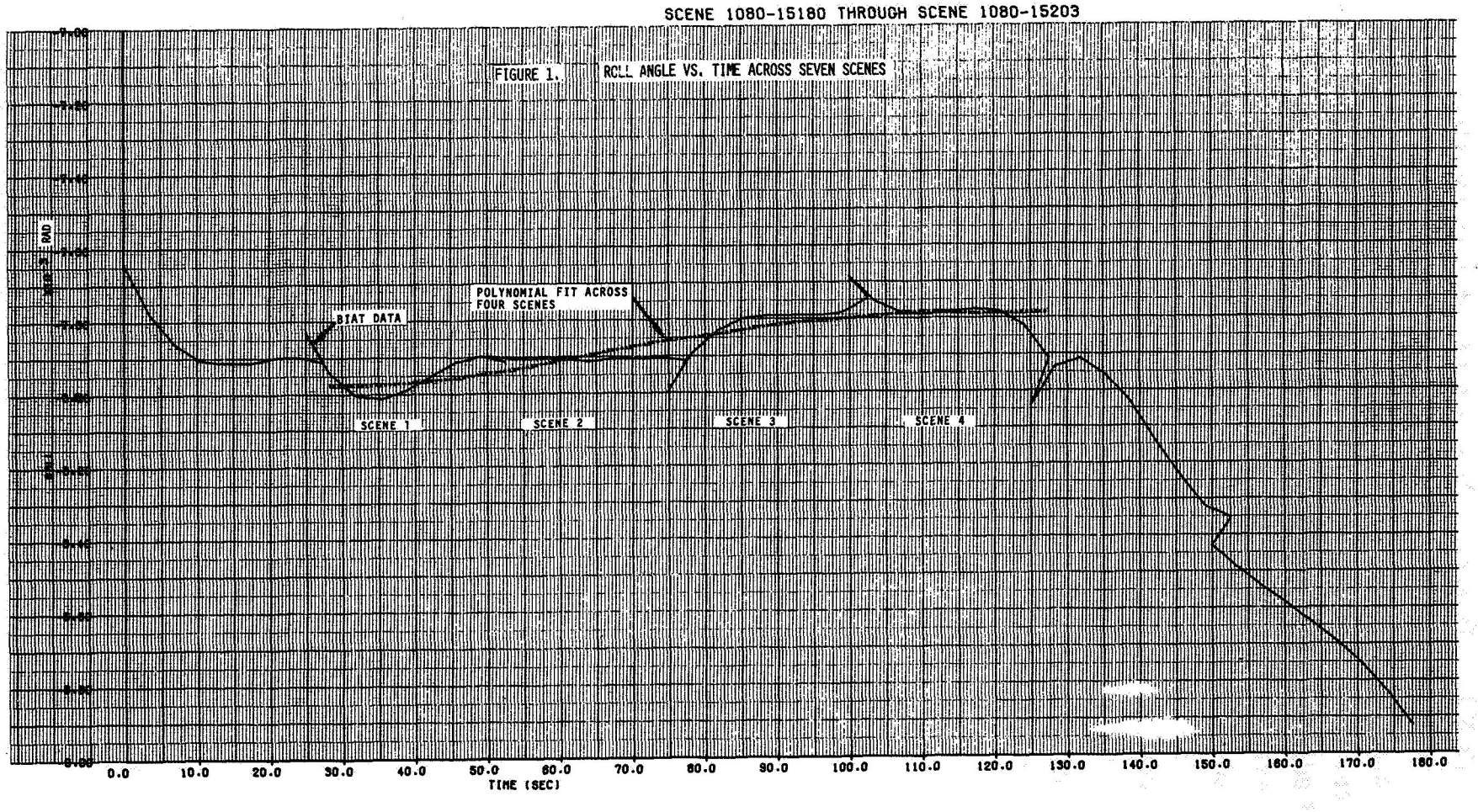
SCENE 1080-15180 THROUGH SCENE 1080-15203
FIGURE 1. ROLL ANGLE VS. TIME ACROSS SEVEN SCENES
POLYNOMIAL FIT ACROSS FOUR SCENES
BIAT DATA
SCENE 1
SCENE 2
SCENE 3
SCENE 4
TIME (SEC)
0.0
10.0
20.0
30.0
40.0
50.0
60.0
70.0
80.0
90.0
100.0
110.0
120.0
130.0
140.0
150.0
160.0
170.0
180.0

Figure 1

tation Tape (BIAT). It appears from a study of this and other such data that the SIAT attitude data is the result of a cubic time series fit to processed telemetry data for attitude, and that the fit is performed on a single scene basis; hence, there is a discontinuity in attitude in the overlap region of two framed adjacent along track MSS scenes.

In order to initialize the multiple scene attitude estimator, a global cubic attitude time series was fit to the aforesaid attitude data obtained from the BIAT. Selected BIAT data in the overlap regions were disregarded in order to achieve a good least squares fit to what appeared to be the underlying attitude data*. Figure 1 also shows the fit data in relation to the BIAT data. The resultant fit errors are shown in Table 3.

GCPs were employed alternately from the GCP rich scenes, to update the estimator. That is, one GCP was employed from the first GCP rich scene, and then another from the second such scene, until the last GCP had been processed. This method was employed to avoid biasing the global time series on the basis of only one GCP rich scene in the sequence. With each GCP update the estimation errors at the statistical control points (GCPs in the GCP poor scenes which do not update the estimator) were evaluated. The errors at each statistical control point (SCP) were evaluated. The error at each statistical control point was computed as the along track, across track and altitude components of the vector difference in earth centered rotating coordinates of the known statistical control point position and the estimated position for the same control point. The estimated control point position was computed on the basis of the previous attitude state vector (resulting from the previous update of the state vector by GCP location data in one of the GCP rich scenes) and the location of the control point feature within the image. The control points are located to $\pm 1/8$ pixel accuracy by a manual control point designation process. This process employs 4:1 digital enlargement by cubic convolution resampling (Reference 9) of a control point feature displayed on an interactive image display system.

---

*Processed attitude data, before polynomial model fitting, could not be obtained.

TABLE 3. Fit Errors over 4 Scenes 1, 2, 3, 4

	Roll	Pitch	Yaw
Maximum Error	0.06 mr (54 m)	.21 mr (190 m)	.065 mr (6 m)
RMS Error	.03 mr (27 m)	.108 mr (97 m)	.035 mr (3.2 m)

3. RESULTS

The results for two types of scenarios are presented. The first type of scenario corresponds to the case in which one or more GCP poor scenes lie between two or more GCP rich scenes. This interpolation scenario contrasts to the extrapolation scenario, in which one or more GCP poor scenes precede or follow one or more GCP rich scenes.

A. Interpolation Results

Interpolation results are listed in Table 4 for the scenarios identified by scene in Table 1. The Bulk Error corresponds to rms errors (meters) measured at GCPs which do not update the estimator (SCPs), on the basis of the NASA BIAT attitude defined for the individual GCP poor scene of each scenario.

A Priori Error is the rms estimation error (meters) measured at the SCPs in the GCP poor scene of each scenario, on the basis of the smooth global attitude time series (single cubic time series spanning 4 scenes). The remaining two columns are the a posteriori estimation errors for all the GCP rich scenes, and the GCP poor scene of each scenario.

A total of 10 GCPs were employed, regardless of the number of GCP rich scenes. It was found that the estimator converged rapidly with no more than 10 GCP updates.

Comparison of the Bulk Error data to the A Posteriori Error for the same GCP poor scene is a direct measure of the efficacy of the global attitude estimator in comparison with processing such scenes in the absence of GCPs (in said scenes). The scene errors are dramatically reduced in all cases. There is a small remaining altitude component of error, but along track errors are reduced to 60% of the Bulk Error and across track errors are reduced typically to 50% of the corresponding Bulk Error values.

B. Extrapolation Results

Extrapolation results are presented in Table 5 for the scenarios identified by scene in Table 1. In this case, not all scenarios exhibit improved performance, and those with non-contiguous single GCP rich/poor scenes are distinctly worse off than the corresponding Bulk Errors. Contiguous single GCP rich/poor scenes are improved somewhat and significant performance improvement is achieved with two or more contiguous GCP rich scenes contiguous with a GCP poor scene.

TABLE 4. Interpolation Results

Scenario	Bulk Error (M, RMS) Over GCP Poor Scene	A Priori Error (M, RMS) Over GCP Poor Scene	A Posteriori Error (M, RMS) Over GCP Rich Scenes	A Posteriori Error (M, RMS) Over GCP Poor Scene
101*	AT 759	900	49	418
	CT 556	661	63	266
	H 30	30	33	35
10*1	AT 759	900	58	401
	CT 556	661	54	320
	H 30	30	33	36
1*01	AT 1057	947	58	414
	CT 582	577	58	135
	H 36	33	33	38
1011	AT 759	900	93	481
	CT 556	661	74	276
	H 30	30	33	34
1101	AT 1057	1050	45	603
	CT 582	591	87	98
	H 36	31	36	36

AT = Along Track
CT = Cross Track
H = Altitude

* Scene Not Utilized
0 GCP Poor Scene
1 GCP Rich Scene

TABLE 5. Extrapolation Results

Scenario	Bulk Error (M, RMS) Over GCP Poor Scene	A Priori Error (M, RMS) Over GCP Poor Scene	A Posteriori Error (M, RMS) Over GCP Rich Scenes	A Posteriori Error (M, RMS) Over GCP Poor Scene
10**	AT 759	900	87	600
	CT 556	661	55	408
	H 30	30	39	37
1*0*	AT 1057	1050	87	1532
	CT 582	591	55	522
	H 36	31	39	41
1**0	AT 907	684	87	1562
	CT 631	579	55	728
	H 42	29	39	39
110*	AT 1057	1050	49	614
	CT 582	591	92	86
	H 36	31	36	36
11*0	AT 907	684	34	697
	CT 631	579	90	182
	H 42	29	34	35
1110	AT 907	684	53	594
	CT 631	579	65	140
	H 42	29	39	34

AT = Along Track
CT = Cross Track
H = Altitude

* Scene Not Utilized
0 GCP Poor Scene
1 GCP Rich Scene

4. CONCLUSIONS

In general, it was found that interpolation mode error statistics were stable, that is, not sensitive to GCP processing order or location error of the GCPs. On the other hand, the extrapolation mode tended to be relatively less stable if extrapolated from one GCP rich scene. Not unexpectedly, performance deteriorates with separation of GCP rich and poor scenes in the extrapolation mode. However, extrapolation with two or more GCP rich scenes significantly increases stability and accuracy.

Clearly, more work needs to be done to examine the effects of attitude modeling errors, number of scenes which can be processed and the distribution of GCPs. Nonetheless, a significant improvement in geometric accuracy performance for scenes without GCPs can be expected with the use of a global state vector updated by GCPs in nearby sites.

REFERENCES

1. S. S. Rifman, "Digital Rectification of ERTS Multispectral Imagery," Symposium on Significant Results Obtained from the Earth Resources Technology Satellite-1, New Carrolton, Md., NASA SP-327, p. 1131 (March 5-9, 1973).

2. S. S. Rifman, "Evaluation of Digitally Corrected ERTS Imagery," Symposium on Management and Utilization of Remote Sensing Data, Sioux Falls, South Dakota, p. 284 (Obtober 29-November 1, 1973).

3. J. E. Taber, "Evaluation of Digitally Corrected Images," Third Earth Resources Technology Satellite-1 Symposium, Washington, D.C., NASA SP-351, p. 1837 (December 10-14, 1973).

4. R. H. Caron, "Evaluation of Full-Scene Registered ERTS MSS Imagery Using a Multitemporal/Multispectral Bayes Supervised Classifier," Fourth Annual Remote Sensing of Earth Resources Conferences, University of Tennessee Space Institude, Tullahoma, Tennessee (March, 1975).

5. S. S. Rifman, et al., "Second Generation Digital Techniques for Processing LANDSAT MSS Data," Earth Resources Survey Symposium, Houston, Texas (June 8-12, 1975).

6. R. H. Caron and K. W. Simon, "Attitude Time-Series Estimator for Rectification of Spaceborne Imagery," Journal of Spacecraft and Rockets 12, 27 (January 1975).

7. S. S. Rifman and W. B. Allendoerfer, "LANDSAT MSS Rectification and Registration Results Obtained by Using a Precision Attitude Estimator," paper present to The Flight Mechanics/Estimation Theory Symposium, NASA, Greenbelt, Maryland (October 29-30, 1975).

8. LANDSAT Data Users Handbook, NASA Document No. 76SDS4258 (September 2, 1976).

9. K. W. Simon, "Digital Image Reconstruction and Resampling for Geometric Manipulation," Symposium on Machine Processing of Remotely Sensed Data, West Layfayette, Indiana (June 3-5, 1975).

AUTONOMOUS ATTITUDE ESTIMATION VIA STAR SENSING AND PATTERN RECOGNITION

J. L. Junkins and T. E. Strikwerda

Engineering Science and Mechanics
Virginia Polytechnic Institute and State University

ABSTRACT

We report results to date on the development of an autonomous, on board, near real time spacecraft attitude estimation technique. The approach will use CCD based star sensors to digitize relative star positions. Three microcomputers are envisioned, configured in parallel, to (i) determine star image centroids and delete spurious images, (ii) identify measured stars with stars in an on board catalog and determine discrete attitude estimates, (iii) integrate gyro rate measurements and determine optimal real time attitude estimates for use in the control system and for feedback to the star identification algorithm.

We present improved algorithms for the star identification. The discrete attitude estimation algorithm recovers thermally varying interlock angles between two star sensors. The optimal state estimation process recovers rate gyro biases in addition to real time attitude estimates.

Discussion of Slide Material

Figure 1.

For this technique, two star sensors are fixed to the spacecraft and to each other with interlock angles of, say, 60°-90°. Both fields of view (FOV) are sampled at the same instant in time and the star data are used to determine the vehicle attitude. We note that each field can be used independently to yield attitude but if both fields of view are functioning, the data are combined to yield an orientation with higher precision and to recover interlock angles as well. We expect to attain a pointing accuracy of at least $\leq$ 10 arc-sec. and probably $\leq$ 5 arc-sec.

Figure 2.

This figure shows schematically the parallel processing nature of this technique. Process A will cycle independently of Processes B and C since it will likely be the most rapid. Process B will obtain image coordinates from Process A at the beginning of each cycle and at the same time obtain estimated orientation angles from the Runge-Kutta integrator section of Process C. The run time of Process B will probably be the longest of the three but will also be quite variable. The output of Process B consists of three orientation angles and the covariance matrix obtained from the least-squares correction. These are used by Process C along with the estimated angles. We propose a Kalman filter algorithm to determine the optimal state estimate at the time associated with the current data from Process A. Process C will also update the estimated rate gyro biases. These are then used for the next Runge-Kutta integration. Process C will likely have a relatively fixed time budget.

Figure 3.

Figure 3 displays a summary of functions performed by Process A. CCD integration time is typically 0.1 - 1.0 sec. and readout time is < 0.1 sec. The primary function of Process A is to determine image centroids. Star images are defocused slightly to spread images over 3 x 3 or 4 x 4 pixels. The response of each pixel is used to interpolate positions to an accuracy of, say, one-tenth of a pixel.

A second important function is to detect and delete spurious images. Images which are moving relative to other stars will be deleted. Since the cycle time should be quite short we can track images over several frames before Process B requests new data.

The output of Process A will consist of image coordinates and brightness at the latest epoch, for all stars with intensity above some threshold. Each FOV is treated separately and passed to Process B.

Figure 4.

Process B is the most challenging process. Input data consist of image coordinates from each FOV and estimated attitude angles for the time associated with the image measurements. An on-board star catalog is accessed to yield coordinates for all catalog stars within some uncertainty border around the estimated FOV. These are sorted according to angle from the estimated boresight of the star sensor.

Angles between measured stars are compared with angles between catalog stars until a tentative match occurs. The three orientation angles are adjusted to bring computed image coordinates of catalog stars into agreement (in a least-squares sense) with the image coordinates from the FOV. We next test for additional star matches and repeat the adjustment.

The above steps are performed for both FOVs. If both sensors are functioning, the data are then combined to refine the attitude angles and the three interlock angles between FOV1 and FOV2.

Output of Process B is three orientation angles at the time associated with the image measurements.

Figure 5.

The image placement on a CCD star sensor is a function of six parameters: spacecraft orientation angles (ϕ,θ,ψ), star coordinates (α, δ), and the sensor focal length, f. The colinearity equations of Figure 5 express this relationship for (x,y) placement.

To simplify the computation we chose to store direction cosines for the star coordinates rather than (α,δ). Note that once [C] is computed for an estimated orientation, image coordinates are simple algebraic equations.

Figure 6.

In process B, the cosines of interstar angles are computed and compared. Computation involves only algebraic expressions containing no trignometric functions. The star catalog contains direction cosines for each star rather than right ascension and declination (α,δ). Although more memory is required by the catalog, the speed gain by eliminating many sine and cosine calculations justifies the storage of direction cosines.

Figure 7.

Once a tentative star pair cosine from the catalog matches a measured pair cosine, the estimated orientation is iteratively adjusted

by least-squares differential correction. This scheme is used for both fields and the combined solution. In the latter case, three interlock angles are solved for as well as the three orientation angles.

Figure 8.

Figure 8 displays the stars accessed from the catalog for a typical case. The dashed line is the estimated FOV and the solid line represents the true FOV. The boxed stars are the stars that provided the first match with the measured stars.

The sky has been divided into 256 non-overlapping cells, all nearly the same size. One or more cells are accessed for stars near the bore-sight. Only those stars that are within an uncertainty border (~11°) are used in the pairing logic. In this example, three cells were accessed giving 73 stars of which 38 were used in pairing logic. A match was found on the 38th attempt and, after correction, all four measured stars were matched with catalog stars.

Only one cell, containing 24 stars, was needed for FOV2. A match was found on the fourth attempt and 1 additional star of the 5 measured stars was identified in the catalog after correction. The remaining 2 measured stars were not contained in the catalog.

Table 1.

In this table we list the angle corrections obtained by a typical least-squares solution in Process B. The three attitude angles have been perturbed by approximately three degrees and the interlock angles by 1 arc-minute.

As can be seen from the table, most of the attitude corrections are obtained by the FOV1 solution. The attitude is corrected again by the FOV2 solution due to poor interlock angles. Finally, the combined solution recovers both the attitude and interlock angles.

Figure 9.

Figure 9 presents an outline of the main function of Process C. The actual algorithms to be used have not been finalized pending evaluation of Process B execution time in a microcomputer system. Short run times for Process B will allow less complexity in Process C algorithms.

Presently, there are two primary tasks for Process C:

1) Integrate the equations of motion ahead to the time of Process A output to B. This will use the last output of Process C for the initial attitude state and gyro rates will have biases subtracted.

2) Use Extended Kalman Filter formulation to obtain the optimal best estimate of the spacecraft attitude at the instant of Process A output. Optimal estimates of gyro biases are also calculated. This algorithm requires the estimated angles from 1) above, the discrete attitude and associated covariance matrix obtained from the Process B solution, and the state covariance matrix from the last Kalman filter update. The best estimates of angles and biases are then used for subsequent integration of the motion equations.

Figure 10.

This figure demonstrates the behavior of the Kalman filter on simulated data. The plotted data show the deviations of the first attitude angle (ϕ) from the true orientation. Attitude from Process B is simulated by perturbing the true orientation angles (standard deviation of 8.8 arc-sec). The gyro rates are perturbed from a constant value ($\sim 4 \times 10^{-4}$ rad./sec.; standard deviation of 1.5×10^{-6} rad./sec.) each time they are needed and biases are set to 4.8×10^{-6} rad./sec. The initial estimated state is off

10° in each angle from the truth (very conservative) and biases are set to zero.

The attitude state is integrated ahead in 1 minute intervals and the deviation from the truth calculated (shown as "X"). Simulated data from Process B then becomes available and the Kalman filter applied. The deviations of the filtered results from the truth is denoted by crosses ("+"). Due to noisy gyro rate data and the 1 minute integration time, the filtered attitude nearly equals the Process B attitude.

The dashes ("-") are the estimated deviations as calculated from the updated covariance matrix after each pass through the Kalman filter.

Note that after only three Kalman filter applications the attitude and biases have been recovered, and the steady state attitude errors are less than 10 arc-seconds in all cases and usually less than 5 arc-seconds. The one minute interval between star-determined orientation estimates (from Process B) will in practice be variable and typically less than one minute; the precision of these simulated converged estimates is therefore felt to be conservative.

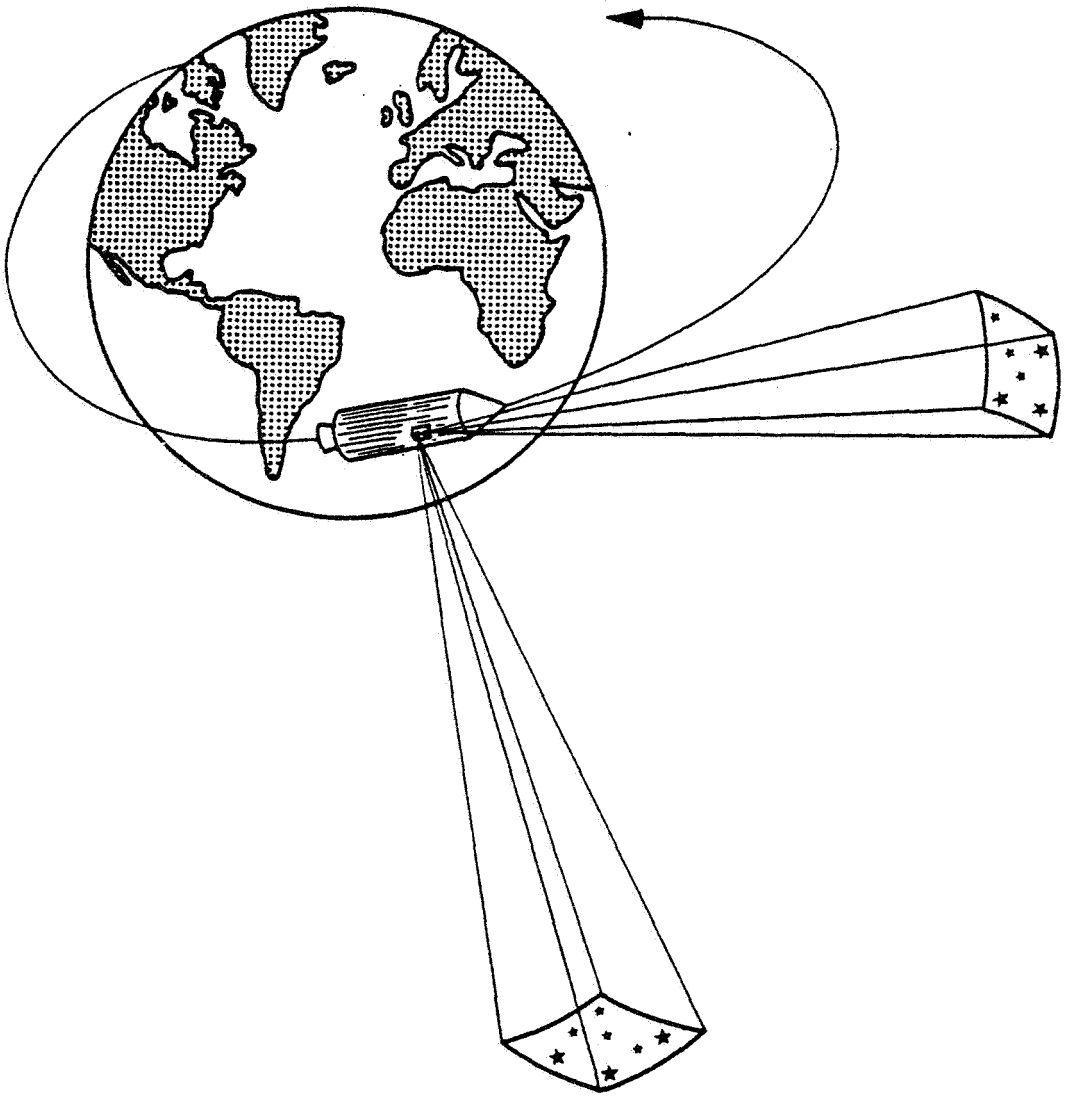

FIGURE 1 UVASTAR An electro-optical/software system capable of real time readout of digitized star coordinates, and ultimately, autonomous, near-real time star pattern recognition and attitude determination.

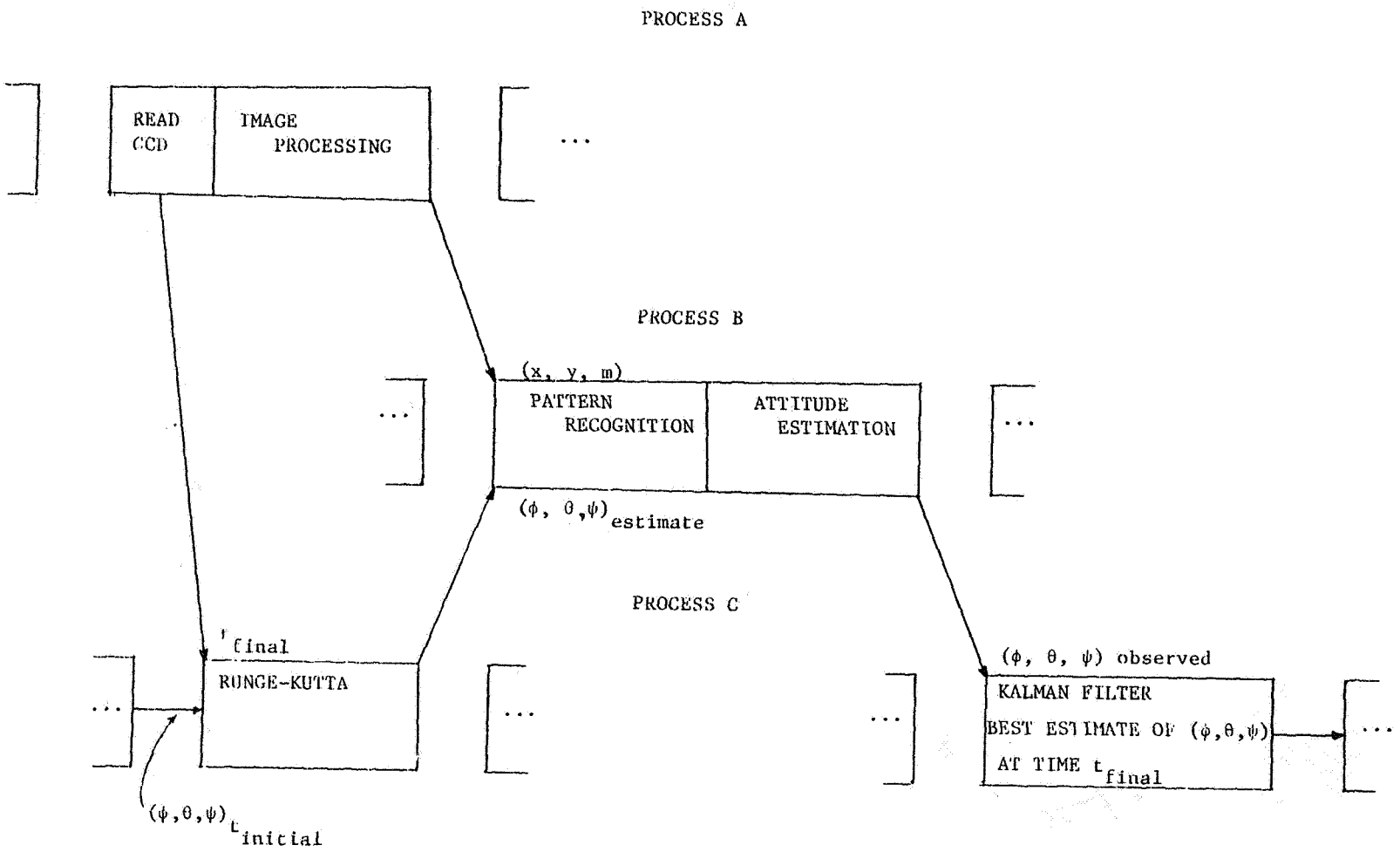

Figure 2: Three parallel process technique of star pattern recognition/attitude determination. Time runs from left to right.

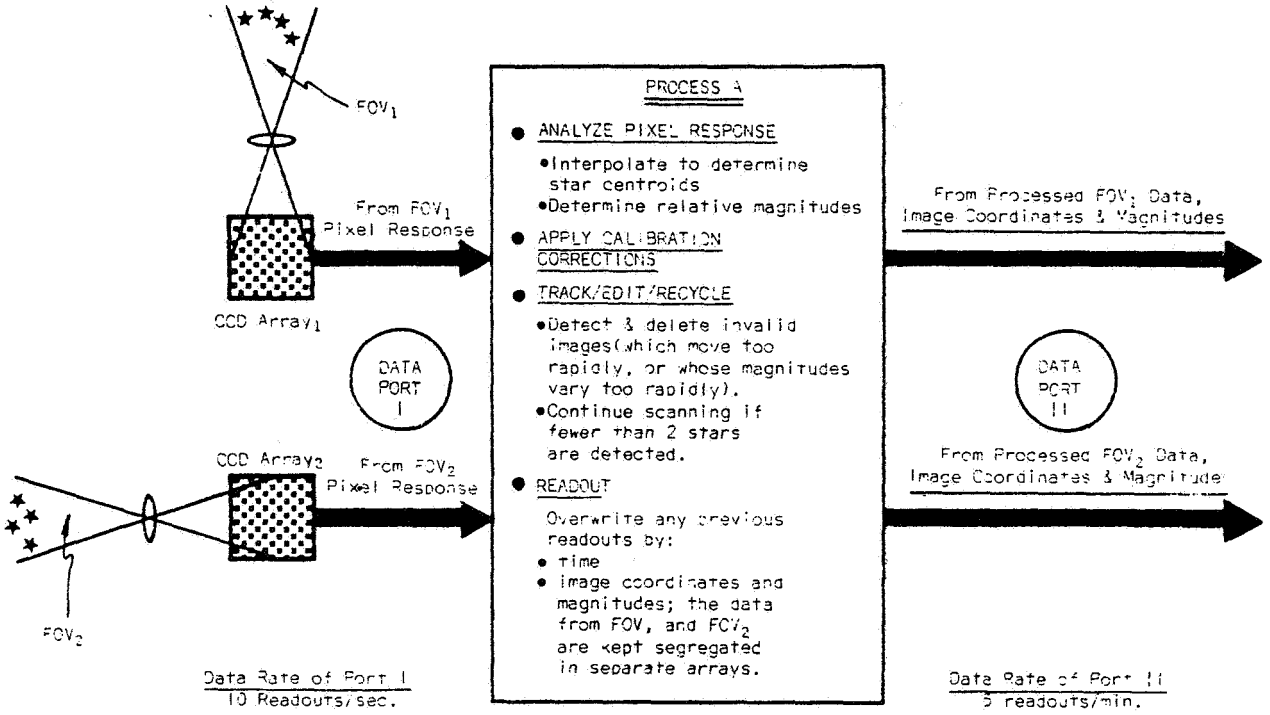

Figure 3: Major tasks of Process A.

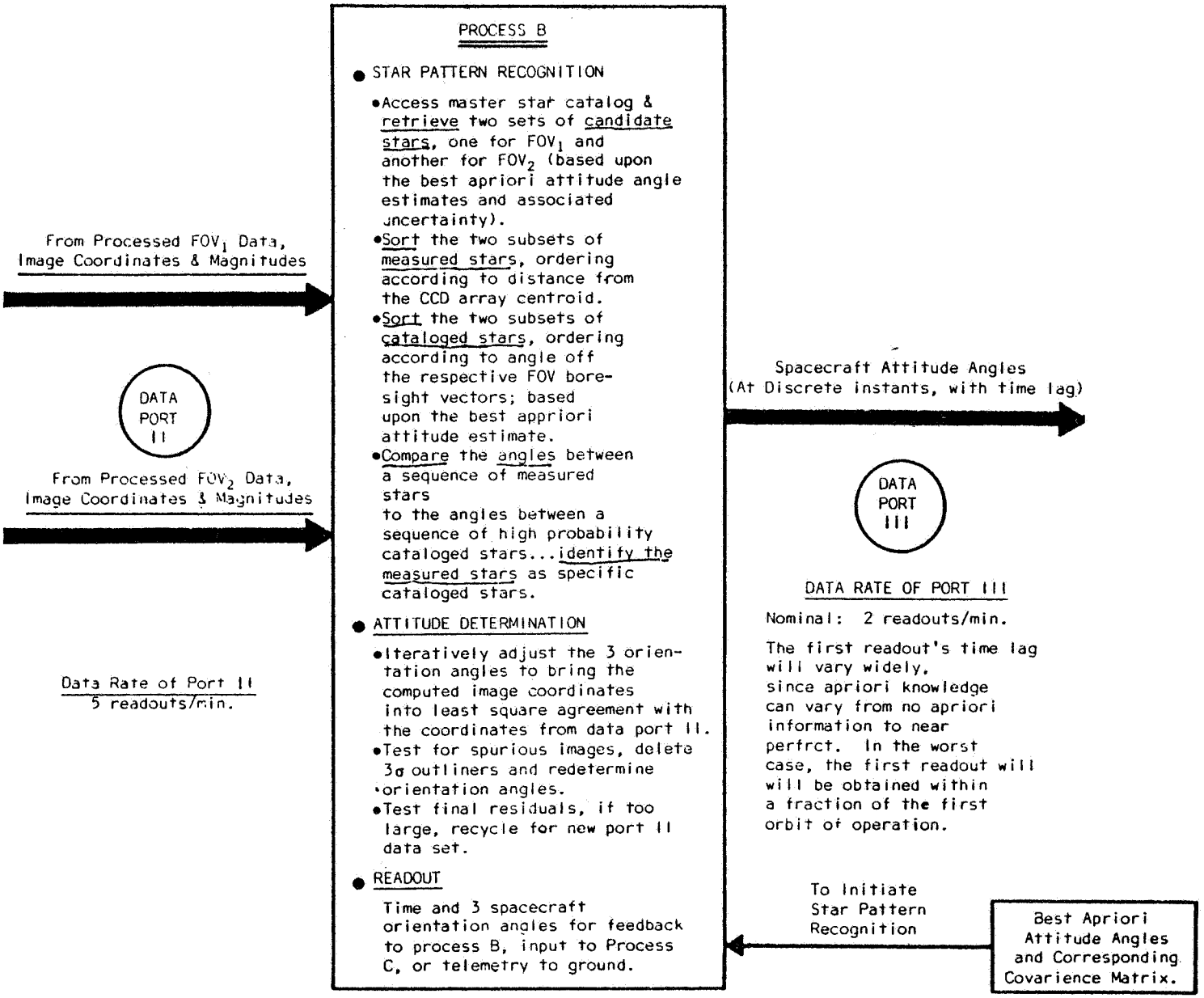

Figure 4: Major tasks of Process B.

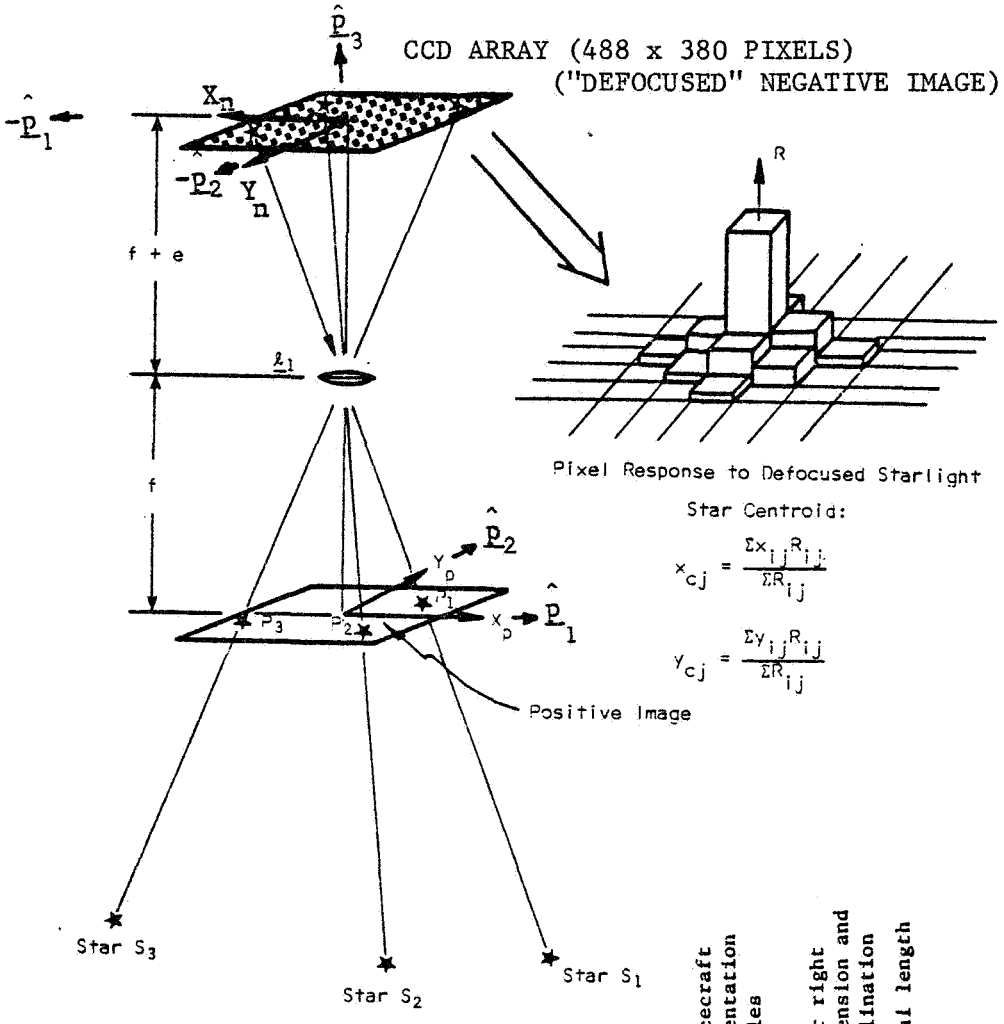

Colinearity Equations:

$$X_n = f\left[\frac{C_{11}L_1 + C_{12}L_2 + C_{13}L_3}{C_{31}L_1 + C_{32}L_2 + C_{33}L_3}\right] = \text{function}\ (\underbrace{\phi, \theta, \psi}_{\text{Spacecraft Orientation Angles}}, \underbrace{\alpha, \delta}_{\text{Star right Ascension and Declination}}, \underbrace{f}_{\text{Focal length}})$$

$$Y_n = f\left[\frac{C_{21}L_1 + C_{22}L_2 + C_{23}L_3}{C_{31}L_1 + C_{32}L_2 + C_{33}L_3}\right] = \text{function}\ (\phi, \theta, \psi, \alpha, \delta, f)$$

where

$$\left.\begin{aligned} L_1 &= \cos\delta\cos\alpha \\ L_2 &= \cos\delta\sin\alpha \\ L_3 &= \sin\delta \end{aligned}\right\} \text{ star direction cosines, } [C_{ij}] = \begin{bmatrix} \cos\psi & \sin\psi & 0 \\ -\sin\psi & \cos\psi & 0 \\ 0 & 0 & 1 \end{bmatrix} \begin{bmatrix} \cos\theta & 0 & -\sin\theta \\ 0 & 1 & 0 \\ \sin\theta & 0 & \cos\theta \end{bmatrix} \begin{bmatrix} 1 & 0 & 0 \\ 0 & \cos\phi & \sin\phi \\ 0 & -\sin\phi & \cos\phi \end{bmatrix}$$

FIGURE 5: Formation of Image on the CCD Array.

STAR PAIR COSINE CALCULATION

Measured Star Pair Cosine

$$\cos\theta_{mij} = \frac{\underline{\ell}_i \cdot \underline{\ell}_i}{|\underline{\ell}_i| \cdot |\underline{\ell}_j|}$$

$$= \frac{x'_i x'_j + y'_i y'_j + 1}{\sqrt{x'^2_i + y'^2_i + 1} \cdot \sqrt{x'^2_j + y'^2_j + 1}}$$

where $x' = x/f.l.$

$y' = y/f.l.$

(x,y) output of Process A

Cataloged Star Pair Cosine

$$\cos\theta_{cIJ} = \underline{L}_I \cdot \underline{L}_J$$

where $\underline{L}_I$ = unit vector towards I^{th} star in

catalog subset = $\begin{Bmatrix} L_{x_I} \\ L_{y_I} \\ L_{z_I} \end{Bmatrix} = \begin{Bmatrix} \cos\alpha_I \cos\delta_I \\ \sin\alpha_I \cos\delta_I \\ \sin\delta_I \end{Bmatrix}$

$\underline{L}_J$ = unit vector towards J^{th} star in catalog subset

(α,δ) = catalog right ascension and declination of stars from catalog.

Figure 6: Star pair cosine calculations for measured star pairs and catalog star pairs. f.l. is the star sensor focal length.

$$\begin{Bmatrix} \phi \\ \theta \\ \psi \end{Bmatrix}^{(k+1)} = \begin{Bmatrix} \phi \\ \theta \\ \psi \end{Bmatrix}^{(k)} + [(A^T A)^{-1} A^T]^{(k)} \begin{Bmatrix} x_i - x_i^{(k)} \\ y_i - y_i^{(k)} \\ x_j - x_j^{(k)} \\ y_j - y_j^{(k)} \end{Bmatrix}$$

where $A^{(k)} =$

$$\begin{bmatrix} \frac{\partial x_i^{(k)}}{\partial \phi^{(k)}} & \frac{\partial x_i^{(k)}}{\partial \theta^{(k)}} & \frac{\partial x_i^{(k)}}{\partial \psi^{(k)}} \\ \frac{\partial y_i^{(k)}}{\partial \phi^{(k)}} & \frac{\partial y_i^{(k)}}{\partial \theta^{(k)}} & \frac{\partial y_i^{(k)}}{\partial \psi^{(k)}} \\ \frac{\partial x_j^{(k)}}{\partial \phi^{(k)}} & \frac{\partial x_j^{(k)}}{\partial \theta^{(k)}} & \frac{\partial x_j^{(k)}}{\partial \psi^{(k)}} \\ \frac{\partial y_j^{(k)}}{\partial \phi^{(k)}} & \frac{\partial y_j^{(k)}}{\partial \theta^{(k)}} & \frac{\partial y_j^{(k)}}{\partial \psi^{(k)}} \end{bmatrix}$$

Figure 7: Method of least squares for estimated attitude angle correction. (ϕ,θ,ψ) are orientation angles and (x,y) are image coordinates.

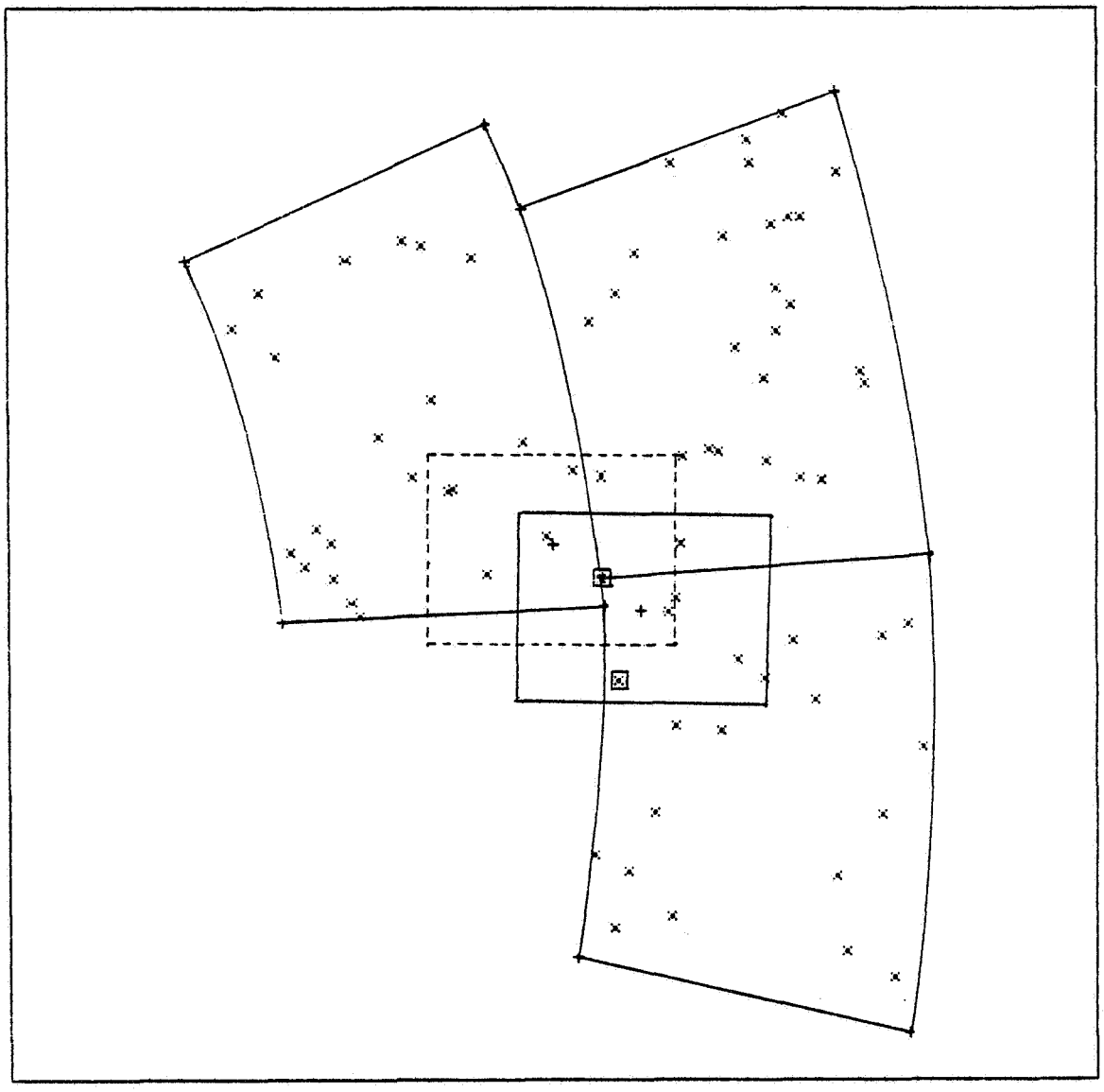

Figure 8: Boundaries of the true field of view (solid rectangle) and estimated field of view (dashed rectangle). Center of each FOV is denoted by "+". The three large sectors are the three cells accessed by Process B. The pair of boxed stars is the first pair to match the measured stars. FOV is approximately 7° x 9°.

TABLE 1: Iterative Least Square Attitude Determination

	Iteration	Orientation Angles (rad.) ϕ	θ	ψ	Interlock Angles (rad.) γ_1	γ_2	γ_3	Residual RSM (mm)	No. of Stars
FOV1	0	2.46254	0.03454	1.42654	—	—	—	3.550	2
	1	2.41509	0.08674	1.47404	—	—	—	0.166	2
	2	2.41254	0.08474	1.47688	—	—	—	0.011	2
	3	2.41254	0.08453	1.47689	—	—	—	0.001	2
	4	2.41253	0.08453	1.47672	—	—	—	0.002	4
FOV2	0	2.41253	0.08453	1.47672	1.57051	-1.57051	-1.57109	0.019	2
	1	2.41275	0.08289	1.47674	—	—	—	0.000	2
	3	2.41277	0.08345	1.47678	—	—	—	0.002	3
COMBINED (FOV1 + FOV2)	0	2.41277	0.08345	1.47678	1.57051	-1.57051	-1.57109	0.042	7
	1	2.41253	0.08453	1.47672	1.57059	-1.57085	-1.57003	0.002	7
	True	2.41254	0.08454	1.47654	1.57080	-1.57080	-1.57080	0.0034	

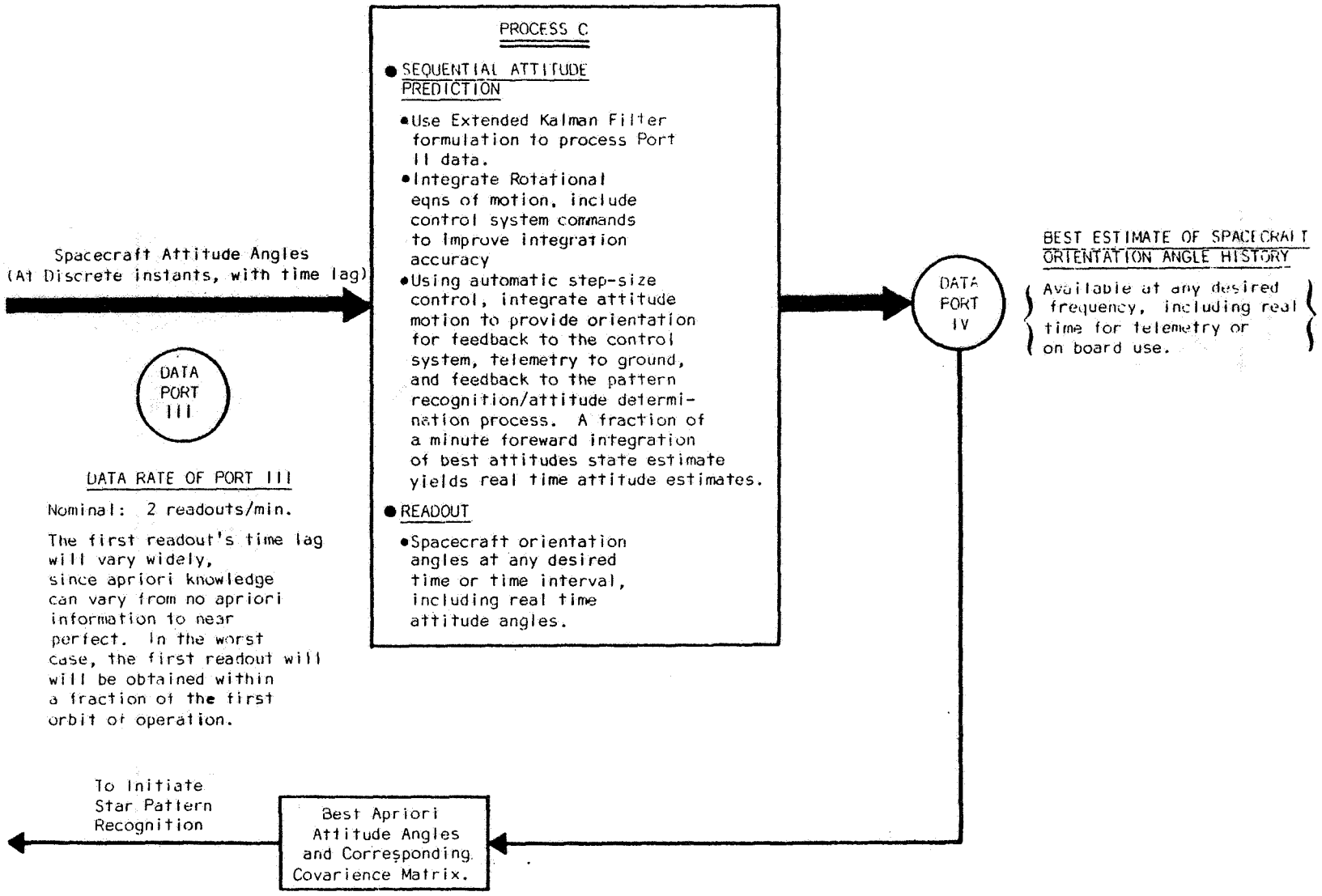

Figure 9: Major tasks of Process C.

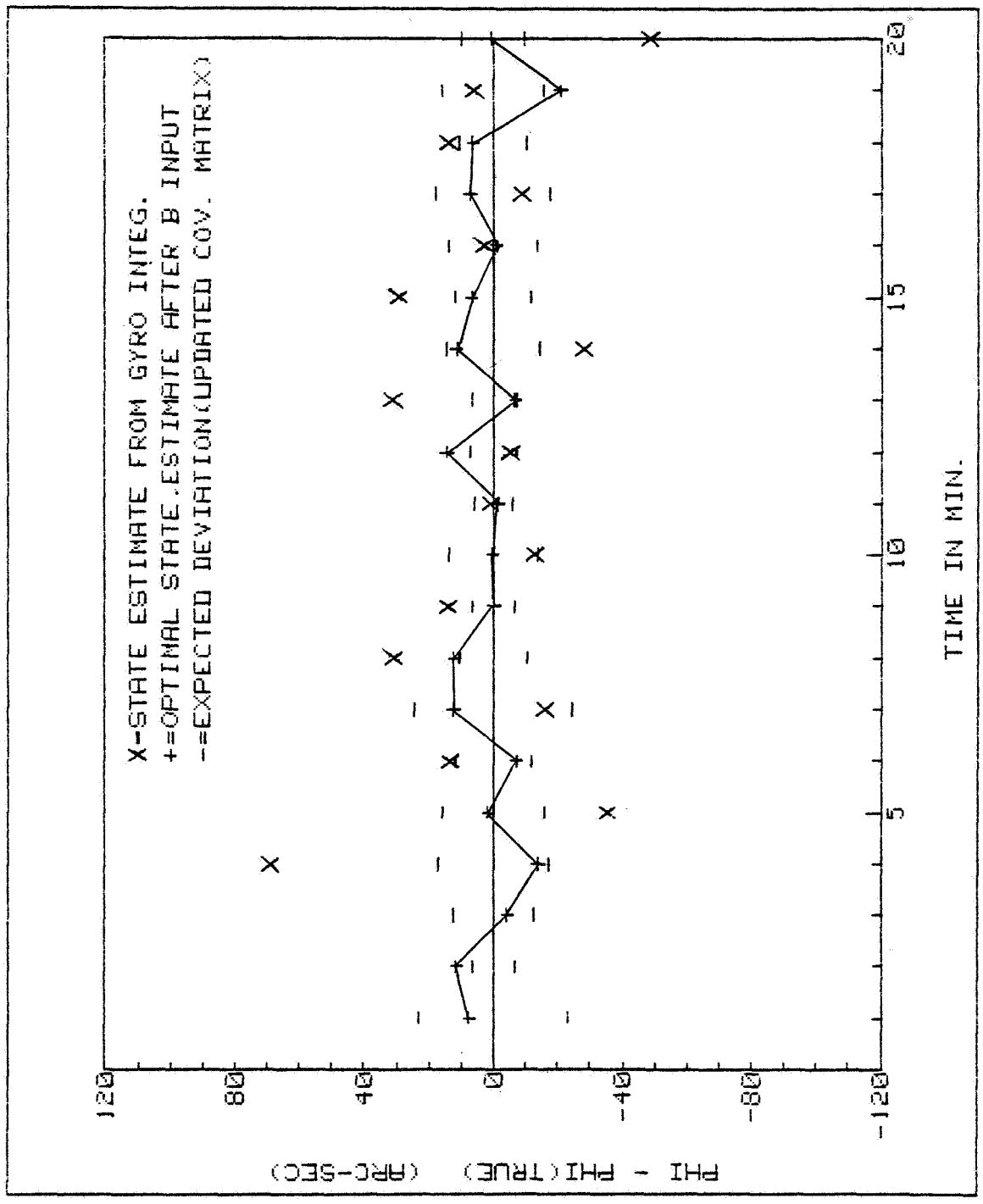

Figure 10: Behavior of Kalman filter for first

Figure 11: Concluding Remarks

- A new spacecraft attitude estimation approach is under development. Key features are:

  *Electro-optical star sensors with no moving parts

  *On board, near real time attitude estimation

  *Sub ten arc-second precision appears feasible.

- A three parallel process division of labor is proposed:

  A - Star-sensing/Image processing

  B - Star identification/Discrete attitude estimation

  C - Motion integration/Attitude estimation

- The software for Processes B and C is currently being implemented on microcomputers. The algorithms will be tested, evaluated and modified to maximize data throughput and accuracy.

- Area of major effort and/or problems:

  *Limited precision and speed obtained with on-board microcomputers

  *Data acquisition rate vs. Process B run time

  *Process B run time vs. Process C complexity.

References

Junkins, J. L., White, C. C., and Turner, J. D., "Star Pattern Recognition/ Attitude Determination using Digital Star Sensing," Proceedings of the Flight Mechanics/Estimation Theory Symposium (Goddard Space Flight Center, Greenbelt, Maryland, October, 1976).

Junkins, J. L., White, C. C., and Turner, J. D., "Star Pattern Recognition for Real Time Attitude Determination," Journal of the Astronautical Sciences, Vol. XXV, No. 3, July-Sept. 1977, 251-270.

NAVIGATION AND ATTITUDE REFERENCE FOR AUTONOMOUS SATELLITE LAUNCH AND ORBITAL OPERATIONS

S. P. Kau

Avionics Division Honeywell Inc.

ABSTRACT

This paper investigates the navigation and attitude reference performance of a strapdown system for applications to autonomous satellite launch and orbital operations. It is assumed that satellite payloads are integrated into existing missile systems and that the boost, orbit insertion and in-orbit operations of the satellite are performed autonomously without relying on external support facilities. Autonomous and long term accurate navigation and attitude reference are provided by a strapdown inertial navigation system aided by a star sensor and earth landmark sensor. Sensor measurement geometry and navigation and attitude update mechanizations are discussed. Performance analysis data are presented for following functional elements:

a. prelaunch alignment,
b. boost navigation and attitude reference,
c. post boost stellar attitude and navigation updates,
d. orbital navigation update using sensor landmark measurements,
e. in-orbit stellar attitude update and gyro calibration.

The system performance are shown to satisfy the requirements of a large class of satellite payload applications.

NAVIGATION AND ATTITUDE REFERENCE FOR AUTONOMOUS SATELLITE LAUNCH AND ORBITAL OPERATIONS

S. P. KAU

AVIONICS DIVISION
HONEYWELL INC.
ST. PETERSBURG, FLORIDA

1. INTRODUCTION

This paper explores the feasibility of a guidance system using currently available sensor technology for autonomous satellite launch and orbital applications. One possibility of such applications may be stemmed from considerations on the survivability of satellite functions vital to national defense. Reconnaissance and communication payloads may be integrated into existing silo or submarine based missile systems to enhance their initial survivability. These payloads will be boosted and deployed without relying on external launch support and mission control facilities that may not be available during a national emergency. To support such mission applications a system consisting of onboard sensing and data processing elements is required to provide the navigation and attitude reference functions with necessary accuracy over the duration of the mission.

This paper considers an Autonomous Navigation System (ANS) consisting of an IMU, a star sensor, a down sensor for landmark sightings, a radar altimeter, a long term stable clock, and an on-board computer and resident softwares. To facilitate the discussions here, two autonomous satellite launch missions are hypothesized. The first involves the boost and deployment of a payload satellite into a 185 Km circular orbit, the second, a 370 Km x 40000 Km 12-hour Molnya orbit after temporary dwellings in parking orbit for appropriate orbit phasing. These two missions are believed suitable for a wide class of satellite payloads and within the capabilities of available booster candidates. To provide navigation and attitude reference functions supporting these missions, the ANS system elements are mechanized into the following operation modes:

(1) IMU self alignment mode prior to boost,

(2) Pure inertial mode during boost and ΔV thrustings for orbit insertion and in-orbit maneuvers,

(3) Stellar inertial mode for post boost and in-orbit attitude update and gyro calibration,

(4) Orbital navigation mode for in-orbit navigation and update.

An artist's conception of ANS in an autonomous satellite mission is presented in Figure 1.

In the following discussions the ANS performances for each of the functional elements are assessed. The error budget assumed in the performance analysis is summarized in Table 1. The sensor characteristics are based on existing system capabilities (Reference 1.) The down sensor landmark sighting accuracy is projected from the engineering test model developed on the Autonomous Navigation Technology (ANT) program (Reference 2.) It should be pointed out here that results reported here do not represent a particular mission operation nor a specific system design. Rather, they should be interpreted as what can be achieved with currently available technology for functional elements likely to be included in any autonomous satellite applications.

2. IMU SELF ALIGNMENT

IMU self alignment is performed prior to boost. It involves the determination of the ANS attitude defined in terms of a coordinate transformation matrix between the inertially fixed navigation frame and an ANS fixed frame to which sensor measurements are referenced. It is accomplished through velocity matching processing supplemented by an optical azimuth reference. For a land based system the reference velocity is calculated from earth rate and known location of launch site. For a submarine based system the velocity and location of the vehicle are provided by a shipborne IMU. The level components of the self alignment errors are limited by the bias errors of the horizontal accelerometers and the reference velocity errors with the latter more significant for a mobile system than a land fixed system. Optical azimuth reference is required to supplement that obtained from a pure velocity matching. Without such an optical reference the azimuth error would become excessive because of the inability to reorient a strapdown IMU for calibrating out the gyro bias errors.

Assuming the ANS IMU and shipborne IMU characteristics, the alignment accuracy is found to be adequate to support a boost and orbit insertion within the landmark acquisition bounds for later navigation update.

Since satellite payloads are integrated into existing missile systems, it is possible that the booster IMU will be retained. A boost phase velocity matching may be performed to align the ANS IMU with respect to the booster IMU. Being a platform system with reorientation capability the booster IMU can be aligned with respect to the navigation frame more accurately than a strapdown system with equivalent quality sensors. In this case the azimuth alignment for ANS becomes non-critical. Discussions on a technique of in-flight alignment transfer is contained in Reference 3.

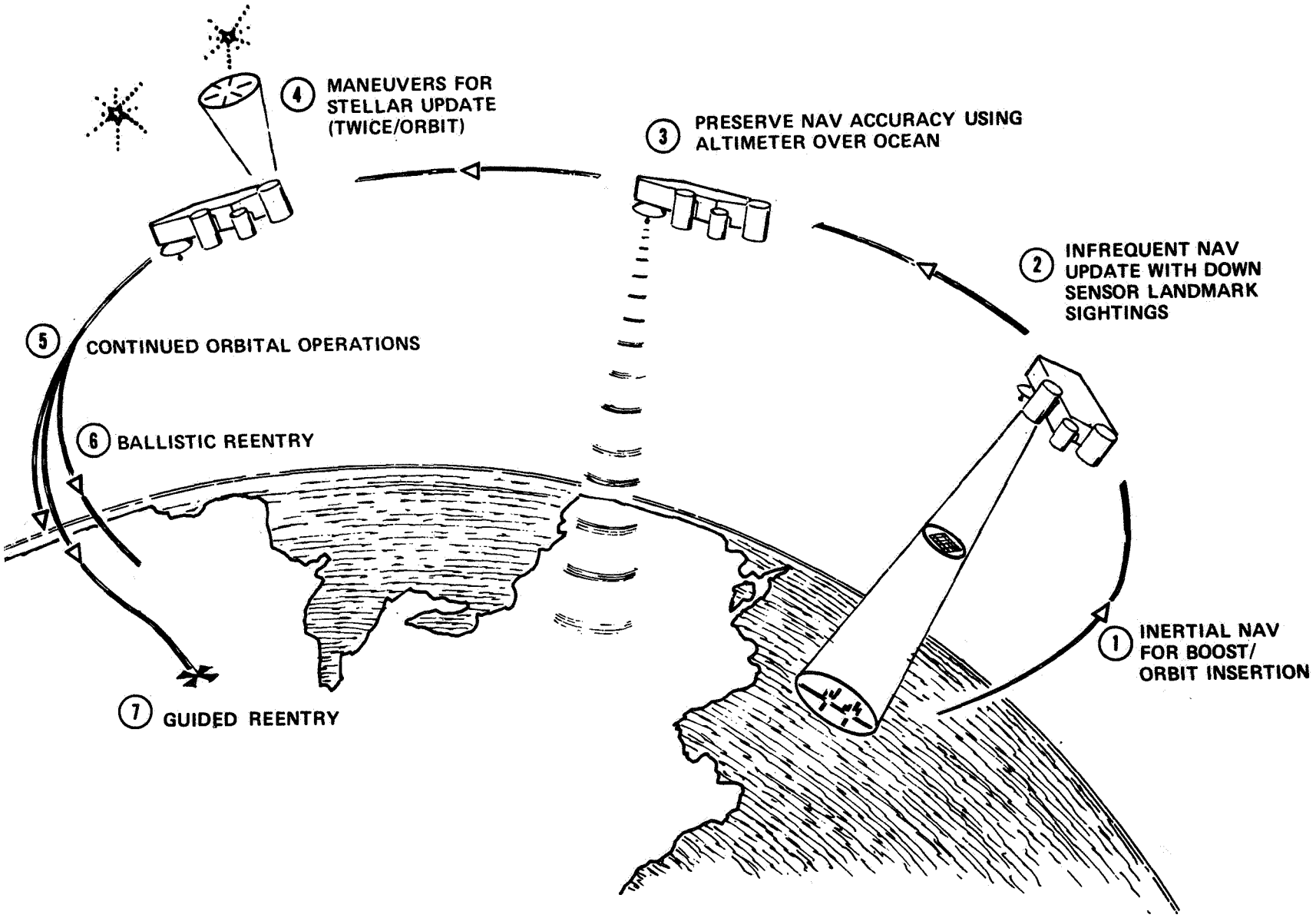

FIGURE 1. AUTONOMOUS NAVIGATION SYSTEM OPERATIONS BY MISSION PHASES

TABLE 1. ANS ERROR BUDGET (1 SIGMA)

GYRO:

● BIAS	0.04 DEG/HR
● SCALE FACTOR	75 PPM
● MUSA	0.02 DEG/HR/G
● MUIA	0.01 DEG/HR/G
● ANISO	0.01 DEG/HR/G^2
● MISALIGNMENT	13 ARC-SEC

ACCELEROMETER:

● BIAS	30 μG
● SCALE FACTOR	35 PPM
● SF ASYMMETRY	10 PPM
● MISALIGNMENT	7 ARC-SEC

STAR SENSOR:

● BIAS	6 ARC-SEC
● RANDOM	6 ARC-SEC

DOWN SENSOR:

● BIAS	30 ARC-SEC
● RANDOM	30 ARC-SEC

ALTIMETER:

● RANDOM	50 FEET

MODELING RESIDUE:

● GEOID ALTITUDE	45 FEET
● GRAVITY	1.25 μG
● DRAG: EXOSPHERIC TEMP	100^{o} /K
C_D	10 PERCENT

The alignment errors will propagate into position and velocity errors during boost. These errors can be significantly reduced via a post boost stellar update.

3. INERTIAL NAVIGATION

Inertial navigation is performed for all powered portions of an autonomous satellite mission including boost and ΔV thrustings for orbit insertion and in-orbit maneuvers. The gyro measured angular rate is integrated using the attitude initialized during self alignment. This attitude reference solution is used to transform the applied accelerations measured by the vehicle fixed accelerometers into the inertially fixed navigation frame. Vehicle position and velocity are obtained through integrating the measured thrust acceleration and the gravitational acceleration evaluated from a gravity model. These navigations and attitude reference solutions are used for generating booster steering and thrust termination commands during boost as well as the vehicle attitude control and ΔV thrustings for post boost maneuvers performed as part of orbit insertion and orbit transfer.

Boost navigation and attitude reference error sensitivities to IMU and initial alignment errors have been evaluated considering realistic missile boost trajectories. It is found that the initial alignment error dominates inflight sensor errors in their contributions to boost position and velocity errors. However, it is found that the boost errors are well within the acquisition bounds assumed for down sensor landmark sightings for in-orbit navigation updates.

Since the boost navigation states are computed using the attitude reference solution for coordinate transformation, the sensed acceleration provides the linkage between the navigation errors and the attitude errors. Through integration of the error propagation equation using the sensed acceleration as the driving function, it is possible to compute the correlation between the navigation error and the attitude error which is dominated by initial alignment error. This correlation allows the derivation of navigation error estimates from a post boost stellar attitude update.

The inertial navigation performance during thrustings for orbital maneuvers is evaluated assuming a ΔV level of approximately 2500 m/sec. This corresponds to the perigee burn required for the 12 hour Molnya orbit or a 18.5° plane change for the low altitude circular orbit. Assuming ANS IMU characteristics the velocity errors accumulated during the ΔV thrusting along the vehicle roll (nominal thrust direction), pitch and yaw axes are only 0.09, 0.26 and 0.22 m/sec (1σ) respectively. With these disturbances the total navigation errors are still within the down sensor acquisition bounds.

4. STELLAR INERTIAL ATTITUDE REFERENCE

The attitude solution obtained from integration of gyro angular rate measurements provide the basic attitude reference throughout the mission duration. Star sensor measurements are acquired for attitude and navigation update immediately following boost and for periodic in-orbit attitude update and gyro calibration.

The ANS star sensor consists of a telescope with a set of six detector slits placed on its image plane as depicted in Figure 2. A transit pulse is produced when the image of a star moves across a detecing slit. The basic star sensor measurement is the time when the star transit occurs. Each transit time measurement contains only one component of vehicle attitude information. Multiple transits from a single pass over the reference star can be combined to provide the equivalent measurement of the LOS-vector to the star. Vehicle maneuvers that provides repeated multiple scans between two reference stars (Figure 2) produce star transit measurements containing information for 3 axes attitude update as well as gyro bias and scale factor calibrations. A discussion of the star sighting strategy and Kalman filter mechanization for stellar attitude update is contained in Reference 4.

For post boost stellar update a single scan over a star located in the down range direction provides transits with maximum observability on the initial azimuth error, the dominant boost navigation error source. The navigation error can be obtained from stellar attitude measurements using the correlations between these two types of errors described earlier. Cross-track velocity error due to initial azimuth uncertainty can be reduced to 0.23 m/sec assuming ANS star sensor accuracy and 7800 m/sec vehicle velocity for 185 Km circular orbit.

In-orbit stellar update will be accomplished by performing the Figure 2 star acquisition maneuvers once per half orbit while the vehicle is over polar regions. Assuming ANS gyro and star sensor characteristics and 45 minute between update maneuvers the peak vehicle attitude errors can be bounded to approximately .15 m rad (Fig. 3) with gyro bias trimmed to 0.005 deg/hr (1σ) and scale factor calibrated to 25 PPM (1σ).

5. AUTONOMOUS ORBITAL NAVIGATION

After orbit insertion, the accelerometer output will be bypassed in the orbital navigation computation to avoid integration of the sensor bias error which is more significant than the input drag acceleration. An atmospheric density model will be carried onboard for drag evaluation. Due to errors in the initial conditions handed over from boost and uncertainties in the acceleration models, the error buildup of the orbital navigation solution requires periodic updates using down sensor landmark measurements. Additional navigation updates are provided by radar altimeter or horizon sensor measurements that are more frequently available.

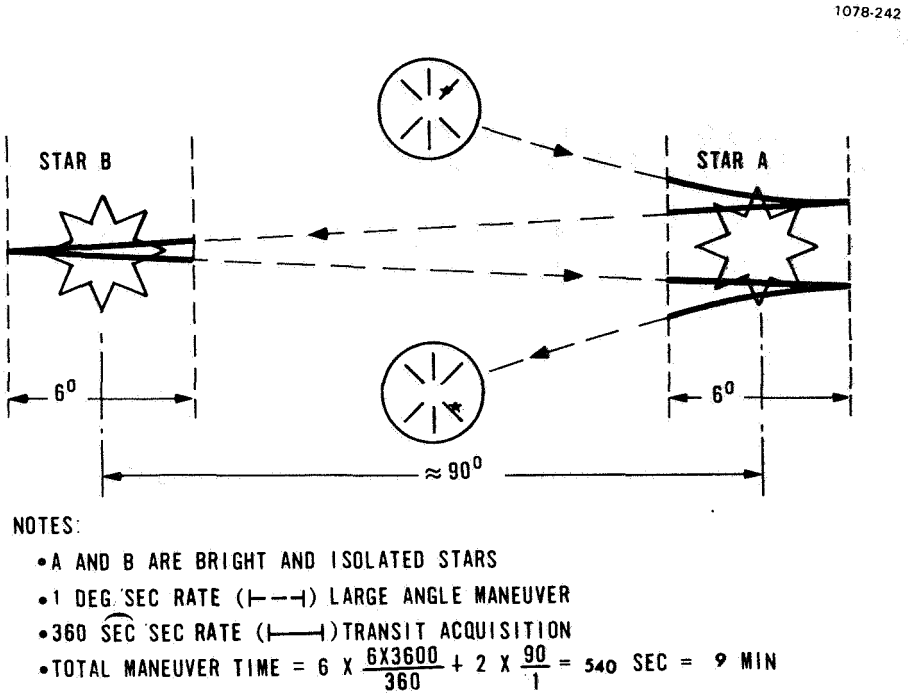

FIGURE 2. STAR ACQUISITION ATTITUDE MANEUVER PROFILE

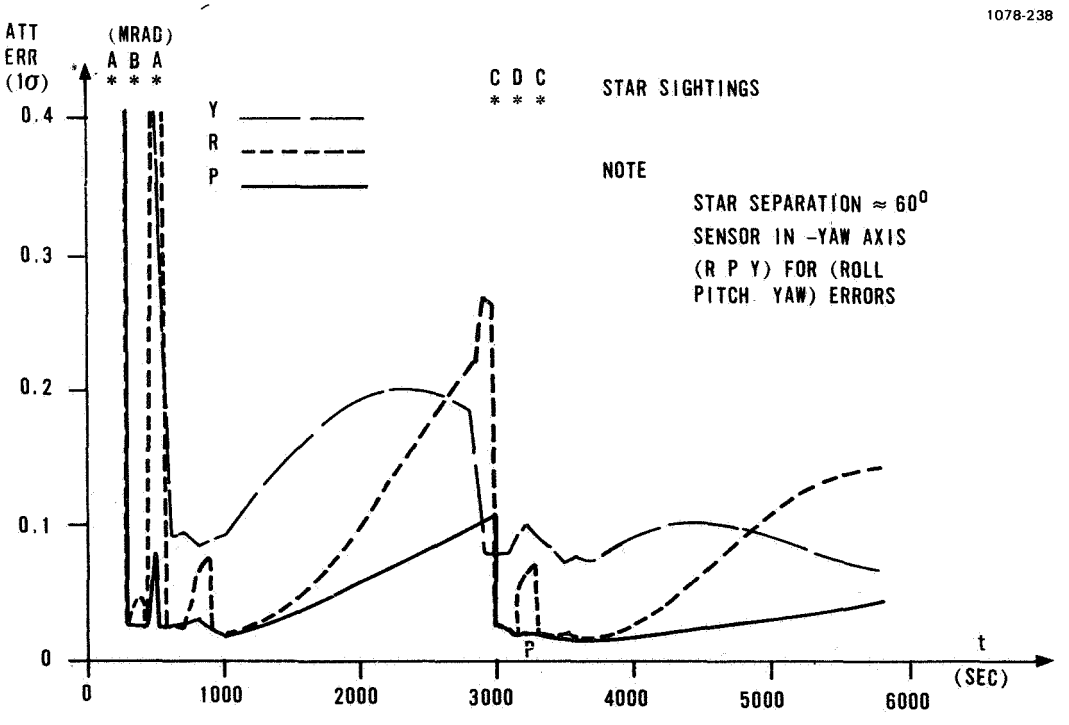

FIGURE 3. STELLAR INERTIAL ATTITUDE REFERENCE PERFORMANCE PLOTS

The ANS down sensor mechanization and navigation update concepts were originally developed on the Autonomous Navigation Technology (ANT) program performed for the Air Force (Reference 2). The ANT down sensor is an electro-optical device consisting of a telescope with two linear silicon detector arrays placed in its image plane as shown in Figure 4. Due to the vehicle motion, successive samplings of a detector array provide a digital image of the original terrain scene. Edge enhancement and feature extraction operations are performed to detect the presence of linear earth features (e.g. highways, rivers and coastlines), and to determine the orientation and the centroid of the segment of the feature appearing in the sensor Field Of View (FOV) as depicted in Figure 5. Upon down sensor linear feature detection candidate landmarks from an onboard catalog will be examined to identify the features sighted. The procedure involves a comparison of measured feature orientation against the cataloged landmark azimuth. The normal miss from the sensor look point to the candidate landmark that survives the orientation screening are then computed. The sensor look point is defined as the ground intercept of the LOS to the down sensor measured feature centroid. The normal miss is the minimal distance from look point to the linear landmark. The correct candidate is chosen as the one with the normal miss within an a priori tolerance. The landmark sighting is implemented for navigation update only if a unique candidate is identified. The normal miss will be the sensor measurement parameter used in the formulation of the Kalman filter for navigation update. Since the normal miss is a scalar each down sensor landmark sighting provides only one component of navigation state. As an example a landmark oriented normal to the orbit flight path will provide position update in the in-track component. Multiple sightings of landmarks with varied orientations provide complete observability in vehicle position and velocity. Details of navigation concepts are contained in Ref. 5.

In-orbit autonomous navigation performances are evaluated for the 185 Km circular orbit with the sunlit portion of the ground track shown in Figure 6. A down sensor landmark sighting schedule is hypothesized by first masking out the sunlit ground track using the average seasonal cloud cover probability. A 750 Km mean distance between linear landmark sightings is then applied to obtain the schedule shown in Figure 7. A covariance analysis program is utilized for navigation performance evaluation. Navigation errors for a three orbit period are plotted in Figure 7. These results are obtained assuming the down sensor, radar altimter and acceleration modeling errors defined in Table 1. Initial position and velocity errors of 2 Km/axis (1σ) and 2 m/sec/axis (1σ) are assumed. These errors are extremely conservative when compared with the boost inertial navigation performance. The stellar inertial attitude reference is not simulated in detail in the navigation analysis. It is characterized by a simple model consisting of 0.5mrad/axis (1σ) bias and 0.5 m rad/axis (1σ) random errors. Again these errors are conservative in view of the steady state attitude reference errors reported earlier. Navigation error plots shown in Figure 7 indicate that the high observability of down sensor landmark sightings enables rapid convergence from large initial

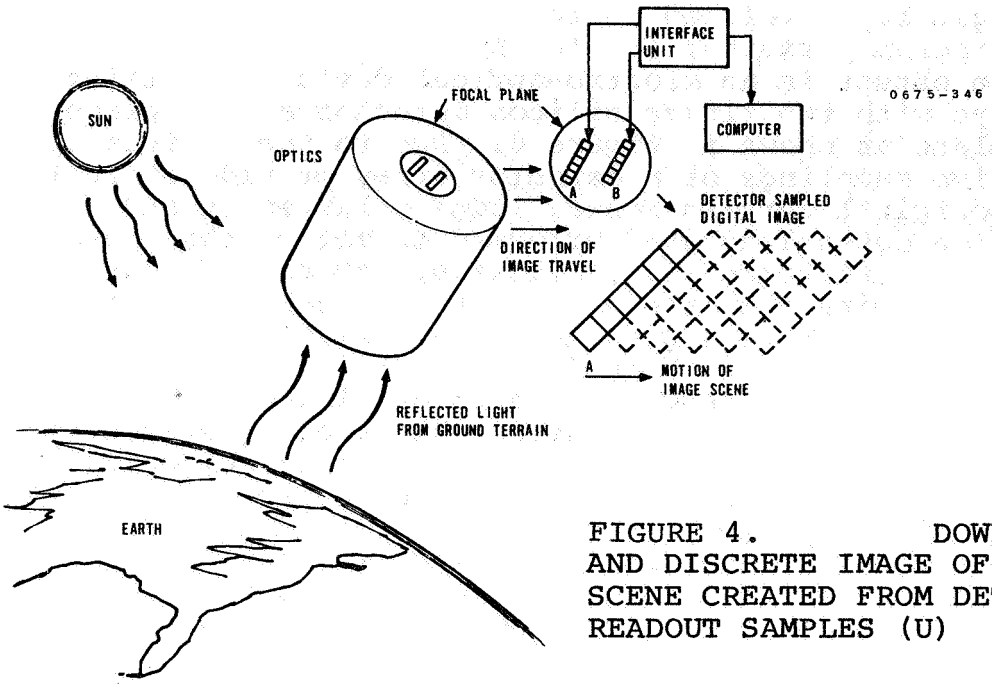

FIGURE 4. DOWN SENSOR AND DISCRETE IMAGE OF TERRAIN SCENE CREATED FROM DETECTOR CELL READOUT SAMPLES (U)

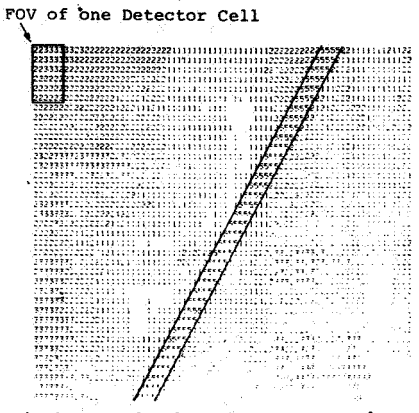

(a) Original Terrain Scene of 50-Ft Wide Road

(c) Thresholded Image of (b)

(b) Superpositioned Image From Consecutive Detector Readout Samples

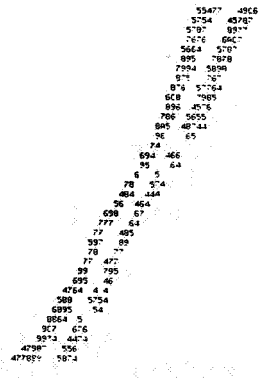

(d) Gradient of Image of (c)

FIGURE 5. DOWN SENSOR LINEAR LANDMARK PROCESSING

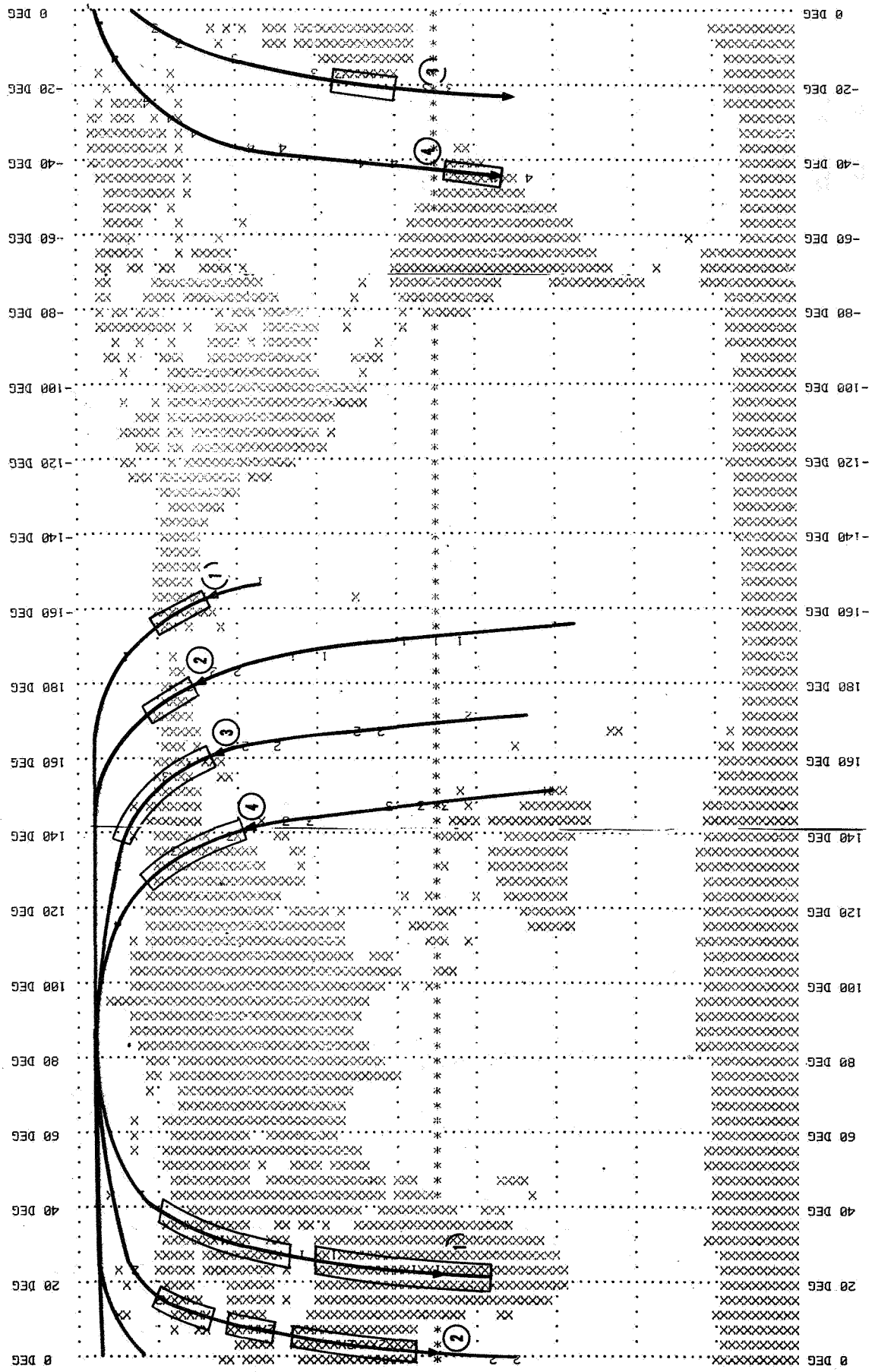

FIGURE 6. SUNLIT PORTION OF REFERENCE ORBIT CHOSEN FOR ANS IN-ORBIT NAVIGATION ANALYSIS

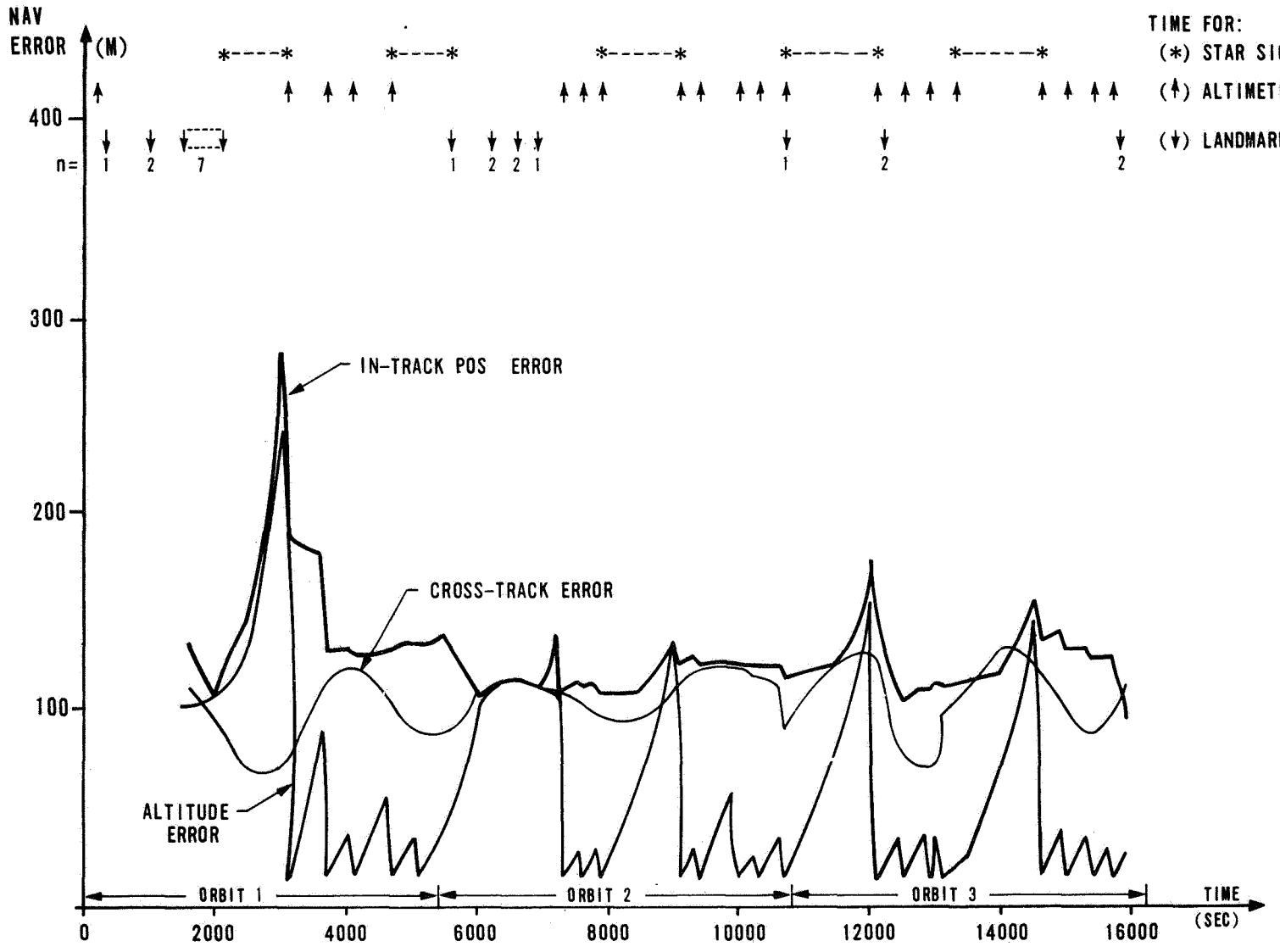

FIGURE 7. POSITION ERROR WITH LANDMARK UPDATES

errors. Also, navigation accuracy acquired from down sensor measurements can be preserved over intervals where landmark sightings are not available. This is accomplished by making radar altimeter measurements over the ocean where the geoid height can be accurately modeled onboard in $5^{o} \times 5^{o}$ grids. The cross coupling between the vertical and in-track components of navigation errors allows the bounding of in-track velocity error through vertical measurements. The ability to preserve navigation accuracy relieves the requirement on the landmark sighting frequency. A second case is run assuming identical conditions except that the landmark sightings after the first orbit are not implemented for navigation update. Navigation errors for this case are plotted in Figure 8 showing the ability of radar altimeter measurements in preserving the navigation accuracy over an extended period without landmark sightings. It should be pointed out here that once the attitude reference error is converged to steady state value the corresponding navigation error will be reduced to approximately 50 m (1σ) for in-track and cross track components.

Navigation performance for the 12-hour Molnya orbit is analyzed considering the ground track shown in Figure 9. To maximize down sensor landmark sighting opportunity it is mounted with the LOS pointed 15^{o} from the orbit plane and 15^{o} ahead of the nadir. It is shown that extending the limiting altitude of down sensor can significantly increase the landmark availability. The performance analysis results given in Figure 10 are obtained corresponding to h_1 = 1852 Km. Initial position and velocity errors assumed here are 500 m/axis (1σ) and 0.5 m/sec/axis (1σ). They are conservative compared with the navigation accuracy achievable in the low altitude parking orbit. Intrack and cross track position errors plotted in Figure 10 suggest that the LOS from vehicle to a point on Earth's surface can be computed to within 0.05 m rad at the apogee altitude using the onboard position information.

6. Summary and Conclusions

An ANS system concept has been described in this paper. It is shown how various system components can be mechanized to provide navigation and attitude reference supporting an autonomous satellite mission. The ANS performance has been evaluated for two hypothetical missions based upon existing sensor characteristics. The ANS navigation and attitude reference performances are evaluated for four major functional elements likely to be included in any autonomous satellite launch missions. These results show that it is feasible to develop an ANS system using existing sensor technology. In fact, most of the ANS functions (alignment, boost navigation, and stellar update) have already been demonstrated in various operational systems. The most critical ANS function is that of autonomous navigation update using down sensor landmark sightings. An engineering model down sensor has been built and tested in the ANT program. The remaining task is to prove the down sensor and navigation update concepts through a flight experiment.

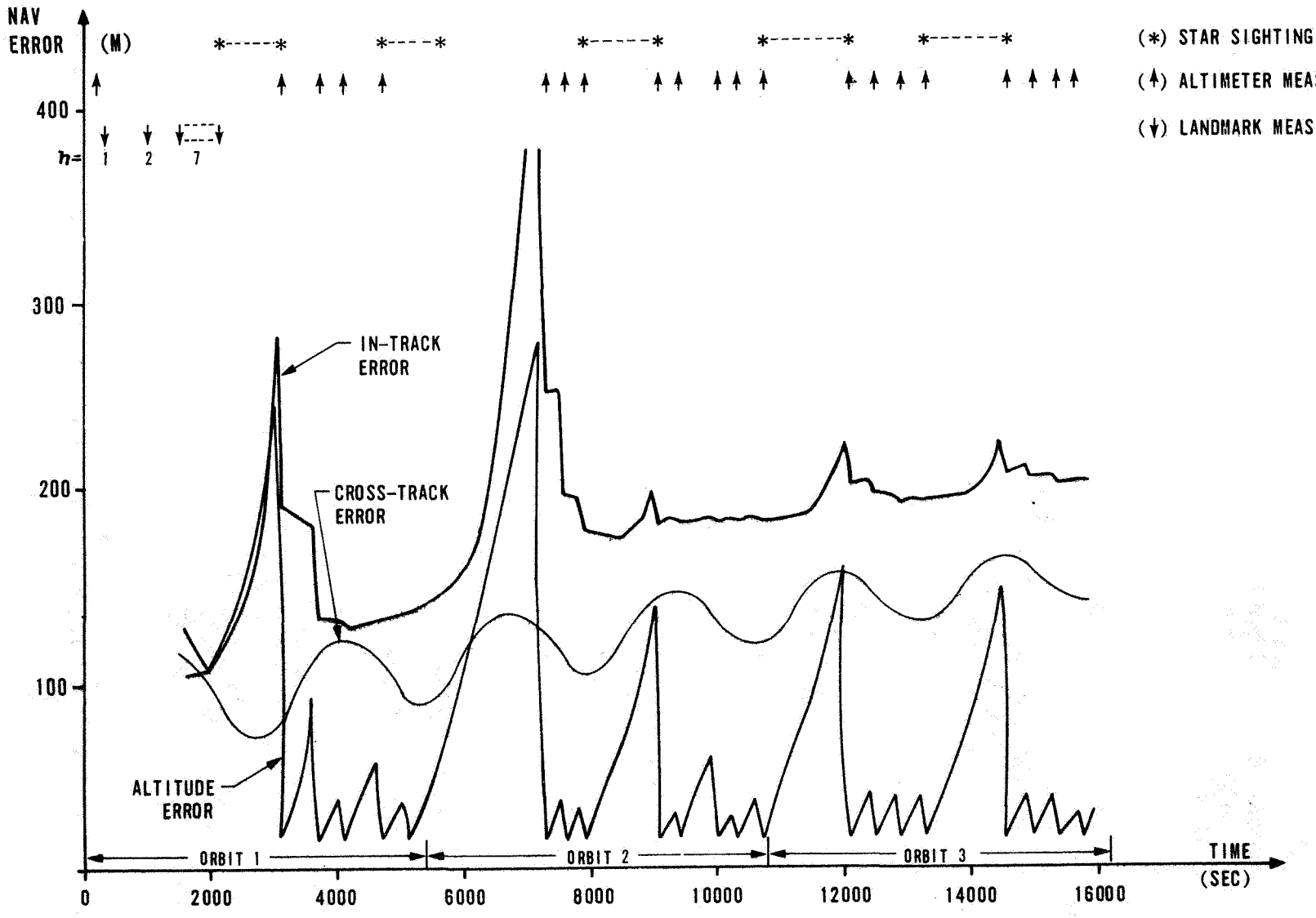

FIGURE 8. PLOTS OF POSITION ERRORS WITH 10 LANDMARK UPDATES

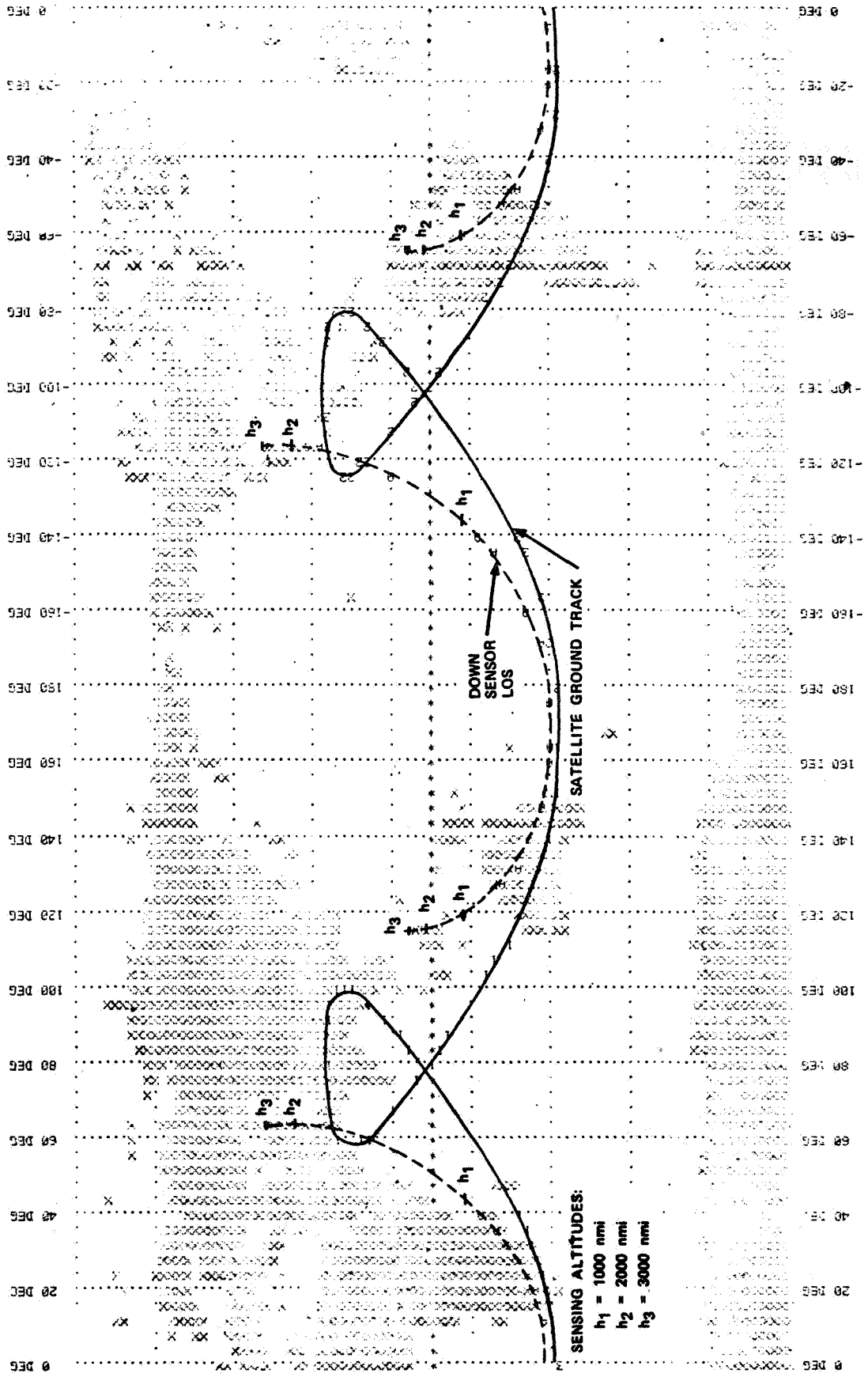

FIGURE 9. DOWN SENSOR LOS AND SATELLITE GROUND TRACK FOR MOLNYA ORBIT

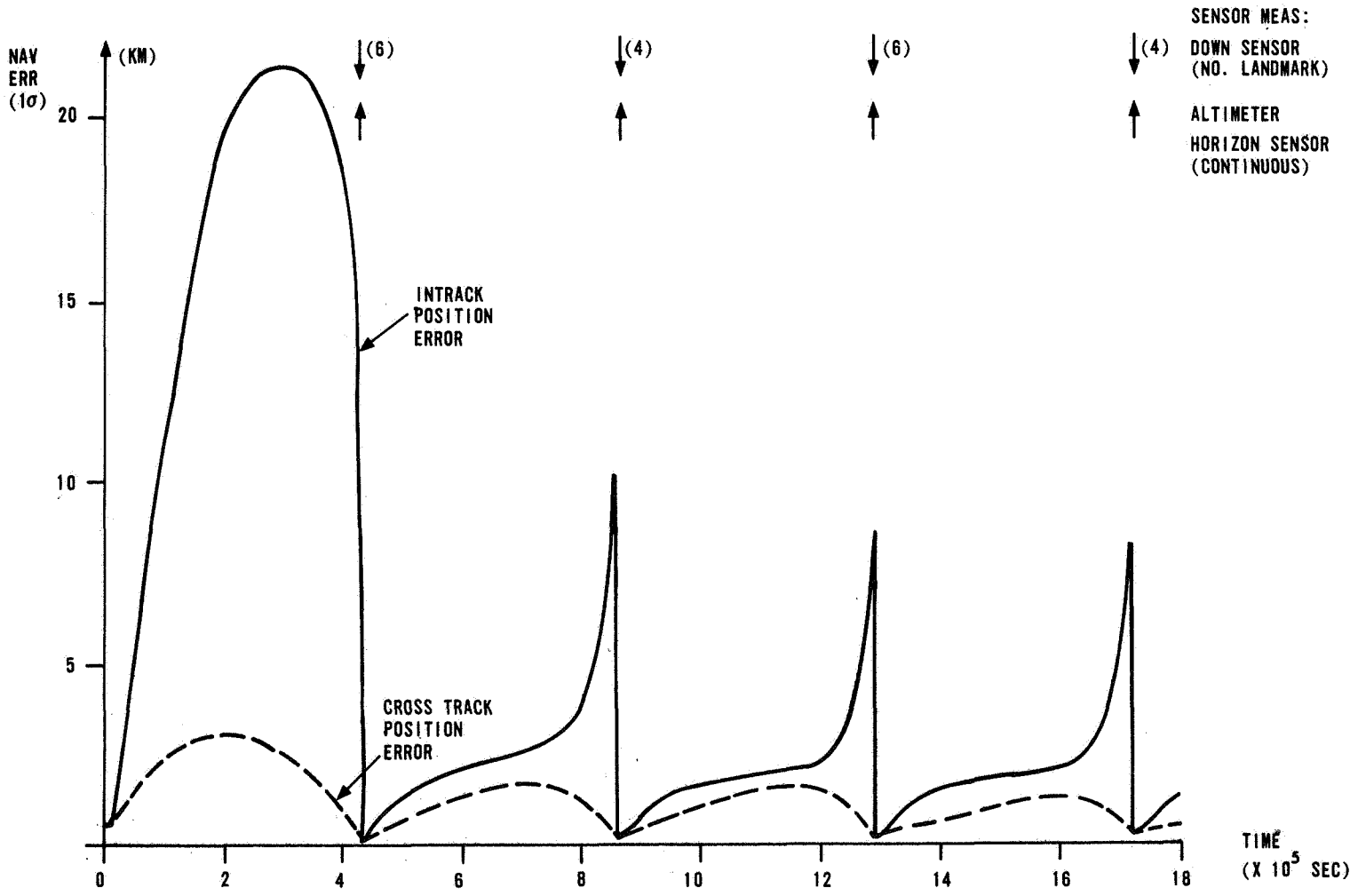

FIGURE 10. NAVIGATION ERROR FOR MOLNYA ORBIT WITH PERIGEE AT LOCAL 6 AM

REFERENCES

1. "Inertial Measurement Unit" Honeywell Avionics Division Specification (DS-DLG-8088).

2. "Autonomous Navigation Technology" Phase 1A Study Final Report, SAMSO FR 74-221, Aug. 1974.

3. "In-Flight Alignment of Laser Strapdown Systems", S. P. Kau, IEEE Decision and Control Conference, Dec. 1977.

4. "Update Strategy for a Strapdown Stellar - Inertial Navigation System", S. P. Kau and S. S. Steadman, IEEE Decision and Control Conference, Dec. 1976.

5. "Autonomous Satellite Orbital Navigation Using Known and Unknown Earth Landmarks", S. P. Kau, AIAA Guidance and Control Conference, August 1975.

OPTIMAL ESTIMATION FOR THE SPACECRAFT ATTITUDE USING STAR TRACKER MEASUREMENTS

James Ting-Ho Lo

Control and Decision Laboratory

ABSTRACT

An optimal estimation scheme is presented, which determines the satellite attitude using the gyro readings and the star tracker measurements of a commonly used satellite attitude measuring unit. The scheme is mainly based on the exponential Fourier densities that have the desirable closure property under conditioning. By updating a finite and fixed number of parameters, the conditional probability density, which is an exponential Fourier density, is recursively determined.

Simulation results indicate that the scheme is effective and robust. It is believed that this approach is applicable to many other attitude measuring units. As no linearization and approximation are necessary in the approach, it is ideal for systems involving high levels of randomness.

When a system involves little randomness and linearization is not expected to incur much error, the approach can provide a benchmark against which such suboptimal estimators as the extended Kalman filter and the least-squares estimator can be compared. In this spirit, simulated data for HEAO-A were processed to compare the optimal scheme and the extended Kalman filter. The results are presented.

MULTIPLE OBJECT TRACKING WITH NON-UNIQUE DATA-TO-OBJECT ASSOCIATION VIA GENERALIZED HYPOTHESIS TESTING

D. W. Porter and R. M. Lefler

Business and Technological Systems, Inc.

ABSTRACT

A generalized hypothesis testing approach is applied to the problem of tracking several objects where several different associations of data with objects are possible. Such problems occur, for instance, when attempting to distinctly track several aircraft maneuvering near each other or when tracking ships at sea. Conceptually the problem is solved by first associating data with objects in a statistically reasonable fashion and then tracking with a bank of Kalman filters.

The objects are assumed to have motion characterized by a fixed but unknown deterministic portion plus a random process portion modeled by a shaping filter. For example, the object might be assumed to have a mean straight line path about which it maneuvers in a random manner. Several hypothesized associations of data with objects are possible because of ambiguity as to which object the data comes from, false alarm/detection errors, and possible uncertainty in the number of objects being tracked.

The statistical likelihood function is computed for each possible hypothesized association of data with objects. Then the generalized likelihood is computed by maximizing the likelihood over parameters that define the deterministic motion of the object. This forms the basis of the generalized hypothesis testing approach.

The computational burden is dominated by combinatoric considerations. Procedures are addressed that relieve the computational burden.

MULTIPLE OBJECT TRACKING WITH NON-UNIQUE DATA-TO-OBJECT ASSOCIATION VIA GENERALIZED HYPOTHESIS TESTING

D. W. Porter R. M. Lefler

BUSINESS AND TECHNOLOGICAL SYSTEMS, INC.
Aerospace Building, Suite 440
10210 Greenbelt Road,
Seabrook, Maryland 20801

1. Introduction

This paper deals with the problem of tracking multiple objects where it is unclear which measurements can be associated with which objects. Such problems arise, for instance, when tracking aircraft maneuvering near each other or when tracking ships at sea. The problem is approached by first performing data-to-object association in a statistically reasonable fashion and then tracking with a bank of Kalman filters.

A recent survey paper Reference 1 describes the various Bayesian and likelihood approaches that have been developed to handle multiple object tracking problems. This paper follows the likelihood line of development pioneered by Sittler in Reference 2 and carried forward by various researchers, notably by Morefield in Reference 3. The contribution of this paper is the use of a generalized likelihood approach to deal with unknown system parameters. The conceptual approach is applicable to a wide variety of parameters including process noise covariances and time constants in shaping filter models for object motion. The specific theory developed here applies to unknown

parameters that enter measurements linearly. Examples of such parameters are position and velocity coordinates at track initiation or parameters describing a fixed but unknown mean path for object motion.

The next section describes the problem in more detail and states previous results. This is followed by a section presenting new results with a discussion of computational consideration and a section presenting an analytical example.

2. Previous Results

Object motion is usually modeled with a state space shaping filter where different classes of objects having different models may be considered. It is assumed that the objects move independently of each other. Several sensors of different types may be in use with associated sensor error models. The parameters of the models in previous work have usually been assumed known. This paper includes unknown parameters entering the measurements z_k linearly through initial conditions and forcing terms according to the following model for an object in a given class:

$$\begin{aligned} x_{k+1} &= \Phi_k x_k + G_k w_k + B_{2k} b_2 \\ z_k &= H_k x_k + v_k \\ x_o &= B_1 b_1 + x_{or} \\ k &= 0, 1, \ldots, M \end{aligned} \qquad (2\text{-}1)$$

$b = \begin{bmatrix} b_1 \\ b_2 \end{bmatrix}$ - Fixed but unknown parameter vector

w_k - Zero mean, white, Gaussian process noise with covariance Q_k

v_k - Zero mean, white, Gaussian measurement noise with covariance R_k

x_{or} - Zero mean and Gaussian with covariance $P_{x_{or}}$

For the remainder of this section $b_1 = b_2 = 0$, but b_1 and b_2 are nonzero in the next section.

The data association problem is displayed by Figure 2-1. Given

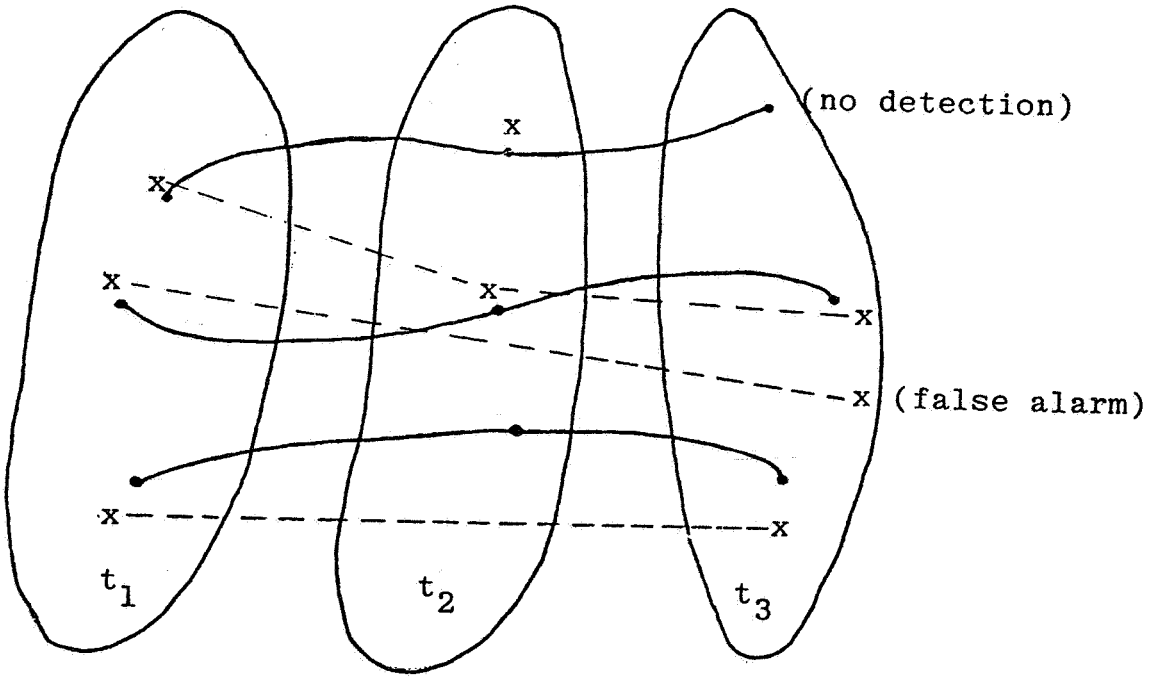

—o— Object path with dot at measurement time t_i

x Position measurement

--- Hypothesized data association

Figure 2-1. Data Association Hypotheses

the data, there are a number of reasonable data associations. Many factors may have to be considered. Different sensors or the same sensor at different times may have a different coverage region, false alarm and detection errors may occur, and the number of objects may be initially unknown. In order to focus attention on new results, it is assumed in the remainder of the paper that the sensor coverage region includes all objects at each measurement time and that there are no false/alarm detection errors. Further, it is assumed that no *a priori* probabilistic information is available as to the correctness of a given data association.

Previous results compute the statistical likelihood function with a bank of Kalman filters as shown in Figure (2-2) and maximize the likelihood over hypothesized data associations. The hypothesizer selects

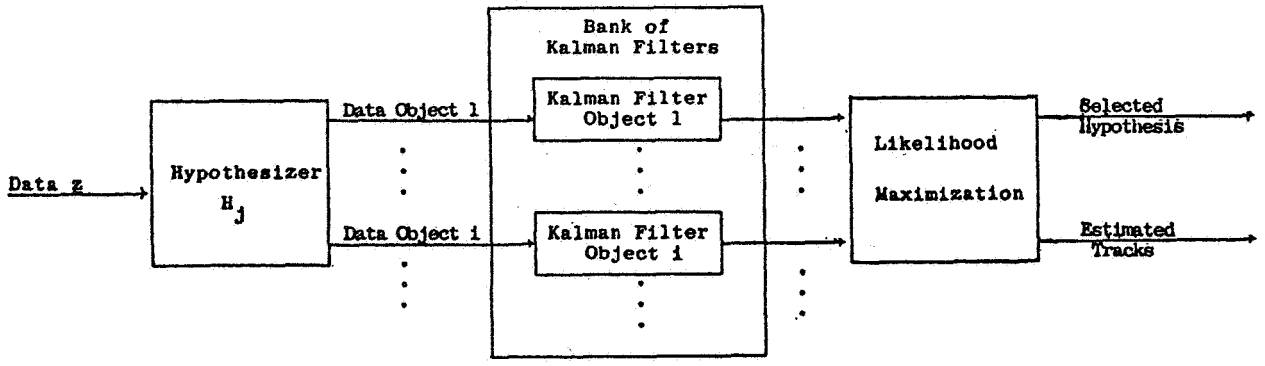

Figure 2-2. Likelihood Maximization

the data association, and then the data is whitened by a bank of Kalman filters using appropriate object class models. Consequently, negative twice the log likelihood can be computed efficiently by the equation

$$-2\ell n p(z;H_j)$$

$$= \sum_i \sum_k \left(\ell n \left|P_{\tilde{z}^j_{i,k}}\right| + \tilde{z}^{j\,T}_{i,k} \; P^{-1}_{\tilde{z}^j_{i,k}} \; \tilde{z}^j_{i,k}\right) \qquad (2\text{-}2)$$

$$+ m \; \ell n 2\pi$$

$\tilde{z}^j_{i,k}$, $P_{\tilde{z}^j_{i,k}}$ - Residual and residual covariance for hypothesis H_j, object i, at time k

m - Total number of scalar measurements.

The data dependent part of equation (2-2) is chi-square with degrees of freedom m (χ^2_m). Then the likelihood is maximized by minimizing equation (2-2). In this manner a statistically reasonable hypothesis is selected and tracking is performed by the bank of Kalman filters.

3. New Results

The contribution of this paper is the inclusion of fixed but unknown parameters in the object motion model. The generalized likelihood approach provides a solution by maximizing the likelihood over the parameters before maximizing over hypotheses. This is accomplished by replacing the Kalman filter for object i in Figure 2-2 by the equation shown in block diagram form in Figure 3-3 where the i and j subscripts are suppressed. The Kalman filter is based on the model of equation 2-1 with b = 0 This is indicated by subsripting filter computed quantities with "fb = 0" The filter residuals and residual covariance are used in a set of auxilliary equations to compute a maximum likelihood estimate $\hat{b}_k$ with estimate error covariance $P_{\tilde{b}_k}$ These results are used in turn to compute the portion of the likelihood

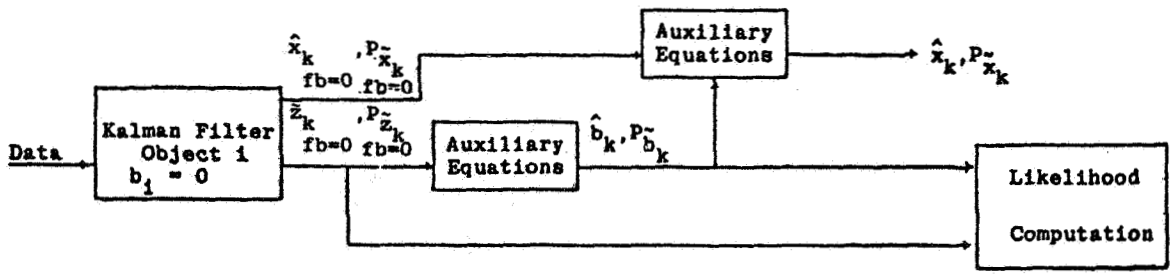

Figure 3-3. Generalized Likelihood Computation

for the object under consideration. Then using the filter estimate for the state and the estimate for b recovered from the filter residuals, the minimum variance and unbiased estimate $\hat{x}_k$ of the state and its estimate error covariance $P_{\tilde{x}_k}$ are computed.

The estimate for b and the estimate uncertainty are given by

$$\hat{b}_k = \left(\sum_{\ell=0}^{k} T_{1\ell}^T H_\ell^T P_{\tilde{z}_\ell}^{-1} H_\ell T_{1\ell} \right)^{-1} \sum_{\substack{\ell=0 \\ fb=0}}^{k} T_{1\ell}^T H_\ell^T P_{\tilde{z}_\ell}^{-1} \tilde{z}_\ell \quad (3\text{-}1)$$

$$P_{\tilde{b}_k} = \left(\sum_{\ell=0}^{k} T_{1\ell}^T H_\ell^T P_{\tilde{z}_\ell}^{-1} H_\ell^T T_{1\ell} \right)^{-1}$$

$$T_{1,\ell+1} = \Phi_\ell (I - K_\ell H_\ell) T_{1\ell} + [0_{n \times n_1} \vdots B_{2\ell}]$$

$$T_{10} = [B_1 \vdots 0_{n \times n_2}]$$

K_ℓ - Kalman gain at ℓ^{th} time

n_1, n_2 - Number of elements in b_1 and b_2

n - Number of elements in x.

Note that the above equations can be implemented recursively. The minimized negative twice log likelihood for the given object is expressed as

$$-2\ell n\ p(z;\hat{b}_M) = \left(\sum_k \ell n \left|P_{\tilde{z}_k}\right|_{fb=0} + \tilde{z}_k^T{}_{fb=0} P_{\tilde{z}_k}^{-1}{}_{fb=0} \tilde{z}_k{}_{fb=0}\right) - \hat{b}_M^T P_{\tilde{b}_M}^{-1} \hat{b}_M + m\ \ell n\ 2\pi \tag{3-2}$$

Now, including the i and j subscripts, the generalized negative twice log likelihood over all objects is

$$-2\ \ell n\ p(z;H_j,\hat{b}^j_{1M},\cdots\hat{b}^j_{iM},\cdots) = \sum_i\left(\sum_k \ell n \left|P_{\tilde{z}^j_{ik}}\right|_{fb=0} + \tilde{z}^{j\,T}_{ik}{}_{fb=0} P_{\tilde{z}^j_{ik}}^{-1}{}_{fb=0} \tilde{z}^j_{ik}{}_{fb=0}\right) - \hat{b}^{j\,T}_{iM} P_{\tilde{b}^j_{iM}}^{-1} \hat{b}^j_{iM} + m\ \ell n\ 2\pi \tag{3-3}$$

The data association is accomplished by minimizing the above equation over H_j. It can be shown that the data dependent part of equation 3-3 is chi-square with degrees of freedom equal the total number of scalar measurements minus the total number of elements in all the b_1 and b_2 vectors under hypothesis H_j.

The generalized likelihood has been computed but valid state estimates for the objects still remain to be specified. It can be shown that the following equations give the minimum variance unbiased estimate and its uncertainty for a given object, again suppressing the i, j subscripts:

$$\hat{x}_k(+) = \underset{fb=0}{\hat{x}_k(+)} + T_{2k}\,\hat{b}_k$$

$$P_{\tilde{x}_k}(+) = \underset{fb=0}{P_{\tilde{x}_k}(+)} + T_{2k}\,P_{\tilde{b}_k}\,T_{2k}^T \qquad (3\text{-}4)$$

$$T_{2k} = (I - K_k H_k)\,T_{1k}$$

It is worthwhile to compare the new results of this section with the previous results of Section 2 where the noninformative prior approach is used to deal with the parameters b. The distribution of the data dependent part of the negative twice log likelihood is chi-square in the total number of scalar measurements for the previous results but is chi-square in the number of scalar measurements minus the total number of elements in all the b_1 and b_2 vectors for the new results. However, it can be shown that the actual numerical value of the data dependent parts is the same. On the other hand, comparison of equations (3-3) and (2-2) shows that the model dependent parts are different. Further, it can be shown that the state estimate obtained from the Kalman filter in the previous results is the same as that given by equation (3-4). There are clearly basic similarities and basic differences between the two approaches and caution must be exercised in selecting which approach is most appropriate.

Numerical considerations are of major importance to the application of the new results as they are to previous results. It is easily verified that even for a modest number of objects and measurement times that a combinatoric explosion occurs in the number of hypothesized data associations. Much use can be made of pre-processing techniques to greatly limit the number of hypotheses. For example, if two position measurements require an object to exceed its maximum possible velocity then those measurements can not both come from the same object. Also examination of filter residuals directly can be used to exclude

clearly unlikely data associations. In general, however, such preprocessing does not appear to stop the combinatoric explosion, but only to slow it. Thus, suboptimal approaches appear to be required for most realistic problems. For example, data association can be performed at each measurement time saving only tracks from the "best" hypotheses up to a maximum number of tracks. It is more efficient to save tracks than hypotheses since two hypotheses may have many tracks in common. Another technique is to again perform data association at each point in time but consider only hypotheses that can be generated by back tracking N steps in time. Some mathematical programming techniques are also applicable such as integer programming techniques (Reference 3). Ultimately, the best technique is determined by the details of the specific problem at hand. In general, what is desired as an algorithm with storage requirements that do not grow in time and with execution time that grows only linearly in time.

4. Analytical Example

A simple example is presented to provide some "feeling" for the generalized likelihood approach. The example is actually somewhat more general than the theory of the preceding section in that a power spectral density parameter is to be estimated from the data.

The objects under observation move in a plane as random walks about straight mean paths with constant mean velocity where parameters describing the mean path are fixed but unknown. The power spectral density of the process noise will be considered known in one case and unknown in another. Measurements are taken at a constant interval Δt and are accurate enough to be considered noise free. It is assumed that all objects are observed at each measurement time and that no false alarm or detection errors occur.

The analysis model for the i^{th} object under the j^{th} hypothesis is

$$\begin{bmatrix} r_{1,i,k+1} \\ r_{2,i,k+1} \end{bmatrix} = \begin{bmatrix} r_{1,i,k} \\ r_{2,i,k} \end{bmatrix} + \begin{bmatrix} u_{1,i} \\ u_{2,i} \end{bmatrix} \Delta t + \begin{bmatrix} w_{1,i,k} \\ w_{2,i,k} \end{bmatrix} \tag{4-1}$$

$$\begin{bmatrix} z^j_{1,i,k} \\ z^j_{2,i,k} \end{bmatrix} \quad \begin{bmatrix} r_{1,i,k} \\ r_{2,i,k} \end{bmatrix}$$

$k = 0,1,\cdots,M$

$r_{1,i,o}$, $r_{2,i,o}$, $u_{1,i}$, $u_{2,i}$ - Fixed but unknown parameters

$w_{1,i,k}$, $w_{2,i,k}$ - zero mean, white Gaussian each having variance $Q_i \Delta t$ and uncorrelated with each other

The first measurement estimates initial position exactly so it will no longer be considered unknown. Using Kalman filter equations, the negative twice log likelihood for the object of equation (4-1) is found to be

$$-2 \ln p \left(\cdots z^j_{i,k}, \cdots; u_{1,i}, u_{2,i}, Q_i\right) + \text{constant}$$

$$= \sum_{k=1}^{M} 2 \ln Q_i \Delta t + \frac{\left(z^j_{1,i,k} - z^j_{i,i,k-1} - u_{1,i}\Delta t\right)^2}{Q_i \Delta t} + \frac{\left(z^j_{2,i,k} - z^j_{2,i,k-1} - u_{2,i}\Delta t\right)^2}{Q_i \Delta t} \tag{4-2}$$

Now minimize equation (4-2) with respect to $u_{1,i}$ and $u_{2,i}$ to obtain the maximum likelihood estimates

$$\hat{u}^j_{1,i} = \frac{1}{M\Delta t} \sum_{k=1}^{M} z^j_{1,i,k} - z^j_{1,i,k-1}$$

$$\hat{u}^j_{2,i} = \frac{1}{M\Delta t} \sum_{k=1}^{M} z^j_{2,i,k} - z^j_{2,i,k-1} \qquad (4\text{-}3)$$

These estimates are valid whether Q_i is known or not. Now assume Q_i is unknown and minimize equation (4-2) to obtain

$$\hat{Q}^j_i = \frac{1}{2M\Delta t} \sum_{k=1}^{M} (z^j_{1,i,k} - z^j_{1,i,k-1} - \hat{u}^j_{1,i}\Delta t)^2 + (z^j_{2,i,k} - z^j_{2,i,k-1} - \hat{u}^j_{2,i}\Delta t)^2 \qquad (4\text{-}4)$$

Now consider the case where the Q_i are known and form the generalized negative twice log likelihood over all objects minimized over $u_{1,i}$ and $u_{2,i}$

$$-2 \ln p(z; \cdots, \hat{u}^j_{1,i}, \hat{u}^j_{2,i}, \cdots) + \text{constant}$$

$$\frac{1}{\Delta t} \sum_i \frac{1}{Q_i} \sum_{k=1}^{M} (z^j_{1,i,k} - z^j_{1,i,k-1} - \frac{1}{M} \sum_{\ell=1}^{M} (z^j_{1,i,\ell} - z^j_{1,i,\ell-1}))^2 + (z^j_{2,i,k} - z^j_{2,i,k-1} - \frac{1}{M} \sum_{\ell=1}^{M} (z^j_{2,i,\ell} - z^j_{2,i,\ell-1}))^2 \qquad (4\text{-}5)$$

For the case of Q_i unknown, the generalized likelihood is maximized by minimizing the following expression

$$\prod_i \sum_{k=1}^{M} \left(z^j_{1,i,k} - z^j_{1,i,k-1} - \frac{1}{M}\sum_{\ell=1}^{M}(z^j_{1,i,\ell} - z^j_{1,i,\ell-1})\right)^2 + \left(z^j_{2,i,k} - z^j_{2,i,k-1} - \frac{1}{M}\sum_{\ell=1}^{M}(z^j_{2,i,\ell} - z^j_{2,i,\ell-1})\right)^2 \tag{4-6}$$

Equations (4-5) and (4-6) have a term that sums over time in common. This common term is simply a measure of the variation of position change about mean position change for a given object. Both equations qualitatively attempt to perform data association by minimizing the variation in position change over all objects. However, in equation (4-5) where Q_i is known, the variation in position change is weighted heavily for small Q_i. This is intuitively reasonable since a small variation would be expected. It might seem reasonable that if Q_i is unknown that equation (4-5) should still apply but with $Q_i = 1$. However, the variation in position change for objects that truly have a small Q_i would be swamped out by that for objects with large Q_i. The multiplication of equation (4-6) keeps this swamping effect from occurring.

References

(1) Y. Bar-Shalom, "Tracking Methods in a Multitarget Environment", IEEE Trans. Auto. Control, Vol. AC-23, Aug. 1978.

(2) R. W. Sittler, "An Optimal Data Association Problem in Surveillance Theory", IEEE Trans. Mil. Electron., Vol. MIL-8, April 1964.

(3) C. L. Morefield, "Application of 0-1 Integer Programming to Multitarget Tracking Problems", IEEE Trans. Auto. Control, Vol. AC-22, June 1977.

INTELSAT IV IN-ORBIT LIQUID SLOSH TESTS AND PROBLEMS IN THE THEORETICAL ANALYSIS OF THE DATA

Victor J. Slabinski

ABSTRACT

Each INTELSAT IV dual-spin spacecraft carries liquid hydrazine in four conispheric propellant tanks mounted on the spinning rotor section. The destabilizing effect of the liquid on attitude-nutation stability was determined from an extensive series of in-orbit tests. The liquid slosh driving frequency ratio (rotor nutation frequency/rotor spin rate) was varied over the range of 0.58 to 0.70 for the tests by rotating the spacecraft antenna platform at different rates in inertial space. A rotor-mounted accelerometer sensed the spacecraft nutation. The observed time constant for the nutation angle increase or decrease was corrected for the stabilizing contribution of the platform-mounted pendulum dampers to yield the net destabilizing dedamping contribution from the liquid slosh.

The in-orbit tests show two unexpected maxima in the dedamping contribution at driving frequency ratios that vary with the propellant loading. The rotor nutation frequency at the maxima is about one-third of the lowest mode liquid slosh frequency given by ground test data for unspun tanks, and thus does not correspond to a simple resonance of the liquid. Ground tests with spinning systems have produced the same maxima, but the phenomenon is not yet understood.

A preliminary version of this paper appeared in the Proceedings of the CNES-ESA Conference on "Attitude Control of Space Vehicles: Technological and Dynamical Problems Associated with the Presence of Liquids," Toulouse, France, October 10-12, 1977 (ESA SP-129), pp. 87-102. The final version appears in the COMSAT Tech. Rev. 8, 1-40 (Spring 1978).

This paper is based upon work performed at COMSAT-Plaza under the sponsorship of the International Telecommunications Satellite Organization (INTELSAT). Views expressed in this paper are not necessarily those of INTELSAT.

Introduction

Definitions

A dual-spin spacecraft such as INTELSAT IV consists of a spinning rotor section and a normally despun antenna platform, with the two sections connected by a bearing assembly. The bearing axis is the intended spin axis for the spacecraft. This is an unstable axis because, by the common definition of dual-spin spacecraft, it is not the axis of maximum moment of inertia. The bearing axis may exhibit a small motion about the spacecraft's rotational angular momentum vector which is the result of two coning motions, a steady-state motion at a cone half-angle θ_W called the *wobble angle*, and a transient motion called *nutation* whose instantaneous cone half-angle θ_N is the *nutation angle*.

The INTELSAT IV spacecraft carry liquid hydrazine in four partially filled propellant tanks mounted on the rotor section. The liquid motion in response to nutation tends to increase the nutation angle at the rate $k_L\theta_N$, while the platform-mounted pendulum dampers tend to decrease the nutation angle at the rate $k_D\theta_N$. At small nutation angles, the nutation angle is observed to vary exponentially with time t:

$$\theta_N = \theta_{N,0} \exp\left[-\frac{t - t_0}{\tau}\right] \tag{1}$$

where τ is the time constant for nutation angle decay (τ positive) or growth (τ negative). Its inverse can be expressed as the difference of two positive numbers:

$$\frac{1}{\tau} = k_D - k_L \tag{2}$$

where k_D is the *damping contribution* from the platform dampers and k_L is the *dedamping contribution* from liquid slosh on the rotor. The latter contribution will be called "dedamping" for brevity. Spacecraft attitude stability requires $k_L < k_D$ so that τ is positive and any initial nutation damps out. A bound on k_L for all expected operating conditions is thus very important for successful spacecraft design and operation.

The liquid motion in the tanks is commonly referred to as "fuel slosh." This term is not strictly correct here, since hydrazine is a propellant rather than a fuel. Fuel is matter that produces power by combustion, that is, by combination with oxygen, while hydrazine produces its thrust on INTELSAT IV by catalytic decomposition. For this reason, the hydrazine motion will be called *liquid slosh.*

An important determining parameter for liquid slosh effects and hence k_L is the driving frequency ratio, ρ, defined as

$$\rho \equiv \frac{f_d}{\omega_{rz}} \tag{3}$$

where f_d is the liquid driving frequency due to nutation, and ω_{rz} is the rotor spin rate about the bearing axis, both expressed in units of rad/s. The importance of this ratio may be seen by considering that the centrifugal acceleration acting on the liquid in the tanks is $\omega_{rz}^2 R$, where R is some mean liquid distance from the spin axis. The restoring force on the liquid when displaced from equilibrium will be proportional to this acceleration so that the natural frequencies of the liquid are proportional to the square root of this quantity, $\omega_{rz} R^{1/2}$. Since the resonant frequencies are proportional to ω_{rz}, the ratio of driving frequency to liquid resonant frequency is proportional to ρ.

A dual-spin spacecraft offers a distinct advantage for the in-orbit determination of liquid slosh effects because ρ can be varied by merely rotating the platform. The liquid driving frequency during nutation is assumed to be the rotor nutation frequency, $\dot{\lambda}_r$, observed from rotor-fixed axes; hence, the variation of ρ with the platform spin rate ω_{pz} in inertial space is given by

$$\rho = \frac{|\dot{\lambda}_r|}{\omega_{rz}} = \left| \frac{I_{rz}}{I_t} \left[1 - \frac{I_{pz}\omega_{pz}}{H_z} \right]^{-1} - 1 \right| \tag{4}$$

where H_z = bearing axis component of the spacecraft's rotational angular momentum (constant to the first order for small nutation angles)

I_{pz}, I_{rz} = platform and rotor moments of inertia about the bearing axis

I_t = spacecraft moment of inertia about a transverse axis through the mass center.

Since a simple spinner can be considered as the rotor of a dual-spin space-

craft which lacks a platform, setting $I_{pz} = 0$ in equation (4) gives

$$\rho = \left| \frac{I_{rz}}{I_t} - 1 \right| \qquad \text{(simple spinner)} \tag{5}$$

which shows that for a simple spinner ρ is fixed by its mass properties.

Test motivation

Prior to the first INTELSAT IV launch, Hughes Aircraft Co. performed ground tests to predict k_L for the expected spacecraft operating conditions (Reference 1, pp. 75–76). These tests indicated that any nutation would quickly decay, and that k_L was sensitive to ρ variations. However, they were performed for only a few different values of *fill fraction* (the percentage of the propellant tank volume occupied by liquid) and did not indicate two troublesome properties of k_L which were only discovered in 1974 as a result of orbital operation of the INTELSAT IV series of spacecraft. These discoveries raised questions concerning the attitude stability of the INTELSAT IV-A series of communications satellites then under development.

The first was that k_L is a strong function of the driving frequency ratio, ρ. This was discovered during the loss of antenna despin control by the INTELSAT IV F-7 spacecraft on March 21, 1974, when the antenna platform spun up to 25 rpm before recovery; k_L decreased twentyfold during a ρ value change of only 0.03. This discovery, that a small change in ρ can increase or decrease k_L by an order of magnitude, raised the possibility that INTELSAT IV-A, operating at different ρ values, might have k_L values significantly larger than those found previously in INTELSAT IV orbital operation.

This discovery also indicated a need for detailed knowledge of the k_L variation over the range of ρ values possible during an antenna platform spin-up. Such data would indicate whether loss of despin control could result in a rapid growth of the nutation angle to $\sim$90°, the "flat spin" condition from which spacecraft recovery might be difficult. Previous liquid slosh tests on the ground had been restricted to the ρ value corresponding to the despun platform condition.

The second discovery was that k_L appeared to become drastically larger with increasing fill fraction. The first five INTELSAT IV spacecraft launched had a 70-percent fill in transfer orbit after their initial spin-up. The sixth, INTELSAT IV F-8, was launched on November 21, 1974, with a 76-percent fill. The extra propellant was carried as ballast to compensate for an oversized solid propellant apogee motor. Nutation tests in transfer orbit

showed that this extra 6-percent fill doubled k_L. Since this fill fraction region had not been included in the ground tests, this raised a question concerning the magnitude of k_L for the INTELSAT IV-A spacecraft which were to use the same propellant tanks with an initial fill of 82 percent.

To resolve these questions, COMSAT conducted an extensive series of in-orbit nutation tests on the nearly identical spacecraft in the INTELSAT IV series in spring 1975. These tests took place in a 0-g environment and thus avoided the uncertainty inherent in ground testing regarding the correction, if any, which is required for the 1-g field.

Nutation test description

The basic test procedure consists of inducing spacecraft nutation and recording the continuously telemetered output of a nutation accelerometer mounted on the rotor. Figure 1 shows a typical nutation trace for a despun platform. In this case, nutation has been induced by firing an axial thruster for 0.5 s. The sensed acceleration from the nutation oscillates with the rotor nutation frequency, $\dot{\lambda}_r$. This frequency may be determined directly from the time code on the strip chart by noting the time interval for a given number of nutation cycles. Scaling the amplitude at selected points along the nutation trace and fitting equation (1) to the measurements gives the time constant τ for the nutation decay or growth. The computed platform damper contribution k_D is then used in equation (2) to obtain the liquid slosh dedamping k_L.

The in-orbit tests experimentally determined k_L as a function of driving frequency ratio, ρ, and propellant tank fill fraction. The driving frequency ratio was varied by spinning the antenna platform at different rates in inertial space over a range of ± 20 rpm. Obviously, the spacecraft did not carry communications traffic during the tests. Spacecraft with greatly different fill fractions were available, since each satellite of the INTELSAT IV series had been in orbit for a different length of time and had depleted its maneuvering propellant by a different amount. Also, INTELSAT IV F-8 was tested before and after large inclination maneuvers to obtain data at fill fractions of about 66, 61, and 56 percent from the same spacecraft. Finally, to test the initial INTELSAT IV-A fill fraction, the last spacecraft to be launched in the series, INTELSAT IV F-1, was put into orbit loaded with an extra 22 kg of hydrazine propellant to give an initial fill fraction of 82 percent. Most of this extra propellant was expended in transfer orbit to help place this heavily loaded spacecraft into geostationary orbit.

The test data obtained and attempts to understand it are the subjects of this paper. The in-orbit test results prompted an extensive series of

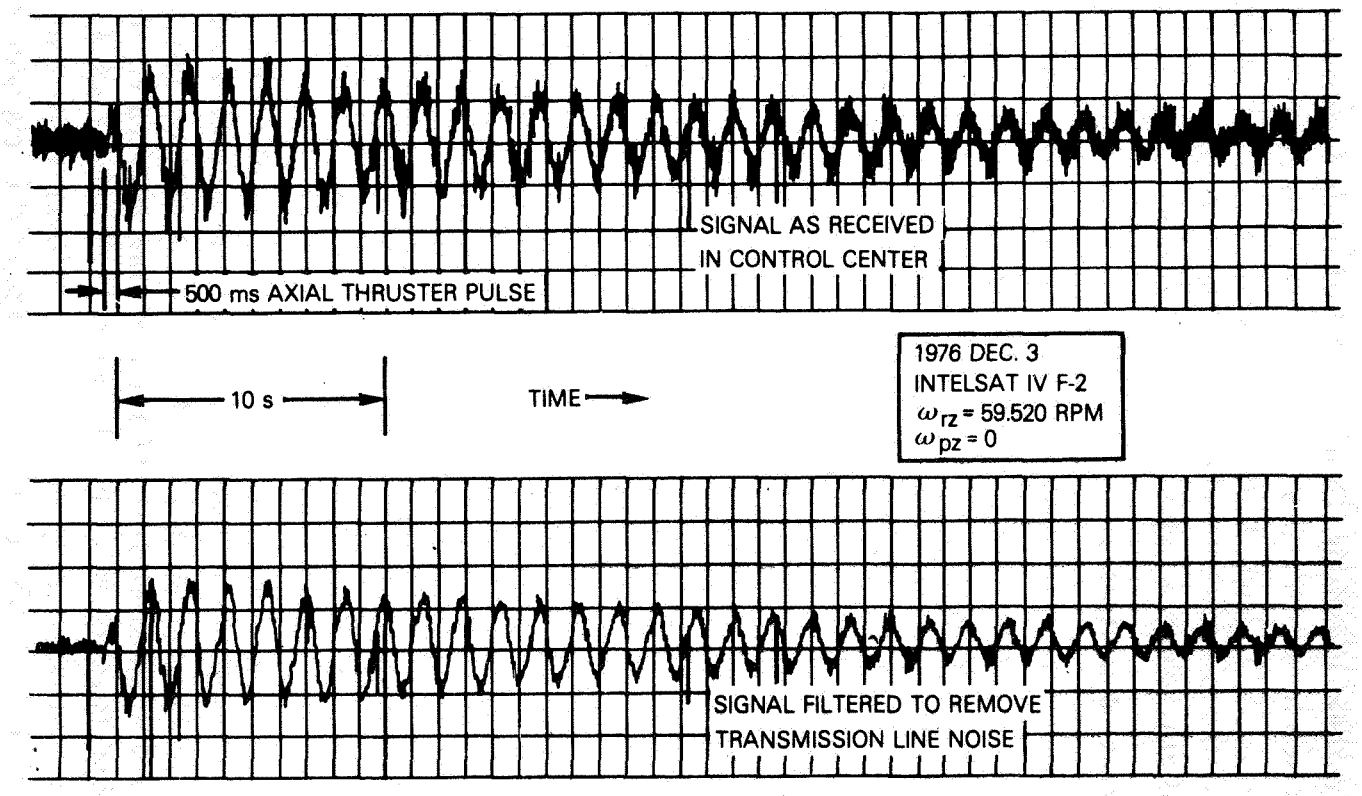

Figure 1. *Nutation Accelerometer Output for a Despun Platform*

liquid slosh ground tests by the spacecraft manufacturer, Hughes Aircraft Co. The large dedamping contributions found in both series of tests resulted in important modifications to the INTELSAT IV-A spacecraft design.

Basic nutation theory

The nutation theory presented herein allows for a cross product of inertia about the platform bearing axis. This cross product introduces additional acceleration frequencies in the rotor propellant tanks. Such additional frequencies due to spacecraft asymmetries may introduce unsuspected slosh effects.

Spacecraft model and platform coordinates

For the present analysis it may be assumed that all damper masses are caged and that the propellant is frozen in its equilibrium position so that each spacecraft section acts as a rigid body. It may also be assumed that the spacecraft is statically balanced so that the mass center of each section lies on the bearing axis. The spacecraft mass center then lies at a point O on the bearing axis which is taken as the origin of a right-handed Cartesian coordinate system $X_pY_pZ_p$ fixed in the platform. The Z_p axis lies along the bearing axis, and the transverse axes X_pY_p are chosen so that there is no platform cross product of inertia about the Y_pZ_p axes. The tensors giving the moments of inertia of the platform and rotor, respectively, are

$$(I_p) = \begin{bmatrix} I_{pt} & 0 & I_{pxz} \\ 0 & I_{pt} & 0 \\ I_{pxz} & 0 & I_{pz} \end{bmatrix}_p \tag{6}$$

$$(I_r) = \begin{bmatrix} I_{rt} & 0 & 0 \\ 0 & I_{rt} & 0 \\ 0 & 0 & I_{rz} \end{bmatrix}_p \tag{7}$$

where the p subscript outside tensor or vector brackets indicates platform-fixed axes. Equation (6) allows for a platform cross product of inertia I_{pxz} since this cross product produces additional acceleration frequencies in the rotor. Equation (7) assumes that the rotor is dynamically balanced so that the bearing axis is a principal axis. Both equations assume equal

moments of inertia I_{pt} and I_{rt} about any transverse axis through O so that the spacecraft moment of inertia about any transverse axis through O is given by

$$I_t = I_{pt} + I_{rt} \tag{8}$$

regardless of the relative orientation between platform and rotor. Another useful quantity is the spacecraft moment of inertia I_z about the bearing axis,

$$I_z = I_{pz} + I_{rz} \tag{9}$$

With respect to the platform-fixed axes, the angular velocities of the platform and rotor sections, respectively, in inertial space are given by

$$\vec{\omega}_p = \begin{bmatrix} \omega_{px} \\ \omega_{py} \\ \omega_{pz} \end{bmatrix}_p \tag{10}$$

$$\vec{\omega}_r = \begin{bmatrix} \omega_{px} \\ \omega_{py} \\ \omega_{rz} \end{bmatrix}_p \tag{11}$$

since the bearing constrains both sections to have the same X_p and Y_p components of angular velocity, ω_{px} and ω_{py}. The $+Z_p$ direction is chosen so that $\omega_{rz} > 0$. The angular momentum, $\vec{H}$, of the spacecraft about its mass center O is then

$$\vec{H} = \begin{bmatrix} H_x \\ H_y \\ H_z \end{bmatrix}_p = (I_p)\,\vec{\omega}_p + (I_r)\,\vec{\omega}_r \tag{12}$$

$$\vec{H} = \begin{bmatrix} I_t\omega_{px} + I_{pxz}\omega_{pz} \\ I_t\omega_{py} \\ I_{pxz}\omega_{px} + I_{pz}\omega_{pz} + I_{rz}\omega_{rz} \end{bmatrix}_p \tag{13}$$

Because the platform-fixed axes rotate with an angular velocity $\vec{\omega}_p$ relative to inertial axes, the time derivative of any vector such as $\vec{H}$ is given by

$$\frac{d\vec{H}}{dt} = \left[\frac{d\vec{H}}{dt}\right]_p + \vec{\omega}_p \times \vec{H} \tag{14}$$

where t is the time, and the brackets around the first term on the right side of the equation indicate a time derivative with respect to rotating axes. In the absence of external torques, $d\vec{H}/dt = 0$ and equation (14) gives

$$\left[\frac{d\vec{H}}{dt}\right]_p = -\vec{\omega}_p \times \vec{H} \tag{15}$$

as the differential equation of motion. In subsequent equations it will be assumed that the despin motor between the platform and rotor sections maintains a constant relative spin rate $\dot{\psi}$ between platform and rotor:

$$\dot{\psi} = \omega_{pz} - \omega_{rz} \tag{16}$$

so that

$$\dot{\omega}_{pz} = \dot{\omega}_{rz} \tag{17}$$

in equation (15), where a dot over a symbol indicates a time derivative.

Steady spin in platform coordinates

The spacecraft model described herein allows steady spin in platform coordinates as given by the following particular solution of equations (13) and (15):

$$\vec{\omega}_{p0} = \begin{bmatrix} \omega_{px0} \\ 0 \\ \omega_{pz0} \end{bmatrix}_p \tag{18}$$

$$\omega_{rz} = \omega_{rz0} = \text{constant} \tag{19}$$

where
$$\omega_{pz0}(I_t\omega_{px0} + I_{pxz}\omega_{pz0}) - \omega_{px0}(I_{pxz}\omega_{px0} + I_{pz}\omega_{pz0} + I_{rz}\omega_{rz0}) = 0 \tag{20}$$

This equation has the solution

$$\frac{\omega_{px0}}{\omega_{rz0}} = \frac{-1 \pm \sqrt{1 + (b\omega_{pz0}/\omega_{rz0})^2}}{b} \tag{21}$$

where b is a dimensionless parameter defined as

$$b = \frac{2I_{pxz}\omega_{rz0}}{I_{rz}\omega_{rz0} + (I_{pz} - I_t)\,\omega_{pz0}} \quad . \tag{22}$$

This paper is concerned with spacecraft for which $|I_{pxz}/I_{rz}| \ll 1$ so that usually $|b| \ll 1$. Then, the ambiguous sign in equation (21) may be taken as positive to obtain a spin vector nearly parallel to the bearing axis. (The negative sign gives the "flat spin" solution.) In this case a binomial expansion of the square root in equation (21) gives

$$\omega_{px0} \simeq \frac{b\omega_{pz0}^2}{2\omega_{rz0}} \tag{23}$$

$$\omega_{px0} = \frac{I_{pxz}\omega_{pz0}^2}{I_{rz}\omega_{rz0} + (I_{pz} - I_t)\,\omega_{pz0}} \quad . \tag{24}$$

Equation (24) shows that, if the platform is spinning ($\omega_{pz0} \neq 0$), a nonzero platform cross product of inertia gives $\omega_{px} \neq 0$ so that steady spin of the spacecraft occurs about a platform-fixed axis that is inclined to the bearing axis. The corresponding rotational angular momentum vector is also fixed in the X_pZ_p plane at an angle θ_W from the bearing axis as obtained from equations (12), (13), (18), and (19):

$$\tan\theta_W = \frac{\sqrt{H_x^2 + H_y^2}}{|H_{z0}|} \tag{25}$$

$$\tan\theta_W = \left|\frac{I_t\omega_{px0} + I_{pxz}\omega_{pz0}}{H_{z0}}\right| \tag{26}$$

where $$H_{z0} = I_{pxz}\omega_{px0} + I_{pz}\omega_{pz0} + I_{rz}\omega_{rz0} \quad . \tag{27}$$

Since $\vec{H}$ is fixed in inertial space, the bearing axis in this motion describes a cone of half-angle θ_W about $\vec{H}$ in inertial space. This is the wobble motion.

Equation (26) may be expressed in a simple form when $|b| \ll 1$ so that equation (24) holds. Equation (24) gives

$$I_{pxz}\omega_{pz0} = \frac{\omega_{px0}}{\omega_{pz0}}\left[I_{rz}\omega_{rz0} + (I_{pz} - I_t)\,\omega_{pz0}\right] \tag{28}$$

which may be used to replace the second term in the numerator of equation (26) to yield

$$\tan\theta_W = \left|\frac{\omega_{px0}}{\omega_{pz0}}\left\{\frac{I_{pz}\omega_{pz0} + I_{rz}\omega_{rz0}}{H_{z0}}\right\}\right| \quad . \tag{29}$$

Equation (27) shows that the expression within the braces is very nearly 1 for a small platform cross product; hence, equations (29) and (24) give

$$\tan\theta_W \simeq \left|\frac{\omega_{px0}}{\omega_{pz0}}\right| \tag{30}$$

$$\tan\theta_W = \left|\frac{I_{pxz}\omega_{pz0}}{I_{rz}\omega_{rz0} + (I_{pz} - I_t)\,\omega_{pz0}}\right| \tag{31}$$

as useful forms for numerical computation. Since H_y is zero here, equations (25) and (30) show that $\vec{\omega}_p$ and $\vec{H}$ are parallel as required by equation (15) for steady spin.

Nutation in platform coordinates

For a dual spin spacecraft, $|I_{pxz}|/I_t$ and $|I_{pxz}|/I_z$ are quantities of the first order of smallness. To sufficient accuracy for this paper, the nutational motion about the steady spin motion is given by

$$\vec{\omega}_p = \begin{bmatrix} \omega_{px0} + \omega_t \cos\lambda_p \\ \omega_t \sin\lambda_p \\ \omega_{pz0} - k_z\omega_t \cos\lambda_p \end{bmatrix}_p \tag{32}$$

$$\omega_{rz} = \omega_{rz0} - k_z\omega_t \cos\lambda_p \tag{33}$$

with

$$k_z \equiv \frac{I_{pxz}}{I_z}\frac{\dot{\lambda}_p + \omega_{pz0}}{\dot{\lambda}_p} \tag{34}$$

and

$$\lambda_p = \lambda_{p0} + \dot{\lambda}_p(t - t_0) \tag{35}$$

where $\dot{\lambda}_p$ is the platform nutation frequency given by

$$\dot{\lambda}_p = \frac{H_{z0}}{I_t} - \omega_{pz0} \quad . \tag{36}$$

λ_{p0} and ω_t are constants of integration, and λ_p essentially gives the azimuth of $\vec{\omega}_p$ about the steady spin solution for platform axes. This solution shows that in the presence of nutation both the platform and rotor spin rates exhibit a small oscillation at the platform nutation frequency when $I_{pxz} \neq 0$, even for the despun platform case ($\omega_{pz0} = 0$).

The accuracy of equations (32) and (33) may be verified by direct substitution into the differential equations of motion, equations (15) and (17). These equations give an exact solution for all ω_t values when $I_{pxz} = 0$; in this case $\omega_{px0} = 0$ from equation (24) and ω_t becomes simply the magnitude of the transverse component of $\vec{\omega}_p$. When $I_{pxz} \neq 0$, the solution is correct for small ω_t values through terms of the first order in $I_t\omega_t/H_{z0}$ provided that $\dot{\lambda}_p$ is not small, more specifically, provided that the inequalities

$$I_t|\dot{\lambda}_p|^j \gg \frac{I_{pxz}^2}{I_z}|\omega_{pz0}|^j \tag{37}$$

hold for $j = 0, 1, 2, 3$. The different j values correspond to different neglected terms in the differential equations. Physically, the platform spin rate $\omega_{pz0} \simeq H_{z0}/I_t$, which gives $\dot{\lambda}_p \simeq 0$, is excluded because the nutational motion assumes a different character which is not of interest for this paper.

For small ω_t values, equations (32), (33), and (13) show that $\vec{H}$ observed from platform axes precesses about its steady spin direction at a nearly constant angle, the nutation angle θ_N:

$$\tan\theta_N \simeq \frac{I_t\omega_t}{H_{z0}} \tag{38}$$

For small angles, θ_N is linearly proportional to ω_t.

Nutation in rotor coordinates

The nutation seen on the rotor is described by using right-handed rotor-fixed Cartesian axes $X_rY_rZ_r$ with the origin at O and the $+Z_r$ axis coin-

cident with the $+ Z_p$ and bearing axes. For these new axes,

$$\vec{\omega}_r = \begin{bmatrix} \omega_{rx} \\ \omega_{ry} \\ \omega_{rz} \end{bmatrix}_r \tag{39}$$

where an r subscript outside vector brackets indicates rotor-fixed axes, and

$$\omega_{rx} = \omega_{px} \cos \psi - \omega_{py} \sin \psi \tag{40}$$

$$\omega_{ry} = \omega_{px} \sin \psi + \omega_{py} \cos \psi \tag{41}$$

where ψ gives the angle about the bearing axis between the $+X_r$ and $+X_p$ directions. Equations (32), (33), (35), (36), and (17) then give

$$\vec{\omega}_r = \begin{bmatrix} \omega_{px0} \cos \psi + \omega_t \cos \lambda_r \\ \omega_{px0} \sin \psi + \omega_t \sin \lambda_r \\ \omega_{rz0} - k_z \omega_t \cos \lambda_p \end{bmatrix}_r \tag{42}$$

where $$\lambda_r = \lambda_p + \psi = \lambda_{r0} + \dot{\lambda}_r (t - t_0) \quad . \tag{43}$$

In equation (43), $\dot{\lambda}_r$ is the rotor nutation frequency given by

$$\dot{\lambda}_r = \dot{\lambda}_p + \dot{\psi} \tag{44}$$

$$\dot{\lambda}_r = \dot{\lambda}_I - \omega_{rz0} \tag{45}$$

where

$$\dot{\lambda}_I = \frac{H_{z0}}{I_t} \quad . \tag{46}$$

$\dot{\lambda}_I$ is the inertial nutation rate at small nutation angles, the rate at which the bearing axis precesses about $\vec{H}$ in inertial space. Note that terms with three different frequencies are present in the rotor angular velocity.

Equation (45) shows that $\dot{\lambda}_r$ may be arbitrarily varied in the in-orbit

tests. Since $I_{pxz} \sim 0$, changing the platform spin rate varies ω_{rz0} but not $\dot{\lambda}_I$ because H_z stays constant. From equation (27), in the absence of thruster pulses,

$$H_{z0} = I_{pz}\omega_{pz0} + I_{rz}\omega_{rz0} = I_{rz}\omega_{rzd} = \text{constant} \tag{47}$$

where ω_{rzd} is the rotor spin rate with the platform despun. Equation (45) may be written as

$$\dot{\lambda}_r = \frac{I_{rz}}{I_t}\,\omega_{rzd} - \omega_{rz0} \quad . \tag{48}$$

Eliminating ω_{rz0} from equations (45) and (47) yields equation (4) for the variation of ρ as a function of ω_{pz0}. An alternate form giving ρ as a function of $\dot{\psi}$ is obtained by eliminating ω_{pz0} and ω_{rz0} from equations (16), (47), and (48):

$$\rho = \left| \frac{I_z}{I_t}\left[1 - \frac{I_{pz}\dot{\psi}}{I_{rz}\omega_{rzd}}\right]^{-1} - 1 \right| \quad . \tag{49}$$

Rotor accelerations and accelerometer

The acceleration $\vec{a}$ about the spacecraft mass center O of a point P fixed in the rotor is obtained as follows. The X_r axis may be chosen so that the position vector for P is given by

$$\vec{r} = \begin{bmatrix} R_p \\ 0 \\ z_p \end{bmatrix}_r \tag{50}$$

This point has a velocity $\vec{\omega}_r \times \vec{r}$ about O; hence, for rotating rotor axes,

$$\vec{a} = \left[\frac{d}{dt}(\vec{\omega}_r \times \vec{r})\right]_r + \vec{\omega}_r \times (\vec{\omega}_r \times \vec{r}) \tag{51}$$

$$\vec{a} = \left[\frac{d\vec{\omega}_r}{dt}\right]_r \times \vec{r} + \vec{\omega}_r(\vec{\omega}_r \cdot \vec{r}) - \vec{r}\omega_r^2 \quad . \tag{52}$$

Keeping terms to first order in ω_{px0} and ω_t in using equation (42) to eliminate $\vec{\omega}_r$ gives

$$\vec{a} = \begin{Bmatrix} R_p\,[-\omega_{rz0}^2 + 2k_z\omega_t\omega_{rz0}\cos\lambda_p] \\ \quad + z_p\,[\omega_{px0}\omega_{pz0}\cos\psi + \omega_t(\dot{\lambda}_r + \omega_{rz0})\cos\lambda_r] \\ R_p[k_z\omega_t\dot{\lambda}_p\sin\lambda_p] \\ \quad + z_p\,[\omega_{px0}\omega_{pz0}\sin\psi + \omega_t(\dot{\lambda}_r + \omega_{rz0})\sin\lambda_r] \\ R_p\,[\omega_{px0}(2\omega_{rz0} - \omega_{pz0})\cos\psi \\ \quad + \omega_t(-\dot{\lambda}_r + \omega_{rz0})\cos\lambda_r] \end{Bmatrix} \tag{53}$$

The large constant term $-R_p\omega_{rz0}^2$ in the X_r axis component gives the centripetal acceleration due to rotor spin.

Equation (53) makes it possible to interpret the output of an accelerometer located at P. There are two accelerometers mounted on the rotor at $R_p = 0.99\ m$ with their sensitive axis parallel to the bearing (Z_r) axis. Filtering their output to pass only frequencies between 0.03 and 35 Hz eliminates any contribution from the large X_r axis constant term that might be sensed due to accelerometer misalignment. The filtered output is transmitted by FM real-time telemetry to the ground where it is detected and displayed versus time on a strip chart recorder. The filter readily passes both Z_r axis terms for INTELSAT IV at its typical 50-rpm rotor spin rate: the wobble term with frequency $\dot{\psi} \sim -5$ rad/s and amplitude

$$A_W = R_p\omega_{px0}(2\omega_{rz0} - \omega_{pz0}) \tag{54}$$

$$A_W \simeq \frac{R_p I_{pxz}(2\omega_{rz0} - \omega_{pz0})\,\omega_{pz0}^2}{I_{rz}\omega_{rz0} + (I_{pz} - I_t)\,\omega_{pz0}} \tag{55}$$

from equations (53) and (24), and the nutation term with frequency $\dot{\lambda}_r \sim -4$ rad/s and amplitude proportional to ω_t, so that it is a measure of the nutation angle. For small platform spin rates, equation (55) gives the approximation

$$A_W \simeq 2R_p\frac{I_{pxz}}{I_{rz}}\,\omega_{pz0}^2 \tag{56}$$

which shows that the wobble term amplitude depends on the ratio I_{pxz}/I_{rz}.

Both the wobble and the nutation terms can appear in the nutation trace and thereby produce a beat phenomenon when the platform spins as shown in Figure 2 for INTELSAT IV-A, for which $I_{pxz}/I_{rz} = 0.06$. This

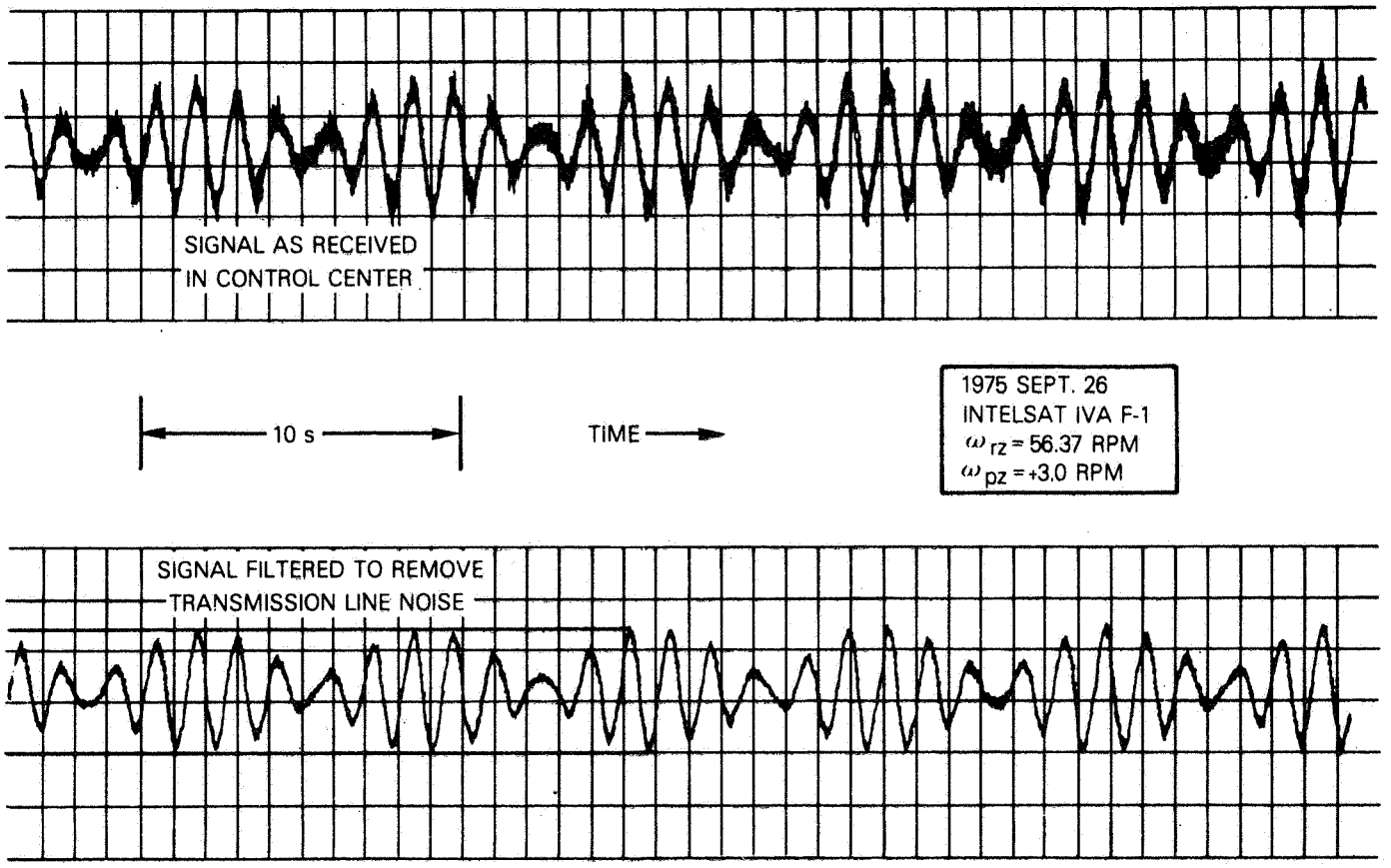

Figure 2. *Nutation Accelerometer Output for a Spinning Platform with a Large Inertial Cross Product*

moment of inertia ratio is large because of the INTELSAT IV-A antenna mast design. The resulting wobble term completely dominates the nutation trace at high platform spin rates and complicates the hand reduction of the nutation strip charts to yield nutation time constants. It is also possible that the liquid excitation by a large wobble term results in a significant contribution to the observed dedamping. INTELSAT IV does not have these problems because its antenna platform was dynamically balanced about the bearing axis to give a small I_{pxz} value. Its observed wobble motion gives $|I_{pxz}| \sim 0.13\ kg \cdot m^2$ so that $I_{pxz}/I_{rz} \sim 0.0006$ for this spacecraft. Thus, INTELSAT IV is ideally suited for spinning platform slosh tests. Its wobble term is detectable for $|\omega_{pz0}| > 8$ rpm, but becomes troublesome only for $\omega_{pz0} \sim 18$ rpm near the $\dot{\lambda}_p \sim 0$ platform resonance.

Note that some terms in $\vec{a}$ with frequency $\dot{\lambda}_p \sim 2$ rad/s are not detected by the rotor accelerometer because they do not appear for the Z_r axis. This observation indicates that all the rotor acceleration frequencies which might produce liquid slosh cannot be determined by merely performing a spectrum analysis of the telemetry record.

If P is a point in the propellant tank liquid, the Y_r and Z_r axis components of $\vec{a}$ give the driving accelerations parallel to the free liquid surface which produce liquid slosh. The terms proportional to ω_t are responsible for the dedamping, since their effect on the liquid increases with the nutation angle. Such terms here have two different frequencies, $\dot{\lambda}_r$ and $\dot{\lambda}_p$, which are not harmonically related. The $\dot{\lambda}_p$ terms are *not* due to nonlinear effects, but arise from a theory linear in ω_t. The $\dot{\lambda}_r$ terms have the largest amplitude by a factor of 100; hence, this paper adopts the usual assumption that these terms give the only significant accelerations producing liquid slosh. The $\dot{\lambda}_p$ terms should not be completely dismissed, however. Although the $\dot{\lambda}_p$ term in the Y_r component has the small factor k_z, the liquid response at this frequency could be very large if $|\dot{\lambda}_p|$ equalled a natural frequency of the liquid. Note that this term persists even for a despun platform.

Theoreticians should develop the complete theory of such small acceleration terms due to vehicle inertia asymmetries and mass center misalignments because of the possibility of frequency coincidence with liquid resonances. It is possible that such a frequency coincidence with a well-understood liquid resonance might explain the anomalous resonances observed in orbit. Similar small acceleration terms should also occur for spinning test fixtures on the ground due to interactions with the earth's gravitational field. The amplitudes of such terms do not necessarily become zero because of a rapid vehicle spin rate.

Nutation test details

Nutation test procedure

The INTELSAT IV pendulum dampers are mounted in an open frame structure on the antenna platform. As a result, their temperature undergoes a large daily variation over a range of 100°C due to changes in shadowing and the direction of the incident sunlight as the earth-pointing antenna platform rotates at 1 rev/day in inertial space. This temperature variation causes a 40-percent change in the eddy-current damping force. To eliminate this variation from an extensive series of nutation tests extending over many hours, the platform was spun in sunlight in a "rotisserie mode" at 1 rpm for 6 hours before the tests to establish an equilibrium temperature.

For each test, the antenna despin control electronics were operated in the rate memory hold mode (Reference 2, pp. 295–299) and commanded to the proper relative spin rate $\dot{\psi}$ computed from equation (49) to give the desired ρ value. Spacecraft telemetry sent through an omnidirectional antenna indicated when the desired platform spin rate had been established. This spin rate can also be measured directly by recording the signal level of a carrier sent through a global beam antenna on the platform; the signal strength rises from zero once each platform spin period as the global beam illuminates the earth. With the spin rate established, accelerometer data were usually obtained over at least one nutation time constant. Only for tests with $\tau > 600$ s was this not always done.

For some unstable platform spin rates, the small nutation already present from starting transients would quickly increase to measurable levels. For other spin rates, measurable nutation was already present from a previous test. An axial thruster was fired to induce nutation only when necessary to avoid violating thermal constraints on thruster restarts at short time intervals. The tests were restricted to nutation angles less than 1°. To reduce the nutation angle following tests that gave unstable nutation, the platform was returned to the rotisserie mode or to some other platform spin rate that gave stable nutation rather than to the despun condition, in order to maintain the damper equilibrium temperature.

For the most accurate presentation of the data, the value of $\dot{\lambda}_r$ used to compute the ρ value actually occurring in each test should be measured on the nutation strip chart recording. For most of the tests, $\dot{\lambda}_r$ was computed from equation (48) simply because the rotor spin rate is readily obtained by telemetry from the rotor-mounted sun and earth sensors. Equation (48) gives a useful check on the spacecraft mass properties com-

puted from prelaunch measurements, but it strictly holds only for a rigid spacecraft. Liquid slosh in response to nutation may result in measurable differences from the values of equation (48). These differences could provide clues to the nature of the anomalous liquid resonances observed in the tests.

Reference 2 describes the INTELSAT IV spacecraft in great detail. Table 1

TABLE 1. MASS PROPERTIES FOR INTELSAT IV F-8

	Transfer Orbit	Synchronous Orbit	
		Start of Life	End of Life
Spacecraft Mass (kg)	1,404	753	608
Hydrazine Mass (kg)	144	142	0
Fill Fraction, f	0.758	0.747	0
Tank Center Location z_T Above Spacecraft Mass Center O (m)	+0.24	−0.24	−0.30
Moments of Inertia (kg m^2)			
I_{pz}	93	93	93
I_{rz}	321	255	201
I_t	1,131	702	663

lists the mass properties of a typical INTELSAT IV spacecraft based on ground measurements; adequate moment of inertia values for other synchronous orbit hydrazine loadings may be found by linear interpolation in the table. The following two subsections provide those details on the platform nutation dampers and propellant tanks necessary for a detailed understanding of the in-orbit tests.

Platform nutation dampers

Neer [1] adequately describes the two platform-mounted pendulum nutation dampers on INTELSAT IV and gives typical parameter values. The damping contribution from the ith damper is given by

$$k_{D,i} = \frac{m_i z_{Di}^2}{I_t} \frac{\dot{\lambda}_I^3(\zeta_i \omega_{ni} \dot{\lambda}_p)}{(\omega_{ni}^2 - \omega_{pz}^2 - \dot{\lambda}_p^2)^2 + 4(\zeta_i \omega_{ni} \dot{\lambda}_p)^2} \tag{57}$$

where m_i = mass of the ith damper pendulum

z_{Di} = distance along the spacecraft bearing axis from the spacecraft mass center to the ith pendulum mass

ω_{ni} = natural frequency of the ith pendulum

ζ_i = damping factor expressed as fraction of critical damping.

Haines and Leondes [3] derive this result using an energy sink model, which is an adequate approximation for this paper. The form of the equation presented here avoids singularities at $\dot{\lambda}_p = 0$. Superposition is assumed to hold so that

$$k_D = k_{D,1} + k_{D,2} \quad . \tag{58}$$

Equations (57) and (58) were evaluated for each nutation test based on preflight ground measurements of the damper parameters. Then the liquid dedamping could be evaluated from the observed nutation time constant τ using equation (2) rewritten in the form

$$k_L = k_D - \frac{1}{\tau} \quad . \tag{59}$$

In some tests, the dedamping contribution is negligible compared to the damping contribution so that the right side of equation (59) involves the difference of two nearly equal numbers. The computed k_L values are very uncertain in such cases; therefore, such values have not been included in this paper.

The pendulum dampers swing in a plane parallel to the bearing axis but are not mounted directly on the bearing axis. At platform spin rates with absolute values above $\sim$10 rpm, centrifugal forces peg the dampers against their stops, which prevents them from swinging. The most accurate dedamping values are determined with the dampers pegged because their damping contribution is then zero and $k_L = -1/\tau$ with no error due to uncertain damper parameters. The pegged dampers contribute an almost negligible 0.2 $kg \cdot m^2$ to I_{pxz}.

Conispheric propellant tanks and fill fraction

Four conispheric tanks are mounted on the rotor at intervals of 90° about the bearing axis. Two such tanks are shown in cross section in Figure 3. The tank interior consists of a spherical section with an internal

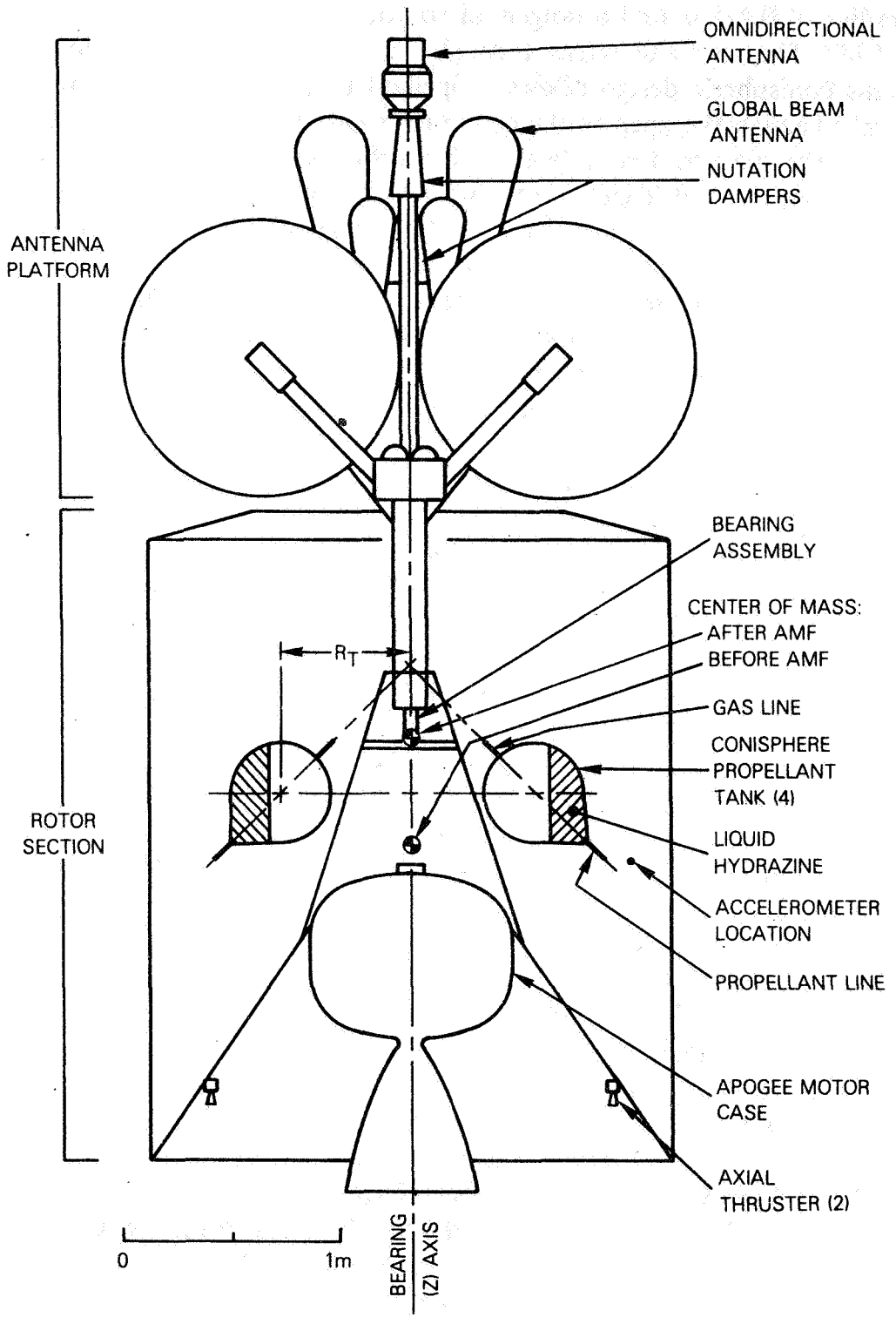

Figure 3. *INTELSAT IV Spacecraft with Cutaway View of Rotor Section*

radius of 0.221 *m* and a tangential conical section with a full cone angle of 85°. The cone axis passes through the bearing axis at an angle of 45°. This conispheric design allows propellant to drain completely from the tank through the apex of the cone under two conditions: on the ground when the spacecraft is vertical, and in orbit during thruster firings under the action of centrifugal forces and nitrogen gas pressurant in the tank. In theoretical discussions for fill fractions greater than 40 percent, the tanks are often assumed to be spherical since the conical section is then nearly full and the free liquid surface lies almost entirely within the spherical section. The cone volume outside a sphere inscribed in the tank is only 3.7 percent of the tank volume.

There are two independent propulsion subsystems; each pair of diametrically opposite tanks is connected to the same subsystem by two lines. A gas pressure equalization line connects at the point on the spherical wall directly opposite the cone apex, and a common propellant line connects at the cone apex so that the two tanks may drain evenly during use and maintain rotor balance. There is no oscillating transfer of liquid between tanks in response to nutation because of the high flow resistance in the connecting propellant line. This resistance is due to the length (3.25 m) and small inside diameter (5.3 mm) of the line. A high resistance is confirmed by the very long (18-min) time constant observed for the in-orbit liquid redistribution between tanks after an initial imbalance [4]. It will be assumed that the two tanks in a subsystem have identical fill fractions.

The center of each spherical section lies at a distance $R_T = 0.578$ m from the bearing axis, and at a bearing axis position $z_T = +0.24$ m above the spacecraft mass center O while in transfer orbit. The expulsion of 650 kg of solid propellant during apogee motor firing (AMF) shifts O toward the antenna platform so that $z_T = -0.24$ m after AMF. Since the tanks are nearly the same distance from O before and after AMF, it should be possible to combine dedamping values determined before and after. This is desirable because of the different ρ values obtainable before and after AMF; ρ due to nutation with the platform despun changes from 0.72 to 0.64.

The following considerations enter into the computation of the tank fill fraction. Hughes Aircraft Co. reports that each INTELSAT IV tank has an internal volume of 0.04689 m^3 on the average with a standard deviation of 0.14 percent. Multiplying this volume by 1.008×10^3 kg/m^3, the density of hydrazine at the tank operating temperature of 20°C, gives 47.26 kg for the hydrazine capacity of an unpressurized tank. The initial nitrogen gas pressure of 1.7 MN/m^2 increases the tank volume by 0.10 percent because of the thin wall construction. This volume increase is

reduced as the gas pressure decreases to 0.7 MN/m² with the depletion of propellant. The volume change should be included in the computation of the fill fraction for comparison of in-orbit tests with ground test data because the ground tests are often made with unpressurized tanks. The fill fraction, f, is computed by correcting the propellant mass, m_p (in kg), in the propulsion system for the propellant in the connecting lines and the spin-up thruster propellant reservoir (about 0.31 kg for each subsystem) to find the mass actually in the tanks; this figure is then divided by the total mass that the two tanks can hold at the existing pressure:

$$f = \frac{m_p - 0.31 \text{ kg}}{2(47.26 \text{ kg})\,[1 + (0.0006 \text{ m}^2/\text{MN})\,p]} \tag{60}$$

where the tank pressure, p (in MN/m²), is given by spacecraft telemetry. This formula has been used to compute all the in-orbit fill fractions quoted in this paper.

The propellant mass on board a spacecraft is somewhat uncertain because it is based on bookkeeping records of maneuvers and a predicted value of propellant flow when a thruster valve is opened. The accuracy of this propellant accounting was recently checked at COMSAT for some INTELSAT III satellites built by TRW, Inc. In May of 1977, the hydrazine was used to exhaustion in propelling these satellites into orbits high above synchronous altitude where they were abandoned. The end of spin speed changes and an accompanying more rapid drop in tank pressure indicated the point of exhaustion. Table 2 lists the hydrazine remaining in each system at this point according to COMSAT's accounting.

TABLE 2. INTELSAT III HYDRAZINE USE ACCOUNTING ERRORS

Parameter	INTELSAT III F-2 Propellant System		INTELSAT III F-6 Propellant System	
	1	2	1	2
Hydrazine at Launch (kg)	10.91	10.91	10.30	10.30
Hydrazine Left According to Accounting at Exhaustion (kg)	0.50	1.13	0.18	0.54
Accounting Underestimate of Propellant Use (%)	4.6	10.4	1.8	5.3
mean (%)	5.5			
standard deviation (%)	±3.1			

Table 2 shows that the accounting underestimated the propellant use by an average of 5.5 percent. If a similar error occurs for INTELSAT IV, the fill fractions listed in this paper for the most depleted tanks will be in error by 1 percent.

Nutation test results and interpretation

Data scaling

It is first necessary to consider whether any scaling should be applied to the observed dedamping values to make the data independent of arbitrary test parameters such as the rotor spin rate. For this discussion, a particular model for liquid slosh is assumed, not because this model accurately reflects reality, but only because it provides a simple illustration of scaling problems. Specifically, it is assumed that liquid slosh produces its destabilizing effect by the back and forth pendulum motion of the liquid mass in response to the nutation. Iorillo [5] models the liquid by an analogous mass-spring-dashpot damper mounted on the rotor at the tank center. This damper will be called the *Iorillo slosh model.* Iorillo shows that the dedamping from longitudinal oscillation (oscillation parallel to the bearing axis) is then given by

$$k_{Lz} = \frac{-R_T^2}{2I_t} \frac{(\dot{\lambda}_r + \omega_{rz})(\dot{\lambda}_r - \omega_{rz})^2 \dot{\lambda}_r c_d}{(\dot{\lambda}_r^2 - \omega_d^2)^2 + (\dot{\lambda}_r c_d / m_d)^2} \tag{61}$$

where c_d is the damping constant (the resistive force per unit velocity), m_d is the mass, and ω_d is the natural frequency of the damper. A similar expression holds for transverse oscillation, with R_T^2 replaced by z_T^2. Because $\dot{\lambda}_r$ is generally negative for a dual spin spacecraft, the driving frequency ratio is given by

$$\rho = \frac{-\lambda_r}{\omega_{rz}} \tag{62}$$

and

$$k_{Lz} = \frac{R_T^2}{2I_t} \frac{(1 - \rho)(1 + \rho)^2 \rho c_d}{(\rho^2 - \rho_{res}^2)^2 + \{\rho c_d / (m_d \omega_{rz})\}^2} \tag{63}$$

where

$$\rho_{res} = \frac{\omega_d}{\omega_{rz}} \tag{64}$$

gives the resonant frequency ratio. For the liquid case, since ω_d is propor-

tional to ω_{rz} as previously explained, ρ_{res} is independent of ω_{rz}.

The following special cases give the two extremes for spin rate scaling. For small damping constants, the expression within braces in the denominator is much smaller than ρ_{res}^2. Then, for frequency ratios far below and far above resonance,

$$k_{Lz} \simeq \frac{R_T^2}{2I_t} \frac{(1-\rho)(1+\rho)^2 \rho c_d}{\rho_{res}^4} \qquad (\rho \ll \rho_{res}) \tag{65}$$

$$k_{Lz} \simeq \frac{R_T^2}{2I_t} \frac{(1-\rho)(1+\rho)^2 \rho c_d}{\rho^4} \qquad (\rho \gg \rho_{res}) \tag{66}$$

and the dedamping is independent of rotor spin rate. This is one scaling extreme. At the damper resonance,

$$k_{Lz} = \frac{R_T^2}{2I_t} \frac{(1-\rho_{res})(1+\rho_{res})^2 m_d^2 \omega_{rz}^2}{\rho_{res} c_d} \qquad (\rho = \rho_{res}) \tag{67}$$

and the dedamping varies as the square of the rotor spin rate. This is the opposite scaling extreme.

These three cases indicate a scaling caveat: the dedamping value measured at a single rotor spin rate cannot be scaled to a different spin rate without some detailed knowledge of the dedamper mechanism such as the relation between the frequency ratio used in the test and resonance. Therefore, scaling will not be applied to the observed dedamping values with the exception of the following application. Equation (63) indicates that the dedamping value k_L measured for a spacecraft varies inversely with its transverse moment of inertia, I_t, so that the dedamping k_L' for a spacecraft with a different transverse inertia I_t' but identical tank geometry relative to the mass center is given by

$$k_L' = \frac{I_t}{I_t'} k_L \quad . \tag{68}$$

This scaling is used to combine transfer orbit data with data taken after AMF.

An important scaling application is the spin rate scaling of ground measurements using spinning test fixtures to orbiting satellites. These

ground tests usually involve very high spin rates to obtain a high Froude number, F_R (the ratio of centrifugal acceleration to gravitational acceleration), at the tank in order to minimize gravitational effects, while the in-orbit satellite has a much lower spin rate. However, the following difficulty arises when scaling isolated dedamping values from ground tests using full scale tanks. For isolated test points, the relation between the driving frequency ratio used and the liquid resonances is not known; hence, the scaling caveat just given warns that a simple scaling is not possible. In addition, an upper bound on the in-orbit dedamping may be obtained by using the scaling extreme from the Iorillo slosh model that gives the highest (most pessimistic) dedamping value. For scaling to lower spin rates, an upper bound is thus obtained by assuming that dedamping is independent of spin rate.

Cautions on the time constant group

The time constant group is discussed here since this quantity is sometimes misapplied in spin rate scaling. From a dimensional analysis, Neer and Salvatore, in Chapter 4 of Reference 6, propose the *dimensionless* time constant group τ_{cg} as a convenient parameter for correlating ground and in-orbit dedamping measurements. They give

$$\tau_{cg} = \frac{n\mu d_T^5 \omega_{rz} \tau_{DD}}{I_t} \tag{69}$$

$$\tau_{cg} = \text{function } (R_e, F_R, f, S, \rho, d_T/R_T, z_T/R_T) \tag{70}$$

where n = number of tanks

μ = mass density of the liquid

d_T = a characteristic tank dimension such as the sphere diameter for conispheric tanks

τ_{DD} = dedamping "time constant"

F_R = Froude number at the tank

$\equiv$ centrifugal acceleration of tanks/gravitational acceleration (an infinite ratio in a 0-g field)

S = tank shape factor

R_T = distance of the tank (sphere) center from the bearing axis

z_T = tank height above spacecraft mass center

$$\tau_{DD} \equiv \frac{1}{k_L} \tag{71}$$

with the Reynolds number R_e defined as

$$R_e = \frac{\rho \omega_{rz} \mu d_T^2}{\eta} \tag{72}$$

where η is the liquid viscosity.

The functional relation in equation (70) is to be discovered empirically by experiment. This functional relation is useful only if the dimensionless parameters in the argument list can be varied individually. However, for the in-orbit dedamping measurements described herein, at least two of the parameters are always varied simultaneously; spinning the antenna platform at different inertial spin rates varies not only ρ but also R_e through the accompanying rotor spin rate change, as shown by equation (72). Therefore, the present paper does not use the time constant group.

For applications, equations (69) and (71) yield

$$k_L = \frac{n \mu d_T^5 \omega_{rz}}{I_t \tau_{cg}} \tag{73}$$

This equation must always be applied cautiously because τ_{cg} can be a function of the other parameters on the right side of the equation. For example, equation (73) gives no definite theoretical relation between k_L and ω_{rz} since equations (70) and (72) indicate that τ_{cg} is a possible function of ω_{rz} through the Reynolds number. From ground test data, Neer and Salvatore conclude in Chapter 7 of Reference 6 that τ_{cg} is independent of ω_{rz} at a resonance (k_L maximum); then k_L varies *linearly* with the rotor spin rate. Equation (67) from the Iorillo slosh model predicts a different result in this case, that k_L varies as *the square* of the rotor spin rate. If the Neer and Salvatore linear dependence could be verified by in-orbit tests, it could provide a valuable clue to the nature of the observed dedamping resonances.

Observed liquid resonances

Figures 4–8 show the observed dedamping values plotted versus the driving frequency ratio for various fill fractions. Figure 8, which com-

pares three different fill fractions, clearly shows that a change of a few percent in the fill fraction can result in a drastic change in the dedamping for a given ρ value. Note especially the increase in dedamping with increasing fill fraction at $\rho = 0.72$, the ratio for a despun platform while in transfer orbit. Each figure lists the dates for the nutation tests, the satellite used, and the satellite I_t value at the time of the tests for data scaling applications using equation (68). Figure 8 includes transfer orbit data scaled to the value $I_t' = 700\ \text{kg}\cdot\text{m}^2$ so that they may be readily compared with the rest of the data taken after AMF. The fill fractions for both propellant systems are always given since they may be very unequal.

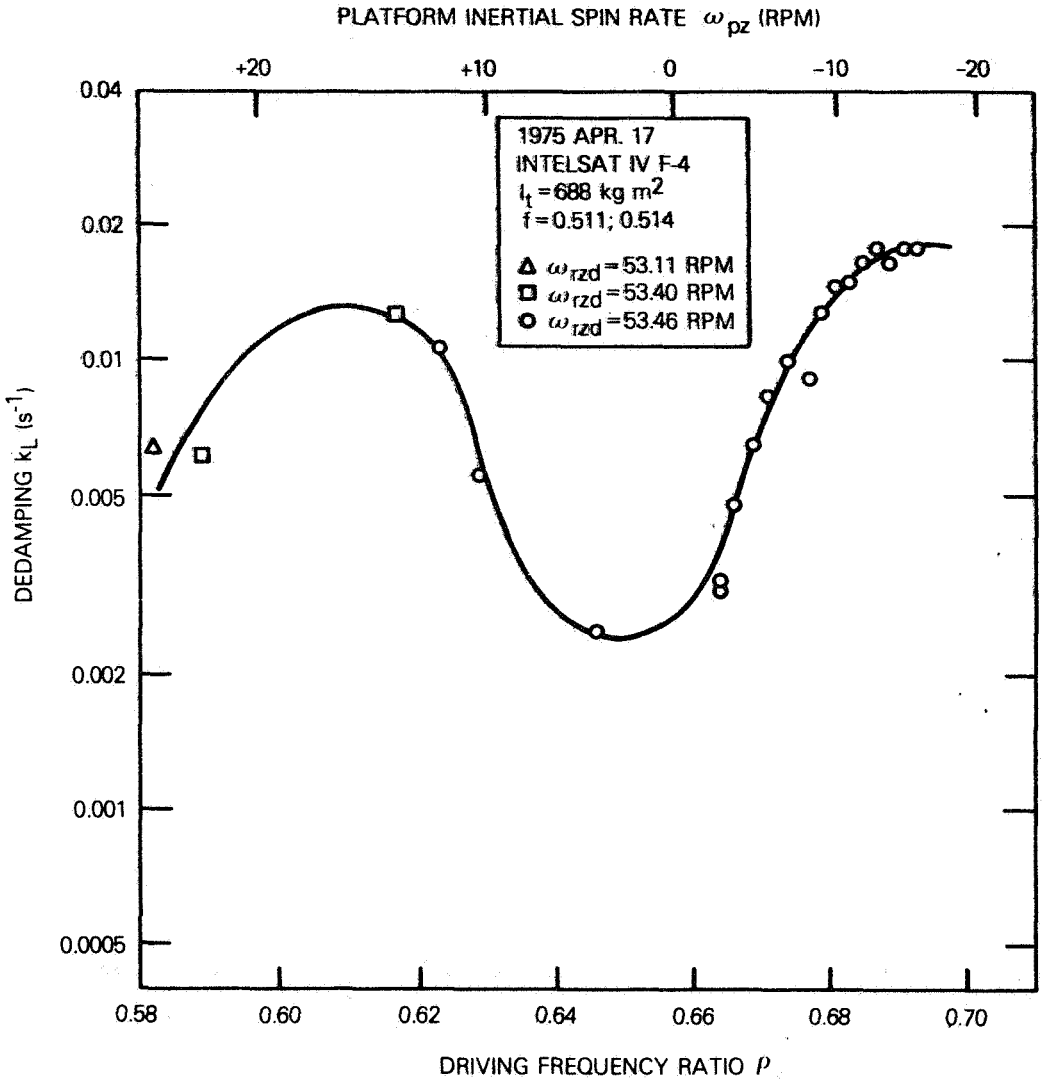

Figure 4. *Tank Liquid Dedamping Contribution for a 51-Percent Fill Fraction*

The data show distinct dedamping maxima which are interpreted as liquid resonances. These are called the *anomalous resonances* since their origin is not known. Two maxima are evident in some of the data: Figure 4 definitely shows two peaks, while Figure 5 shows one peak and part of a second. Figure 9 shows that the frequency ratio ρ_{res} at a maximum moves to higher values with increasing fill fraction, indicating that the anomalous resonances are actually due to the presence of liquid hydrazine on the rotor. Parallel straight lines have been drawn on the graph to indicate the trend of the data.

Thruster firings during some test series changed the spacecraft rota-

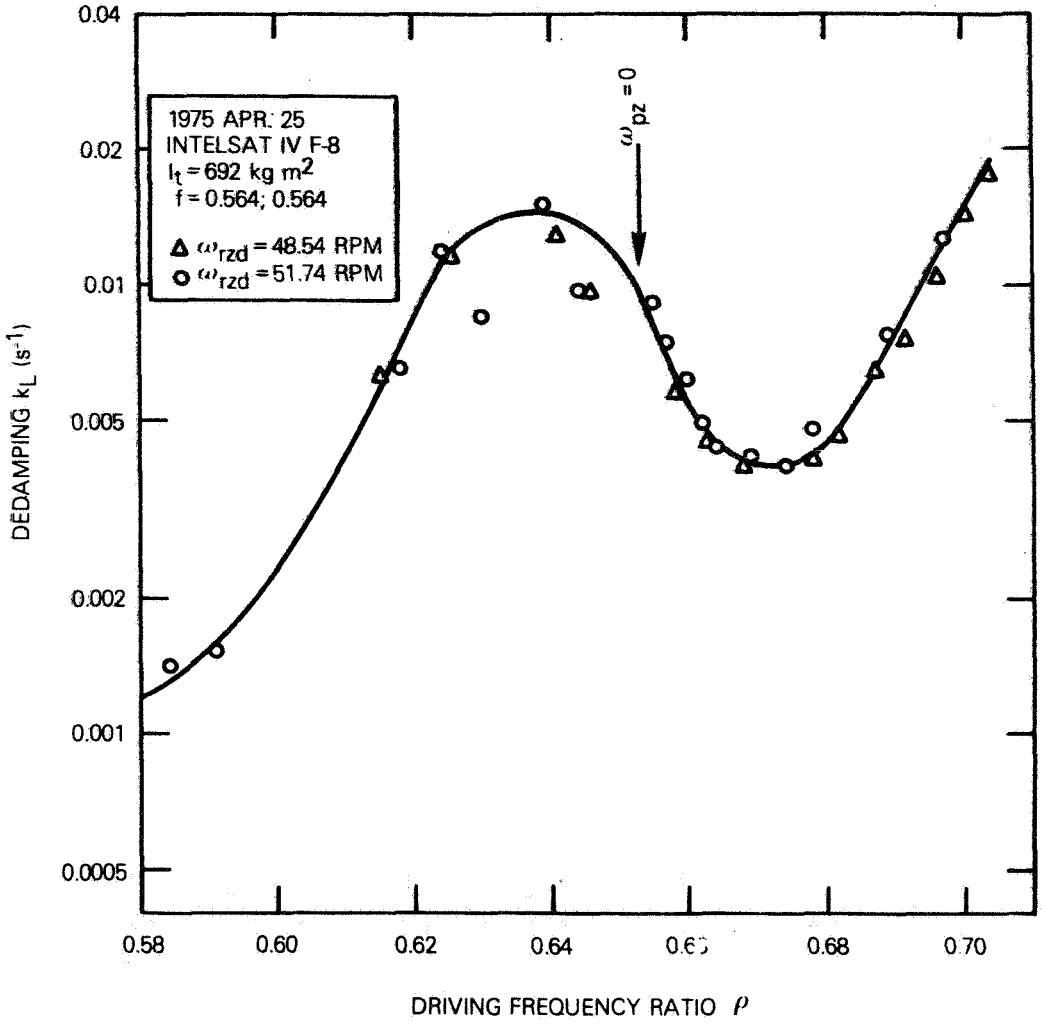

Figure 5. *Tank Liquid Dedamping Contribution for a 56-Percent Fill Fraction*

tional angular momentum so that different data sets for a given fill fraction may correspond to a significantly different rotor spin rate ω_{rzd} with the platform despun. Such data sets are distinguished by different plotting symbols. Figure 5 compares two such data sets taken before and after a rotor spin-up which changed ω_{rzd} from 48.54 to 51.74 rpm. The two data sets fall along the same curve although the data with the higher ω_{rzd} value appear to have slightly higher dedamping values. At the resonance peak, equation (67) from the Iorillo slosh model predicts a 12-percent difference between the data sets, while equation (73) from the time con-

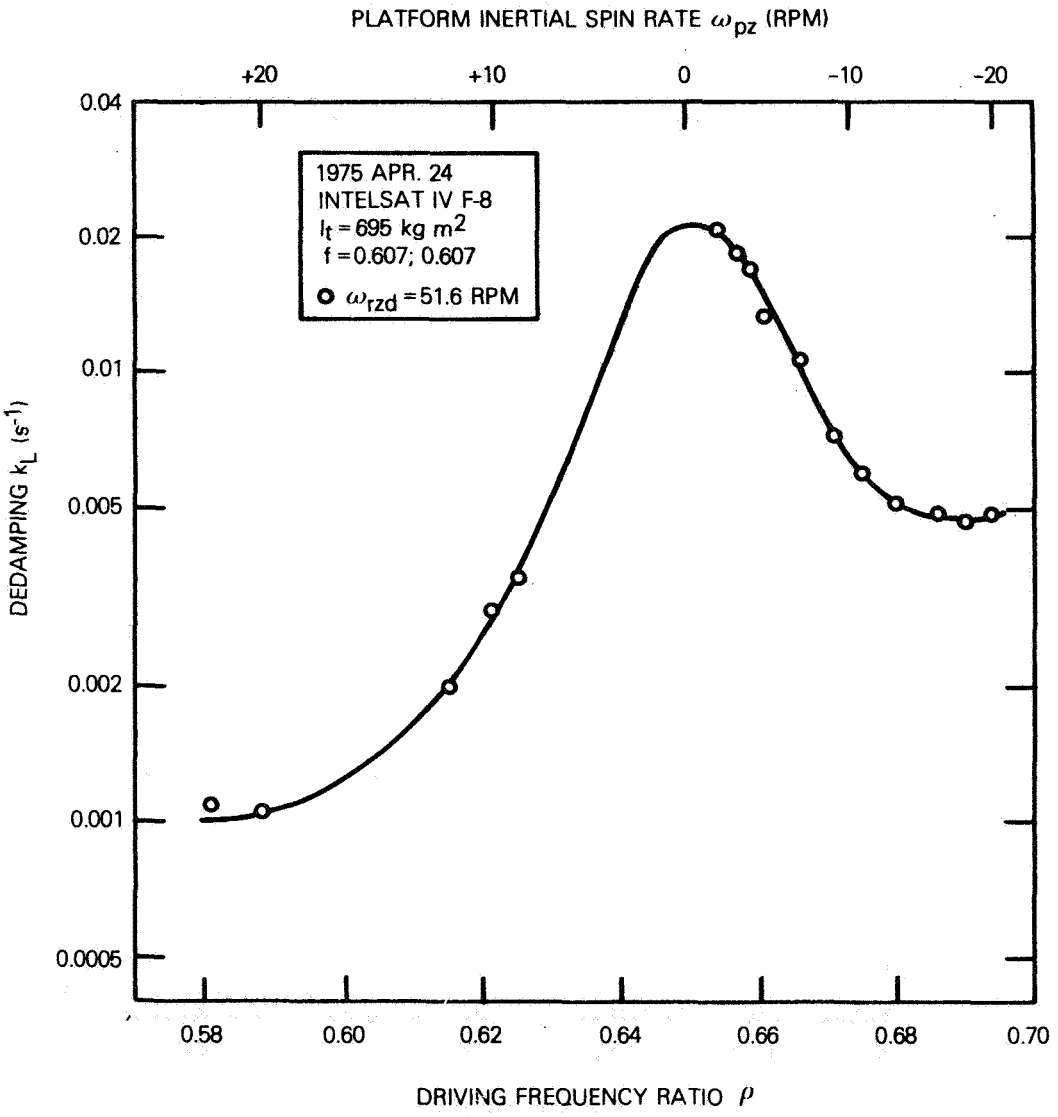

Figure 6. *Tank Liquid Dedamping Contribution for a 61-Percent Fill Fraction*

stant group predicts only a 6-percent difference. There is too much scatter in the data to decide between the two predictions.

Problems in the interpretation of the observed resonances

Before the in-orbit tests, *no* liquid resonance was expected within the range of frequency ratios tested. This opinion was based on ground measurements of the lowest mode natural frequency of the liquid in non-spinning spherical and conispheric tanks. Tests at COMSAT Laboratories

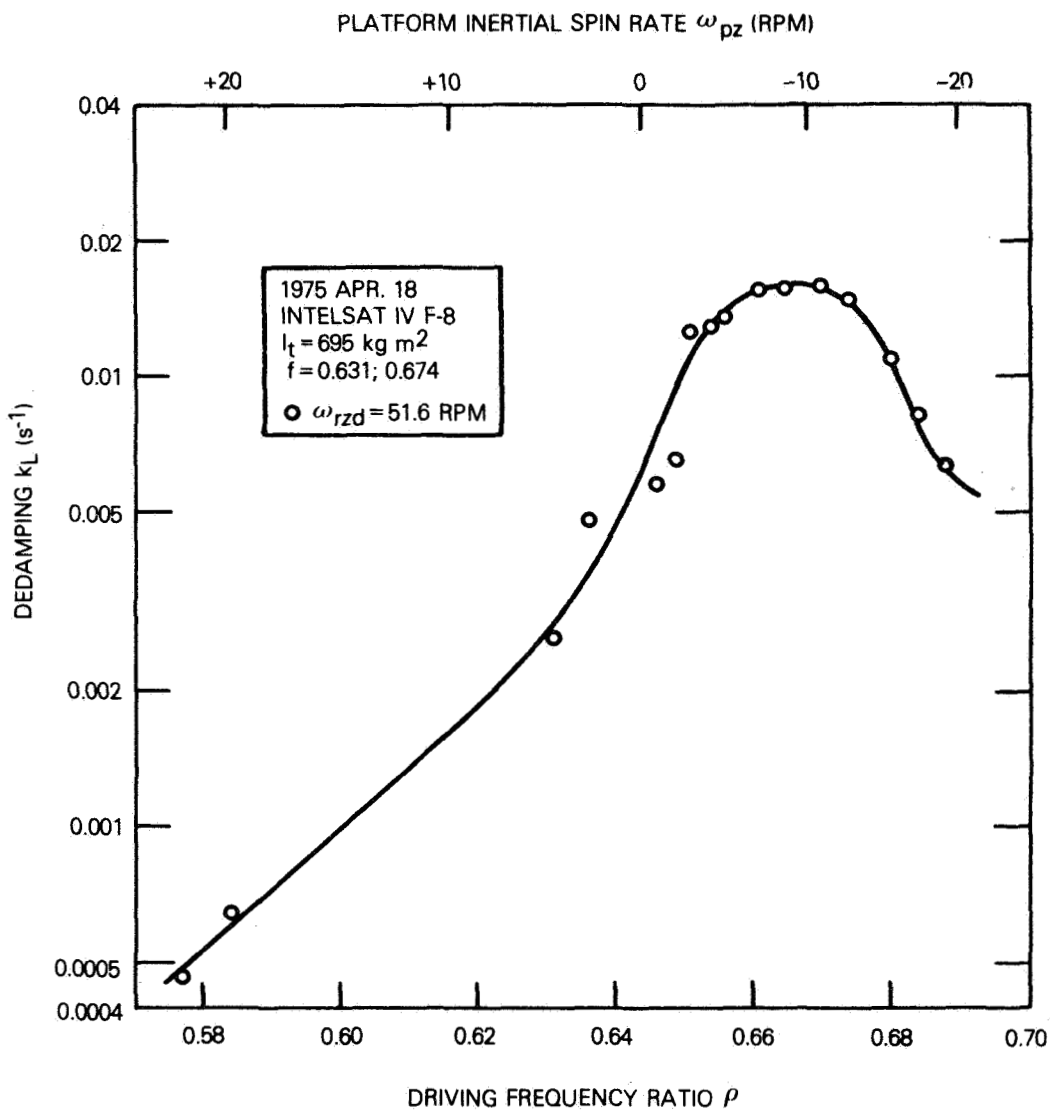

Figure 7. *Tank Liquid Dedamping Contribution for a 63.67-Percent Fill Fraction*

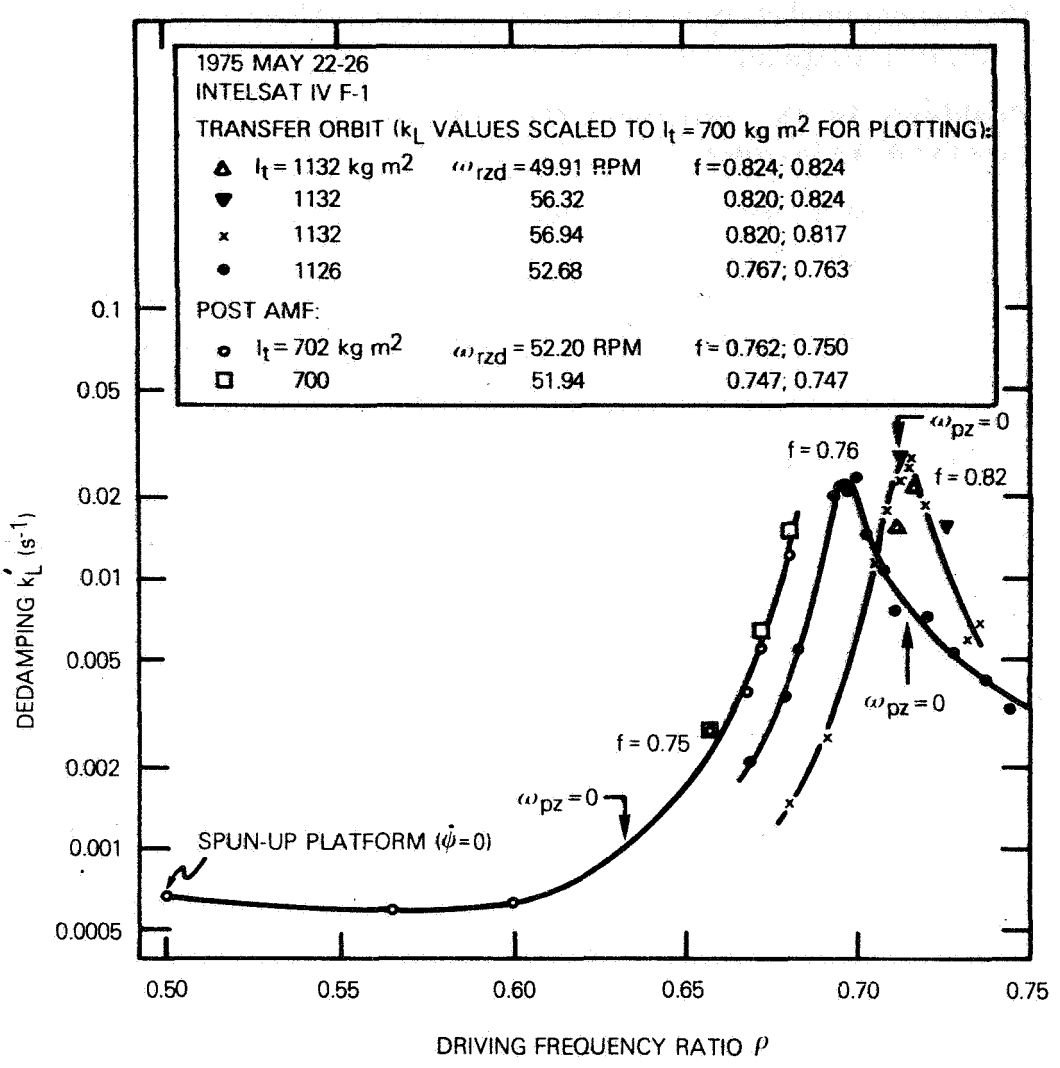

Figure 8. *Tank Liquid Dedamping Contribution for Three Different Fill Fractions Obtained During Launch Operations*

showed that the two tank geometries have the same natural frequency within 10 percent for a given fill fraction between 8 and 81 percent. These measurements indicated that the liquid resonance frequencies would always be much higher than the nutation frequency.

For small amplitudes, the lowest mode oscillation consists of liquid motion in the spherical tank section much like a rigid body undergoing a pendulum oscillation about an axis through the sphere center. This motion with a nearly planar free liquid surface is similar to the residual sloshing motion commonly observed in liquid containers such as water buckets and wine glasses. Because this is a pendulum-like motion, the

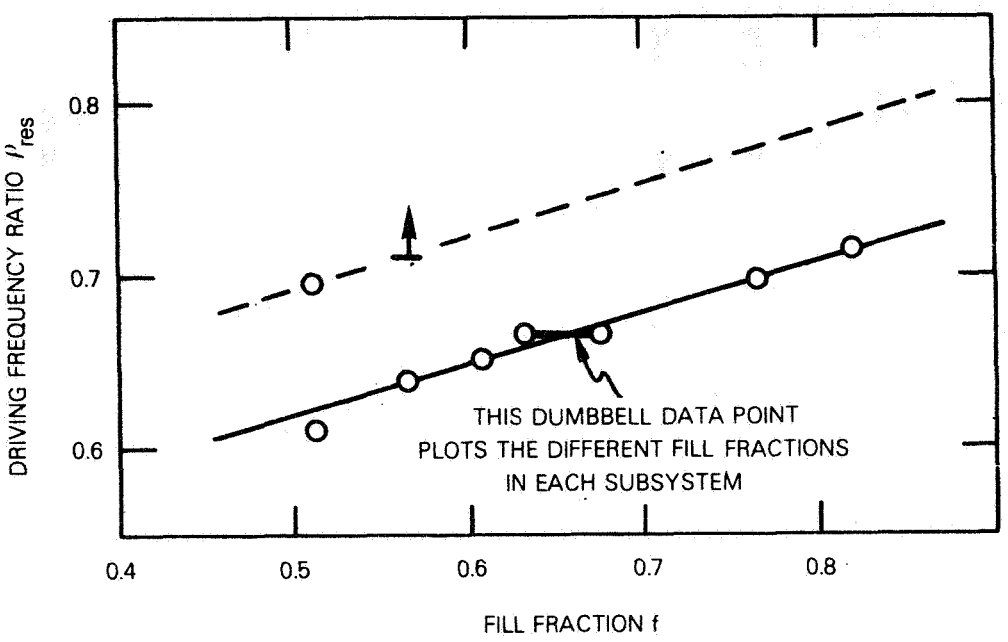

Figure 9. *Driving Frequency Ratio at an Anomalous Resonance vs Fill Fraction for the Conispheric Tanks*

ground measurements of natural frequency collected in Reference 7 can be scaled to in-orbit conditions by replacing the acceleration of gravity, g, in that figure with the appropriate centrifugal acceleration in the spacecraft tank. For longitudinal oscillations this acceleration is $\omega_{rz}^2 R_c$, where R_c is the distance from the bearing axis to the liquid mass center, while for transverse oscillations the effective acceleration is $\omega_{rz}^2 R_T$. The latter acceleration is smaller because, for transverse displacements from equilibrium, the mass center of the equivalent physical pendulum does not approach the bearing axis as rapidly as for longitudinal displacements. Indeed, for a pendulum pivot on the bearing axis ($R_T = 0$), transverse displacements keep the mass center at a constant distance from the bearing axis so there would be no centrifugal restoring force to produce oscillation. Table 3 compares the resulting predictions with the observed resonances for different fill fractions and shows that the predicted values are $\sim$3 times the observed values.

The fact that the predicted frequency ratio for a transverse resonance is roughly three times the observed frequency ratio has led to speculation that a liquid resonance at a multiple of the nutation frequency was excited through nonlinear effects. This superharmonic resonance hypothesis to explain the dedamping peaks can be dismissed by the following two argu-

TABLE 3. OBSERVED IN-ORBIT LIQUID RESONANCES AND PREDICTED LOWEST MODE NATURAL FREQUENCIES*

Parameters	Fill Fraction, f					
	0.512	0.564	0.607	0.631; 0.674 (unequal systems)	0.765	0.819
Ratio of Liquid Depth, h, in Spherical Section to Tank Radius, r	0.991	1.062	1.123	1.157; 1.219	1.356	1.444
Natural Frequency Parameter, $\Lambda_1(h/r) = \omega_d\sqrt{r/g}$ [7]	1.24	1.27	1.29	1.31; 1.34	1.42	1.48
Liquid Mass Center Distance from Bearing Axis for Spherical Section, R_c/r	3.00	2.96	2.92	2.91; 2.87	2.81	2.77
Predicted Natural Frequency Ratios:						
$\rho_{long} = \sqrt{R_c/r}\,\Lambda_1$ for Longitudinal Oscillation	2.15	2.18	2.21	2.23; 2.26	2.38	2.47
$\rho_{trans} = \sqrt{R_T/r}\,\Lambda_1$ for Transverse Oscillation	2.01	2.05	2.09	2.12; 2.16	2.30	2.40
Observed In-Orbit Ratio ρ_{res} for Anomalous Resonance	0.695; 0.610 (two resonances)	0.637	0.650	0.666	0.696	0.714
Predicted Value/Observed Value:						
ρ_{long}/ρ_{res}	3.1; 3.5	3.4	3.4	3.3; 3.4	3.4	3.4
ρ_{trans}/ρ_{res}	2.9; 3.3	3.2	3.2	3.2; 3.2	3.3	3.4

*The radius of the spherical tank section, $r = d_T/2 = 0.221$ m. The distance from the bearing axis to the tank sphere center, $R_T = 0.578$ m.

ments. First, an unpublished analysis by the author shows that, for an oscillating mass motion on the spacecraft in response to nutation, only the frequency component of the oscillation at the nutation frequency contributes to the dedamping. The tank liquid may undergo a large amplitude oscillation at its natural frequency due to a superharmonic resonance, but this oscillation is not at the nutation frequency and thus cannot produce a secular change in the nutation angle. Second, a careful analysis of several dozen nutation strip chart recordings shows that the observed nutation amplitude varies exponentially with time as given by equation (1).* Therefore,

$$\dot{\theta} = \frac{\theta}{\tau} \tag{74}$$

where τ is a constant. The time rate of change of the nutation angle is thus proportional to the nutation angle; *i.e.*, the damping and dedamping mechanisms are operating in their linear range and nonlinear effects are not important.

To illustrate the difficulty of using a liquid pendulum-motion resonance to explain the in-orbit data, it can be attempted to model the dedamping by a simple pendulum of length l_c pivoted at a point fixed in the rotor with the pendulum point mass positioned within the liquid volume. Such pendulum models have the desired property that, as in the case of liquids, their natural frequency, ω_n, is proportional to the rotor spin rate. For longitudinal oscillations,

$$\frac{\omega_n}{\omega_{rz}} = \sqrt{\frac{R_c}{l_c}} \tag{75}$$

where R_c is now the distance of the pendulum mass from the bearing axis. For transverse oscillations,

---

*Some small departures from an exponential fit to INTELSAT IV nutation data have been observed as follows. The amplitude for the first five cycles following a thruster pulse is often less than that predicted by an exponential fit, but this is attributed to an initial transient in the damper and liquid motions. The first few cycles are therefore excluded from the fit. The residuals from an exponential fit to the peaks of the following cycles sometimes show a systematic slow oscillation with period $\sim$30 s, but the amplitude is of the same order as the measurement accuracy so that this is not conclusive evidence for departure from an exponential variation.

$$\frac{\omega_n}{\omega_{rz}} = \sqrt{\frac{R_c}{l_c} - 1} \quad . \tag{76}$$

For the ratio ω_n/ω_{rz} to be equal to the observed dedamping resonance ratio of $\sim$0.66, longitudinal oscillations require $l_c \simeq 2.3\ R_c$; that is, the pendulum mass and pendulum pivot must be on opposite sides of the bearing axis. This is a physically unrealistic model. Transverse oscillations require $l_c \simeq 0.7\ R_c$; that is, the pendulum pivot is outside the tank near the bearing axis instead of near the tank center. This is also an unsatisfactory model.

Conclusions and suggestions for further investigations

The in-orbit dedamping measurements and the considerations of the previous subsection lead to the following conclusions: (a) over the range of ρ values tested, there are two anomalous resonance peaks; (b) their cause is unknown. It is highly desirable to discover the excitation mechanism that causes the anomalous resonances so that mathematical models can be constructed that would allow ground test results to be easily scaled to in-orbit conditions. Useful information could be obtained from a spinning test fixture such as the angular motion fixture described by Martin in Reference 8 (pp. 9–12) or the spinning air bearing fixture at Hughes Aircraft Co. (Reference 6, Chapter 3; also Reference 1, p. 75, Figure 7) since these spinning fixtures also exhibit anomalous liquid resonances. However, these fixtures must be instrumented to provide quantitative measurements of the actual motion of the liquid. A closed circuit television camera is sometimes mounted on the rotating test vehicle to view the liquid contained in a transparent tank. Such cameras have not proven useful in quantitative work because nonlinear effects are likely to be introduced by the large nutational motion usually required to give measurable liquid motion. Such cameras can give useful qualitative results, however.

The author has proposed that *liquid height gauges* be used to obtain quantitative measurements of the amplitude and phase of the rise and fall of points on the free liquid surface. Even coarse (10-percent) measurements could define the surface motion from which the mode of liquid oscillation (longitudinal, transverse, or other) at resonance could be deduced. The gauge proposed here is based on the electrical conductance between an electrical probe and the tap water used in place of hydrazine

as the tank liquid in ground tests. As shown in Figure 10, two bare electrical probes ~2 mm in diameter are required: one probe, called the ground probe, extends several centimeters below the liquid surface, while the second probe, called the surface probe, extends only 2 or 3 mm below the surface. The surface probe should be mounted no closer than 2 mm to the tank wall to prevent water drops from forming between the probe and the tank wall and giving erratic conductivity variations.

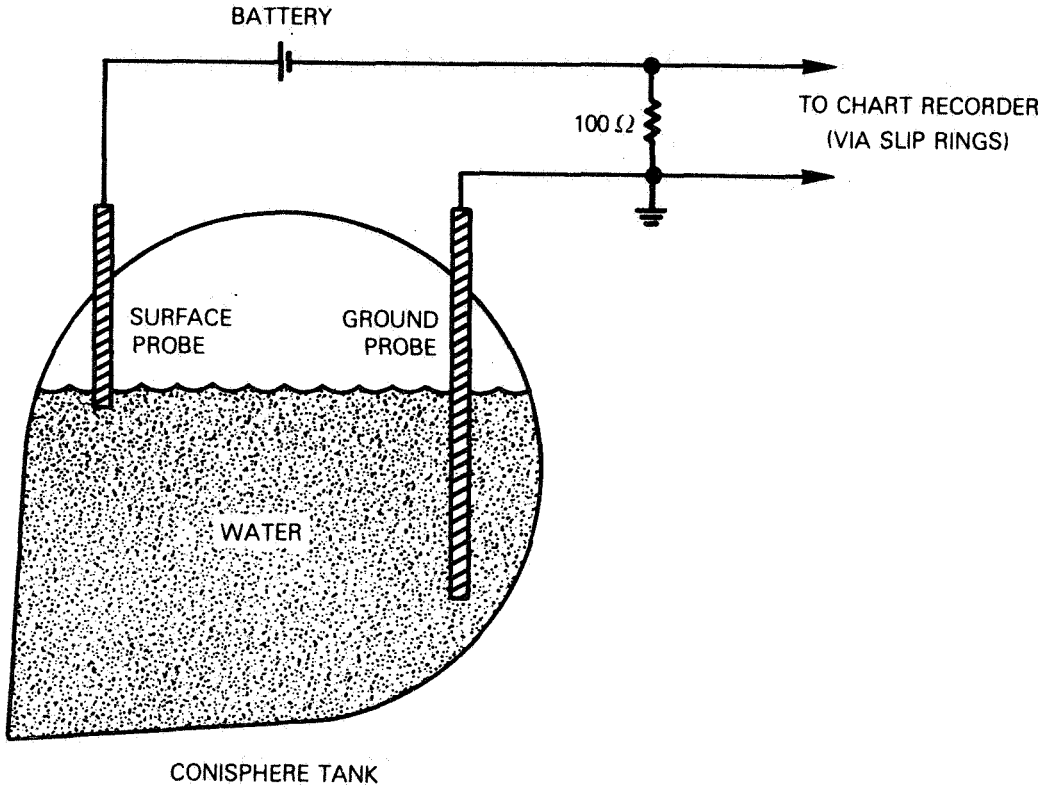

Figure 10. *Liquid Height Gauge Circuit for Liquid-Slosh Quantitative Measurements*

The electrical conductance of the water between the probes is of the order of $(10\ k\Omega)^{-1}$, and is largely independent of the distance between the probes. The liquid slosh measurements are based on the fact that this electrical conductance depends largely on the area of the surface probe in contact with the water. For a probe of uniform cross section, this area varies linearly with the depth of the surface probe in the water. Then, for the circuit shown in Figure 10, the electric current flowing between the probes varies linearly with liquid height as does the resulting voltage across the 100Ω signal resistor.

The voltage across the signal resistor thus reflects the changing height of the fluid at the surface probe due to liquid slosh. The surface motion should be restricted to ± 1 mm to ensure that the surface probe is always in the water, and to maintain a linear relation between voltage and surface height. Because of the small volume of each probe, several surface probes can be mounted at different places in the tank. These height gauges should be located so that different probes are sensitive to different modes of liquid slosh.

R. A. Curtis of COMSAT Laboratories has constructed and tested such a liquid height gauge. The apparatus gives satisfactory performance on the spinning test fixture described by Martin in Reference 8 (pp. 9–12). N. S. Lomas has used the fixture with a single height gauge and a television camera to look for resonances in a conispheric tank containing water at an 86-percent fill. A structural resonance limited the driving frequency ratio to values below 0.53, that is, to values far below the in-orbit resonance values. Liquid resonances associated with transverse and longitudinal oscillations were found for $\rho = 0.349$ and 0.407 respectively. These values are nearly one-half the resonance values of 0.72 and 0.80 predicted for $f = 0.86$ by the straight lines fit to in-orbit data in Figure 9. The liquid was oscillating at the driving frequency. No firm conclusions about these newly observed resonances can be made because the height gauge showed many large-amplitude harmonics of the driving frequency whose presence is unexplained.

Finally, experimental and theoretical consideration should be given to a possible *swirl oscillation* of the liquid, which is explained as follows. The body of the liquid, if treated as a rigid body sliding within a spherical tank, can oscillate with three degrees of freedom about three mutually orthogonal axes. Two of these axes are "parallel" to the equilibrium free liquid surface and correspond to the usual longitudinal and transverse oscillation of the liquid as a physical pendulum. The third axis is normal to the free liquid surface at the surface center and is the axis for swirl motion of the liquid. For a non-spinning tank on the ground, a displacement of the liquid about the swirl axis results in no restoring torque on the liquid; no swirl oscillation occurs in this case. On a spinning satellite, however, the equilibrium free liquid surface is a portion of a cylinder whose axis is the spin axis. A rigid-body displacement of the liquid about the swirl axis results in a restoring torque due to centrifugal forces which attempt to bring the cylindrical surface back into alignment with the *instantaneous* spin axis. The natural frequency of the resulting oscillation about the swirl axis may well correspond to an observed anomalous

resonance. This swirl oscillation would be driven by spacecraft nutation because the direction of the spin axis about the swirl axis oscillates with time.

Acknowledgments

The INTELSAT IV *liquid slosh tests were a cooperative effort by many people at* COMSAT. *The initial analyses that led to the tests were performed by L. B. Ricks and A. A. Satterlee of* COMSAT *and J. O. Salvatore of Hughes Aircraft Co. L. R. Dest of* COMSAT *helped reduce most of the nutation strip chart recordings and suggested many improvements to the text of this paper.*

References

[1] J. T. Neer, "INTELSAT IV Nutation Dynamics," *Progress in Astronautics and Aeronautics*, Vol. 33, 1974, pp. 57–84; AIAA Paper No. 72-537.

[2] Special INTELSAT IV Issue, *COMSAT Technical Review*, Vol. 2, No. 2, Fall 1972, pp. 271–576.

[3] G. A. Haines and C. T. Leondes, "Eddy Current Nutation Dampers for Dual-Spin Satellites," *Journal of the Astronautical Sciences*, Vol. 21, 1973, pp. 1–25.

[4] G. D. Gordon, G. R. Huson, and V. J. Slabinski, "Blocking Bubbles in the INTELSAT IV Fuel Lines," *COMSAT Technical Review*, Vol. 4, No. 2, Fall 1974, pp. 499–506.

[5] A. J. Iorillo, "Nutation Damping Dynamics of Axisymmetric Rotor Stabilized Satellites," American Society of Mechanical Engineers Winter Meeting, Chicago, Illinois, November 1965, *ASME Miscellaneous Papers*, ESL Paper No. 238, pp. 11–19.

[6] J. T. Neer and J. O. Salvatore, "Fuel Slosh Energy Dissipation on a Spinning Body," Report SCG 20047R, Hughes Aircraft Co., February 1972.

[7] Sandor Silverman and H. Norman Abramson, "Lateral Sloshing in Moving Containers," *The Dynamic Behavior of Liquids in Moving Containers*, H. N. Abramson, ed., NASA SP-106, 1966, Ch. 2, p. 52, Figure 2.28.

[8] E. R. Martin, "Experimental Investigations on the Fuel Slosh of Dual-Spin Spacecraft," *COMSAT Technical Review*, Vol. 1, No. 1, Fall 1971, pp. 1–20.

A VARIABLE-ORDER VARIABLE-STEP RUNGE-KUTTA METHOD

D. G. Bettis

Texas Institute for Computational Mechanics
The University of Texas

ABSTRACT

A variable-order variable-step explicit Runge-Kutta algorithm is presented. The algorithm has embedded orders of one through six. The coefficients have been selected so that the local truncation errors are small, and that the absolute stability regions are large for each of the solutions of different order. The strategy for selecting the order and the stepsize is discussed. The algorithm is implemented in SUBROUTINE RKVAR. Comparison tests show that RKVAR is reliable, that it yields solutions that are accurate and that the method is efficient. Two test problems from celestial mechanics are given.

"SHOE-BOX" ORBIT DETERMINATION SYSTEM FOR SMM PRELIMINARY RESULTS

K. K. Tasaki—NASA Goddard Space Flight Center
and
C. Goorevich—Computer Sciences Corporation

ABSTRACT

Currently, most operational orbit determination functions are performed on large main-frame computers. It has already been demonstrated,that, at least for non-real-time orbit determination, a minicomputer can adequately provide the necessary computing power. The question at hand is: What about the use of microprocessors for operational orbit determination support?

During the past year, a study has been conducted to answer this question. The study involves the implementation of both sequential and batch methods of estimation on National Semiconductor IMP-16 microprocessors. The study used simulated data from a Tracking and Data Relay Satellite (TDRS) whose target satellite was the first Multimission Modular Spacecraft (MMS), the Solar Maximum Mission (SMM). An interesting feature of the hardware was the use of two interconnected ("Shoe-Box") IMP-16's. Some preliminary results from the study, as well as the difficulties and advantages in the use of microprocessors, are presented here.

Introduction

The existing operational orbit determination systems, such as the Goddard Trajectory Determination System (GTDS) and Goddard Real-Time System (GRTS), normally run on a large computer system, (i.e., IBM 360/95 or 75). Because these software systems are rather generalized, multi-purpose systems, and are capable of solving a great variety of orbit-related problems, they require a considerable amount of hardware resources. However, for periodic orbit updates of a given class of satellites (i.e., a given set of orbit characteristics), only a small portion of the software system is utilized. For example, the force models for the orbit propagator do not change from one update to another; and the observation types are limited to half-dozen or less. Thus, the parts of the system which are exercised do not change from run to run for a given type of orbit. With this in mind, the primary goal of the current project was set to develop a microprocessor-based orbit determination system for a particular satellite, namely the Solar Maximum Mission (SMM). Limiting the scope of the software system to always solve for a fixed set of parameters using only two types of observations, the complexity of the software, as well as the amount of code generated, could be minimized. If such a specialized system could be successfully built and tested, then the applicability of microprocessors for orbit determination will have been demonstrated.

In October 1977, the project was initiated. During the first 3 months, two pieces of software were designed: the orbit determination

system (ODS) and the data management system (DMS). ODS was designed based on the requirement of maintaining a 300-meter position accuracy using a sequential estimator. In a 574 km circular orbit inclined 33^{o} to the equator with a period of 96 minutes, the satellite was assumed to be tracked 20 minutes per orbit for 14 revolutions per day with the Tracking and Data Relay Satellite (TDRS). DMS, on the other hand, was designed primarily to manage observation data passed to ODS and updated positions and velocities received from ODS. In addition, DMS had to handle user input from the keyboard of a terminal, and had to provide output to the user terminal. Soon, it became apparent that ODS and DMS functions were separate, and should be targeted to two different processors.

At about the same time, three pieces of hardware were purchased, one printer/keyboard terminal (Silent 700 Model 765) from Texas Instruments and two IMP-16 microprocessors from National Semiconductor. The two IMP-16's were then turned over to Goddard's Microprocessor Development Facility for assembly and testing.

By the beginning of 1978, the software design was completed, and the implementation was initiated. During recent weeks, the software to handle the processor-to-processor and processor-to-terminal communications has been tested. Some of the well-tested code is now being moved to the target processors. The major effort here is to store the programs onto programmable read-only memory chips (PROM chips), and physically install them in the target processors for further testing. It is expected that most of the software will be on PROM's by the very early spring of 1979 for full-scale system testing.

Models and Accuracies

Choice of the models was determined by the original problem statement and the numerical accuracies of the IMP software floating point package. Design was carried out for a select class of orbit, namely the SMM orbit.

A software floating point package was used to do the decimal arithmetic. The package uses three 16-bit words to represent a real number. Two words represent a signed mantissa while one complete word is used for the exponent. This results in approximately 10 significant digits for the IMP real numbers as compared to 7 digits for IBM S/360 single precession and 17 digits for IBM S/360 double precession. Use of a software floating point package as compared to performing scaled arithmetic speeds up the development time of the software while significantly slowing down the actual run time. In the problem being solved, our only criterion was to keep up with real-time (process one observation every 10 seconds). Running the orbit propagator over one period (96 minutes) with a step size small enough to maintain a 300 meter rss accuracy takes 10 minutes, indicating that use of the software package can be justified in the lifetime cost of the software. If more significant digits are required this may not be true, and solutions such as performing scaled arithmetic may be required in selected portions of the code.

To determine the most appropriate models and algorithms for the orbit determination problem at hand, studies were carried out prior to and during the first stages of system design. Different force

models, integrations, and step sizes were tested using IBM S/360-95 FORTRAN simulations of the possible algorithms. The algorithms were evaluated as to complexity, size, speed, and accuracy. Most calculations were done in single-precision floating point, with those calculations needing double-precision accuracy being identified. The FORTRAN simulation programs developed in this pre-design phase were not only important tools in evaluation of the algorithms, but proved to be an aid in the coding and implementation phase. Studies concerning the system software and hardware capabilities of the IMP-16 microprocessor were also carried out in the pre-design phase.

The models used in the "shoe-box" orbit determination system are: orbit propagation model and state transition matrix.

The orbit propagation model will be used to propagate the target satellite (SMM) orbit between observation updates. This period is expected to last no longer than 96 minutes. The components which make up the propagator are as follows:

- Fourth-order Runge-Kutta integrator, with modified Fehlberg coefficients
- Up to 6 x 6 Earth Geopotential model including central earth
- Modified Harris-Priester Drag mode (assuming spherical space-craft)

Integration is performed using the Cowell technique of integrating the cartesian coordinates of acceleration and velocity.

The state transition matrix (required to propagate the covariance matrix of the extended Kalman filter) is a truncated Tayler series and includes the following terms:

- Acceleration partials with respect to position central Earth and J_2
- Acceleration partials with respect to velocity assumed to be very small
- Approximated to terms of order Δt^2

Observation Model

The observation model takes at a given observation time, the current "best" estimate of the target satellite's state (SMM), the known relay satellite's state (ATS-6, TDRS), and the station transmitter position and velocity to calculate the expected observations of satellite-to-satellite range sum (km) and the range sum rate (cycles of Doppler frequency counted). ATS-6 satellite-to-satellite tracking format was used instead of TDRS (as planned) because of the availability of simulated and real observations. The model assumes all signal paths (between station, relay satellite, and target satellite) are straight lines traversed at a constant speed of light. The calculations are performed by backwards tracing of the light path. The light-time corrections require both iteration and propagation of satellite states for times less than one second. A Newton-Raphson method is used as the iteration technique, while a second-order Euler propagator, modeling only the central Earth, is used for the small orbit corrections necessary during the iteration. The model accounts for a single relay satellite and models the nondestruct mode of frequency counting. Along with the model observations, partial derivatives of range and range-rate observations with respect to the target satellite's state are calculated.

State Estimation Algorithm

The state estimation algorithm updates the target satellite's position and velocity (satellite's state) based on errors between the observed observation and the calculation observation. Two approaches have been taken, one is a batch least squares estimator and the other is the extended Kalman filter. The batch least squares estimator is currently being implemented in its standard form. A small modification to the standard Kalman filter implementation was made for computational savings. The modification allows processing of a range and range-rate observation pair before making a state update. The matrix operations were performed in as straight-forward a manner as possible while eliminating as many trivial operations (such as multiplying and addition of zero's). The microprocessor code and the pre-design FORTRAN code were compared to results from the Goddard Trajectory Determination System (GTDS). The GTDS runs contained higher order terms and were assumed to represent the real world. The worst case results showed that the lack of significant digits did not greatly affect the orbit propagator over one period but did have a larger than expected affect on the observation model. The difference has yet to be resolved. The following table presents the errors due to having less significant digits in the IMP.

	Microprocessor	Pre-Design FORTRAN
Propagator Position Error Meters rss	116	32
Observation range sum error km	.9	.24

	Microprocessor	Pre-Design FORTRAN*
Observation range sum rate error cycles	6	.4

*Single precision (7 significant bits) used whenever possible.

Software/Hardware

The Shoe-Box system is composed of two IMP-16 microprocessors. The IMP is a 16-bit microprocessor with extended arithmetic to handle two 16-bit words. Typical memory fetches are 5.5 times slower than the IBM S/360-95. An add of a 32-bit integer takes 19 microseconds.

Processor One is called the data base IMP and contains 5K words of random access memory (RAM) and 28K words of erasable programmable read-only memory (EPROM). The data and calculated values are stored in the RAM while non-changing program code is stored in the EPROM. Processor Two, called the computational IMP, contains 9K words of RAM and 56K words of EPROM. A TI Silent 700 Model 765 is used as the system input/output device. If the system was modified to accept raw tracking data, the terminal would be replaced by an input cpu connected to the data lines.

Keeping in mind that the system uses satellite-to-satellite tracking data, the data flow for the extended Kalman filter is as follows:

1. Observation and TDRS ephemeris data are fetched from the bubble memory of the terminal to the data base IMP.

2. Upon request from the computational IMP, a data point composed of observation time, range sum observation, range sum rate observation,

and tracking satellite position and velocity is moved to the computational IMP.

3. The computational IMP propagates the target satellite's orbit to the observation time and performs the orbit update process. The corrected target orbit is then sent through the data base IMP to the terminal as an output report.

The software was developed using a higher level language SM/PL. The language is a structured procedure oriented language. Part of the development effort was to investigate the use of a higher level language on a microprocessor. We found that the code generated was optimized in the sense of organizing the code to perform operations in registers thus reducing the number of memory fetches. Errors in the language processor documentation and the actual code generated did slow up the development process more than was originally anticipated. At times stepping through the code, an instruction at a time, was required to determine exactly what was happening. One major item lacking in the SM/PL language that caused many problems was the inability to declare separately compiled modules as external. Due to this limitation of the system software, external locations had to be resolved by hand, after various subprograms were compiled separately. This process, although appearing only to be a minor inconvenience, caused a great deal of difficulty and unexpected side-effects. Although unexpected time loss was spent in understanding the SM/PL language in what it can or cannot do, the overall time of system development was not longer than it would have been if assembler language would have been used. Future programs coded in

SM/PL should proceed faster.

The data base IMP was divided into the following five modules which perform the following functions:

1.) Initialization

2.) Messages to Computational IMP

3.) Decoding of teletype input

4.) Messages to teletype

5.) Respond to computation IMP request for next observation

The computational IMP was divided into the following five modules which perform the following functions:

1.) Initialization of data, GHA, and station model

2.) Observation retrieved

3.) Orbit propagation

4.) Observation model and partials

5.) Orbit estimation processes

Advantages and Disadvantages

From our experience of developing the microprocessor-based orbit determination, a number of advantages and disadvantages to using microprocessors for mathmatical applications can be pointed out. The greatest disadvantage, especially from the software developer's point of view, has been the lack of adequate system support software, such as a good compiler with floating point arithmetic which produces truly relocatable object code, and a reliable linker or loader which can correctly link-edit the

object code. Due to this lack of adequate support software, programmers must constantly worry about absolute addresses for referencing and debugging. The hardware could also be a potential problem. In most cases, one must assemble, test, and maintain various hardware components, because, unlike the minicomputer and main-frame world, there are usually no installation and/or maintenance services provided by the manufacturers or other electronic firms. The lack of relative speed and accuracy is still a problem in using microprocessors for mathematical applications. This is especially true in performing floating point calculations which are normally accomplished by software.

Of course, there are a number of advantages to using microprocessors. First of all, the hardware is very inexpensive compared to the cost of larger processors. The cost of the Shoe-Box system with two IMP-16's and enough memory to accommodate the data base and orbit determination software was about $3K. The second notable advantage is that the hardware/software system can be totally portable. For example, the shoe-box system can be taken to any site where SMM tracking data is available, and begin processing the data (provided that there exists an appropriate set of initial conditions). Another important advantage is modularity. A microprocessor-based system can be quickly upgraded to meet new project requirements which may be placed after the completion of the initial implementation. Due to modularity, this type of system upgrade can be accomplished either by adding more memory or adding more processors.

Future Considerations

A number of future considerations are now discussed in order of probable implementation. The first enhancement to the Shoe-Box system is to develop a data preprocessor and a data postprocessor. The objective of the preprocessor is to provide the capability to accept raw tracking data from the NASCOM line and to perform the necessary preprocessing functions before the data is passed to the data base IMP. This program is scheduled to be completed in March 1979. The data postprocessor, on the other hand, is envisioned as a set of interface routines which will make the computed orbit available to the user computer. Because these interface routines will have to be user processer-dependent, only a general design of the routines will be completed.

Another area of enhancement is reconfiguration of the Shoe-Box system so that a user will have the choice of executing either the Kalman filter program of the differential correction program, depending on the initial input. Each of these programs will reside on a separate IMP-16, and will be parallel to each other, as shown on the following diagram.

PLANNED SHOE-BOX HARDWARE CONFIGURATION

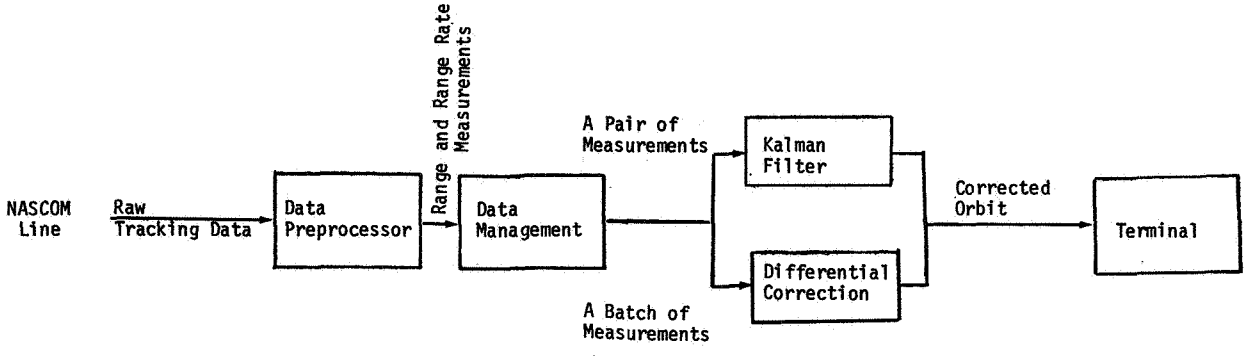

Another possible improvement to the Shoe-Box system may be to solve for both the target and the tracking satellites' position and velocity vectors simultaneously. It is currently believed that this will increase the accuracy of the target satellite's orbit.

Acknowledgements

Messrs. Charles Shenitz and Carl Rabbins of Computer Sciences Corporation have provided much of the software design and programming support for this project, whereas Messrs. Bill Holmes and Ed Zenker of Goddard's Microprocessor Development Facility have contributed a considerable amount of their time in the hardware area. Without these key persons, this project could not have been a success.

OBJECTIVES

1. DEMONSTRATE THE APPLICABILITY OF MICROPROCESSORS FOR ORBIT DETERMINATION
2. INVESTIGATE THE OPERATIONAL ASPECTS OF MICROPROCESSOR-BASED ORBIT DETERMINATION SYSTEM
3. DETERMINE SYSTEM DEVELOPMENT AND MAINTENANCE CHARACTERISTICS

Figure 1

SMM MICROPROCESSOR-BASED ORBIT DETERMINATION

PROBLEM:

MAINTAIN A 300 METER (POSITION-COMPONENT) ACCURACY AT ALL TIMES

GIVEN:

- A 547 KM CIRCULAR ORBIT
- 33° INCLINATION
- 96 MINUTE PERIOD
- 20 MINUTES OF SATELLITE-TO-SATELLITE TRACKING DATA PER ORBIT

Figure 2

DEVELOPMENT OF MICROPROCESSOR ORBIT DETERMINATION SYSTEM

- PURCHASE IMP SOFTWARE DEVELOPMENT SYSTEM
- SELECTION OF MATHEMATICAL MODELS AND ALGORITHMS
- DECISION ON HARDWARE CONFIGURATION
- SOFTWARE DESIGN
- PURCHASE AND ASSEMBLE HARDWARE ("SHOE-BOX")
- IMPLEMENT SOFTWARE ON DEVELOPMENT IMP
- TEST HARDWARE/SOFTWARE COMMUNICATION BETWEEN CPU's
- MOVE SOFTWARE ONTO TARGET SYSTEM
- SYSTEM TESTING

Figure 3

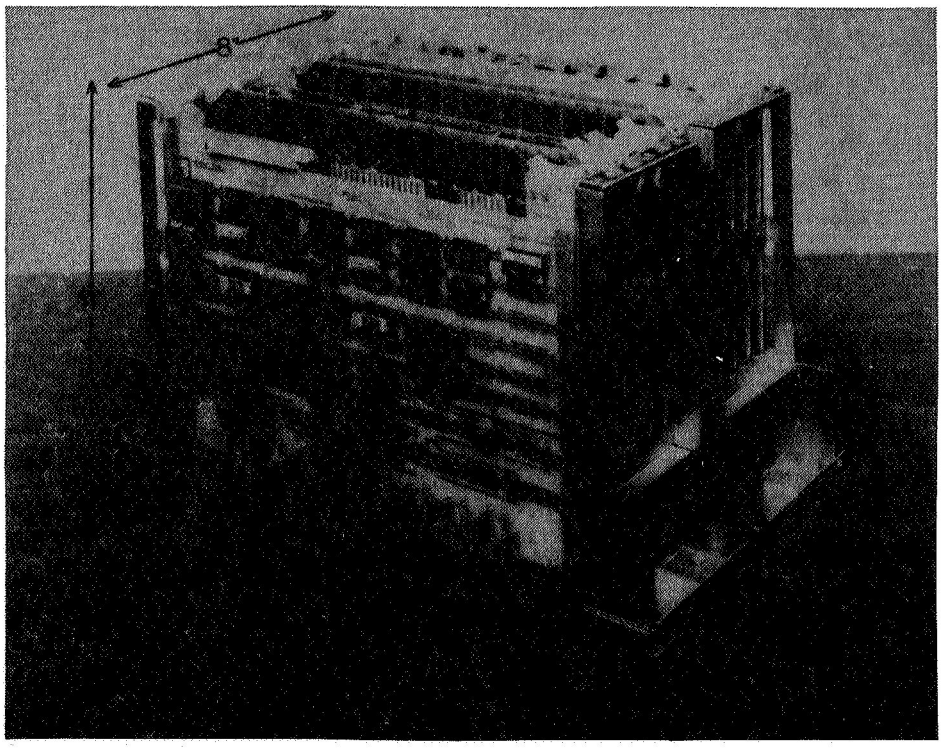

Figure 4

MICROPROCESSOR-BASED ORBIT DETERMINATION SYSTEM

DISADVANTAGES	ADVANTAGES
● LACK OF ADEQUATE SYSTEM SOFTWARE	● CHEAP HARDWARE
● MACHINE-LEVEL WORRIES	● SYSTEM PORTABILITY
● HARDWARE HEADACHES (IN GENERAL, BUT NOT IN OUR CASE)	● FLEXIBILITY FOR HARDWARE ADDITIONS
● LACK OF RELATIVE SPEED AND ACCURACY	● CHIP AND/OR BOARD LEVEL MAINTENANCE AND MODIFICATION

Figure 5

HARDWARE CONFIGURATION AND DATA FLOW

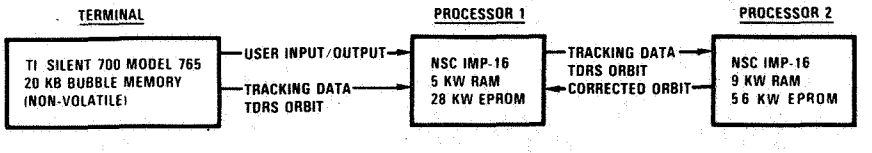

- STORAGE FOR TDRS POSITIONS AND VELOCITIES
- STORAGE FOR TRACKING DATA
- USER INTERFACE TO THE PROCESSORS

- TERMINAL COMMUNICATIONS
- DATA HANDLING

- ORBIT PROPAGATION
- SEQUENTIAL BATCH ESTIMATION

Figure 6

MATHEMATICAL MODELS

ORBIT PROPAGATOR

INTEGRATOR:

FEHLBERG RUNGE-KUTTA (4)

FORCE FIELD:

CENTRAL FORCE FIELD (EARTH)
UP TO 6×6 EARTH FIELD
HARRIS-PRIESTER ATMOSPHERIC DRAG

ORBIT ESTIMATOR

SOLVE FOR PARAMETERS:

TARGET SATELLITE POSITION AND VELOCITY

METHODS:

EXTENDED KALMAN FILTER
AND
BATCH LEAST SQUARES

OBSERVATION MODEL

OBSERVATIONS:

RANGE SUM
RANGE SUM RATE

MODEL:

ATS-6 (TDRS) SATELLITE-TO-SATELLITE TRACKING
LIGHT TIME CORRECTIONS TAKEN INTO ACCOUNT
ONLY ONE TRACKING SATELLITE VISIBLE AT ONE TIME

GROUND STATION

MODEL:

GEODETIC STATION MODEL

Figure 7

NUMERICAL ACCURACIES

- **SIGNIFICANT DIGITS**

IMP-16 FLOATING POINT PACKAGE	10 DIGITS
IBM FORTRAN IV	7 DIGITS FOR SINGLE PRECISION 17 DIGITS FOR DOUBLE PRECISION

- **GTDS COMPARISONS**

ORBIT PROPAGATOR

	IMP MICROPROCESSOR	IBM 360*
POSITION ERROR (METERS RMS)	91-116	32

OBSERVATION MODEL

	IMP MICROPROCESSOR	IBM 360*
RANGE SUM (KM)	.9	.24
RANGE SUM RATE CYCLES	6	.4

*SINGLE PRECISION USED WHENEVER POSSIBLE

GOO-10-78

Figure 8

BASELINE DIAGRAMS OF SOFTWARE

- SOFTWARE DEVELOPED USING HIGHER LEVEL LANGUAGE (SM/PL)
- FLOATING POINT PACKAGE USED FOR NON-INTEGER ARITHMETIC

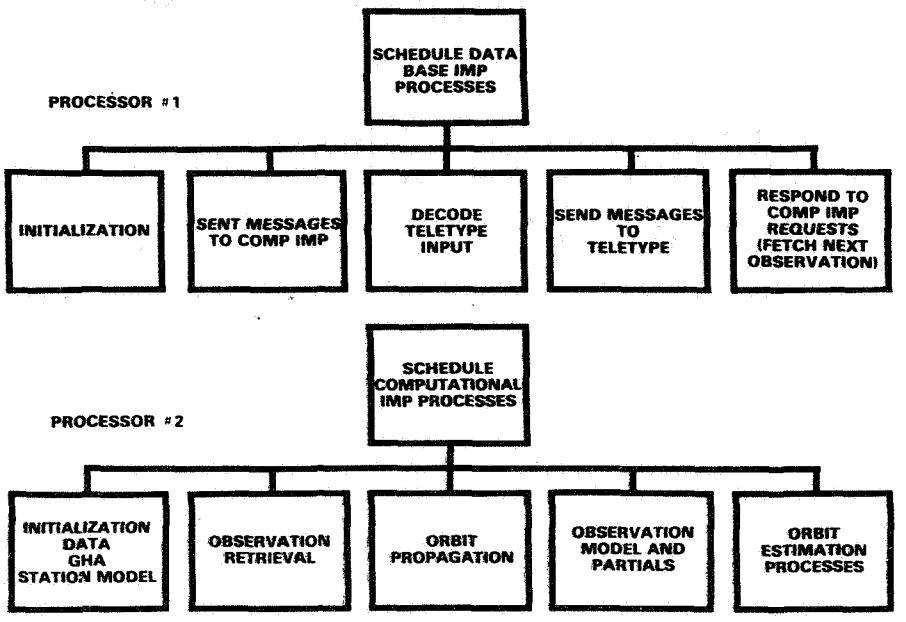

Figure 9

RESULTS OF MICROPROCESSOR SYSTEM DEVELOPMENT

- DEMONSTRATED USING SOPHISTICATED COMPUTATIONAL MODELS ON MICROPROCESSORS
- DEMONSTRATED USE OF HIGHER LEVEL LANGUAGE, BUT FURTHER WORK ON SYSTEM SOFTWARE IS NEEDED
- DEMONSTRATED PRACTICALITY OF USING SEPARATE MICROPROCESSORS (CPU's) TO PERFORM INDIVIDUAL FUNCTIONS
- SPEED AND MEMORY REQUIREMENTS FOR ORBIT DETERMINATION PROBLEM APPEARS NOT TO BE A PROBLEM; ACCURACY IS THE REAL PROBLEM

Figure 10

FUTURE CONSIDERATIONS

- **DATA PREPROCESSOR AND POSTPROCESSOR**

  ACCEPT RAW TRACKING DATA, DETERMINE ORBIT AND STORE THE RESULTS ON A USER PERIPHERAL DEVICE

- **HARDWARE RECONFIGURATION**

  USE BATCH AND SEQUENTIAL FILTER IN PARALLEL

- **GRARR TRACKING DATA PROCESSING**

  ACCEPT RANGE, RANGE RATE, AND ANGLE MEASUREMENTS FROM CONVENTIONAL TRACKING

- **SOLVE FOR BOTH TARGET AND TDRS ORBITS**

Figure 11

ON-BOARD DATA PROCESSING FOR APPLICATIONS SATELLITES

G. Morduch—Old Dominion Systems, Inc.
P. Argentiero—NASA Goddard Space Flight Center
J. Lefler—Old Dominion Systems, Inc.

ABSTRACT

With recent advances in microcomputer technology, on board data reduction for orbit determination is now feasible. On-board data processing would be advantageous for a class of satellite applications which involve a one way Doppler positioning system. Examples are the Nimbus-RAMS system, satellite aided search and rescue, and coastal surveillance in support of the newly imposed 200 mile fishing limit. Orbit determination requirements for these systems are typically in the region of 1 km.

This paper presents a proposal for on-board orbit determination which would rely entirely on reference beacons located within continental United States. The beacons would emit a one way Doppler signal in which is encoded coordinates of the beacon's location. An on-board computer would process the signal and update the satellite ephemeris. When a Doppler signal external to the system is received, the problem is inverted in the sense that the satellite ephemeris is considered as known and the coordinates of the Doppler signal source are estimated and transmitted to the ground. The feasibility of this concept is dependent on the possibility of developing algorithms which are at once compatible with limitations of on-board computers and accurate enough to maintain an adequate satellite ephemeris.

A conventional batch-processing filter is not ideal for this application because of its data storage requirements. Another problem associated with batch-processing of satellite tracking data is that errors in the models of satellite dynamics are such that in order to achieve acceptable accuracies the time span of the data must be limited. A recursive filter appears to be a more logical choice. But conventional recursive processing schemes such as the usual form of the Kalman filter, which do not explicitly account for dynamic modeling errors, encounter similar difficulties. In this case, the problem manifests itself through the computed covariance matrix of the estimate reducing towards zero. This in turn results in new measurement information being effectively ignored. Consequently, measurement residuals will increase, manifesting the well-known Kalman filter divergence phenomenon.

The filter used to generate the results of this paper is recursive from one pass of Doppler data to the next. However, each pass is processed in a conventional batch mode. A "state noise" covariance matrix is added to the computed covariance matrix of the estimate at each step in the recursion, thus preventing the eigen values of the matrix from approaching zero. The form of the state noise covariance matrix is chosen from a priori mathematical considerations and then modified by a multiplicative constant obtained from an examination of residuals. The resulting algorithm is sufficiently simple that it can be implemented on a small computing machine.

Numerical simulations were performed to test the validity of the procedure. Reference beacons were situated at Portsmouth, New Hampshire and San Francisco, California. Epoch elements for a typical TIROS-N orbit were utilized. Data was generated using a 13 x 13 degree reference field. A random number generator added white noise of standard deviation 1 m/sec. The data was reduced using a modified 4 x 4 degree field. Maximum observed position errors were less than 1 km. The same procedure was implemented for real data obtained from Nimbus reference beacons with comparable results.

ON-BOARD ORBIT DETERMINATION FOR APPLICATIONS SATELLITES

G. E. Morduch*, P. D. Argentiero**,
J. G. Lefler*

*Old Dominion Systems, Inc., Gaithersburg, MD 20760
**NASA/Goddard Space Flight Center, Greenbelt, MD 20771

Introduction

With recent advances in the technology of low power, low weight computers, on-board data reduction for orbit determination is now feasible [1,2]. On-board data processing would be advantageous for a class of satellite applications which involve a one-way Doppler positioning system. Examples are the NIMBUS-RAMS system [3], satellite aided search and rescue [4,5], and coastal surveillance in support of the newly imposed 200 mile fishing limit [6]. Orbit determination accuracy requirements for these systems are typically in the region of 1 km.

An examination of the NIMBUS-RAMS system provides insight into the possible usefulness of on-board orbit determination and data processing. Typically, 10 to 15 one-way Doppler measurements from each of up to 50 sources are recorded on the NIMBUS-6 and telemetered on command to a control station such as NASA-Fairbanks, Alaska. The data is then relayed to a central computer at the Goddard Space Flight Center. With the aid of ephemeris information obtained from independent tracking, the data is processed and the results transmitted to individual users. The delay time is several days. The need for faster response has been expressed by several members of the user community. Also, future applications of the satellite Doppler positioning concept (coastal surveillance, satellite aided search and rescue) will require near real time signal processing.

The need for rapid signal processing could be satisfied if tracking data were processed on-board a satellite. In that case ephemeris information based on fresh tracking data would be available at all times to the satellite's computer. Hence a Doppler signal received by the satellite could be processed by the on-board computer and the resulting position estimate transmitted to the ground. Very low telemetry data rates are adequate to transmit position information. With low data rates, the use of omnidirectional or low-gain, wide-beam-width antennas becomes possible and costs are reduced by simplifying the antenna array and antenna drive assembly. Low data rates also permit the use of a geostationary satellite system such as the Tracking and Data Relay Satellite System [7] to relay information to inexpensive receiver terminals. Another significant fact is that the number of Doppler signal sources monitored per satellite pass can be significantly increased as a consequence of the relatively low bit allocation required for each position determination.

This paper presents a proposal for on-board orbit determination which would rely entirely on reference beacons located within the Continental United States. The beacons would emit a signal in which is encoded coordinates of the beacon's location. An on-board computer would process the signal and update the satellite ephemeris. When a Doppler signal external to the system is received, the problem is inverted in the sense that the satellite ephemeris is considered as known and the coordinates of the Doppler signal source are estimated and transmitted to the ground. The feasibility of this concept is, of course, dependent on the possibility of developing algorithms which are at once compatible with the limitations of on-board computers and accurate enough to maintain an adequate satellite ephemeris. This paper recommends a filter which is recursive on a pass-by-pass basis and which has a fading memory to account for the degrading effect of gravity field error. The recursive filter requires the storage of only one pass of data at a time, and hence is suitable for on-board computers with limited storage capacity. The mathematical details are described in the succeeding sections. The paper also provides the results for simulated data and real data reductions as well as suggestions for further analysis and development of these concepts.

A Recursive Filter for Satellite State Estimation

Let $\{Z(T_i)\}_{i\leq N}$ be a set of Doppler passes with each pass referenced to a time T_i which may be taken as the time for the first observation in the pass. Assume that observation set $\{Z(T_i)\}_{i\leq N}$ has been processed to yield a minimum variance estimate, $\delta\hat{X}(T_N)$, of the deviation, $\delta\tilde{X}(T_N)$, of the satellite state at time T_N from a nominal orbit. Data pass $Z(T_{N+1})$ is to be combined with $\delta\hat{X}(T_N)$ in a way which yields a sufficiently accurate estimate, $\delta\hat{X}(T_{N+1})$, of $\delta\tilde{X}(T_{N+1})$. Furthermore, the resulting algorithm is to be compatible with small computing machines.

Assume a linear state transition equation

$$\delta\tilde{X}(T_{N+1}) = \phi(T_{N+1}, T_N)\ \delta\tilde{X}(T_N) + \tau_{N+1} \qquad (1)$$

where $\phi(T_{N+1}, T_N)$ is a six-by-six state transition matrix and where τ_{N+1} is a six dimensional

state noise random vector. Equation 1 is assumed to be referenced to a standard inertial coordinate set. Define

$$E(\delta\hat{X}(T_N)\ \delta\hat{X}^T(T_N)) = P_N \tag{2}$$

Before the data set, $Z(T_{N+1})$, is processed, the optimal estimate of $\delta\tilde{X}(T_{N+1})$ is obtained from Equation 1.

$$\delta\hat{X}^-(T_{N+1}) = \phi(T_{N+1},T_N)\ \delta\hat{X}(T_N) \tag{3}$$

Hence

$$E\left(\delta\hat{X}^-(T_{N+1})\ \delta\hat{X}^{-T}(T_{N+1})\right) = P_{N+1,0} = \phi(T_{N+1},T_N)\ P_N\phi^T(T_{N+1},T_N) = \Delta P_{N+1} \tag{4}$$

where

$$E(\tau_{N+1}\tau^T_{N+1}) = \Delta P_{N+1} \tag{5}$$

Define a linearized observation equation as

$$\delta\tilde{Z}(T_{N+1}) = A_{N+1}\delta\tilde{X}(T_{N+1}) \tag{6}$$

where $\delta\tilde{Z}(T_{N+1})$ represents a vector of deviations of the noiseless or correct representations of the data from nominal values. Since the data are corrupted by noise, we have

$$E\left(\left(\delta Z(T_{N+1})-\delta\tilde{Z}(T_{N+1})\right)\left(\delta Z(T_{N+1})-\delta\tilde{Z}(T_{N+1})\right)^T\right) = Q \tag{7}$$

Given Equations 1 through 7, a minimum variance estimate of $\delta\tilde{X}(T_{N+1})$ is

$$\delta\hat{X}(T_{N+1}) = (A^TQ^{-1}A+P^{-1}_{N+1,0})^{-1}(A^TQ^{-1}\delta Z(T_{N+1}) + P^{-1}_{N-1,0}\delta\hat{X}^-(T_{N+1})) \tag{8}$$

and

$$E\left((\delta\hat{X}(T_{N+1})-\delta\tilde{X}(T_{N+1}))(\delta\hat{X}(T_{N+1})-\delta\tilde{X}(T_{N+1}))^T\right) = P_{N+1} = (A^TQ^{-1}A+P^{-1}_{N+1,0})^{-1} \tag{9}$$

It remains to specify how the covariance matrix, ΔP_{N+1} of τ_{N+1}, is obtained. To generate the results of this paper, the following assumptions are imposed:

A. Components of τ_{N+1} are uncorrelated in the instantaneous along-track, cross-track, and radial coordinate set.
B. Along-track, cross-track, and radial components of τ_N for both position and velocity are in the ratio of 10:5:2.
C. The along-track position component of τ_{N+1} is a linear function of $T_{N+1}-T_N$.
D. The along-track velocity component of τ_{N+1} is three orders of magnitude less than the along-track position component of τ_{N+1}.

Under assumptions A through D, one can write

$$\tau_{N+1} = \psi(T_{N+1})D(T_{N+1}-T_N)x_{n+1} \tag{10}$$

where x_{n+1} is the along-track state noise per unit time, D is a diagonal matrix with diagonal elements (1, .5, .2, 10^{-3}, $.5(10)^{-3}$, $.2(10)^{-3}$), and $\psi(T_{N+1})$ is a rotation matrix which transforms satellite state from an along-track, cross-track and radial coordinate set at time T_N to a standard inertial coordinate set. From Equation 10 we have

$$\Delta P_{N+1} = \left(\sigma_x(T_{N+1}-T_N)\right)^2\psi(T_{N+1})DD^T\psi^T(T_{N+1}) \tag{11}$$

where σ_x is the standard deviation of x_{n+1}. The value of σ_x can be chosen based on a priori considerations or it can be chosen adaptively from previous residuals. Adaptive algorithms based on a maximum likelihood principal [8], or on a minimum variance principal [9] are available and can be implemented on small computers.

A more empirical approach to the problem is to account for the effect of errors in the propagation model in terms of an exponential process.

$$P_{N+1,0} = \left(\phi(T_{N+1},T_N)P_N\phi^T(T_{N+1}T_N)\right) \exp\left((T_{N+1}-T_N)/g_{N+1}\right) \tag{12}$$

The value of g_{N+1} can then be chosen by adaptive techniques.

Both the exponential approach of Equation 12 and the additive approach implied by Equations 11 and 4 were implemented for the real and simulated data reductions discussed in this paper. A totally automated adaptive procedure was not implemented. Instead, the data reductions were performed for numerous values of both σ_x of Equation 11 and g_{N+1} of Equation 12 and the values which maximized performance were chosen.

Data Simulations

In order to test the adequacy of the proposed procedure for data processing, the following simulations were performed.

(i) Simulated data (see Figure 1) of range rate were generated for two stations (Portsmouth, N.H. and San Francisco, Ca.) relative to a satellite with the orbital characteristics of the TIROS-N satellite (see Table 1). The number of passes during which the satellite observed the transmitting stations is shown in Table 2. The satellite orbit was computed using a Goddard Earth Model gravity field [10] truncated to 13 x 13. The simulated measurements were corrupted by the addition of random gaussian noise with a standard deviation of 0.5 meters/second. The choice of a 13 x 13 field was predicated on the assumption that the difference between the 13 x 13 field and that of the real earth would be negligible in comparison with the difference between the 13 x 13 field and the field used in the subsequent orbit recovery.

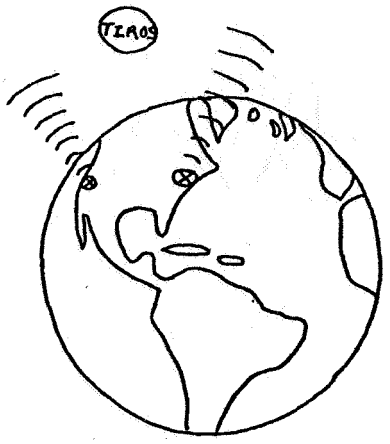

Figure 1. Data Simulation Configuration
Two transmitting stations:
(1) San Francisco, Ca
(2) Portsmouth, NH
TIROS-N IN NEAR POLAR ORBIT WITH A PERIOD OF 100 MIN.

TABLE 1. Orbital Characteristics of TIROS-N

Semi-Major Axis: 7200 KM
Eccentricity: 0.000002
Inclination: 98.7°
Period: 100 Min.

TABLE 2. Number of Observed Passes In The Data Simulations

	0-8 Hr.	8-16 Hr.	16-24 Hr.	Total
DAY 1	1	4	3	8
DAY 2	1	4	3	8
DAY 3	1	4	3	8
DAY 4	2	4	2	8
DAY 5	2	4	3	9
DAY 6	1	5	3	9
DAY 7	1	4	3	8
DAY 8	2	4	2	8
DAY 9	2	4	2	8
DAY 10	2	4	3	9

(ii) Two different fields were used in the orbit recovery: field I, a field containing only the J_2 harmonic coefficient and field II, a 4 x 4 field. The non-zero coefficients of fields I and II differed slightly from the corresponding coefficients of the 13 x 13 field. The filtering algorithm described in the preceding section was implemented to estimate orbits. The resulting orbits were then compared with the orbit used in the data generation. The results are summarized in Figures 2 through 4.

Figure 2 shows the results for the J_2 field, with the covariance matrix of the state noise, as defined in Equation 5, arbitrarily set to zero. As can be seen, the error, which initially is very large, has been substantially reduced by the end of the first day. The error then starts growing. This is caused by force model errors which are not accounted for when the presence of state noise is ignored. The results of Figure 3 were also obtained using a J_2 field but the state noise covariance matrix was obtained from Equation 11 by setting σ_x = 4 M/HR. These results are a substantial improvement over those shown in Figure 2. Figure 4 shows that more impressive results can be obtained with a 4 x 4 geopotential field with σ_x = 2 M/HR. It is also important to notice the long term stability of the filter when the effects of state noise are appropriately modeled. Comparable results were obtained using the exponential model of Equation 12 with g_{n+1} = 2 days.

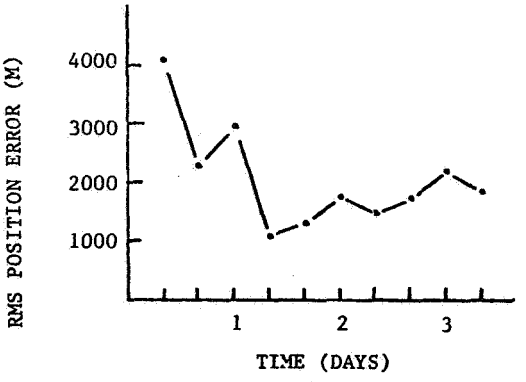

Figure 2.
Satellite Position Error
Recovery Field Includes Only the J_2 Harmonic
TIROS-N Simulated Data
σ_x = 0 M/HR

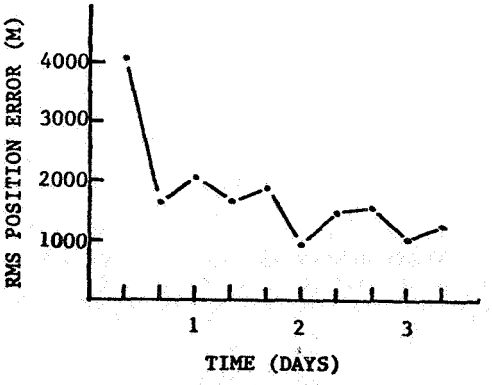

Figure 3.
Satellite Position Error
Recovery Field Includes Only the J_2 Harmonic
TIROS-N Simulated Data
σ_x = 4 M/HR

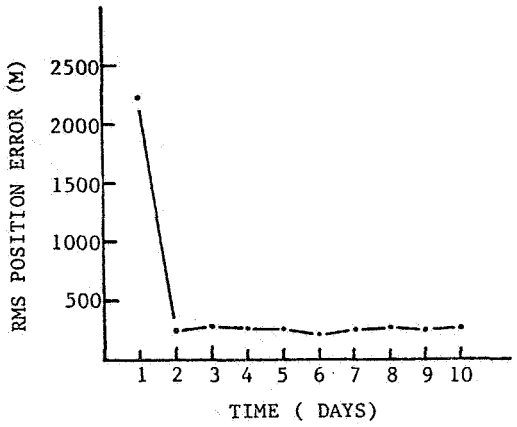

Figure 4.
Satellite Position Error
4 x 4 Recovery Field
TIROS-N Simulated Data
σ_x = 2 M/HR

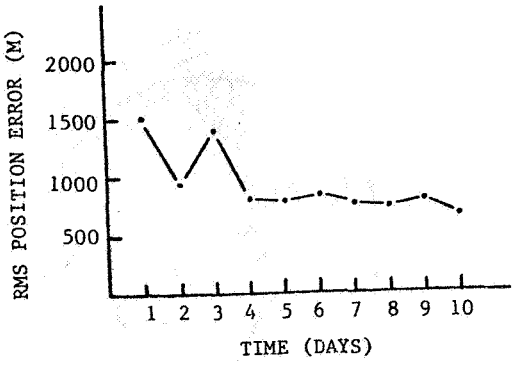

Figure 5.
Satellite Position Error
4 x 4 Recovery Field
NIMBUS-6 Doppler Data
σ_x = 0.5 M/HR

Reduction of NIMBUS-6 Doppler Data

The orbit/transmitter station geometry for the NIMBUS-6 real data reduction experiment was similar to that used in the TIROS-N simulations. The NIMBUS-6 orbit constants are given in Table 3. Data from two transmitter stations were used in the NIMBUS-6 orbit recovery, one station being located at Fairbanks, Alaska and the other one at Goddard Space Flight Center, Maryland. The nominal transmission frequency was 401.2 MHz for both stations. A gravity field complete through order 4 was used in the real data reduction. Data for the first ten days of June, 1977 were processed using the previously described recursive filter.

The NIMBUS-6 orbit, determined as part of this study, was compared with an independently derived orbit based on Mini-track observations processed at GSFC, which has a claimed accuracy of about 500 meters. The orbit position differences shown in Figure 5 are less than 1 km RMS from the third day onward. As in the case of the simulated results, the filter's performance displays both accuracy and long term stability. The number of passes of Doppler data used in the recovery is shown in Table 4. The noise in the Doppler data was approximately 1 m/s RMS. Data corresponding to elevation angles below 5 degrees were ignored. The data were not corrected for atmospheric refraction. The state noise covariance was chosen from Equation 11 with σ_x = 0.5 M/HR. This constant was selected after a few trial runs. No attempt was made to fine tune the system. Comparable results were obtained with the exponential model with g_{n+1} = 5 days.

In reducing the NIMBUS data, the oscillator bias and the bias drift rate were recovered for each transmitter. For the bias model constants actually used, the effective unmodeled drift rate contribution to the bias is shown in Table 5.

TABLE 3. Orbital Characteristics of NIMBUS-6
Semi-Major Axis: 7490 KM.
Eccentricity: .001
Inclination: 99.9°
Period: 107 MIN.

TABLE 4. Number of Passes Used in the Real Data Reduction

	0-6 HR	6-12 HR	12-18 HR	18-24 HR	Total
DAY 1	0	2	3	1	6
DAY 2	1	1	3	1	6
DAY 3	0	2	2	1	5
DAY 4	1	3	3	1	8
DAY 5	2	1	4	3	10
DAY 6	1	4	3	2	10
DAY 7	2	1	2	2	7
DAY 8	1	2	3	3	9
DAY 9	0	3	1	1	5
DAY 10	0	0	4	1	5

TABLE 5. Growth of Bias Uncertainty as a Function of Time

Time From Last Determination of Bias (Hours)	Standard Deviation of Bias Uncertainty (M/S)
1	0.5
2	1.4
4	4.0
8	11.3

Conclusions

For a class of satellite applications which involve a one-way Doppler positioning system, on-board orbit determination would be advantageous. This paper has presented a proposal for on-board orbit determination which would rely entirely on reference Doppler beacons located within the Continental United States.

To demonstrate the feasibility of this concept it is necessary to develop algorithms which are compatible with small computing machines and sufficiently accurate to maintain an adequate satellite ephemeris. The simulations and real data reductions discussed in this paper suggest that an on-board computer equipped with a recursive filter with a fading memory to account for dynamic modeling errors, and two reference beacons, are adequate for the task.

The filter should include a gravity field model with geopotential coefficients complete to degree and order 4. The fading memory characteristics of the filter can be set in advance based on a priori simulations and real data reductions. An alternative possibility is to equip the filter with a feedback mechanism by which the memory would become a function of previous residuals. Several such procedures have been discussed in the literature. The core storage requirements of the resulting algorithms should be compatible with on-board computers.

References

1. Schmid, P.E., Lynn, J. J., "Satellite Doppler Data Processing Using a Microcomputer", NASA TM 78046, December 1977.

2. Hilburn, J. L., Julich, P.M., "Microcomputers/Microprocessors: Hardware, Software and Applications", Prentice-Hall, Inc. Englewood Cliffs, N.J., 1976.

3. Gree, T., "Satellite Doppler Data Processing for Platform Naviagion", IEEE Transactions on Geoscience Electronics, Vol. GE.13, November, 1974.

4. Committee on Aeronautical and Space Sciences, United States Senate, 93rd Congress. First Session, "Toward a Better Tomorrow with Aeronautical and Space Technology", U.S. Government Printing Office, 1973.

5. Schmid, P., Lynn, J., Vonbun, F.O., "Single Pass Doppler Positioning for Search and Rescue Satellite Missions". Presented at IEEE Position Location and Navigation Symposium, San Diego, California, November 1-3, 1976.

6. Satellite Data Collection Newsletter, October 1977, No. 4.

7. Teles, J., Ayres, C., "Advanced Spacecraft Tracking Techniques Using the Tracking and Data Relay Satellite System", presented at the AAS/AIM Astrodynamics Conference, Sept. 7-9, 1977, Grand Teton National Park, Wyoming.

8. Jazwinski, A.H., "Adaptive Filtering in Satellite Orbit Estimation", Conference Record of Second Asilomar Conference on Circuits and Systems, pp. 153-158, Pacific Grove, California, October 1968.

9. Argentiero, P., "Adaptive Filtering with Correlated State Noise", NASA X-551-72-394, October 1972.

10. Lerch, F.J., Kloski, S.M., Laubscher, R.E., "Gravity Model Improvement Using GEOS-3 (GEM 9 & 10)", presented at the Spring meeting of the American Geophysical Union, May 31, 1977, Washington, D.C.

A COMPARISON OF FILTERING ALGORITHMS FOR GPS SATELLITE NAVIGATION APPLICATION

B. D. Tapley, J. G. Peters, and B. E. Schutz

Aerospace Engineering and Engineering Mechanics
University of Texas

ABSTRACT

The limited word size proposed for the GPS navigation computers could precipitate the problem of filter divergence in a standard sequential estimation algorithm. To insure filter reliability during the periods when the GPS observations are being processed, a square-root filter algorithm has been adopted for the GPS navigation computer. Several formulations of square-root filtering algorithms have been developed during the past fifteen years. In implementing the filters, the covariance matrix can be propagated by either integrating the state transition matrix or by integrating a differential equation for the square root of the covariance matrix. The various approaches have different characteristics with regard to computer execution time, accuracy of the estimate, computer storage requirements, and the effort required to code and validate the algorithm. In this investigation the Potter, Carlson-Cholesky, and UDU square-root filters are compared with the standard extended Kalman filter. The characteristics of the algorithms are compared by simulating the application of a phase one GPS system to the determination of a LANDSAT-D Satellite.

A COMPARISON OF FILTERING ALGORITHMS FOR GPS SATELLITE NAVIGATION APPLICATION

B. D. Tapley[1], J. G. Peters[2], B. E. Schutz[3]

The Universtiy of Texas at Austin

INTRODUCTION

The limited word size used in contemporary microprocessor design may lead to problems in autonomous satellite navigation applications. The numerical error introduced when the navigation computations are performed with a short wordlength computer can lead to divergence of a standard extended sequential estimation algorithm. To insure filter reliability for applications where GPS observations are being processed, a square root filter algorithm has been adopted for the GPS navigation computer. Several formulations of square root filtering algorithms have been developed during the past fifteen years. This investigation describes a preliminary comparison of three square root filter formulations with the standard extended Kalman filter. Initial results are obtained regarding the relative computation speed and accuracy of these algorithms in a simulation of LANDSAT-D navigating with a Phase I GPS constellation.

This summary is an overview of results obtained in the study. A complete discussion of the simulation procedure and numerical results can be found in [1].

---

† The research was supported by the National Aeronautics and Space Administration at Goddard Space Flight Center under Grant No. NSG 5154.

[1] Professor, Department of Aerospace Engineering and Engineering Mechanics.

[2] Research Assistant, Department of Aerospace Engineering and Engineering Mechanics.

[3] Associate Professor, Department of Aerospace Engineering and Engineering Mechanics.

ALGORITHMS CONSIDERED

The algorithms compared in this initial study are listed in Table 1. They are classified according to one of four ways of representing the state error covariance matrix and one of two methods of time propagation of this covariance matrix.

The four methods of covariance representation are, briefly:

1. standard Kalman formulation [2],
2. the UDU algorithm [5], which decomposes the state error covariance into an upper unitary matrix, U, a diagonal matrix, D, and U^T,
3. the Carlson-Cholesky algorithm [4], in which the covariance is decomposed into an upper or lower triangular matrix, W, and its transpose W^T; and
4. the Potter algorithm [3] which decomposes the covariance into a general nxn square root covariance S and its transpose, S^T.

The two methods of performing time updates of the covariance are referred to as the transition matrix method and the direct integration method. In the former technique, a system of variational equations is integrated from one measurement epoch to the next, to obtain a transition matrix. The time update of the covariance is performed by the proper multiplication of the covariance by the transition matrix and by the addition of process noise. The process noise matrix is obtained in this study by an approximate analytic integration of a diagonal spectral level density matrix. The direct integration methods involve the numerical integration of the state error covariance matrix directly. Direct integration is often considered for time propagation because, in general, fewer equations must be integrated between observation epochs (n(n+1)/2 versus nxn for transition matrix methods). For

square root algorithms which use a transition matrix method, the inclusion of process noise at each measurement epoch requires a retriangularization of the square root covariance matrix. This extra computational burden is avoided in the direct integration methods as the process noise effects are included directly in the integration of the differential equations.

The direct integration algorithm for the Potter filter requires an nxn matrix inversion at each integration step. As a result of the extreme numerical penalty resulting from the inversion operation, a directly integrated Potter algorithm is not considered.

OBSERVATION SIMULATION PROCEDURE

The filter algorithms were tested using a series of simulated range and range-rate observations made from the LANDSAT-D satellite to navigation satellites of a Phase I GPS constellation. The structure of the dynamic models used in the simulation of the observations is outlined in Table 2. The dynamic model of the motion of LANDSAT-D includes the geopotential effects of a non-spherical earth and the effects of atmospheric drag. The geopotential model used is GEM7 truncated to order and degree 8. The drag on the satellite is modeled as the function of a ballistic coefficient, the atmospheric density and the square of the user's velocity relative to the atmosphere. The atmospheric density is determined from an exponential density model.

In the observation simulation model, the GPS satellites are assumed to be in two-body circular orbits about a point mass earth. No other perturbations are assumed to affect them.

TABLE 1

ALGORITHMS COMPARED

Transition Matrix Methods:

- EKF($\dot{\Phi}$)
- UDU($\dot{\Phi}$)
- CARLSON-CHOLESKY($\dot{\Phi}$)
- POTTER($\dot{\Phi}$)

Direct Integration Methods:

- EKF($\dot{P}$)
- UDU($\dot{U}\dot{D}$)
- CARLSON-CHOLESKY($\dot{W}$)

TABLE 2

OBSERVATION SIMULATION MODEL

User Model:

- 8 × 8 Geopotential (GEM7)
- Atmospheric Drag
- Clock Errors

GPS Satellites Model:

- Two-Body Propagation Model
- Clock Errors

The performance of the user's clock and the GPS satellites' clocks are important factors in determining potential navigation accuracy. The phase error for each of the clocks is modeled in the simulation as the sum of three terms:

1. a deterministic phase error modeled as a first-order polynomial,
2. the integral of an exponentially correlated frequency error, and
3. a random walk phase error.

The frequency error of each clock is the sum of derivatives of the first two terms of the phase error.

Initial conditions for the Phase I GPS and for LANDSAT-D are shown in Table 3 and Table 4, respectively. The true anomaly of LANDSAT-D and the difference in the epoch times of the orbital elements can be varied to alter the pattern of GPS satellites visible from LANDSAT-D. The LANDSAT-D epoch elements are specified at a GPS system time of $t = 0$. The GPS epoch elements are specified at a GPS system time of -7200 seconds.

Given these initial conditions, and given the dynamic models described previously, the history of GPS satellite visibility shown in Figure 1 was generated. Over the 21,500 sec. simulation period, the number of GPS satellites visible to LANDSAT-D varies from zero to six. From this visibility history, a set of simulated range and range-rate observations was determined for processing by the navigation simulation program. The observations were generated on the CDC6600/6400 system at the University of Texas at Austin.

TABLE 3

PHASE I GPS CONFIGURATION

Satellite	Long. of Asc. Node (Deg.)	Mean Anomaly (Deg.)
1	-130.	0.
2	-130.	40.
3	-130.	80.
4	110.	40
5	110.	80.
6	110.	120.

Inclination: 63°

Eccentricity: 0.0

TABLE 4

LANDSAT-D EPOCH ORBITAL ELEMENTS

$a \equiv 7.086901 \times 10^6$ m

$e \equiv 0.001$

$i \equiv 98\overset{\circ}{.}181$

$\Omega \equiv 354\overset{\circ}{.}878$

$\omega \equiv 180\overset{\circ}{.}$

f(true anomaly) $\equiv -185\overset{\circ}{.}$

FIGURE 1

GPS SATELLITE VISIBILITY VS TIME

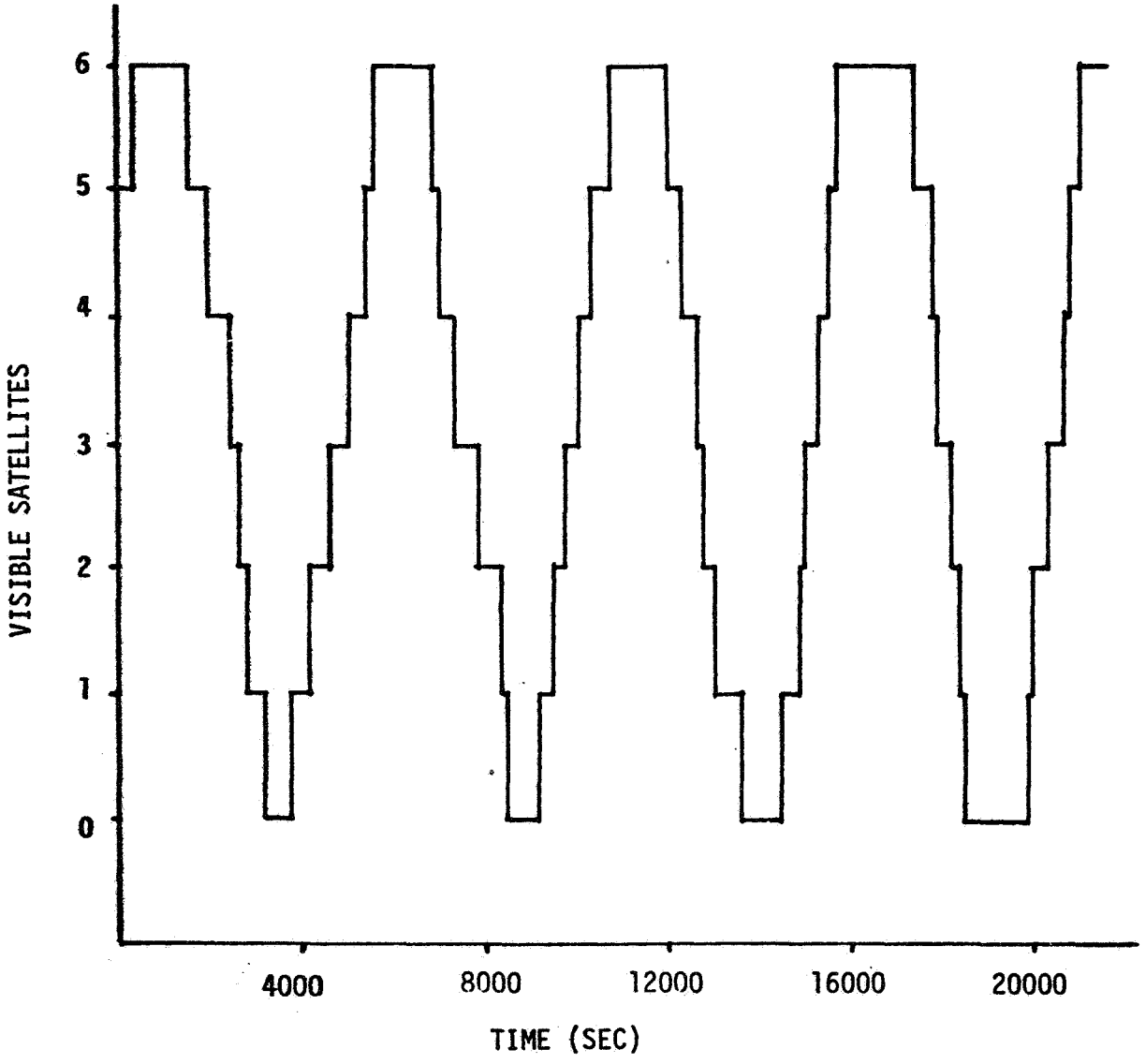

FILTER STRUCTURE

The limited size of satellite on-board computer necessitates the use of simplified dynamic models in the navigation filter. Table 5 shows the dynamic model structure assumed by the filter for the user satellite and for the GPS satellites.

The geopotential affecting the user satellite is of lower degree and order than that used to generate the simulated observations. The drag acceleration calculation uses an exponential model of atmospheric density, as does the observation generation program, but the ballistic coefficient of the user satellite is estimated. The bias of the user's clock at a given time is predicted by a linear equation. The coefficients of this equation, the clock bias and drift at an epoch, are estimated. The estimation of the ballistic coefficient and of the clock parameters attempts to account for modeling errors caused by the reduced size of the filter's geopotential.

The filter prescribes a two-body point mass geopotential as the dynamic model for the GPS satellites. Each GPS satellite's clock bias is predicted between observation epochs by a linear equation whose coefficients are predetermined to fit the clock's error behavior. For these simulations, the clock coefficients have been set to zero. This implies that the filter assumes perfect GPS clocks. Therefore, timing errors from all sources are accounted for in the estimation of the user's clock coefficients.

Preliminary simulations have been performed with an eleven-state navigation filter. The differential equations of the states are shown in Table 6. The eleven states are: position (1-3), velocity (4-6), ballistic coefficient (7), drag correlation parameter (8), user clock bias (9), user clock drift (10), and clock drift correlation parameter (11). Important

TABLE 5

FILTER SIMULATION MODEL

User Model:

- 4 × 4 Geopotential (GEM7)
- Atmospheric Drag (Ballistic Coefficient Estimated)
- Clock Error Polynomial (Coefficients Estimated)

GPS Satellites Model:

- Two-Body Propagation Model
- Clock Errors (Predetermined Coefficients)

TABLE 6

FILTER DIFFERENTIAL EQUATIONS

11-STATE FILTER:

$\dot{\bar{r}} = \bar{v}$	(position)
$\dot{\bar{v}} = \bar{a}_g + \bar{a}_d + \xi_v$	(velocity)
$\dot{d} = -\beta_d\, d + \xi_d$	(ballistic coefficient)
$\dot{\beta}_d = \xi_{\beta_d}$	(drag correlation parameter)
$\dot{b}_\rho = b_{\dot{\rho}}$	(user clock bias)
$\dot{b}_{\dot{\rho}} = -\beta_{b_{\dot{\rho}}}\, b_{\dot{\rho}} + \xi_{b_{\dot{\rho}}}$	(user clock drift)
$\dot{\beta}_{b_{\dot{\rho}}} = \xi_{\beta_{b_{\dot{\rho}}}}$	(drift correlation parameter)

assumptions in the form of the differential equations are that the ballistic coefficient and user clock drift are first-order Gauss-Markov processes and that the correlation parameters of the Markov processes are random walks. Additionally, the user clock's bias is modeled as the integral of its drift.

Parameters in the forcing functions of the equations in Table 6 are the following:

$\bar{a}_g \equiv$ gravitational acceleration

$\bar{a}_d \equiv$ drag acceleration.

The $\bar{\xi}_i$ are white noise forcing functions with statistics

$$E[\bar{\xi}_i] = 0 \quad ; \quad E[\bar{\xi}_i \bar{\xi}_i^T] = Q_i$$

FILTER PERFORMANCE

Figures 2 and 3 are plots of position error magnitude and velocity error magnitude of the estimates versus time. Two trends in the error history are evident from the examination of the plots. Catastrophic increases in the error magnitudes occur during periods of poor satellite visibility (less than four satellites in view). A comparison of Figures 1, 2 and 3 reveals the correlation between satellite visibility and error magnitude. The peaks of these errors reach over one kilometer in position, and over 1 meter per second in velocity.

The second trend is observable by studying the long-term history of the errors. Although the errors decrease significantly when good satellite visibility is recovered, there is a long-term growth in the navigation error recorded during the periods of good visibility. As

FIGURE 2

RSS POSITION ERROR VS TIME

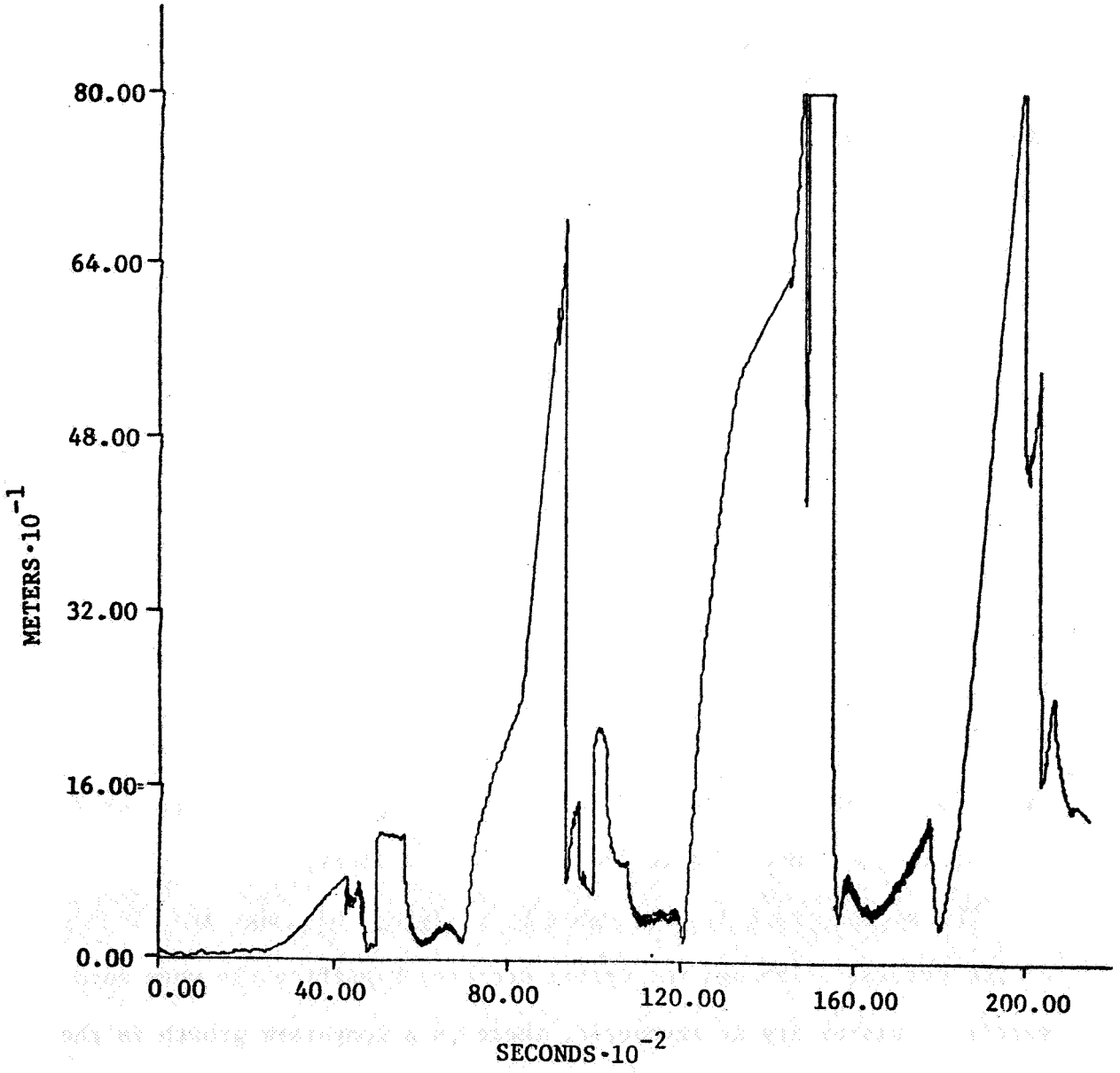

FIGURE 3

RSS VELOCITY ERROR VS TIME

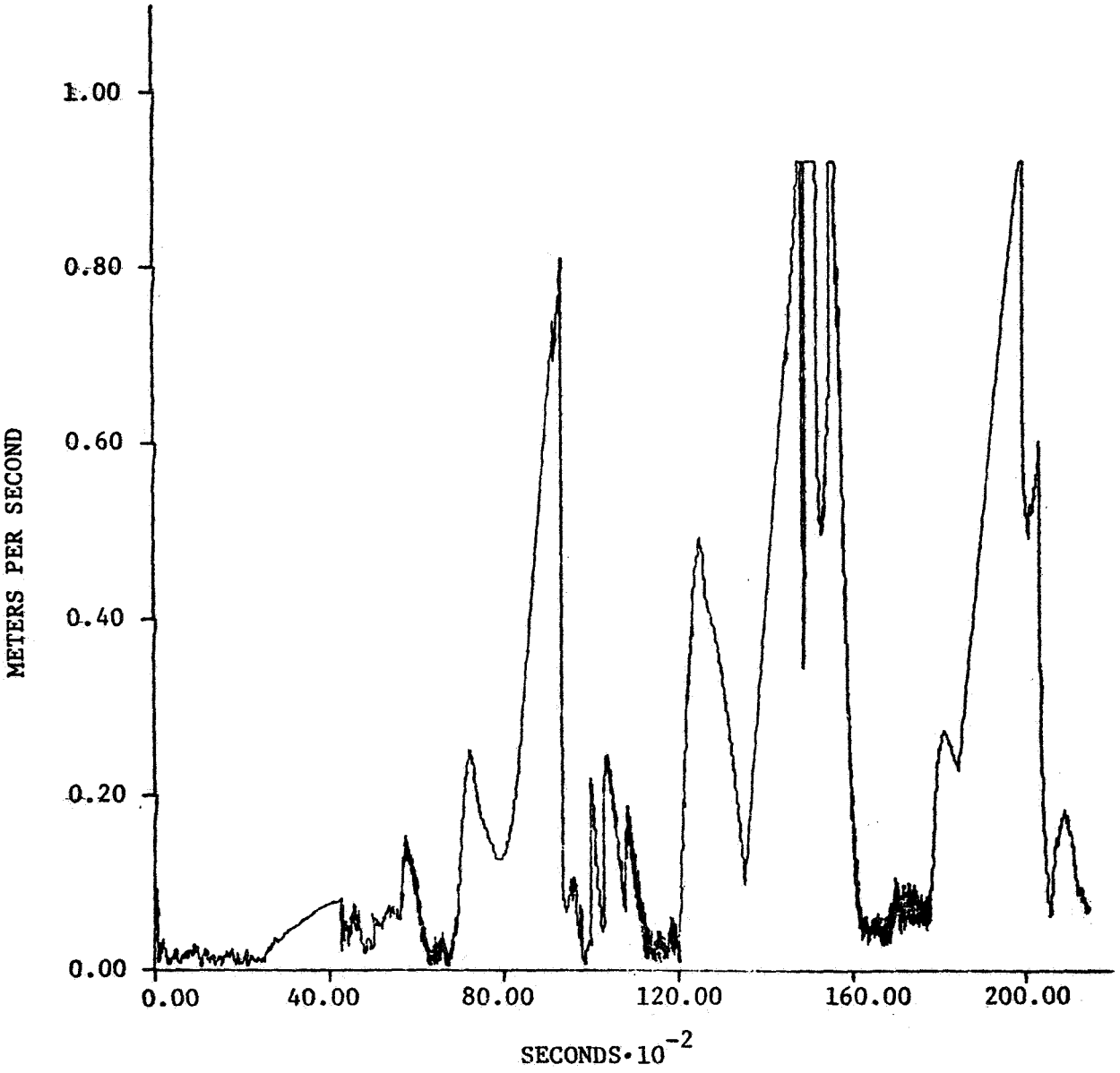

an example, the position error before the first period of poor satellite visibility is at or below the 20 meter level. After the third period of poor visibility (approximately 16,000 sec.) position error has grown to approximately 100 meters. This indicates a secular or long period trend in the position error. A similar trend exists in the history of the velocity error magnitude.

Although both error trends are significant and are deserving of further study, the goal of this investigation has been to consider relative efficiencies of different algorithms. Therefore, current simulations have not been directed toward the removal of the error problems. This is to be the topic of follow-on studies.

INITIAL NUMERICAL RESULTS

The time propagation and measurement update algorithms described in the previous sections were tested on the 21,500 sec. arc of observations, using four different numerical integration schemes. The four schemes are:

1) a variable step RK(7)8 with integration tolerances: absolute error = 10^{-6}, relative error = 10^{-10},
2) a variable step RK(2)4 with integration tolerances: absolute error = 10^{-2}, relative error = 10^{-6},
3) a fixed step RK8 with a step size of 6 seconds, and
4) a fixed step RK4 with a step size of 6 seconds.

Simulations with these integration algorithms are intended to establish bounds on errors for navigation computations performed on the CDC6600 system. The results of further studies using the lower order integrators proposed for the actual GPS computer can be compared to the results

shown here to determine the loss in navigation accuracy caused by using lower order integration methods.

Initial navigation simulations, using the different filter algorithms over the entire 21,500 sec. observation arc, produced position error histories nearly identical to that in Figure 2. Specifically, no algorithm reduced the catastrophic position error growth during the third data drop-out (approximately 12,000 sec.), or removed the long term error growth. Therefore, for the purpose of reducing computer use, the simulations for performance comparisons were run over the first 10,000 seconds of observations only.

The results of the initial set of simulations appear in Tables 7 through 10. The pertinent values tabulated are: the total computation time for time update, the total computation time for measurement update, the total computation time (the sum of time update and measurement update computation times), the total computation time normalized by the fastest total time, and the RMS error of the position estimate for the 10,000 seconds of data. All computation times are tabulated in milliseconds, and RMS errors are written in meters. The algorithms are listed in the order of increasing computation time.

The results for the different filtering algorithms can be compared on the basis of computation time, estimation accuracy, and algorithm stability. Briefly, a comparison of the algorithms reveals the following trends.

Computation Time

The computation times of the algorithms display the following general characteristics:

TABLE 7

RELATIVE ALGORITHM PERFORMANCE
RK(7)8 TOL: 10^{-6} - 10^{-10}

	COMP. TIME (msec)				ACC(m)
ALG	TIME UPDATE	MEAS UPDATE	TOTAL UPDATE	NORMED UPDATE	RMS POS ERR
EKF($\dot{\Phi}$)	160.601	9.435	170.036	1.000	128.4
UDU($\dot{\Phi}$)	172.119	17.621	189.740	1.116	128.7
POTT($\dot{\Phi}$)	179.924	17.585	197.509	1.162	95.0
CARL($\dot{\Phi}$)	173.760	24.968	198.728	1.169	95.0
EKF($\dot{P}$)	357.728	9.442	366.720	2.157	129.0
CARL($\dot{W}$)	390.763	24.772	415.535	2.444	128.9
UDU($\dot{U}\dot{D}$)	530.734	18.286	549.020	3.229	128.4

TABLE 8

RELATIVE ALGORITHM PERFORMANCE
RK(2)4 TOL: 10^{-2} - 10^{-6}

	COMP. TIME (msec)				ACC (m)
ALG	TIME UPDATE	MEAS UPDATE	TOTAL UPDATE	NORMED UPDATE	RMS POS ERR
EKF($\dot{\Phi}$)	67.310	10.215	77.525	1.000	128.4
UDU($\dot{\Phi}$)	77.234	17.629	94.863	1.224	128.7
POTT($\dot{\Phi}$)	85.569	18.308	103.894	1.340	95.0
CARL($\dot{\Phi}$)	78.683	25.256	103.939	1.341	95.0
CARL($\dot{W}$)	92.598	24.560	113.158	1.550	128.3
UDU($\dot{U}\dot{D}$)	144.782	19.499	164.281	2.119	140.1
EKF($\dot{P}$)	-----	----	-----	----	----

TABLE 9

RELATIVE ALGORITHM PERFORMANCE

RK 8, 6 SEC FIXED STEP

	COMP. TIME (msec)				ACC (m)
ALG	TIME UPDATE	MEAS UPDATE	TOTAL UPDATE	NORMED UPDATE	RMS POS ERR
EKF($\dot{\Phi}$)	231.178	8.957	240.135	1.000	128.4
UDU($\dot{\Phi}$)	243.286	18.493	261.779	1.090	128.7
POTT($\dot{\Phi}$)	252.709	17.675	270.384	1.126	95.0
CARL($\dot{\Phi}$)	245.504	26.009	271.513	1.131	95.0
CARL($\dot{W}$)	444.624	26.329	470.953	1.961	129.0
UDU($\dot{U}\dot{D}$)	479.770	18.191	497.961	2.074	128.8
EKF($\dot{P}$)	523.195	8.801	531.996	2.215	128.8

TABLE 10

RELATIVE ALGORITHM PERFORMANCE
RK 4, 6-SEC FIXED STEP.

	COMP. TIME (msec)				ACC(m)
ALG	TIME UPDATE	MEAS UPDATE	TOTAL UPDATE	NORMED UPDATE	RMS POS ERR
EKF($\dot{\Phi}$)	83.881	8.408	92.289	1.000	128.4
UDU($\dot{\Phi}$)	95.613	17.553	113.146	1.229	128.7
POTT($\dot{\Phi}$)	103.956	17.884	121.840	1.320	95.0
CARL($\dot{\Phi}$)	96.959	25.574	122.533	1.328	95.0
CARL($\dot{W}$)	130.071	25.632	155.703	1.687	128.6
EKF($\dot{P}$)	153.496	9.887	163.383	1.770	128.9
UDU($\dot{U}\dot{D}$)	-----	----	-----	----	----

1) transition matrix algorithms consistently have lower computation times for time update than do the direct integration methods,

2) the relative performance of computation times of the direct integration algorithms is not predictable from one set of integration parameters to the next, contrary to the predictability of the transition matrix methods,

3) for this computer system, the transition matrix square root methods do not suffer large computation time penalties relative to the EKF($\dot{\Phi}$) algorithm,

4) fixed step algorithms have larger computation times for time update and total computation time than do their variable-step counterparts.

Accuracy

Each algorithm generates an RMS position error of 128–129 meters, with two exceptions: the $\dot{U}\dot{D}$ simulation with the RK(2)4 integrator records an RMS error of 140 meters and the Carlson($\dot{\Phi}$) and Potter($\dot{\Phi}$) algorithms each record 95 meter RMS errors. The increased error of the $\dot{U}\dot{D}$ simulation results from the integration tolerances (10^{-2} and 10^{-6}) not being strict enough to maintain the error at the 128 meter level. The integrator exceeds the error limit set for each step by the tolerances. The 95 meter RMS errors of the Carlson($\dot{\Phi}$) and Potter($\dot{\Phi}$) algorithms are thought to result from an assumption in the coding of the noise update sections of these two algorithms. Currently, the reason for such a large drop in the position RMS is not known and, therefore, the error improvement offered by these algorithms should be viewed with caution.

With the exception of the two cases just mentioned, no algorithm pays a penalty in estimation error by decreasing the order of the numerical integrator.

Numerical Stability

No algorithm appears to offer any clear cut advantage in stability in the problem conditions tested and for this computer system. However, the transition matrix equations do appear to be smoother and are, therefore, easier to integrate than are equations of the direct integration methods. This is evidenced by the generally lower integration times of the transition matrix codes and by the failure of two of the direct methods to successfully finish simulations. Both vailures resulted from the discovery of a negative valued diagonal element in the covariance matrix brought about, it is believed, by an inability of the integrator to maintain an adequate single-step error, thus causing a fatal global error growth.

Additional Results

In the previously discussed set of navigation simulations, the integration of the state and state-error covariance matrix through data dropout periods is performed with one call to the numerical integrator. When only one integration call is made to span the entire data dropout, position error magnitudes during the dropout are not included in the navigation program's calculation of the total RMS position error. As these errors should be included in the RMS calculation, the navigation program has been modified to integrate in six-second intervals during dropouts and to calculate the position error at the end of each six-second interval. This means that numerical integration and process noise accumulation are

performed in six-second increments until observations are obtained at the end of the dropout. As well as correcting the RMS position error calculation, this modification creates a better model of the operation of the actual GPS data processing system.

A plot of the RSS position error, as generated by the modified navigation program, is shown in Figure 4. Tables 11 and 12 contain the results of a set of navigation simulations in which the first 10,000 seconds of observations only were processed. The simulations were performed with each of the algorithms tested previously and with the RK(2)4 and RK4 integrators. The results given in Tables 11 and 12 are analogous to those contained in Tables 8 and 10, respectively, but were generated by the modified navigation program.

A comparison of the data in Tables 11 and 12 with those of Tables 8 and 10 shows no significant changes in the relative performance of the algorithms. The RMS position errors for most of the algorithms have grown from approximately 128 meters to approximately 166.5 meters because the position errors occurring during the data dropouts have been included in the calculation of the RMS error. The Carlson($\dot{\Phi}$) and Potter($\dot{\Phi}$) methods still have the lowest errors, but the values of the errors have experienced a growth roughly proportional to that experienced by the other algorithms. For the same reasons mentioned in the previous section, the lower RMS errors of these algorithms should be viewed with caution. Integration times and total computation times have increased as well. The increases result because the newly imposed six-second integration interval in the data dropouts forces a step size limit on the variable step integrator, causes more matrix retriangularizations for the transition matrix methods,

FIGURE 4

RSS POSITION ERROR VS TIME

(Modified Program)

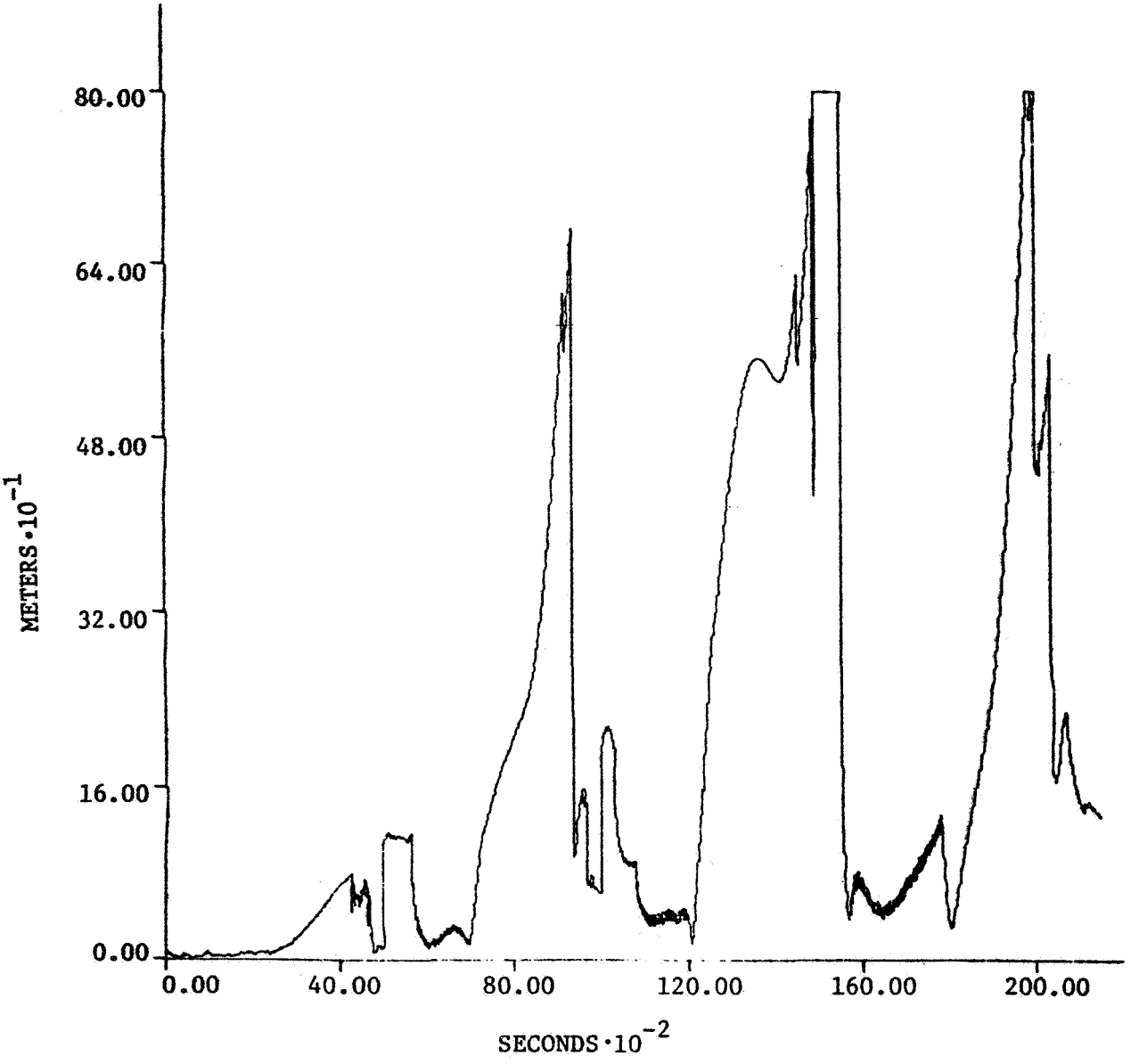

TABLE 11

RELATIVE ALGORITHM PERFORMANCE
RK(2)4, TOL: $10^{-2} - 10^{-6}$

	COMP. TIME (msec)				ACC (m)
ALG.	TIME UPDATE	MEAS UPDATE	TOTAL UPDATE	NORMED UPDATE	RMS POS ERR
EKF($\dot{\Phi}$)	79.296	9.618	88.914	1.000	166.5
UDU($\dot{\Phi}$)	91.916	19.536	111.452	1.253	166.5
CARLSON($\dot{\Phi}$)	95.750	26.607	122.357	1.376	109.6
POTTER($\dot{\Phi}$)	104.488	19.361	123.849	1.393	109.6
EKF($\dot{P}$)	119.353	8.575	127.928	1.439	166.9
UDU($\dot{U}\dot{D}$)	225.471	19.697	244.968	2.755	166.9
CARLSON($\dot{W}$)	274.643	26.735	301.378	3.390	166.6

TABLE 12

RELATIVE ALGORITHM PERFORMANCE

RK4, 6-SEC FIXED STEP

	COMP. TIME (msec)				ACC (m)
ALG.	TIME UPDATE	MEAS UPDATE	TOTAL UPDATE	NORMED UPDATE	RMS POS ERR
EKF($\dot{\Phi}$)	91.196	9.040	100.236	1.000	166.5
UDU($\dot{\Phi}$)	104.366	19.316	123.682	1.234	166.5
CARLSON($\dot{\Phi}$)	107.833	26.065	133.898	1.336	109.6
POTTER($\dot{\Phi}$)	116.608	19.320	135.928	1.356	109.6
CARLSON($\dot{W}$)	136.829	27.048	163.319	1.635	166.5
EKF($\dot{P}$)	163.799	8.652	172.451	1.720	166.0
UDU($\dot{U}\dot{D}$)	-	-	-	-	-

and generally creates a higher computation overhead due to a greater number of integrator calls.

The unexpected results in this new set of simulations are the improved performances of the $\dot{P}$ and $\dot{U}\dot{D}$ algorithms in conjunction with the RK(2)4 integrator. In this set of simulations, both methods have RMS errors consistent with the errors of the other algorithms (approximately 166.5 meters). Yet in the original simulations, those recorded in Table 8, the $\dot{P}$ method failed to complete its simulation run and the $\dot{U}\dot{D}$ code had a higher RMS error than did the other algorithms. The error improvements are believed to occur because the step size limit imposed by the six-second integration interval insures an accuracy in the integration of the $\dot{P}$ and $\dot{U}\dot{D}$ equations that the integration tolerances cannot insure.

SUMMARY

It is reemphasized that these results apply to simulations on the CDC6600 system only. Although it is believed that these results do establish important trends in the relative performance of these algorithms, additional simulations on other comuter systems, particularly those with small wordlengths, are essential. Such simulations are currently being carried out.

This article is intended as a general overview of the simulation method and initial results. A more exhaustive analysis of these results, as well as detailed descriptions of the simulation models and filter algorithms can be found in [1].

REFERENCES

1. B. D. Tapley, J. G. Peters, B. E. Schutz, "A Comparison of Square Root Estimation Algorithms for Autonomous Satellite Navigation," IASOM TR79-1, University of Texas at Austin, February 1979.

2. B. D. Tapley, "Statistical Orbit Determination Theory," presented at NATO Advanced Study Institute in Dynamical Astronomy, Cortina d'Ampezzo, Italy, August 1972.

3. R. H. Battin, "Astronautical Guidance," McGraw-Hill Book Company, Hightstown, New Jersey, 1964, pp. 388-389.

4. N. A. Carlson, "Fast Triangular Formulation of the Square Root Filter," AIAA Journal, Vol. 11, pp. 1239-1265, September 1973.

5. G. J. Bierman, "Factorization Methods for Discrete Sequential Estimation," Academic Press, New York, New York, 1976.

RELATIVISTIC INFORMATION OF THE GPS-NAVSTAR POSITION DETERMINATION ALGORITHM

W. Baer

Gravitonics Systems Engineering Consultants

ABSTRACT

A relativistic formulation of the timation navigation position algorithm is developed. The use of satellite proper time as integration variable and space-time correlation handling are examined for means to reduce computational requirements. Implementation architectures are discussed with emphasis on minimization of computer configuration hardware requirements. Selected benchmark experiment results are presented to size processor requirements for achieving GPS-NAVSTAR navigation accuracies in both the User and Control Segments.

1) An introduction to Timation Navigation in Relativistic Notation.

Relativistic Timation Navigation is a technique for calculating the position of an event by measuring it's distance from at least four events of known location. A set of repetitive events, such as the completion of a clock cycle, can mark the trajectory of an object in which those events occur. Figure 1 shows the trajectory of a spacecraft marked by constant time ticks as measured by a standard on-board clock located in an earth-centered coordinate system X. Each clock tick (TSN) is located by three positions (X1SN, X2SN, X3SN) and a time coordinate (X4SN).

To show how relativistic notation can be used in the NAVSTAR Program, the following sets of equations are introduced and summarized in the Figure 1 insert.[1]

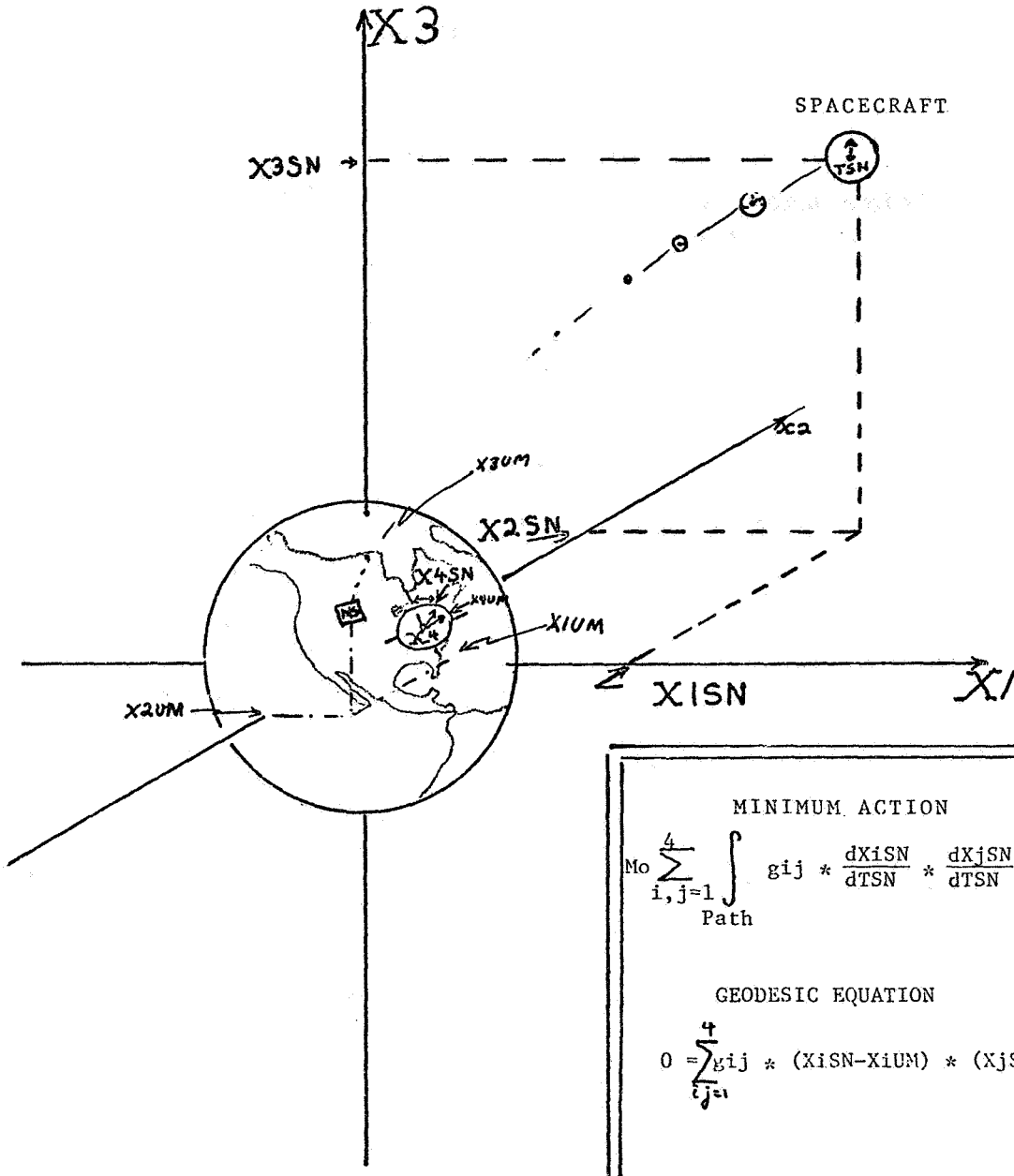

MINIMUM ACTION

$$Mo \sum_{i,j=1}^{4} \int_{Path} gij * \frac{dXiSN}{dTSN} * \frac{dXjSN}{dTSN} \quad dTSN$$

GEODESIC EQUATION

$$0 = \sum_{i,j=1}^{4} gij * (XiSN-XiUM) * (XjSN-XjSM)$$

a) The solution of motion of satellite clock N in the NAVSTAR constellation:

X1SN = F1SN (TSN)

X2SN = F2SN (TSN)

X2SN = F3SN (TSN)

X4SN = F4SN (TSN)

Where X4SN = coordinate time

TSN = proper time of the Nth Satellite Clock

F2SN (TSN) = a function of TSN

This can also be written as:

XiSN = FiSN (TSN) i = 1,4

b) The solution of motion for a satellite clock can be found by applying a four-dimensional minimum action principle, i.e.,

$$Mo \sum_{i,j=1}^{4} \int_{Path} \sqrt{gij * \frac{dXiSN}{dTSN} * \frac{dXjSN}{dTSN}}$$

dTSN = a minimum along the actual path

Where Mo = the rest mass of the satellite clock.

gij = the metric tensor or gravitational potential

The action integral can be minimized in a search algorithm of the type presented in Figure 3. The basic clock cycle in a NAVSTAR satellite is the repetition of the navigation message occurring every 6 seconds measured in satellite time. For a

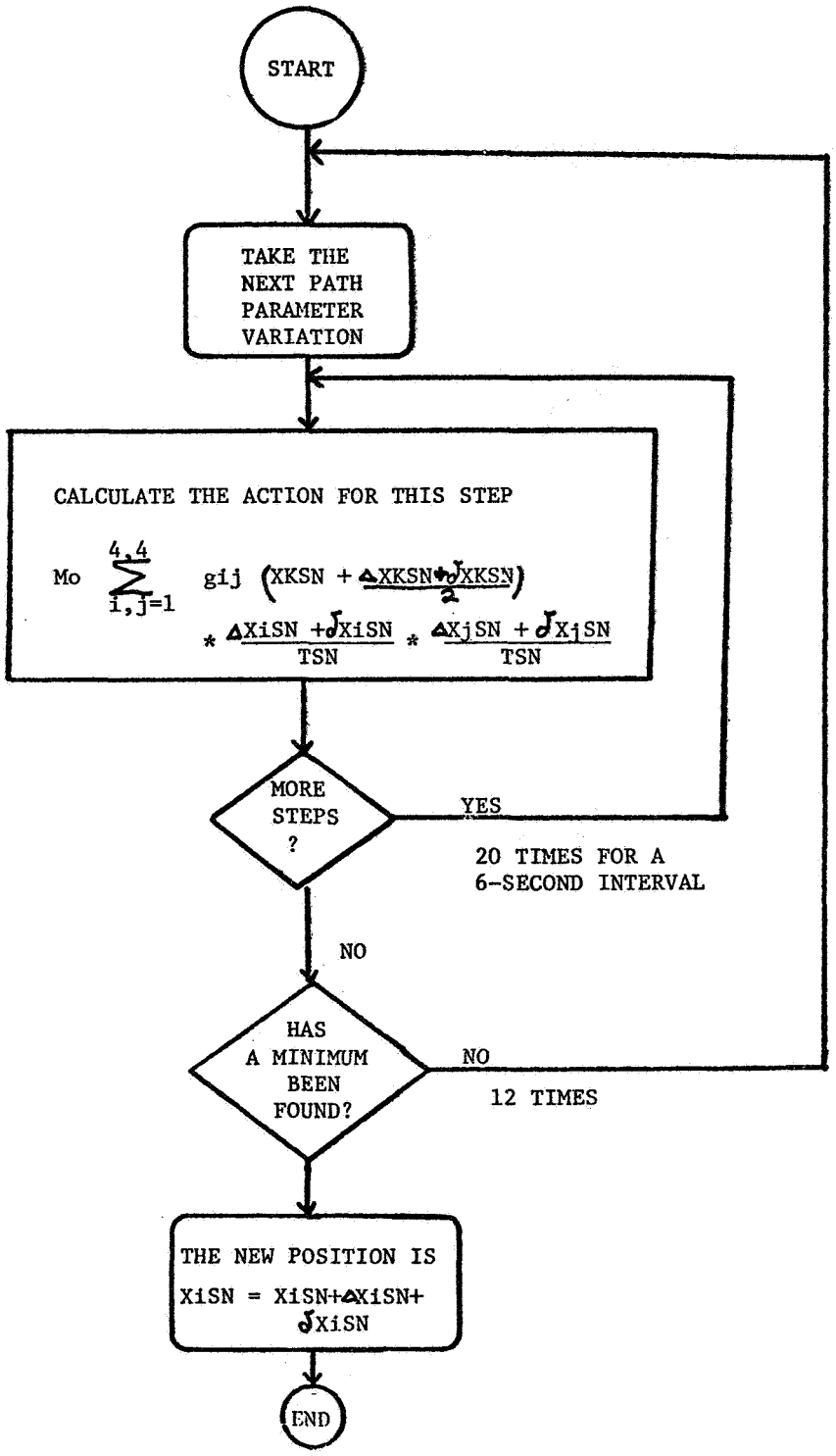
START
TAKE THE NEXT PATH PARAMETER VARIATION
CALCULATE THE ACTION FOR THIS STEP
Mo $\sum_{i,j=1}^{4,4}$ gij $\left(XKSN + \Delta XKSN + \frac{\delta XKSN}{2}\right)$ * $\frac{\Delta XiSN + \delta XiSN}{TSN}$ * $\frac{\Delta XjSN + \delta XjSN}{TSN}$
MORE STEPS ?
YES
20 TIMES FOR A 6-SECOND INTERVAL
NO
HAS A MINIMUM BEEN FOUND?
NO
12 TIMES
THE NEW POSITION IS
XiSN = XiSN+ΔXiSN+ δXiSN
END

12-hour synchronous satellite traveling at 4 km per second it is estimated that approximately 20 steps are required to avoid granularity introduced by numerical integration. Assuming that the gravitational potentials (gij) are known,(2) the action contribution for each step requires the execution of approximately 20 additions and 20 multiplications and must be performed 240 times for a total 9.6K instructions to calculate the time and position of the next NAVSTAR message cycle.

c) The solution of motion for a user or monitor station clock M in the NAVSTAR system:

X1UM = F1UM (TUM)

X2UM = F2UM (TUM)

X3UM = F3UM (TUM)

X4UM = F4UM (TUM)

or

eq. 1b: XiUM = FiUM (TUM) i=1,4

Where TUM - the proper time of a user or monitor station M.

For the purposes of this paper, monitor station solutions of motion are assumed to be known quantities derived from site surveys and the rotational motion of the earth derived from the pole wander service.

d) The geodesic equations defining the square of the distance between two events in an arbitrary coordinate system X with a metric tensor of gij are:

$$(SSNUM)^2 = \sum_{i=1}^{4} \sum_{j=1}^{4} gij * (XiSN-XiUM) * (XjSN-XjSM)$$

Where: SSNUM = the distance between the two events SN, UM
XiSN = coordinates of the event SN i = 1,4
XjUM = coordinates of the event UM j = 1,4

To first approximation, the metric tensor of an earth-centered initial coordinate system is:

$$gij = \begin{bmatrix} 1 & & & \\ & 1 & & \\ & & 1 & \\ & & & -C^2 \end{bmatrix}$$

Where C = the speed of light in the vicinity of the earth in vacuum.

Also, the first approximation the distance between any two events connected by a light pulse is zero, or stated another way, light travels along null geodesics.

Hence the geodesic equation when the two events in question are the transmission of an electromagnetic wave feature by a satellite and the reception of the same feature by a user or monitor station reduces to:

eq. 1c: $$0 = (X1SN - X1UM)^2 + (X2SN - X2UM)^2 + (X3SN - X3UM)^2 - C^2\ (X4SN - X4UM)^2$$

which is the standard equation connecting range to time intervals and also known as the user equation.[3]

2) Clock Ephemeris Determination

The determination of clock ephemeridies requires a measurement of clock position over an arc. The measurement instrument used in the NAVSTAR Program is a set of up to eight monitor stations on the semi-rigid rotating earth crust.

Single Point Clock Tick Position Measurement

The emission of the wave feature, representing a clock tick, from a satellite antenna is a single event which can be labelled by the proper time (TSN) of emission and occurs at unique space time coordinate values XiSN for i=1 to 4.

The arrival time of the wave feature at a monitor station M is tagged with the monitor station proper time TAM. Since we have assumed knowledge of monitor station motion (eq. 1b) as a function of TAM, for each monitor station satellite pair the geodesic equation (eq. 1c) applies.

$$0 = \sum_{i=1}^{4} \sum_{j=1}^{4} gij * (XiSN - XiUM) * (XjSN - XjSM)$$

If four monitor stations receive the signal, the four geodesic equations can be constructed and solved for the four unknown c-ordinates of the satellite clock tick event (XiSN for i=1,4) for an initial estimate.

Filter Techniques

Typically many measurements using more than four monitor stations and multiple clock ticks will be used to construct a clock ephemeris. Consequently filter techniques are applicable. If we assume to have a guess of an initial satellite position (XISN1) and a good four-dimensional stepper, then one can find the best satellite position by minimizing the sum total satellite weighted error calculated over all measurements as shown in Figure 4.

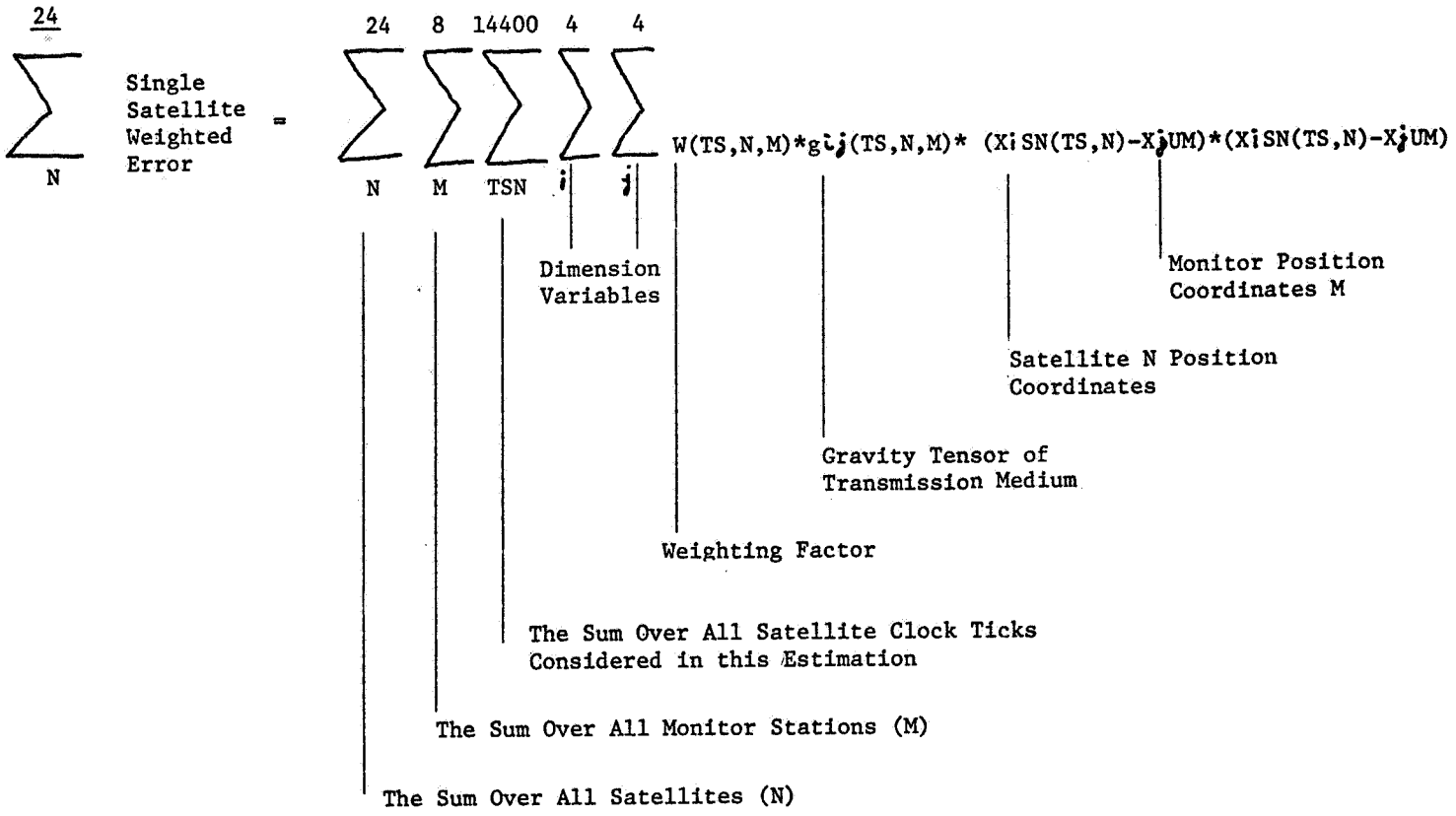

Add/Sub 36×10^6 Mult/Div 36×10^6

To achieve a 300-fold reduction in the single point estimation as anticipated for NAVSTAR III, a day's measurements might be required. Then each satellite weighted error calculation would require 36 mega add/subtract, multiply/divide, and trajectory steps to perform - a sizable computer load to use in a search loop.

The same minimization can be performed directly using a filter algorithm as shown in Figure 5, in which the total error is minimized recursively.

3) Features of the Relativistic Formulation

The advantage of using relativistic notation is that the satellite proper time TSN is the independent variable physically available to the NAVSTAR Spacecraft. Proper time is measured by counting the output of precision frequency standard (rubidium or cesium) which is a physically independent device. All on-board processing, transmission frequencies, bit rates, etc. can be derived from this device. Hence, real time schedules and navigation processing loops are naturally indexed with the TSN variable.

A second advantage is derived form the property that the relativistic formulation is coordinate independent, hence solutions of motion can be obtained directly in any coordinate system of interest.

The relativistic formulation also allows clock rates and clock drifts, as well as space time correlations to be automatically included. A fourth component of force can be added to account for clock rate

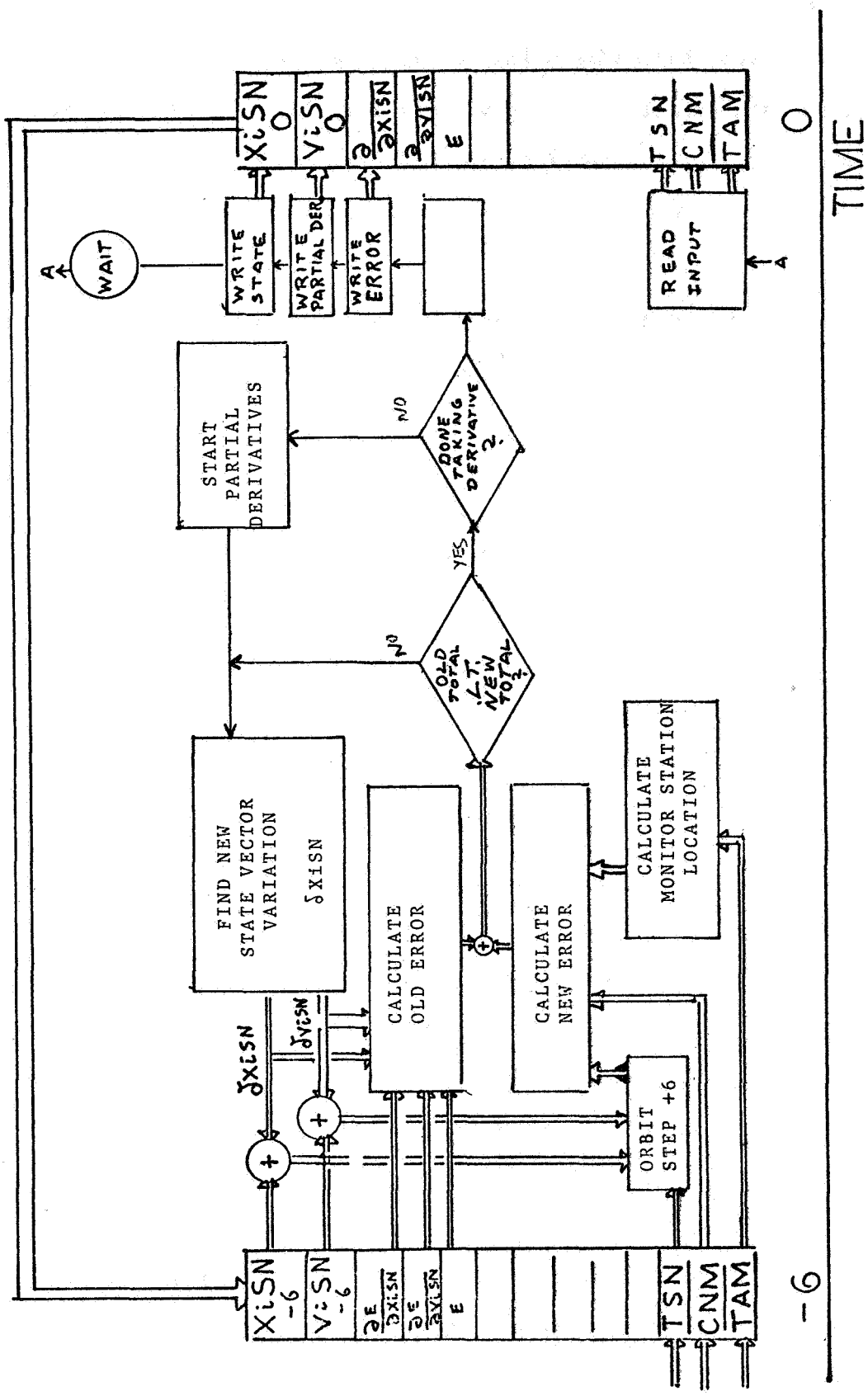
TIME
0
-6
XiSN 0
ViSN 0
∂E/∂XiSN
∂E/∂ViSN
E
TSN
CNM
TAM
WAIT
A
WRITE STATE
WRITE PARTIAL DER
WRITE ERROR
READ INPUT
START PARTIAL DERIVATIVES
DONE TAKING DERIVATIVE 2.
NO
YES
OLD TOTAL ≠ NEW TOTAL ?
NO
FIND NEW STATE VECTOR VARIATION
δXiSN
δViSN
CALCULATE OLD ERROR
CALCULATE NEW ERROR
CALCULATE MONITOR STATION LOCATION
ORBIT STEP +6
XiSN -6
ViSN -6
∂E/∂XiSN
∂E/∂ViSN
E
TSN
CNM
TAM

variations much as the three space components of solar and thruster pressure determine mass point velocity variations.

4) Implementation and Computer Sizing Considerations

A simplified data flow diagram of the NAVSTAR Control System is shown in Figure 6. For purposes of this paper, the satellite is assumed to radiate a navigation message which is simply a table of four XiSN values plus information such as satellite clock offset ionospheric correrrtion coefficients, etc. In practice, polynomial approximations to the satellite clock motion will be used to accommodate operational requirements. Nevertheless a simple table of XiSN position and time coordinates could be stored in a 32-bit 128K core memory and clocked out every 6 seconds for the first week to satisfy position accuracy requirements of better than 1 meter.

The radiated message is received at monitor stations in view of the satellite (SN). The signal is tagged with the Time of Arrival at each monitor station (TAM), the best speed of light estimate (CSNM) calculated and communicated to the Master Control Station (MCS). Messages from each monitor station are multiplexed into the MCS Navigation Process (Figure 2). The four coordinates are used for performance evaluation, while the values TSN, TAM and CSNM are used as measurements for position determination.

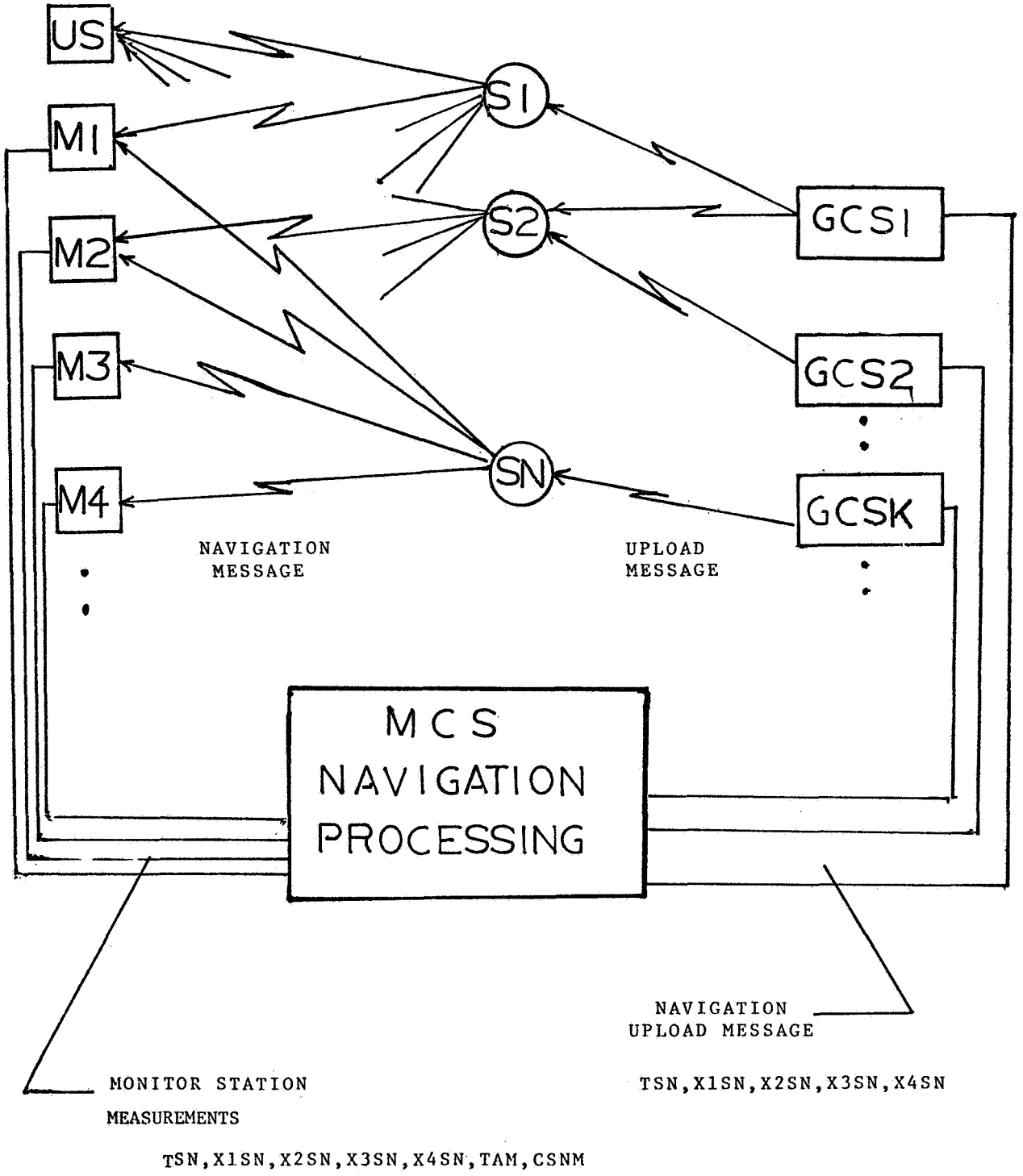
US
M1
M2
M3
M4
S1
S2
SN
GCS1
GCS2
GCSK
NAVIGATION
MESSAGE
UPLOAD
MESSAGE
MCS
NAVIGATION
PROCESSING
NAVIGATION
UPLOAD MESSAGE
TSN,X1SN,X2SN,X3SN,X4SN
MONITOR STATION
MEASUREMENTS
TSN,X1SN,X2SN,X3SN,X4SN,TAM,CSNM

The ingest data rate from eight monitor stations and twenty-four satellites is sixteen measurements per second since on the average only half the satellites will be visible from any one station.

The Navigation Processing Block Diagram (Figure 7) shows two major programs, the Position Update Algorithm and the Position Prediction Algorithm. Figure 8 gives a summary of their software characteristics. In calculating transaction rates, it was assumed that each space vehicle will require a maximum of two upload messages per day and predictions to one week. The instruction mix is derived from the average operation count for the relativistic formulations presented above.

A summary of computer resource requirements is shown in Figure 9. The kip rate is typical of mini computers generally available in today's market.

An operational NAVSTAR Timation Navigation Control Center would require substantial increases in computing power to handle error checking, reporting, initialization, look up table calculations, satellite control, display and general site utility functions. The detail in this paper is not intended to provide hardware recommendations for an operational system, but present a theoretical method. However, the essential parts of a simplified navigation subsystem have been studied sufficiently to suggest that mini-computer-based relativistic software could be considered for advanced systems, simulations and validations or commercial piggy-back packages.

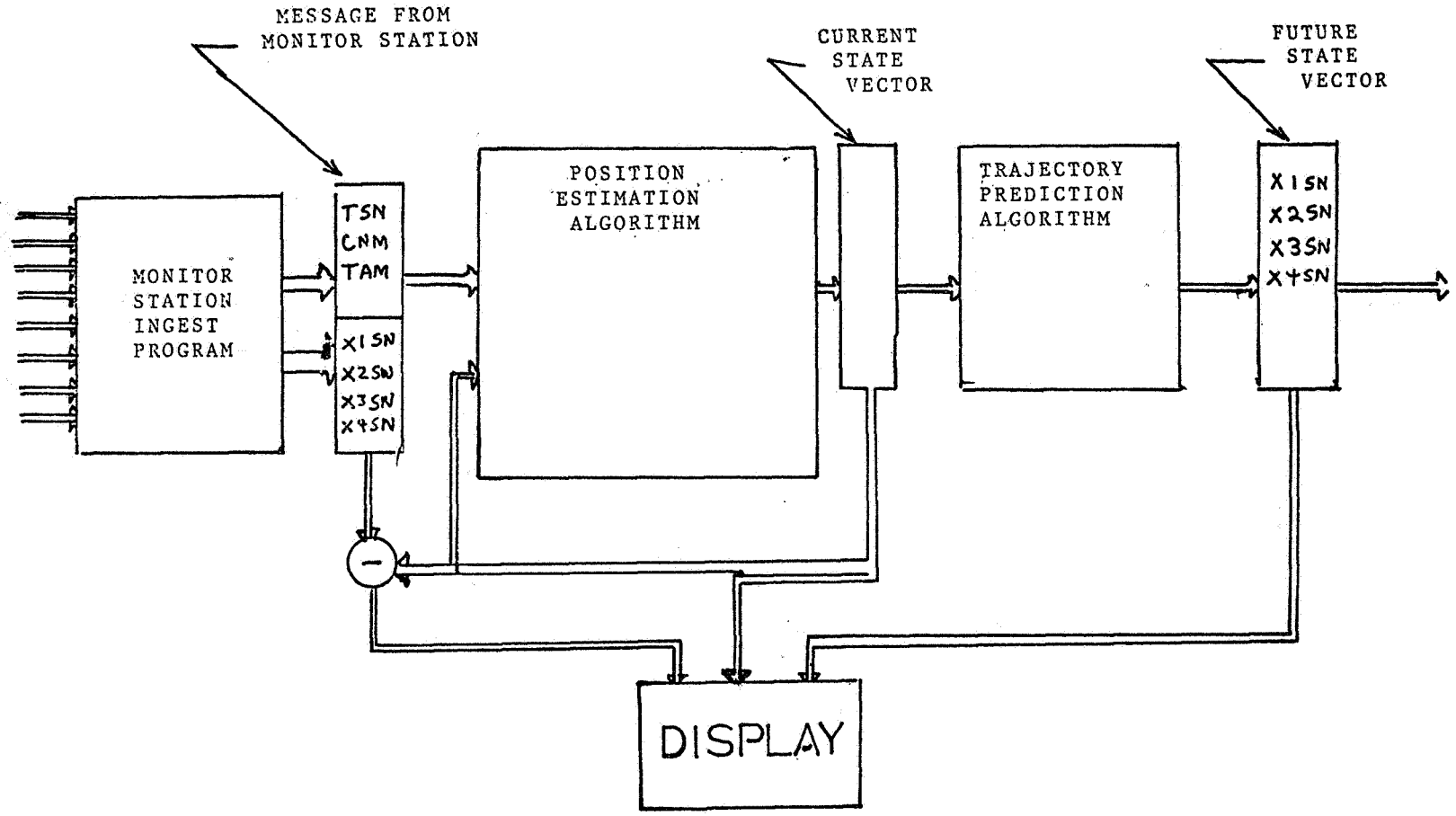
MESSAGE FROM
MONITOR STATION
CURRENT
STATE
VECTOR
FUTURE
STATE
VECTOR
MONITOR
STATION
INGEST
PROGRAM
TSN
CNM
TAM
X1SN
X2SN
X3SN
X4SN
POSITION
ESTIMATION
ALGORITHM
TRAJECTORY
PREDICTION
ALGORITHM
X1SN
X2SN
X3SN
X4SN
DISPLAY

TRANSACTION NAME	NO. OF EXECUTIONS 1000/HR	NO. OF INSTRUCTIONS	NO. OF INSTRUCTIONS PER LOOP	NO. OF LOOPS EXECUTED PER TRANSACTION	I/O ACCESS	I/O BUFF SIZE
POSITION PREDICTION	.002	300	40	240/STEP 100K $\frac{\text{STEPS}}{\text{WEEK}}$	1/STEP	84
POSITION DETERMINATION	57.6	700	100	80	1	164

NOTE: INSTRUCTIONS ARE 50% ADD/SUB, 50% MULTIPLY

FIGURE 8 - ESTIMATED NAVIGATION PROCESSING SOFTWARE CHARACTERISTICS FOR 24 SATELLITES, EXCLUDING ELECTROMAGNETIC TERMS.

REQUIRED ESTIMATE COMPUTER LOAD 128 KIPS

TYPICAL MINICOMPUTER CAPABILITIES WITH SINGLE PRECISION FLOATING POINT HARDWARE:

DATA GENERAL ECLIPSE
DEC PDP 11/45
HP 1000 SERIES

} ~ 150 KIPS

REFERENCES

1) The Theory of Relativity, C. Moller; Clarenton Press 1972 2nd Ed. pg. 259, pg. 276

2) Relativistic Time for Terrestrial Circumnavigations, Y. C. Hafele, AJP Volume 40, Jan. 1972 pg. 81

3) The GPS Control Segment and its Service to the GPS USER,M. Y. Hurley, Y. L. Kramer, D. D. Thornburg IEEE 1976 Position Location and Navigation Symposium pg. 197

SHORT-TERM SOLAR PRESSURE EFFECT AND GM UNCERTAINTY ON TDRS ORBITAL ACCURACY A STUDY OF THE INTERACTION OF MODELING ERROR WITH TRACKING AND ORBIT DETERMINATION

Bertrand T. Fang

EG&G Washington Analytical Services Center, Inc.

ABSTRACT

The interaction of modeling errors with the tracking and orbit determination of TDRS satellites is studied. For orbit determination instead of long-term orbit prediction and station-keeping, it is convenient to express TDRS orbital errors as radial, along-track and cross-track deviations from a nominally circular orbit. Simple analytical results are given for the perturbation of TDRS orbits as a result of GM uncertainty; as a result of changes in epochal elements; as a result of solar radiation uncertainty, with the TDRS modeled as a combination of a sun-pointing solar panel and an earth-pointing plate. Based on this simplified model, explanations are given for the following orbit determination error characteristics: inherent limits in orbital accuracy, the variation of solar pressure induced orbital error with time of the day of epoch, the insensitivity of range-rate orbits to GM error, and optimum bilateration baseline. The result should also shed some light on the general subject of the interaction of modeling error with orbit determination.

SHORT-TERM SOLAR PRESSURE EFFECT AND GM UNCERTAINTY ON TDRS ORBITAL ACCURACY - A STUDY OF THE INTERACTION OF MODELING ERROR WITH TRACKING AND ORBIT DETERMINATION*

Bertrand T. Fang
EG&G/Washington Analytical Services Center, Inc.
Riverdale, Maryland 20840

I. INTRODUCTION

It is known (Ref. 1,2) that uncertainties in GM and solar radiation pressure force are two major sources of error for the orbit determination accuracies of the geosynchronous Tracking and Data Relay Satellities (TDRS). The magnitudes of the resulting orbit errors depend on the configuration of tracking baseline and the time of the day chosen as epoch. These and other perplexing phenomena observed in the course of error analysis results from a complex interplay between modeling error induced orbit perturbations and compensations provided by tracking and orbital computations. The present study is undertaken to seek a better physical understanding of modeling error and its interaction with tracking and orbit determination. Analytical derivations are pursued, together with a digestion of available numerical results. Although the impetus of the present study concerns TDRS orbital accuracy, it is hoped the results will shed some light on the subject in general.

Sections II and III below give simple analytical results for the perturbation of TDRS orbits in the presence of solar radiation pressure and GM uncertainty. From these results, the inherent limit of orbit determination accuracy in the

*This investigation is supported by NASA Goddard Space Flight Center (GSFC). Additional details are contained in an EG&G/WASC report to GSFC.

presence of modeling errors is derived in Section IV. The information conveyed by range and range-rate measurements is studied. Based on the information content of measurements and the orbital perturbations resulting from modeling errors, certain idiosyncrasies in orbit determination errors and characteristics are explained.

II. SHORT-TERM SOLAR RADIATION PERTURBATION OF TDRS ORBITS

Perturbation of artificial satellites by solar radiation pressure has been studied extensively (Ref.3). However, with very few exceptions, these studies are mainly concerned with the long-term perturbations of the Keplerian elements of a spherical satellite, and with the shadow effect.

For the present purpose, the following model shall be adopted:

1. The unperturbed TDRS orbit is a circular orbit about a homogeneous spherical earth.

2. The sun-to-TDRS vector may be considered a constant in inertial space during the short period (several days) of interest.

3. The TDRS satellites may be modeled as the combination of a sun-pointing solar panel and an earth-pointing perfectly reflecting flat disk. Any shadowing by the earth or by part of the satellite itself is neglected.

The relative geometry of the TDRS, the Sun, and the unperturbed TDRS orbit is shown in Fig. 1. The equations of motion governing the "cross-track", "radial" and "along-track" perturbations

from a nominally circular orbit may be expressed in the following convenient forms (Ref. 4,5):

$$\ddot{z} + z = f_Z \qquad (1)$$

$$\delta\ddot{\rho} - 3\delta\rho - 2R\dot{\delta\theta} = f_\rho \qquad (2)$$

$$R\ddot{\delta\theta} + 2\dot{\delta\rho} = f_\theta \qquad (3)$$

where a superposed dot denotes differentiation with a normalized time τ, which represents the nominal angular position of TDRS. R is the nominal orbital radius of TDRS. The f's are components of the solar radiation force per unit TDRS mass. For our model f_Z is a small constant quantity. The cross-track perturbation as given by the solution of Eq. (1) represents small oscillations uncoupled to the other perturbations and shall not be considered further. Eq. (2) and (3) may be rearranged as

$$\delta\ddot{\rho} + \delta\rho = f_\rho + 2\int f_\theta d\tau \qquad (2a)$$

$$R\dot{\delta\theta} = -2\delta\rho + \int f_\theta d\tau. \qquad (3a)$$

which show that solar radiation force components at the orbital frequency, as well as any constant tangential component, will cause secular perturbations and are of primary importance. Eq. (3a), with the term $-2\delta\rho$ moved to the left-hand side of the equality sign, relates the tangential force to the change in orbital angular momentum.

Let us consider the Sun-pointing solar panel first. For this case one may write

$$f_\rho = f_{xy}\,\mathrm{Cos}(\phi-\tau)$$

$$f_\theta = f_{xy}\,\mathrm{Sin}(\phi-\tau)$$

where f_{xy} is the component of the solar radiation force on the solar panel in the TDRS orbital plane and $(\phi-\tau)$ is the angle between his force component and the TDRS orbital radius. It is straight-forward to show Eq. (2) and (3) admit the following general solution under these forces:

$$\begin{bmatrix} \delta\rho(\tau) \\ \dot{\delta\rho}(\tau) \\ R\delta\theta(\tau) \\ R\dot{\delta\theta}(\tau) \end{bmatrix} = [A] \begin{bmatrix} \delta\rho(0) \\ \dot{\delta\rho}(0) \\ R\delta\theta(0) \\ R\dot{\delta\theta}(0) \end{bmatrix} + f_{xy} ([B] + \tau[C]) \tag{4}$$

$$[A] = \begin{bmatrix} 4-3\cos\tau & \sin\tau & 0 & 2(1-\cos\tau) \\ 3\sin\tau & \cos\tau & 0 & 2\sin\tau \\ 6(\sin\tau-\tau) & 2(\cos\tau-1) & 1 & 4\sin\tau-3\tau \\ 6(\cos\tau-1) & -2\sin\tau & 0 & 4\cos\tau-3 \end{bmatrix} \tag{5}$$

$$[B] = \begin{bmatrix} \frac{3}{2}\sin\phi\sin\tau - 2\cos\phi(1-\cos\tau) \\ -\frac{1}{2}\cos\phi\sin\tau \\ -\cos\phi\sin\tau - 5\sin\phi - 5\sin(\tau-\phi) \\ 3\cos\phi - 3\cos\phi\cos\tau - 2\sin\phi\sin\tau \end{bmatrix} \tag{6}$$

$$[C] = \begin{bmatrix} \frac{3}{2}\sin(\tau-\phi) \\ \frac{3}{2}\cos(\tau-\phi) \\ 3\cos\phi + 3\cos(\tau-\phi) \\ -3\sin(\tau-\phi) \end{bmatrix} \tag{7}$$

Notice the first term on the right-hand side of Eq. (4) is the homogeneous solution which represents orbit perturbations resulting from changes in the initial conditions. The "state transition matrix" [A] is well-known, see for instance Ref. 6.

The solution as given in Eq. (7) indicates the more important effect of solar radiation is to cause a linearly diverging oscillatory (at the orbital rate) perturbation in radial and along-track motion. In addition, the perturbation in the along-track orbital position depends on the initial sun angel ϕ as illustrated in Figures 2 and 3. The least perturbation occurs when the sun vector is parallel to the satellite velocity vector in the beginning. The worst perturbation doubles that of the least perturbation and occurs when the sun is overhead or underfoot in the beginning. This dependence on initial sun angle may seem a bit perplexing. The explanation lies in that starting from the time the sun is overhead there is a duration of one-half orbit for the building-up of angular momentum. On the other hand, starting from the time when the sun is directly behind the satellite velocity vector there is only one-quarter of an orbit for the orbital angular momentum to build-up before the satellite turns around and is opposed by the solar radiation force. Similar situations occur when the sun is underfoot or directly opposed to the satellite velocity vector.

The non-homogeneous part of the above solution, represting perturbations of a sun-pointing or spherical satellite, in various equivalent forms, are well-known, although the dependence of the solution on initial sun angle has not been empasized.

For the earth-pointing part of TDRS, the solar radiation force may be expressed as

$$f_\rho = K|\cos(\phi-\tau)|\cos(\phi-\tau)$$

$$f_\theta = o,$$

the latter vanishes because this part of TDRS is modeled as a perfectly-reflecting disk. The term $|\cos(\tau-\phi)|$ represents the projected area which intercepts the incoming radiation. The absolute sign presents a minor complication and can be handled by the standard Fourier expansion technique. The particular solution of Eq (2) and (3) describing the perturbation of an earth-pointing perfectly-reflecting flat disk can then be written as

$$\delta\rho = \frac{4K}{3\pi}\tau\sin(\tau-\phi) - \frac{4K}{3\pi}\sin\phi\sin\tau + \frac{8K}{\pi}\left\{\frac{\cos 3(\tau-\phi)-\cos 3\phi}{(1-3^2)(1\cdot 3\cdot 5)} - \frac{\cos 5(\tau-\phi)-\cos 5\phi}{(1-5^2)(3\cdot 5\cdot 7)} + \ldots\right\} \quad (8)$$

$$R\delta\theta = \frac{8K}{3\pi}\left\{\tau\cos(\tau-\phi) - \sin\tau\cos\phi\right\} - \frac{16K}{\pi}\left\{\frac{\frac{1}{3}[\sin 3(\tau-\phi)+\sin 3\phi]-\cos 3\phi}{(1-3^2)(1\cdot 3\cdot 5)} - \right. \quad (9)$$

$$\left. - \frac{\frac{1}{5}[\sin 5(\tau-\phi)+\sin 5\phi]-\cos 5\phi}{(1-5^2)(3\cdot 5\cdot 7)} + \ldots\right\}$$

It is seen the primary perturbations are still diverging oscillations at the orbital rate. As compared with that of a sun-pointing surface, the solar pressure perturbation of a perfectly reflecting earth-pointing surface is:

1. About $\frac{1}{3}$ as large.
2. Less dependent on the initial sun angle.
3. Also characterized by small oscillations at multiples of the orbital rate.

These conclusions are predicated on the assumption of a perfectly reflecting and perfectly earth-pointing thin-plate satellite model. Perhaps the weakest aspect of the model is its implication that the along-track component of the solar radiation force does not exist. Real surfaces are bound to absorb and irradiate some incoming radiation and a non-infinitesimally-thin plate will experience along-track push of solar radiation. Although complicated satellite surface geometry and optical property make a realistic modeling difficult, perhaps a first step in the refinement of our model is to assume a certain percentage of the incoming photon tangential momentum is absorded; i.e., there exists a tangential component of the solar radiation force

$$F_r \propto \sin(\tau-\phi) \mid \cos(\tau-\phi) \mid$$

Additional refinements can also be made, although much more spohisticated modeling is probably unjustified in the presence of uncertainties in the satellite surface geometry and optical property.

As long as the solar radiation force on the satellite may be considered periodic from one orbit to another, the Fourier series method may be used to determine the orbital perturbations. As discussed before, the primary perturbations would come from force components at the orbital frequency and any constant along-track comonent.

III. EFFECT OF GM UNCERTAINTY ON TDRS ORBITS

On account of spherical symmetry, uncertainty in GM is quivalent to the following set of perturbative forces:

$$f_\theta = f_z = o, \quad f_\rho = R\,\frac{\delta GM}{GM}, \quad \left(\frac{\delta GM}{GM} = \text{fractional GM uncertainty}\right)$$

Accordingly Eq. (2) and (3) admit the following solution representing perturbations due to uncertainties in our knowledge of GM

$$\begin{bmatrix} \delta\rho(\tau) \\ \dot{\delta\rho}(\tau) \\ R\delta\theta(\tau) \\ R\dot{\delta\theta}(\tau) \end{bmatrix} = \frac{\delta GM}{GM} \begin{bmatrix} -R(1-\cos\tau) \\ -R\sin\tau \\ 2R(\tau-\sin\tau) \\ 2R(1-\cos\tau) \end{bmatrix} \tag{10}$$

The homogeneous part of the solution representing the free motion is of course still described by the matrix [A] in Eq. (5). It is seen from Eq. (10) that in addition to sinusoidal oscillations of the radial and along-track motion at the orbital rate, there is also an along-track position deviation which increases linearly with time.

The effect of GM uncertainty may be easily explained. At an orbital radius and with a circular velocity that corresponds to a slightly erroneous GM, the actual orbit is slightly elliptical with a slightly different orbital period. This is reflected in a sinusoidal variation in the radial motion plus an along-track position deviation which not only oscillates but also increases linearly with time. As expected, GM uncertainty does not cause cross-track perturbations or changes in orbital inclinations.

IV. LIMITS IN ORBIT DETERMINATION ACCURACY IN THE PRESENCE OF MODELING ERRORS

The perturbation of TDRS orbits resulting from uncertainties in our knowledge of the solar radiation force and GM was studied in the preceding sections. These perturbations represent prediction errors in the absence of tracking measurements. Measurements generally temper, but may occasionally aggravate, these errors. The ways and the extent that tracking and orbit determination strategy affect orbit accuracies in the presence of modeling errors are studied in this and the following sections.

It is usual to represent a satellite orbit by six epochal orbital elements, which, together with the dynamic model, generate a fictitious trajectory over some time span of interest. It is the role of orbit determination to pick these orbital elements such that the fictitious trajectory fits tracking measurements in some way. Thus orbit determination, as it is commonly practiced, is in essence a representation or approximation problem: i.e., seeking the representation of a real-world trajectory by a fictitious trajectory generated by six epochal elements which are to be determined. The fictitius trajectory governed by the imperfect model has a particular time characteristic which may be entirely different from that of a real-world trajectory. For instance, it maybe seen from Eq. (4) through (7) in Section II that the "real-world trajectory in the presence of solar radiation has a diverging sinusoidal variation, while a fictitious trajectory neglecting solar radiation is characterized by a linear time variation modulated by constant-amplitude sinusoidal variations. Unless the time characteristics are similar, it is obviously impossible to determine a set of <u>six</u> orbital elements which fit <u>hundreds</u> of measurement data perfectly. Thus there is an inherent limit to "orbit determination accuracy" in the presence of modeling errors.

For precision orbit determination which we are concerned with, the trajectories may be represented by small deviations from some nominal trajectory. The "true" and the "fictitions" trajectory deviations may be expressed as

$$[\delta x(t)] = \sum_i \alpha_i \, [G_i(t)] \tag{11}$$

and

$$[\Delta x(t)] = [\phi(t,t_o)][\Delta x(t_o)] \tag{12}$$

respectively. In Eq. (11) α_i represent the uncertain parameters in the model and $[G_i(t)]$ characterizes the time history of the trajectory perturbations caused by the uncertainties. The expression $[\phi(t,t_o)]$ in Eq. (12) is the state transition matrix of our imperfect trajectory model and $[\Delta x(t_o)]$ are epochal orbital elements.* The state transition matrix $[\phi(t,t_o)]$ and the trajectory perturbation matrix $[G_i(t)]$ may be readily computed from any error analysis or orbit determination program. Section II and III illustrate the simpler situation where analytical expressions for these matrices may be found.

Ideally the orbital elements $[\Delta x(t_o)]$ should be chosen such that some measure of the trajectory error ($[\delta x(t)-[\Delta x(t)]$) is minimized. A reasonable and convenient measure may be taken to be the weighted mean-square trajectory error defined as

*For simplicity we use the term orbital elements and their deviations interchangeably.

$$\frac{1}{T}\int_o^T ([\delta x(t)]-[\Delta x(t)]^T[W(t)]([\delta x(t)]-[\Delta x(t)])dt$$

$$= \frac{1}{T}\int_o^T ([\delta x(t)]-[\phi(t,t_o)](\Delta x(t_o)])^T[W(t)] \qquad (13)$$

$$([\delta x(t)]-[\phi(t,t_o)]\,[x(t_o)])dt$$

$$= [\Delta x(t_o)]^T[P][\Delta x(t_o)]-2[\Delta x(t_o)]^T[Q]+[R]$$

$$= ([\Delta x(t_o)]-[P]^{-1}[Q])^T[P]([\Delta x(t_o)]-[P]^{-1}[Q])$$

$$- [Q]^T[P]^{-1}[Q]+[R]$$

where

$$[P] \triangleq \frac{1}{T}\int_o^T ([\phi(t,t_o)]^T[W(t)][\phi(t,t_o)])dt$$

$$[Q] \triangleq \frac{1}{T}\int_o^T ([\phi(t,t_o)]^T[W(t)][\delta x(t)])dt$$

$$[R] \triangleq \frac{1}{T}\int_o^T ([\delta x(t)]^T[W(t)][\delta x(t)])dt$$

$[W(t)] \triangleq$ a non-negative weighting matrix

Since [P] is positive-definite, it is obvious from Eq. (13) that the mean-square trajectory error has the minimum value

$$[R]-[Q]^T[P]^{-1}[Q] \tag{14}$$

which is achieved if the epochal orbital elements are taken as

$$[\Delta x(t_o)]=[P]^{-1}[Q]$$

$$=\left\{\int_o^T ([\phi(t,t_o)^T[W(t)][\phi(t,t_o)]dt\right\}^{-1} \tag{15}$$

$$\sum_i \alpha_i \int_o^T [\phi(t,t_o)]^T[W(t)][G_i(t)]dt$$

The corresponding trajectory error in time becomes

$$[\delta x(t)]-[\phi(t,t_o)][\Delta x(t_o)] \tag{16}$$

$$=\sum_i \alpha_i \left([G_i(t)]-[\phi(t,t_o)]\left\{\int_o^T [\phi(t,t_o)]^T[W(t)]\right.\right.$$

$$\left.\left.[\phi(t,t_o)]dt\right\}^{-1}\int_o^T [\phi(t,t_o)^T[W(t)][G_i(t)]dt\right)$$

obviously the trajectory error vanishes if

$$\sum_i \alpha_i \, [G_i(t)] = [\phi(t,t_o)][K],$$

i.e., if the time characteristics of the actual trajectory perturbations are similar to these of the fictitious trajectory. As mentioned above, the trajectory perturbation matrices $[G_i(t)]$ and the state transition matrix $[\phi(t,t_o)]$ are readily avaibable from most orbit error analysis programs. Thus, once the expected levels of model uncertainties α_i are specified, Eq. (13) and (16) may be readily integrated to give the time history of the expected limiting orbital accuracy as well as the minimum weighted mean-square trajectory error.

Although not a prescription for the optimum tracking and orbit determination strategy, the limiting accuracy thus computed plays a very useful role, i.e., as a yardstick for measuring the performance of any tracking and orbit determination strategy. Once a particular tracking and orbit determination procedure is proposed, the expected trajectory error may be computed from an orbital error analysis program such as ORAN (Ref. 7). A comparison of this error with the limiting accuracy tells us whether that particular strategy is already close to the optimum, or whether there is considerable room for improvement and other strategies should be tried.

To illustrate the result of this section we shall make use of the state-transition matrix and the solar radiation perturbation matrix derived in Section II to study the limiting orbital accuracy in the presence of uncertainties in solar radiation pressure. In essence, solar radiation perturbation appear as diverging sinusoids $\tau\sin\tau$ (sun overhead initially) and $\tau\cos\tau$ (sun behind velocity vector initially). The orbit

determination process may compensate for this perturbation by linear variations in time plus simple sinusoids, i.e., $\alpha+\beta\tau+\gamma\sin\tau+\delta\cos\tau$. The optimum approximations are shown in Fig. 4 and 5 and indicate the approximation for $\tau\cos\tau$ is quite good while that for $\tau\sin\tau$ is less satisfactory. One sees that, ideally, with tracking and orbit determination, it may be possible to reduce the along-track orbital error to approximately $0.512/2\pi \approx 0.08$ of its maximum perturbations for the case when the sun is initially over-head. On the other hand, for the case when the sun is initially behind the satellite velocity vector, tracking and orbit determination is much less effective, and can only reduce the along-track error to approximately $1.5/(3\pi/2) \approx 0.3$ of its maximum perturbations. This is the explanation for the seemingly perplexing phenomenan that although perturbations caused by solar radiation are much more serious starting from the position when the sun is directly over-head, yet the use of tracking may reduce the error considerable so that the orbit determination error may only be one-third as large as the corresponding error starting from the epoch that the sun is behind the satellite velocity vector. The latter case was shown to be comparatively less sensitive to solar radiation perturbations in the absence of tracking.

V. INFORMATION CONVEYED BY RANGE MEASUREMENTS AND VARIATION OF TDRS ORBITAL ERROR WITH TRACKING BASELINE

Since the modeling uncertainties are unknown, it is not possible to compute the optimum orbital elements according to Eq. (15) in the preceeding section. In practice, the orbital elements are computed such that the resulting fictitious trajectory fits the measurements. Different kinds of measurements convey information about different aspects of the trajectory. If the measurements contain more information about

the orbital height, then the computed orbit would tend to fit the correct height at the expense of, say, along-track accuracies. Thus it is important to know the information content of the measurements in order to understand orbit determination accuracies in the presence of modeling errors.

Tracking of TDRS consist of bilateration from two ground stations (Fig. 6). Expressed in terms of deviations from the nominal, the range measurements may be written as

$$\delta\rho_1 = \vec{\delta R} \cdot \vec{i}_1$$

$$\delta\rho_2 = \vec{\delta R} \cdot \vec{i}_2$$

where $\vec{\delta}_R$ is the satellite position deviation and the $\vec{i}$'s are unit vectors in station-to-TDRS directions. One may consider these equations as describing the resolution of the unknown position deviation $\vec{\delta R}$ along the directions defined by the unit vectors $\vec{i}_1$ and $\vec{i}_2$. For the high altitude TDRS, these are close to the orbital radius direction. In other words, individial measurements convey mostly orbital height information Along-track and cross-track information is contained in an equation obtainable by multiplying the above equations by the range ρ_1 and ρ_2 respectively and then subtracting one from the other, i.e.,

$$\rho_1\delta\rho_1 - \rho_2\delta\rho_2 = \vec{\delta R}\cdot(\vec{\rho}_1 - \vec{\rho}_2) = \vec{\delta R}\cdot(\vec{r}_1 - \vec{r}_2),$$

where $(\vec{r}_1 - \vec{r}_2)$ is the tracking baseline, i.e., the vector connecting the two tracking stations. To increase the sensitivity and therefore the information content one should select the tracking stations such that

1. $|\vec{r}_1 - \vec{r}_2|$ is as large as possible.

2. $\vec{r}_1 - \vec{r}_2$ should have a large component in the important along-track direction. However it should also have some component in the cross-track direction to sense cross-track errors.

Error analysis results on TDRS orbital accuracy for a series of different ground transponder locations are given in Ref. 2. The central ground terminal is considered fixed at White Sands, New Mexico (254° Longitude, 32° Latitude). Tracking baseline geometry changes with ground transponder location which varies at certain increments of longitude and latitude. To bring out the connection between orbital errors and bilateration baseline, the orbital errors given in Ref. 2 were correlalated with parameters defining the tracking baseline such as the baseline great circle length and inclination, along-track and cross-track baseline length, and latitude and longitude separation of the two stations. Representative results showing the close correlation between the along-track and cross-track orbital errors and the corresponding tracking baseline components are presented in Table 1 and Fig. 7, from which the following information may be extracted:

1. For the error model considered, orbital errors vary from approximately 110 meters to 350 meters. The latter occurs when the transponder location is unfavorable.

2. There is good correlation between cross-track orbital error and the component of tracking baseline in the cross-track direction. When the cross-track error is less than 50 meters, it has a negligible contribution to the RSS total error. In general this requires the tracking baseline to have a component in the cross-track direction greater than 0.7 of the earth's radius.

3. There is also good correlation between along-track orbital error and the component of tracking baseline in the along track direction. To limit the along-track error below 140 meters, a baseline component length of 1.2 earth radius is required. A baseline component lenght of 1.5 earth radius is required to keep the along-track error under 120 meters.

4. Since the TDRS's considered have 7° inclination, they are not quite geo-stationary. The along-track and cross-track components of the bilateration baseline used in the preceeding paragraphs are somewhat arbitrarily computed assuming the TDRS's are at the ascending node. More convenient but less precise characterizations of the along-track and cross-track baseline components are the longitude and latitude separations of the two stations. For the central terminal fixed at 254° Longitude and 32° Latitude, the transponder should preferably be located in the southern hemisphere with a longitude separation as large as practicable.

VI. RANGE-RATE MEASUREMENTS AND INSENSITIVITY OF RANGE-RATE ORBIT SOLUTIONS TO GM ERROR

The range-rate from a tracking station to a satellite may be expressed as

$$\dot{\rho}=\vec{v}\cdot\vec{i}_{\rho}$$

where $\vec{v}$ is the velocity of the satellite relative to the rotating earth. Thus the deviations are,

$$\delta\dot{\rho}=\vec{v}\cdot\delta\vec{i}_{\rho}+\delta\vec{v}\cdot\vec{i}_{\rho}$$

The unit vector i_ρ is close to the radial direction. δi_ρ is orthogonal to $\vec{i}_\rho$ and is primarily the result of the along-track and cross-track position deviations. Thus the range-rate measurement convey radial velocity information together with some positional information. For the geosynchronous TDRS $\vec{v}$ is primarily in the cross-track direction. Thus the along-track positional information content is weak in the range-rate measurements.

Since the TDRS is nearly geo-stationary, range tracking contains much more information than range-rate tracking, and the TDRS orbits are computed essentially from range measurements. However it is known from error analysis studies that orbits of TDRS or other high altitude satellites such as the GPS spacecraft are much less sensitive to GM errors if the orbit solutions are based on range-rate rather than range trackings. This may be explained as follows. It was shown in Section III that GM uncertainty causes a perturbation which as the following time characteristics

$$\begin{bmatrix} \text{Height} \\ \text{Radial Velocity} \\ \text{Along-Track Position} \end{bmatrix} \propto \begin{bmatrix} \cos\tau - 1 \\ -\sin\tau \\ 2(\tau - \sin\tau) \end{bmatrix}$$

On the other hand, trajectory error propagated from initial height error has the following characteristics

$$\begin{bmatrix} \text{Height} \\ \text{Radial Velocity} \\ \text{Along-Track Position} \end{bmatrix} \propto \begin{bmatrix} \frac{4}{3} - \cos\tau \\ \sin\tau \\ 2(\sin\tau - \tau) \end{bmatrix}$$

Since range-rate measurements convey mostly radial velocity information, the computed orbit tends to fit the radial velocity perturbation by attributing it to an initial height deviations. The above equations show this also gives a correct along-track position while there would be a constant height error. Indeed this is what error analysis result tells us. Physically this is also obvious. With a correct orbital period, an incorrect GM would result in an incorrect semi-major axis or height. On the other hand, an orbital solution based on range tracking would tend to fit the height and as the above equations show, must result in along track errors. Along-track errors are usually larger than height errors, thus range tracking orbital solutions are more susceptible to GM errors.

In general, perturbation due to GM uncertainty has a time characteristic quite similar to the time characteristic of a trajectory propagated from some initial conditions. Thus tracking can compensate for GM uncertainty much more than, say the solar radiation uncertainty.

VII. ORBIT DETERMINATION ERROR CHARACTERISTICS

Much of the orbit determination error characteristics may be illustrated or explained based on the simplified orbit model derived in Section II. It is shown there that by adjusting the epochal elements $[\delta\rho(0)\ \dot{\delta\rho}(0)\ R\delta\theta(0)\ R\dot{\delta\theta}(0)]$, trajectory deviations of the following form may be obtained.

$$\begin{bmatrix} \delta o(\tau) \\ \dot{\delta\rho}(\tau) \\ R\delta\theta(\tau) \\ R\dot{\delta\theta}(\tau) \end{bmatrix} = \begin{bmatrix} 4-3\cos\tau & \sin\tau & 0 & 2(1-\cos\tau) \\ 3\sin\tau & \cos\tau & 0 & 2\sin\tau \\ 6(\sin\tau-\tau) & 2(\cos\tau-1) & 1 & 4\sin\tau-3\tau \\ 6(\cos\tau-1) & -2\sin\tau & 0 & 4\cos\tau-3 \end{bmatrix} \begin{bmatrix} \delta\rho(0) \\ \dot{\delta\rho}(0) \\ R\delta\theta(0) \\ R\dot{\delta\theta}(0) \end{bmatrix}$$

The following characteristics of the trajectory time history as described by the above equations may be emphasized:

1. Along-track position may have constant deviations, linear growth, as well as sinusoidal variations at orbital frequency.

2. Other orbital position and velocity deviations may exhibit constant biases plus sinusoidal variations at orbital frequency.

3. The trajectory may be shifted by a constant amount in along-track position without affecting other aspects of the trajectory.

In contrast, "real perturbations", governed by the equations of motion (2a) and (3a), may consist of linearly diverging oscillations, constant amplitude high frequency oscillations, as well as linear and quadratic growth in the along-track position. Thus orbits computed cannot account for the high frequency components, nor any secular growth in the orbital height, nor any diverging oscillations or any "super-linear" growth in along track position.

- Large Errors Near Beginning And End of Tracking Arc, Oscillatory Behavior of Orbital Errors, and Deterioration of Accuracy With Length of Tracking Arc

The phenomena described by the above statement are frequently observed in the course of orbital error analysis studies. The explanation for the occurrence of these phenomena is almost obvious from the preceding discussions. Generally, along-track orbital errors are the most serious, as any perturbations in orbital rate will propagate into large along-track position errors. Fig. 8 illustrates that the along-track position

perturbations generally consist of "super-linear" growth with diverging oscillations at the orbital rate together with possible constant-amplitude high frequency oscillations characteristics of some perturbation forces. On the other hand, computed orbits tend to approximate this perturbation by linear gorwths plus constant amplitude sinusoidal oscillations (not shown) at the orbital rate. Line A represents perhaps the best approximation one may hope for. Line B and C represent progressively worse orbits. In any case, orbital accuracies are going to deteriorate as tracking arc lenghtens. If tracking measurements convey along-track position information, most commonly one has the situation represented by the line B, which is characterized by larger and opposite errors at the beginning and the end of the tracking arc, and reduced errors in the middle. It is also obvious that high frequency excitations contained in the perturbative force will persist as high frequency orbital errors although the amplitudes may be somewhat attenuated because, as shown before, the satellite radial motion behaves as a simple harmonic oscillator tuned at the orbital frequency and that there exists coupling between the radial and along-track motions.

The above theory has since been validated and found fruitful applications in the study of the effect of drag on low altitude satellite orbit determination (Ref. 8).

VIII. REFERENCES

1. Fang, B.T., and Gibbs, B.P., "TDRSS Era Orbit Determination Review Study," Planetary Sciences Department Report No. MT010-75, Wolf Research and Development Group, EG&G Washington Analytical Services Center, Inc., December 1975.

2. Campion, R.E., "TDRS Error Analysis," Tracking Data Evaluation Office, Bendix Corp., October 17, 1977.

3. Shrivastava, S.K., "Orbital Perturbations and Station Keeping of Communication Satellites," J. of Spacecraft, March-April, 1978.

4. Fang, B.T., "Short-Term Solar Pressure Effect and GM Uncertainty on TDRS Orbital Accuracy - A Study of the Interaction of Modeling Error With Tracking and Orbit Determination," Applied Systems Department Report No. 002-78, EG&G Washington Analytical Services Center, Inc., October, 1978.

5. Geyling, F.T., and Westerman, H.R., "Introduction to Orbital Mechanics," Addison Wesley, Reading, Mass.. 1971.

6. Fang, B.T., and Brown, J.H., "Orbital Guidance and Rendezvous Using Perturbation Method," AIAA Paper No. 67-55, January 1967.

7. Hatch, W., and Goad, C., "Mathematical Description of the ORAN Error Analysis Program," Wolf Research and Development Corporation Report No. 009-23, August 1973.

8. Fang, B.T., "Orbit Determination and Navigation Studies (TDRSS/GPS)" Applied Systems Department Report No. 004-78, EG&G Washington Analytical Services Center, Inc. November 1978.

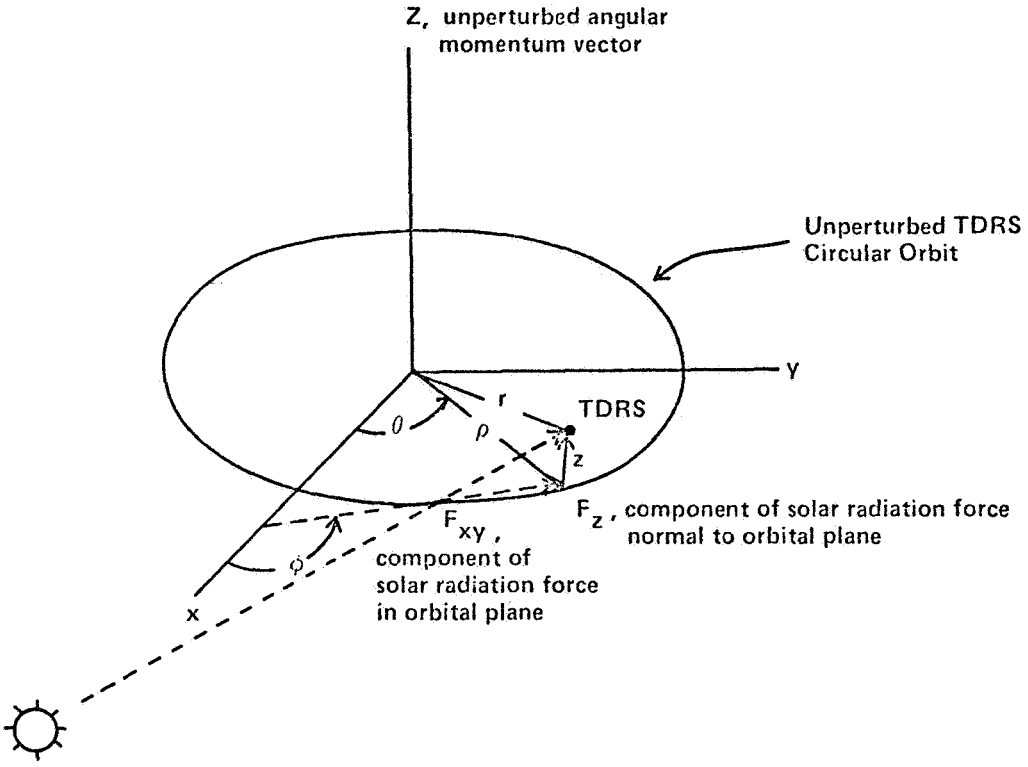

FIGURE 1. COORDINATE AXES AND RELATIVE GEOMETRY OF TDRS AND SUN

f_{xy} = component of solar radiation force (normalized) in TDRS orbital plane

ϕ = angle between f_{xy} and orbital radius vector at $\tau = 0$

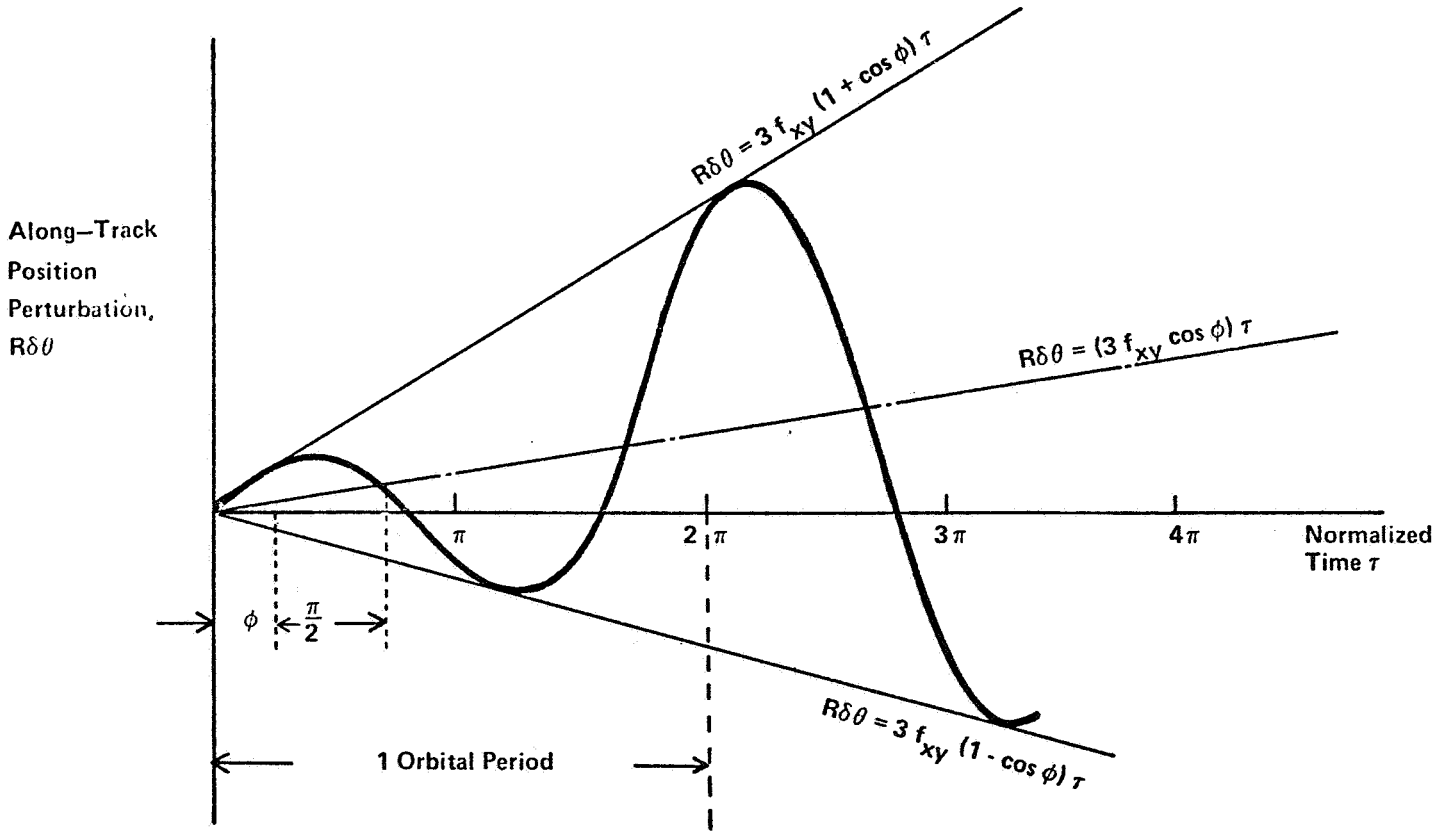

FIGURE 2. VARIATIONS OF ALONG–TRACK ORBITAL POSITION PERTURBATION Rδθ WITH NORMALIZED TIME τ AND INITIAL SUN ANGLE ϕ

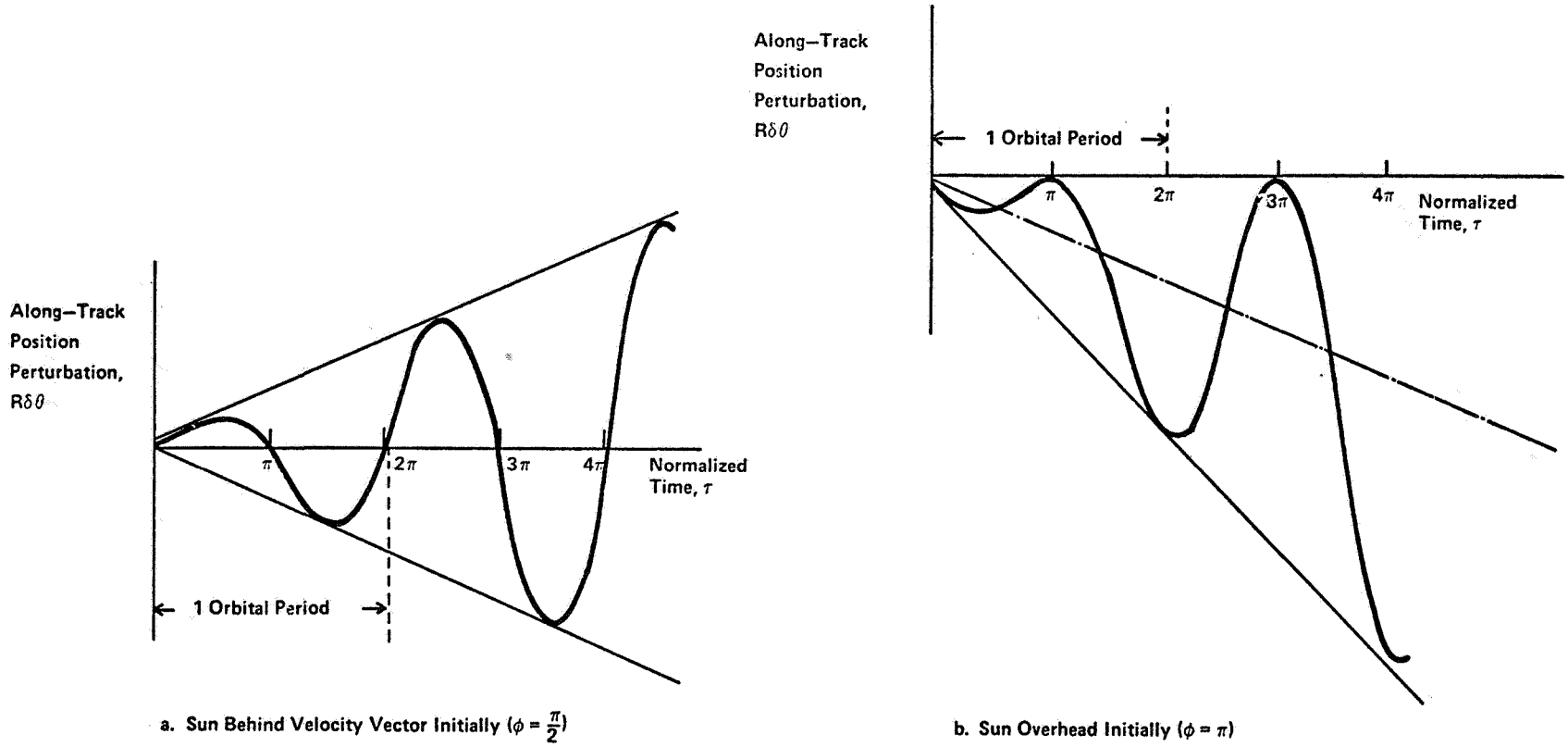

a. Sun Behind Velocity Vector Initially ($\phi = \frac{\pi}{2}$)

b. Sun Overhead Initially ($\phi = \pi$)

FIGURE 3. ALONG TRACK POSITION PERTURBATION CAUSED BY SOLAR RADIATION PRESSURE

FIGURE 4. DIVERGING SINUSOID $\tau \sin \tau$ AND THE APPROXIMATION BY $\pi \sin \tau - \frac{1}{2} \cos \tau - 1$

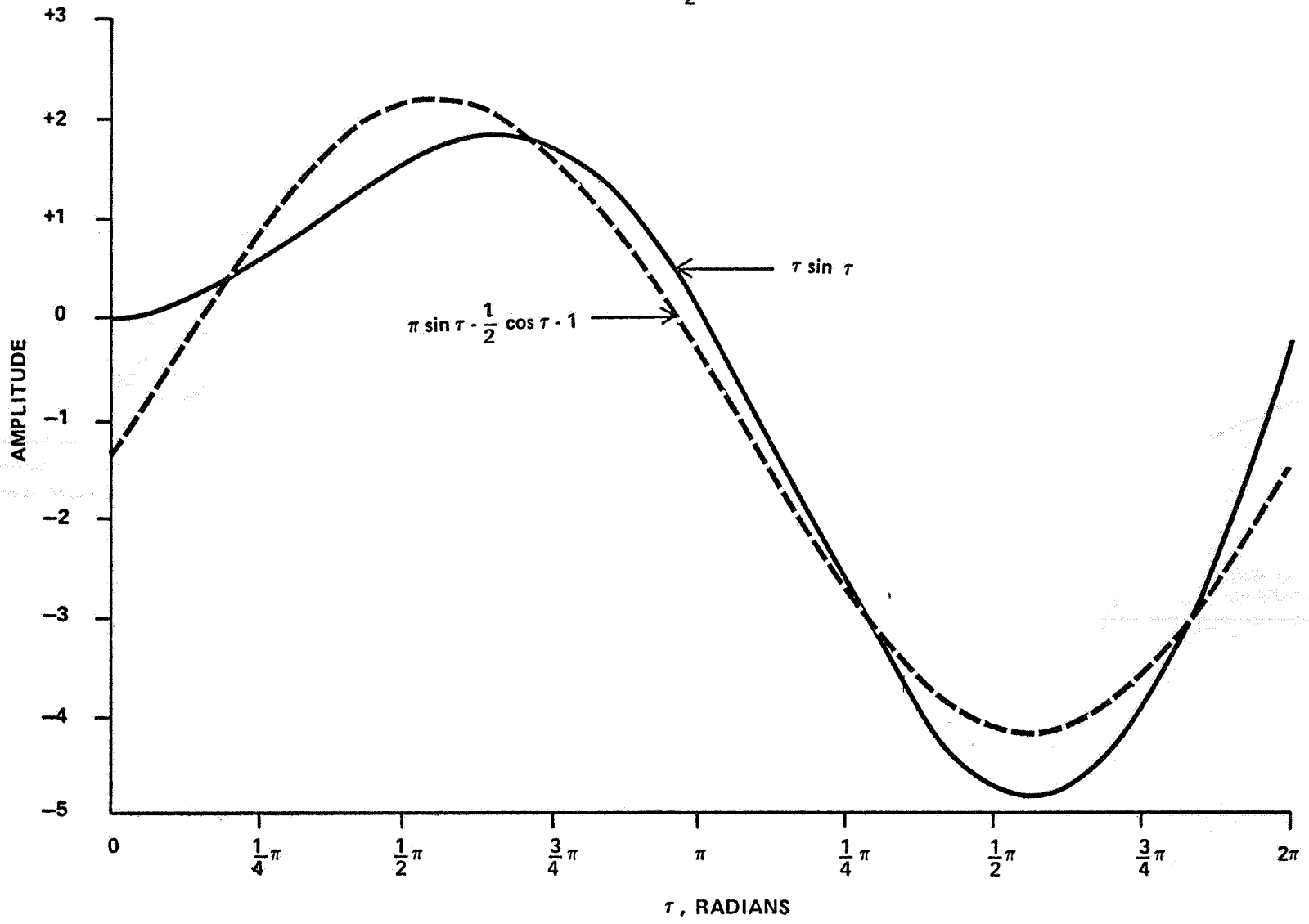

FIGURE 5. DIVERGING SINUSOID $\tau \cos \tau$ AND APPROXIMATIONS BY
$\pi \cos \tau + 1.8258 \sin \tau + 1.1634 \tau - 3.6534$

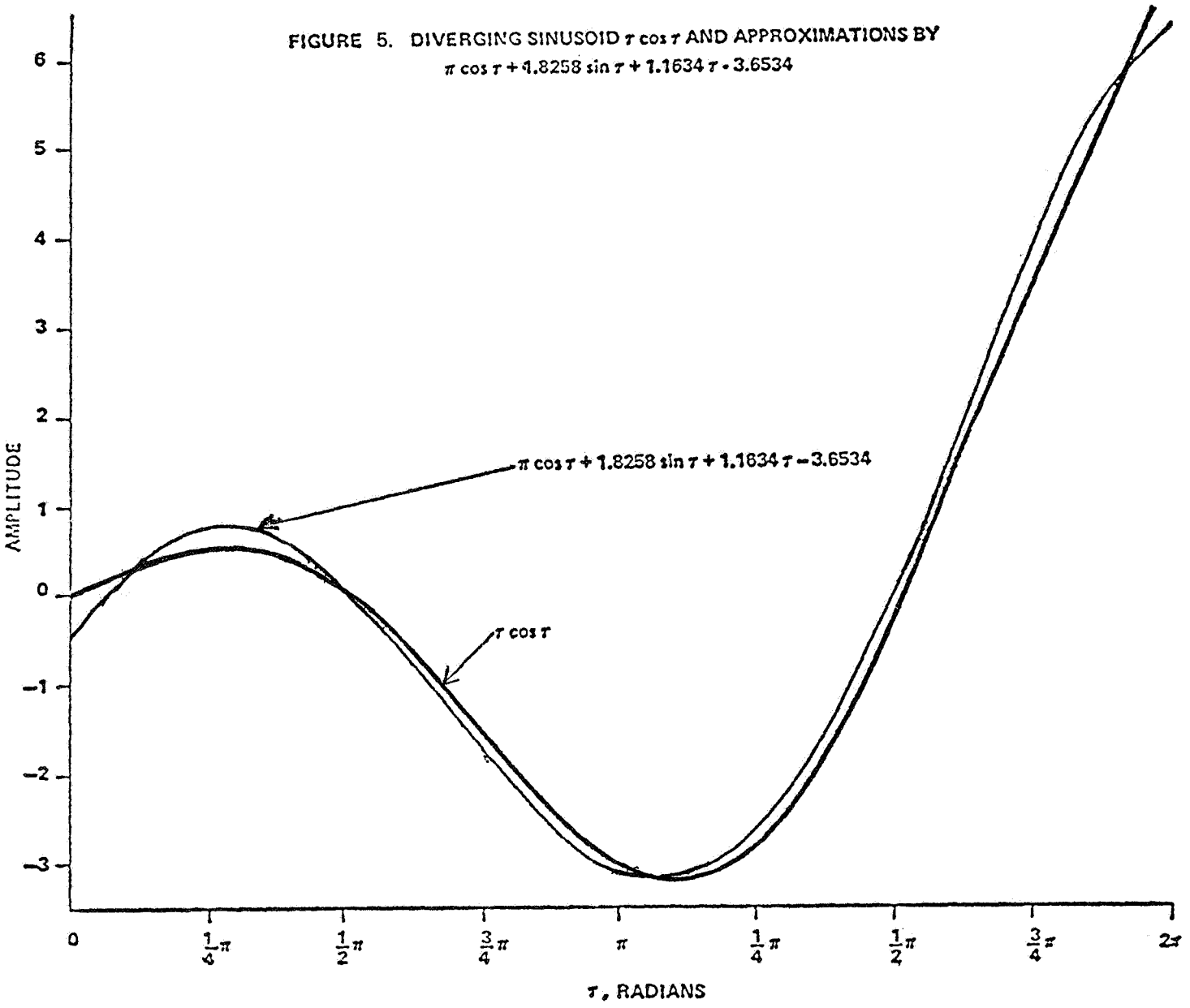

FIGURE 6. INFORMATION CONTENT OF RANGE MEASUREMENTS

INDIVIDUAL MEASUREMENTS GIVE HEIGHT INFORMATION

$$\delta\rho_1 = \delta\bar{R} \cdot \bar{i}_1$$

$$\delta\rho_2 = \delta\bar{R} \cdot \bar{i}_2$$

BILATERATION GIVES INFORMATION ALONG TRACKING BASELINE

$$\rho_1 \delta\rho_1 - \rho_2 \delta\rho_2 = \delta\bar{R} \cdot \underline{(\bar{r}_1 - \bar{r}_2)}$$

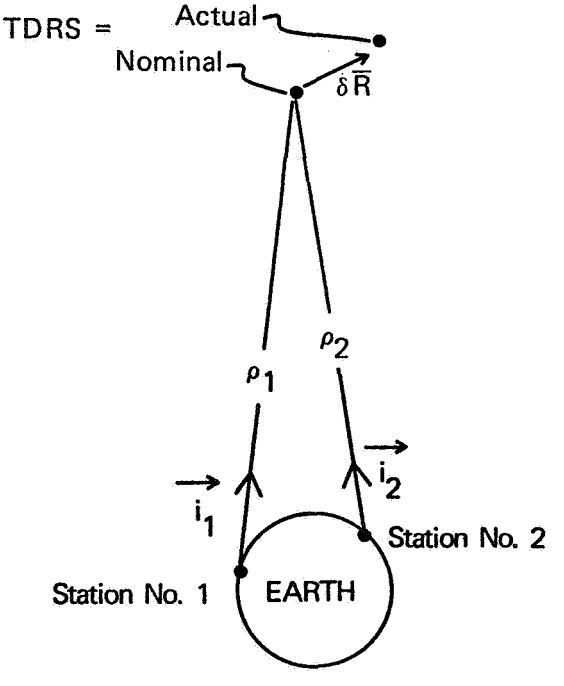

FIGURE 7. TDRS–W ALONG–TRACK POSITION ERROR VS. BILATERATION BASELINE ALONG–TRACK COMPONENT

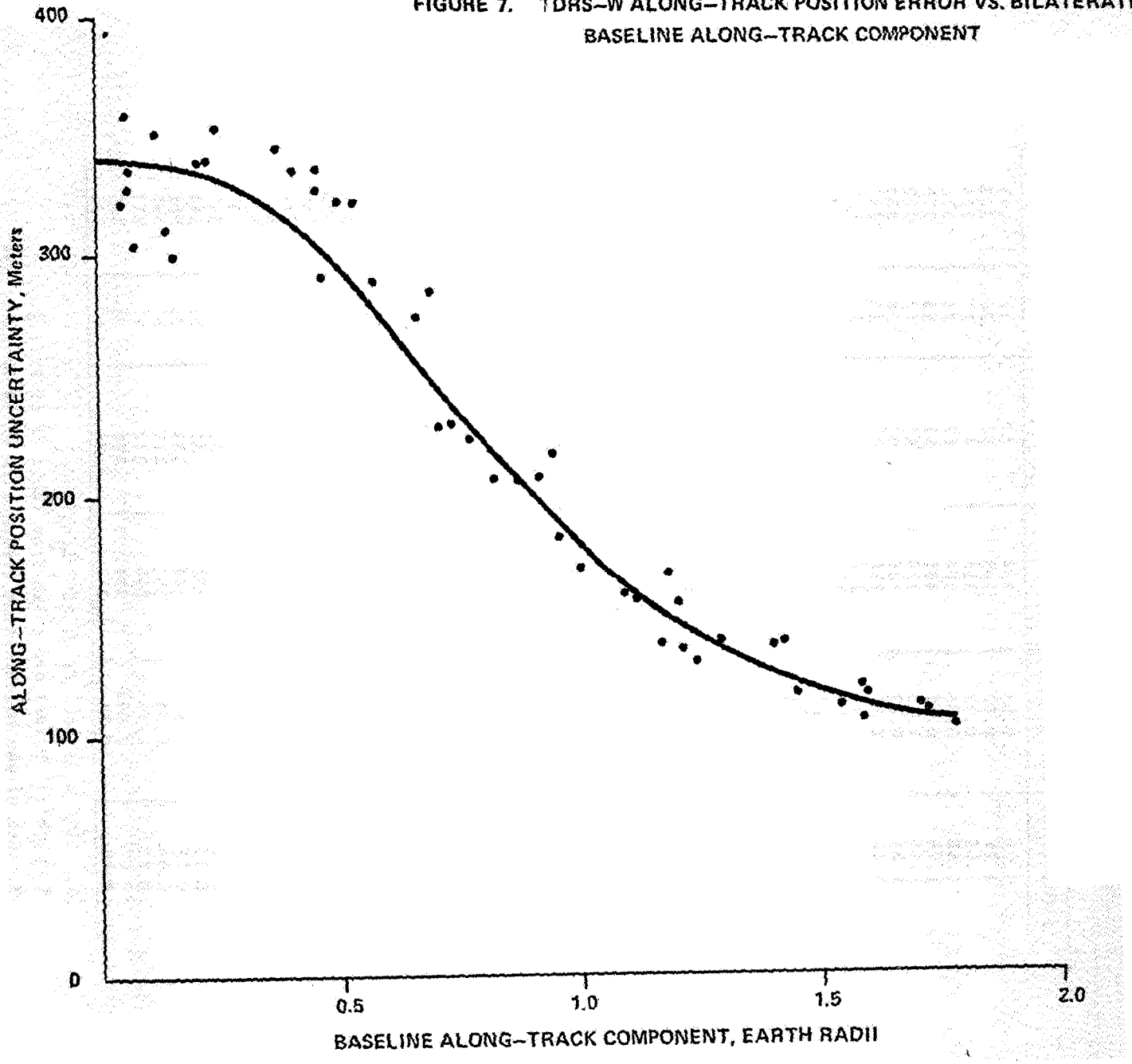

Table 1. Correlation of TDRS-W Orbital Error With Bilateration Baseline Geometry

BILATERATION BASELINE COMPONENT (earth rad.)		ORBITAL ERROR (m.)			
ALONG-TRACK	CROSS-TRACK	ALONG-TRACK	CROSS-TRACK	RADIAL	RSS TOTAL
1.78	0.58	104	67	16	111
1.71	0.82	109	51	16	113
1.53	0.71	111	49	17	115
1.58	0.35	104	81	16	116
1.78	0.32	103	91	15	122
1.58	1.03	119	41	17	122
1.24	0.39	128	64	18	134
1.40	1.21	136	35	18	139
1.29	1.04	137	32	19	139
1.21	0.57	135	47	19	139
1.17	0.22	136	88	18	147
1.71	0.68	108	132	18	159
1.09	0.77	168	35	21	161
1.44	0.00	115	138	18	166
1.18	1.33	165	34	21	169
1.20	0.45	154	96	20	178
1.13	0.26	155	105	22	179
1.42	0.32	136	124	20	184
1.00	0.06	168	122	21	188
1.59	0.15	115	166	22	192
0.96	0.52	181	108	21	205
0.87	0.86	205	32	25	208
0.82	0.44	205	38	25	209
0.92	1.20	206	30	25	209
0.94	1.40	215	37	26	219
0.73	0.32	227	95	28	237
0.77	0.02	222	129	27	241
0.71	0.52	226	106	24	245
0.66	0.82	273	35	31	275
0.69	1.40	283	41	32	287
0.57	0.11	287	109	31	303
0.14	0.56	298	42	36	304
0.07	0.81	303	30	37	307
0.46	0.58	289	114	30	308
0.53	1.14	319	36	36	321
0.50	0.65	320	37	35	323
0.05	1.02	320	32	38	323
0.14	0.30	309	100	35	326
0.06	0.53	326	42	37	331
0.40	0.50	325	63	34	333
0.45	1.33	333	37	37	335
0.40	0.49	333	42	36	337
0.21	0.87	337	32	39	340
0.23	1.20	338	32	39	341
0.37	0.17	343	138	38	361
0.24	0.34	351	118	37	368
0.12	0.16	350	142	37	377
0.07	0.06	334	198	39	385
0.06	0.16	357	184	40	396

1. TDRS-W is located at 189° Longitude.
2. Orbital errors are taken from Table 38 of Ref. 2.
3. One of the bilateration stations is White Sands at 254° Longitude and 32° Latitude. The other station (transponder) location varies, giving rise to different baseline geometry.

TRANSFER TRAJECTORY DESIGN FOR A SHUTTLE LAUNCHED GEOSYNCHRONOUS PAYLOAD

R. L. DeFazio

Goddard Space Flight Center

ABSTRACT

Some geosynchronous payloads deployed from the Space Shuttle will require the use of a Spin Stabilized Upper Stage (SSUS) to place the spacecraft on its transfer trajectory. The SSUS is a solid propellant motor with fixed impulse and is to be manufactured in two sizes. The SSUS-A is being designed to boost payloads that previously would have been placed into the transfer orbit by an Atlas-Centaur launched vehicle. For lighter payloads of the Delta launch vehicle class, the SSUS-D is being designed. This discussion will involve the use of a SSUS-A motor to launch a geosynchronous payload from the Shuttle.

When designing the transfer trajectory, the performance characteristics of the SSUS should be matched with those of the payload's Apogee Kick Motor (AKM) to provide a mission orbit that will best satisfy all requirements. Occasionally, cost considerations will dictate that a particular SSUS and AKM be used together even if they seem somewhat incompatible. The pairing of two such motors will be discussed by observing the problems which were noted and their possible solutions. During the discussion, the SSUS will also be referred to as the Perigee Kick Motor (PKM).

I. INTRODUCTION

In the case to be examined, a SUSS-A will be used for the Shuttle launching of the next series of Geostationary Operational Environmental Satellites (GOES). The SSUS-A has significantly more propulsion capability than the GOES spacecraft requires from a PKM. On the other hand, the AKM provided for GOES is somewhat undersized. In designing a transfer trajectory for GOES, an attempt will be made to choose an orbit which tends to balance the excess capability of the SSUS-A and the deficiency of the AKM. The transfer orbit design must include an evaluation of the PKM as it is fired to move the spacecraft from the Shuttle parking orbit to the transfer trajectory. Then the firing of the AKM to place the spacecraft from the transfer to the drift orbit must be factored in. See Figure 1. Once the two motors have been fired, the yardstick for evaluating the acceptability of the transfer orbit is the amount of trim fuel required to get the spacecraft to its desired geostationary position. This trim fuel is hydrazine for the spacecraft's auxiliary propulsion system. It is used to perform a series of maneuvers at apogee and perigee in the drift orbit to attain the geosynchronous orbit. These maneuvers, also called a station acquisition sequence, are carefully planned such that the final maneuvers will stop the spacecraft at the desired on-station longitude. See Reference 1.

II. STUDY PARAMETERS AND ASSUMPTIONS

Before examining study procedures, it is appropriate to review all the parameters and assumptions used in this study. Table 1 contains the study parameters, including information about PKM and AKM firing errors. In the case of AKM errors, it was possible to draw from actual experience that included results on eight previous AKM firings. PKM firing information was extracted from Shuttle documentation with no actual firing experience available. This situation concerning PKM errors will continue until actual flight data can be evaluated. Assumptions made in the study can be reviewed in Table 2.

III. COMPARISON OF MOTORS

When given a PKM and AKM that are mismatched in propulsion capability, the design of the transfer orbit is complicated. For a clearer picture for how PKM and AKM sizes can vary, a comparison is made of the solid motors associated with the GOES-C and GOES-D missions. In Table 3, one observes that the PKM delta-V for GOES-C (actually the Delta 3rd Stage) is substantially less than the GOES-D PKM delta-V. This is not surprising, for as stated earlier, the SSUS-A has the same payload capability as the Atlas-Centaur launch vehicle. On the other hand, the GOES-C AKM is larger than the GOES-D AKM by over 200 meters/second. By some method the extra capability of the SSUS-A must be managed in such a way as to minimize any problems caused by this excessive PKM delta-V, and, if possible, to compensate for the undersized AKM.

IV. EXCESSIVE PKM PERFORMANCE

When a solid motor such as the SSUS-A is too large, the delta-V can be reduced in at least three ways which are summarized in Table 4. The motor's propellant may be off-loaded if the costs involved are not prohibitive. In the example under consideration, a fixed price contract made this choice unacceptable. A second choice involved a non-optimum trajectory where the excess performance can be dissipated by proper placement and orientation of the velocity vectors.[a] Whereas, this method handles excess delta-V, it also generates some additional problems. The nominal trim delta-V required to attain the mission orbit is significantly greater than for the other methods. Also new operational problems arise such as increasing the possibility of violating the solar aspect angle constraint[b] when targetting the PKM and AKM. Additionally the mission operations may involve large drift rates, greater than 50 degrees per day, following AKM firing. The third possibility concerns planning a fuel optimum transfer trajectory by adding ballast. Up to 1480 pounds of ballast can be added to the SSUS-A, thereby allowing the PKM delta-V to vary between 3659 and 2821 meters per second. See Table 5. This main portion of this study involves examining a strategy which considers adding ballast to the SSUS-A, to obtain a suitable transfer trajectory.

V. IDENTIFYING ERROR SOURCES

To gain a perspective on this study, an attempt was made to identify the major errors resulting from the PKM and AKM burns. The effect of these errors was of particular interest as they related to trim delta-V penalty. Also, any complications caused in the mission operations were noted. Those errors considered in this study were of three basic types.

1. Timing error when firing the PKM and AKM.
2. Pointing error for the PKM and AKM.
3. Thrust error for the PKM and AKM.

The errors having the most significant effect of trim delta-V penalty will be noted.

(a) Reference 2
(b) This is a thermal constraint which states that the sun must at all times be within $\pm$ 30 degrees of the spacecraft's spin plane.

Timing Error - A PKM firing error of 10 seconds contributes less than 4 meters/second to trim delta-V penalty. See Figure 2. The results are symmetric for a plus or minus timing error. Current estimates indicate that PKM firing will occur within 5-6 seconds of the desired time, thus PKM firing time error has a minor effect. The AKM firing error is even less significant. Errors of up to ±1 minute would only cause a few meters/second increase in trim fuel penalty.

Thrust and Pointing Errors - When thrust and pointing errors were examined for the PKM and AKM firings, it was observed that trim delta-V was extremely sensitive to changes in PKM declination. See Figure 3. For small changes in PKM declination, the trim fuel can change rapidly. Next, it was important to understand how this major error source combined with other potential errors. In Figure 4, on the upper curve, all (3σ) thrust and pointing errors for the PKM and AKM are considered. Assuming all these errors are independent, they can be root-sum-squared (RSS) If all the thrust and pointing errors except PKM declination are taken at their (3σ) levels and RSS together, they yield a (3σ) trim delta-V of 33 meters/second. Then, as PKM declination error is RSS with this total (reflected on the lower curve), the upper and lower curves move together rapidly. For example, if the total (3σ) trim delta is 60 meters/second, this reflects a trim delta-V penalty of 50 meters/second due to PKM declination error alone. Based on these results and for the purpose of this study, PKM declination error will be the dominant error source considered when designing the transfer trajectory.

VI. STUDY PROCEDURES

The procedure used to evaluate the method of ballasting the SSUS-A is outlined as follows:

1. For a given PKM size, study the effect of PKM declination, the most significant error source, on transfer inclination and apogee height.

2. For each transfer inclination/apogee bias combination, define the drift orbit resulting from AKM targetting to 1.0 degree inclination and a 90^{0} nodal rotation.

3. For each drift orbit, define trim delta-V reqirements.

4. Select a PKM declination which "optimizes" delta-V requirements for that PKM size. This selection will yield the nominal transfer trajectory.

5. Repeat the experiment for various PKM sizes.

VII. CHOOSING A NOMINAL

The selection of a nominal transfer trajectory in item (4) above requires careful evaluation. For nearly all pre-Shuttle geosynchronous missions, the nominal was chosen as that transfer trajectory which provided for minimum trim delta-V usage when obtaining the mission orbit. Such a method was very satisfactory because the motor involved was well matched to the mission. However, for this study, PKM attitude errors coupled with excess PKM propulsion capability result in significantly larger transfer orbit dispersions than on previous missions. Therefore, in attempting to minimize the impact of these dispersions, the effect of PKM pointing error will be factored into the choice of a nominal.

The example illustrated in Figure 5 will explain how a nominal is chosen. Suppose the minimum delta-V was chosen as the nominal with trim fuel equal to 125 meters/second. If PKM declination decreased by 2.2 degrees, the trim delta-V would rise to nearly 240 meters/second, which exceeds the fuel budget. Instead, let the nominal be at the mid-point of a range of PKM declinations any of which can satisfy the trim delta-V budget. Choosing the mid-point may add a small amount of delta-V to the nominal. However, this technique adds a margin of assurance that trim delta-V will remain within the fuel budget even if the PKM declination error reaches the (3σ) level.

VIII. RESULTS

After a series of nominal transfer trajectories was computed for various PKM delta-V's, the next step was a comparison of these results. In Figure 6, the transfer inclinations vs the PKM delta-V's is shown. For the no ballast case, the nominal inclination is 10.9 degrees and rises to 20.1 degrees for the full ballast case. This is the amount of inclination remaining after the PKM removes a portion of the Shuttle parking orbit inclination. The AKM is used to remove the balance of the inclination leaving the final inclination at the value desired for the mission orbit. Since the AKM is already under-sized, it requires additional help to accomplish the larger plane changed necessitated by adding ballast to the SSUS. The help for the AKM comes in the form of a larger apogee bias in the transfer trajectory. An apogee bias is defined as the difference between apogee radius in the transfer orbit and geosynchronous radius. As apogee bias increases, the AKM delta-V can accomplish more because it is working against a lower apogee velocity in the transfer orbit.

Before examining the apogee biases that correspond to the inclinations mentioned, a quick look will be taken at inclination dispersions in the transfer orbit. For a ($\pm 3\sigma$) error in PKM thrust and pointing, dispersions in inclination stay within $\pm$ 0.6 degrees over the range of PKM delta-V's. See Figure 6.

Transfer trajectory apogee biases for the various ballast situations are shown in Figure 7. The apogee bias for the no ballast case is +1381 km and increases to +5064 km for the full ballast case. Dispersions in apogee bias are also shown in Figure 7. For lower ballast cases the dispersions are much larger because any PKM thrust or pointing errors present will produce more dispersion for a larger delta-V. Thus, adding ballast seems to decrease the magnitude of dispersions for apogee bias. If apogee biases are significantly higher or lower than the nominal the following can occur:

1. Increased trim delta-V is required to attain the on-station location.

2. The drift rate of the s/c will probably increase.

3. The number of maneuvers needed to arrive on station will increase.

Thus, apogee bias dispersions can lead to increased trim fuel usage and numerous operational problems.

As PKM delta-V is changed by adding ballast, the trim delta-V for the nominal and dispersion cases also changes. See Figure 8. For the no ballast case, the nominal trim delta-V is 55 meters/second. This value rises to 172 meters/second for full ballasting of the SSUS-A. The (3σ) trim delta-V is 214 meters/second for no ballast and decreases to a minimum of about 150 meters/second if approximately 1000 lbs of ballast is used. The curve labelled (3σ) trim delta-V in Figure 8 reflects the maximum trim delta-V when comparing a (3σ) high case and a (3σ) low case for each PKM delta-V. The minimum is the intersection of the (3σ) high and (3σ) low curves. The (3σ) error discussed here reflects a Shuttle deployment error of 2.0 degrees and an Automatic Nutation Control error of 1.0 degrees. When these are RSS together the (3σ) error becomes 2.2 degrees. From the information shown on Figure 8 the principal conclusions can be drawn on the use of ballasting to manage PKM delta-V.

Clearly, adding ballast lowers the dispersion trim fuel. However, the nominal trim fuel rises when ballast is added. For example if enough ballast is added to minimize the (3σ) trim fuel, the nominal trim fuel rises from 55 meters/second (no ballast) to 130 meters/second (1100 lbs of ballast). By minimizing the (3σ) trim fuel the chance of staying within the fuel budget increases, but the nominal trim fuel rises to almost the level of the dispersion trim fuel. In the event of a contingency, even the nominal mission could be jeopardized.

The decision on minimizing dispersions by adding ballast to the SSUS, becomes a question of the philosophy that a spacecraft project will adopt. It has already been stated that adding enough ballast to minimize the (3σ) trim fuel will also increase the nominal trim fuel substantially. Most probably a spacecraft project would not choose such an option. The majority of transfer trajectory dispersions are either within (1σ) or they are greater than (3σ). A more likely choice for a project is to add enough ballast to lower the (3σ) trim fuel to the level of the fuel budget. Such a move would assure the possibility of handling a (3σ) dispersion while only increasing the nominal trim fuel slightly. In Figure 8, the fuel budget can be met for a (3σ) trim fuel dispersion by adding about 200 lbs. of ballast. This amount of ballast only increases the nominal trim fuel from 55 to 70 meters/second.

The key to making the decision on adding ballast, is the Shuttle deployment error. Until several spacecrafts using a SSUS-A are deployed, both Johnson Space Center (JSC) and the originators of these payloads will be forced to live with conservative forecasting of deployment errors. JSC will continue to quote very conservative Shuttle deployment errors until post-flight calibrations disprove these estimates. Meanwhile, the spacecraft projects will have to live with these error estimates and try to reduce their most adverse effects by adding some ballast to the SSUS.

In Table 6 a summary is provided of the 8 cases used to study the effect of adding ballast to the SSUS-A. Most of this information has been shown in graphical form with one exception that should be noted. The drift rate following AKM firing is shown for the nominal in each case. When the nominals were chosen, drift rate was not one of the parameters considered. However, it became apparent that the method chosen for selecting the nominal yielded relatively low drift rates, less than 5 degrees/day. From an operational point-of-view, this result was very desirable. Following AKM firing a low drift rate in the drift orbit allows more time for planning the station acquisition sequence. On the other hand a high drift rate requires immediate action if the spacecraft is drifting in the wrong direction or could drift past the station.

From previous experience on geosynchronous satellites the mission operations are most easily performed when the apogee bias in the drift orbit is above geosynchronous altitude and the perigee bias is below geosynchronous. The principal benefits of this type of drift orbit are:

1. Fewer spacecraft reorientations if axial jets are used to perform station acquisition maneuvers.

2. Drift rates are generally kept lower during the station acquisition sequence by moving toward a geosynchronous orbit in steps along the zero degree drift rate line.

In Figure 9, observe that the desired situation occurs in the fourth quadrant. The broken lines show biases and drift rates for various amounts of ballast. From Figure 9, it is possible to observe what dispersions can do to the biases and drift rate. Without adding considerable ballast to the SSUS-A, i.e. more than 1100 lbs., dispersions of (3σ) or less can cause the drift orbit conditions to fall outside this fourth quadrant. Unfortunately adding this much ballast drives the nominal trim delta-V to a level more than 3 times greater than for the no ballast case. Thus, operational considerations will probably assume a secondary role to that of keeping trim fuel at acceptable levels when adding ballast to choose a nominal. Thusfar, Shuttle deployment error, which is really pointing error for the SSUS, has been shown to be the largest error source in this study. A plot was generated to show the maximum allowable pointing error that can be tolerated as a function of the ballast added and the fuel budget allotted. See Figure 10. The broken lines in Figure 10, point out the dispersions for the Shuttle launch of the GOES-D mission. If (3σ) pointing error is 2.2 degrees and the trim fuel budget is 200 meters/second, about 200 lbs of ballast on the SSUS-A is required to meet dispersions of this magnitude. This same information was seen in Figure 8. However, if post flight calibration of other STS payloads reduce the error estimate, e.g. to the (2σ) level on Figure 10, no ballast would be required and a 40 meters/second margin in trim fuel would be available.

IX. CONCLUSIONS

In concluding this discussion, a review of the principal findings is made. When a Shuttle payload must use a SSUS that is oversized to obtain the transfer trajectory, the options include: off-loading the SSUS; planning a non-optimum trajectory; or adding some ballast to the SSUS. In terms of cost saving and conserving trim fuel, the adding of ballast to the SSUS is the best choice. After a method had been chosen for handling the oversized SSUS, the next step is identifying the errors which would most effect the design of the transfer orbit. Of all the errors considered, the dominant one proves to be SSUS pointing error, particularly declination error. The PKM declination error dominates so extensively that when RSS with the other timing, thrust and pointing errors of the AKM and PKM, the effect of these other errors is insignificant.

Adding ballast to the SSUS decreases the impact that PKM declination error had on the trim delta-V. This result is quite reasonable since a pointing error will cause a smaller dispersion if the delta-V of the SSUS is smaller. However, when adding ballast to minimize the effect of dispersions, the nominal trim fuel rises significantly. Such an increase in the nominal trim fuel is undesirable because certain contingencies, e.g. a leaking fuel tank, could jeopardize the nominal mission. Therefore, the amount of ballast that should

be added depends on the philosophy that the spacecraft project chooses to adopt. If minimizing the dispersion trim duel is too costly in terms of increasing the nominal trim fuel, then another approach could be followed. Add just enough ballast to bring the (3σ) dispersion trim fuel within the mission's allotted fuel budget. The nominal will rise slightly and if a (3σ) dispersion is realized it can be handled.

The firing of a fixed impulse SSUS following Shuttle deployment of a geosynchronous payload has been examined in detail. Design of the transfer trajectory has been discussed in terms of finding both a nominal and possible dispersion cases that can be handled operationally within the allotted trim fuel budget. However, the reminder is given that the dominant errors affecting this study will remain as estimates until adequate post-flight calibrations of the SSUS firings can be performed.

X. REFERENCES

1. C. J. Petruzzo, W. C. Bryant, Jr., and K. G. Nickerson, "A Geostationary Longitude Acquisition Planning Algorithm", Messrs Petruzzo and Bryant, Goddard Space Flight Center; Mr. Nickerson, Computer Science Corporation; given at AAS/AIAA Astrodynamics Specialist Conference, Jackson Lake, Wyoming, September 1977.

2. "GOES D&E Compatibility on STS PAM-A", McDonnell Douglas Astronautics Company-West, Huntington Beach, California, January 1978, (Prepared under NASA Contract NAS7-906)

PKM DELTA-V:	
NO BALLAST	3659 M/S
MAXIMUM BALLAST	2821 M/S
AKM DELTA-V	1469 M/S
STATION ACQUISITION DELTA-V BUDGET	200 M/S
ORBITER PARKING ORBIT:	
CIRCULAR ALTITUDE	296 KM (160 NM)
INCLINATION	28.5°
GEOSYNCHRONOUS ORBIT:	
CIRCULAR ALTITUDE	35787 KM
INCLINATION	1.0°
PKM FIRING ERRORS (3-SIGMA):	
POINTING--RSS	2.2°
2.0° DEPLOYMENT ERROR 1.0° SSUS NUTATION ERROR	
THRUST	0.5%
AKM FIRING ERRORS (3-SIGMA):	
POINTING	1.0°
THRUST	0.5%

- SSUS-A IS FIRED ON THE EQUATOR
- TWO-BODY PROPAGATION OF THE ORBIT
- HOHMANN TRANSFER TO OBTAIN GEOSYNCHRONOUS ORBIT
- 90.0 DEGREE NODAL ROTATION AT AMF; MISSION ORBIT HAS INCLINATION = 1.0 DEGREE
- (3σ) STS POINTING ERROR = 2.0 DEGREES
- (3σ) NUTATION ERROR = 1.0 DEGREE

	GOES-C/DELTA	GOES-D/SSUS-A
PKM ΔV		2821-3659 M/S
AKM ΔV	1689 M/S	1469 M/S

- OFF-LOAD PROPELLANT FROM THE SSUS
- PLAN A NON-OPTIMUM TRANSFER TRAJECTORY
- ADD BALLAST TO THE SSUS

PKM ΔV (M/S)	SSUS-A BALLAST (LBS)
3659	0
3514	200
3381	400
3259	600
3147	800
3042	1000
2945	1200
2821	1480 (FULL BALLAST)

GOES-D PKM AND AKM RESULTS FOR SSUS-A

	NOMINAL						(3σ)
BALLAST	ΔV PKM	i_T	ΔR_A	ΔR_P	$\dot{\lambda}$	ΔV	MAXIMUM ΔV FOR "WORST" CASE
(LBS)	(M/S)	(DEG)	(KM)	(KM)	(D/D, +E)	(M/S)	(M/S)
0	3659	10.87	+1381	-1614	1.5 E	55.0	213.7
200	3514	12.21	+1789	-1965	1.1 E	69.0	199.9
400	3381	13.49	+2220	-2324	0.6 E	83.6	187.6
600	3259	14.73	+2671	-2688	0.1 E	98.6	175.2
800	3147	15.94	+3143	-3054	0.6 W	114.0	162.5
1000	3042	17.14	+3651	-3427	1.5 W	130.1	149.0
1200	2945	18.35	+4197	-3802	2.5 W	147.0	156.8
** 1480	2821	20.10	+5064	-4323	4.7 W	172.1	181.9

** FULL BALLAST FOR SSUS-A

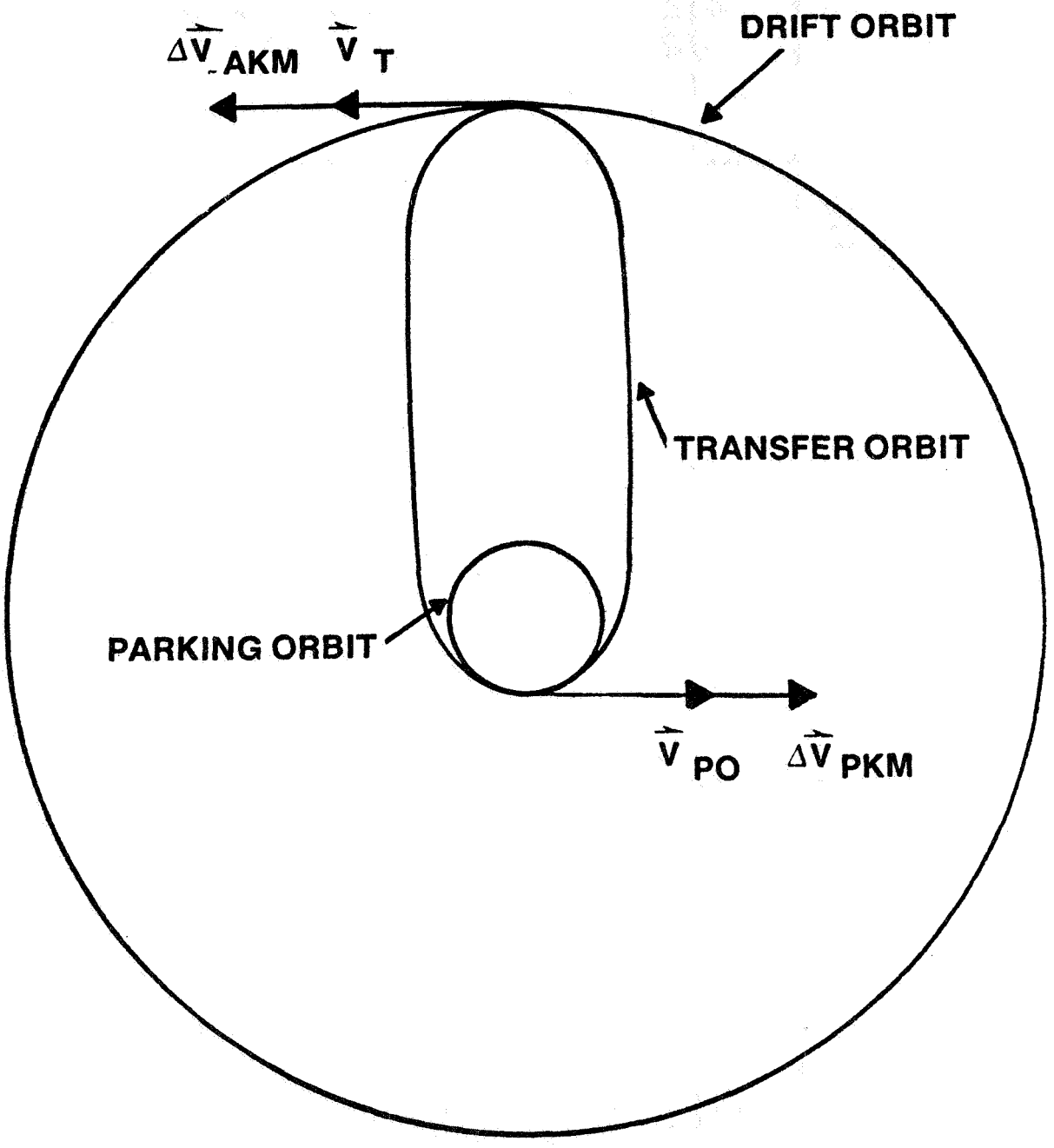

Figure 1. GOES-D Orbital Evolution Following a Shuttle Deployment

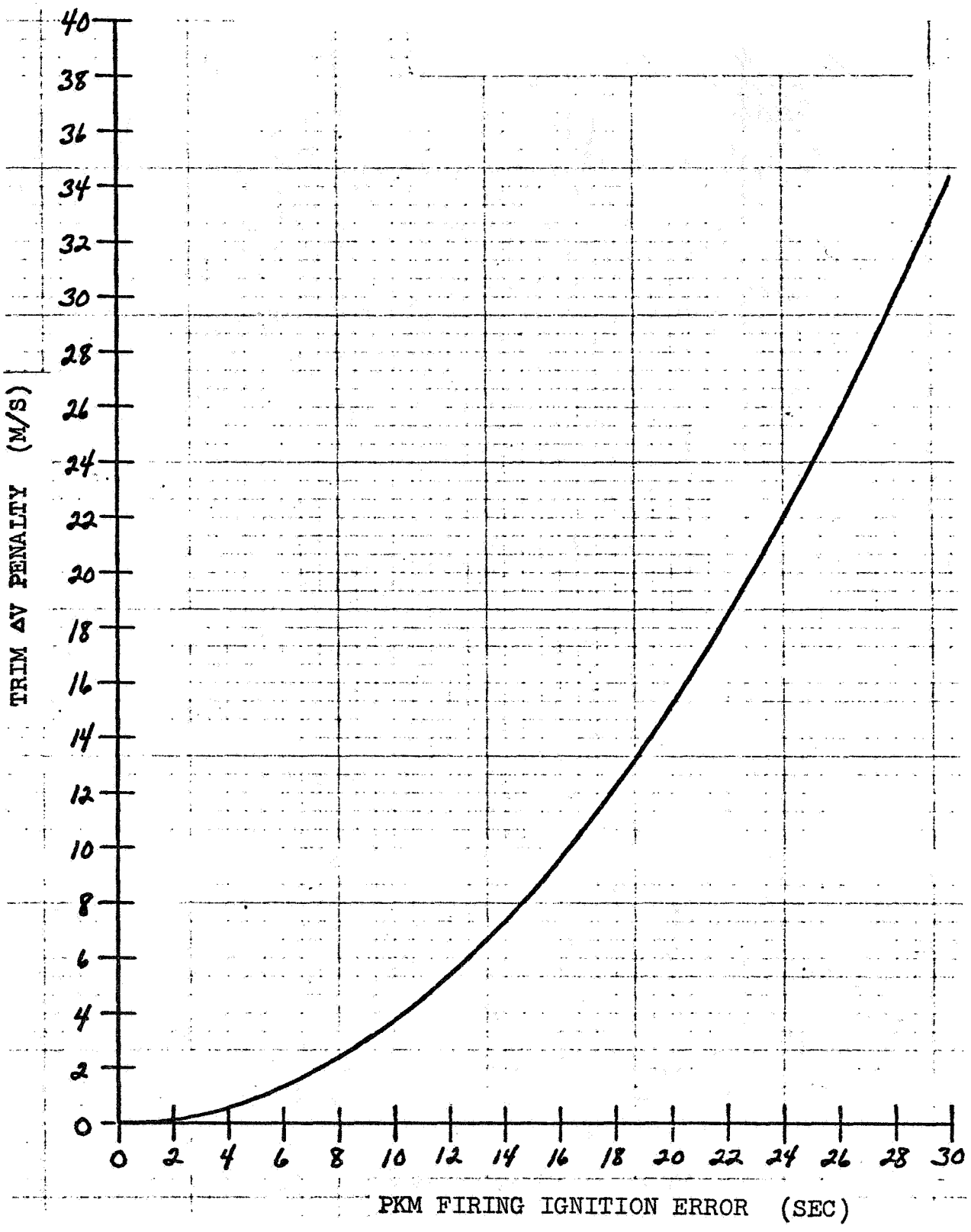

Figure 2. GOES-D Trim ΔV Penalty vs. PKM Firing Ignition Error

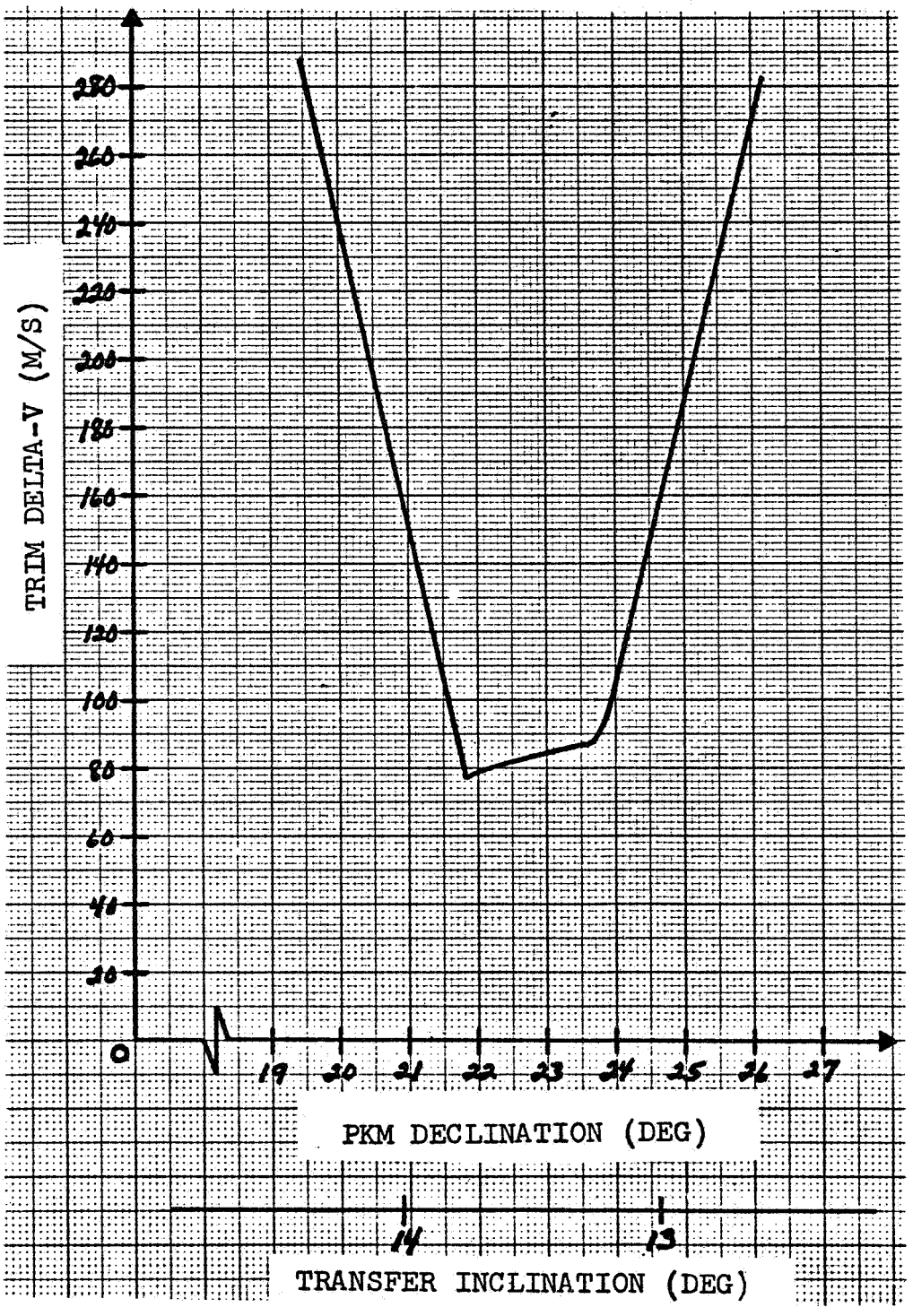

Figure 3. Trim Delta-V vs. PKM Declination

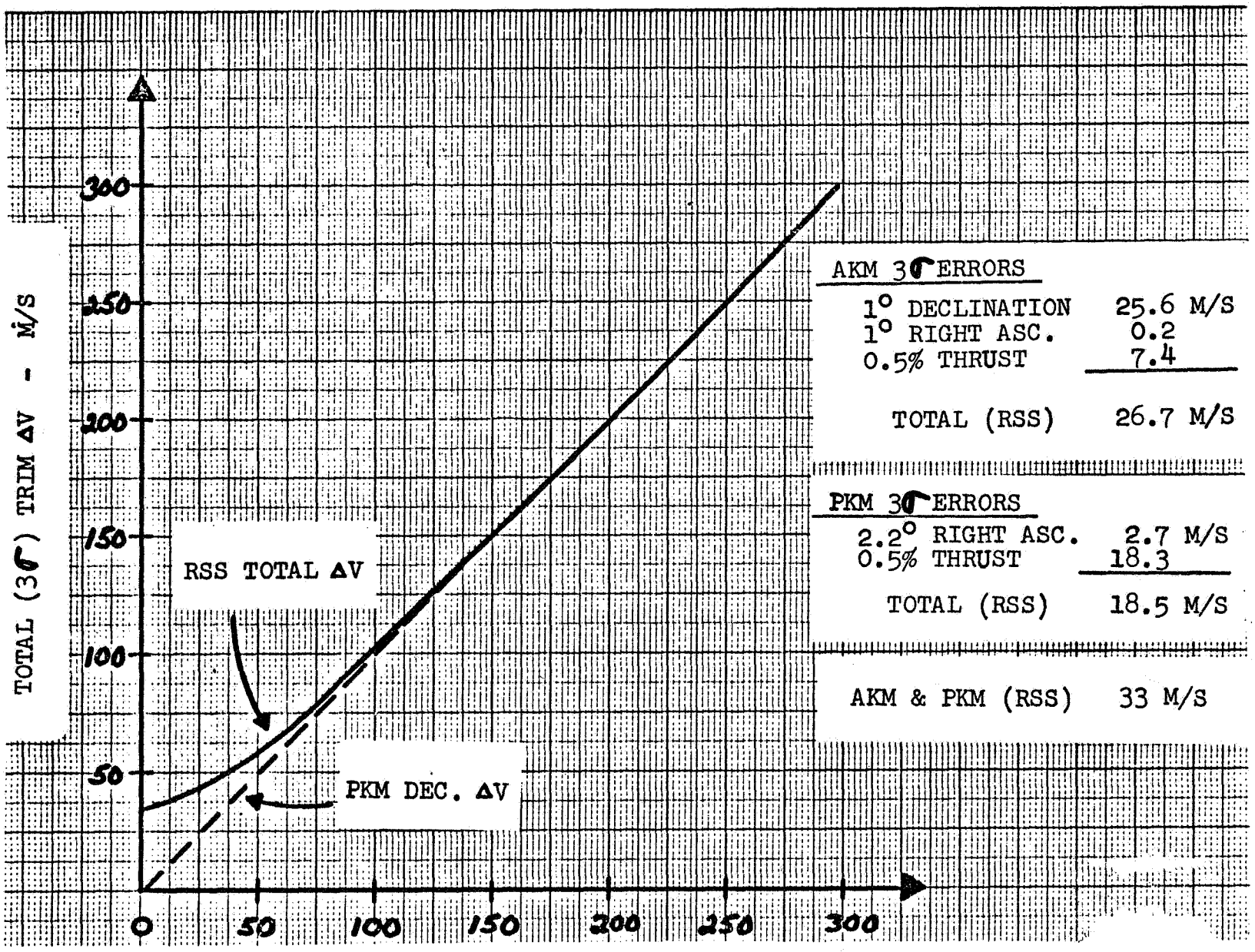

Figure 4. Trim ΔV Necessitated by PKM Declination Error – M/S

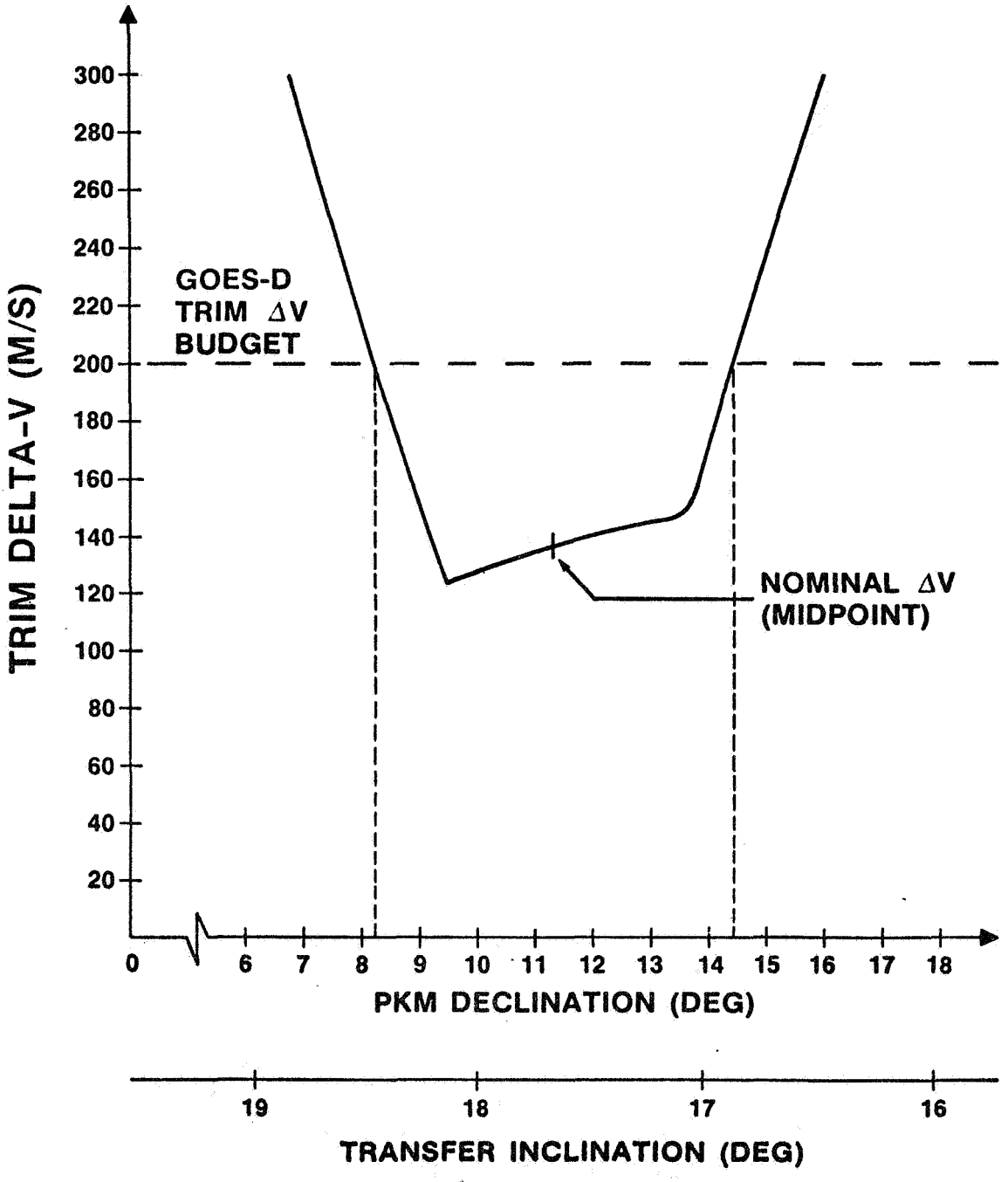

Figure 5. Method for Determining Nominal ΔV SSUS-A, ΔV PKM = 3000 M/S

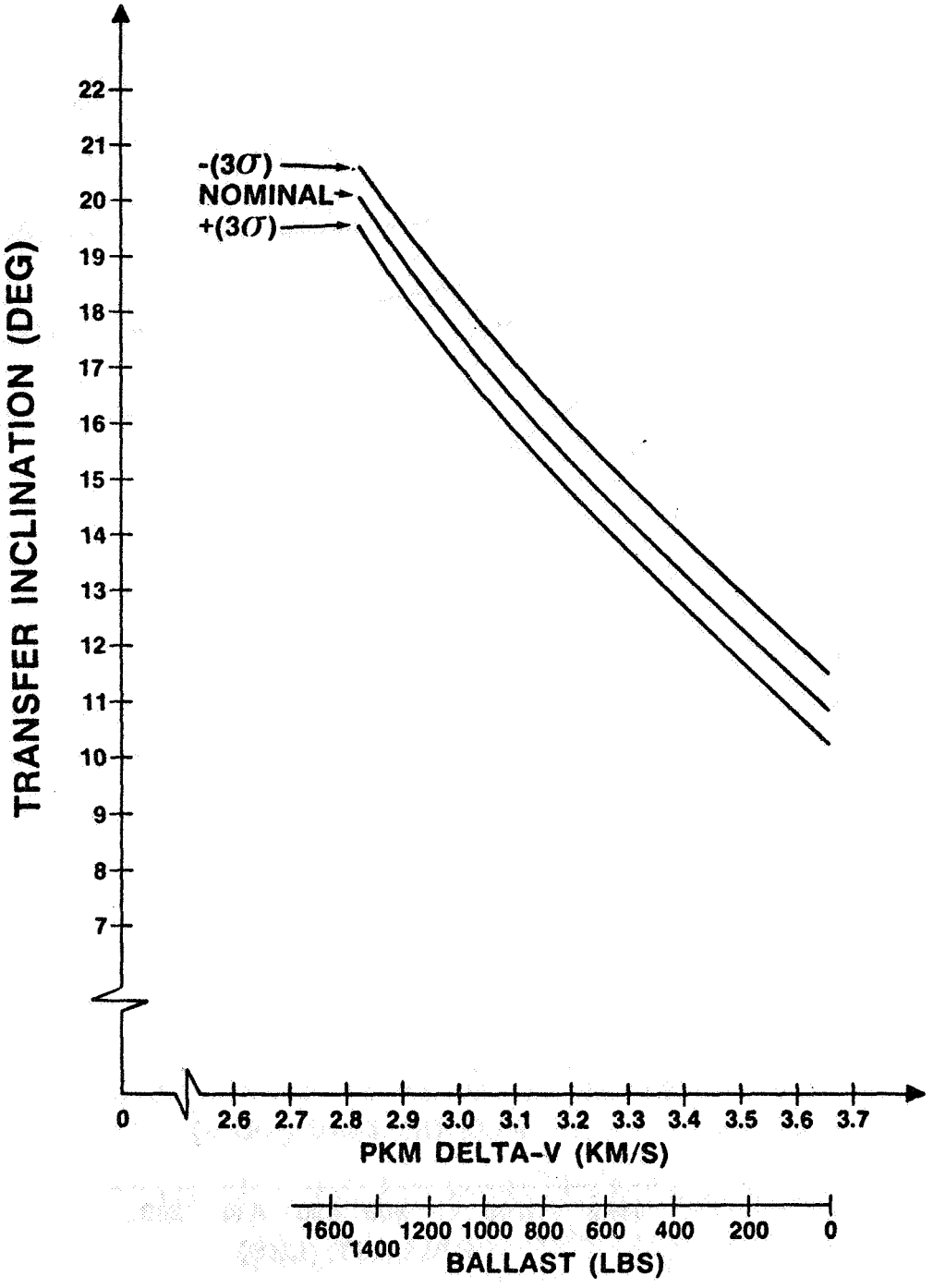

Figure 6. Transfer Inclination vs. PKM Delta-V for GOES-D (SSUS-A)

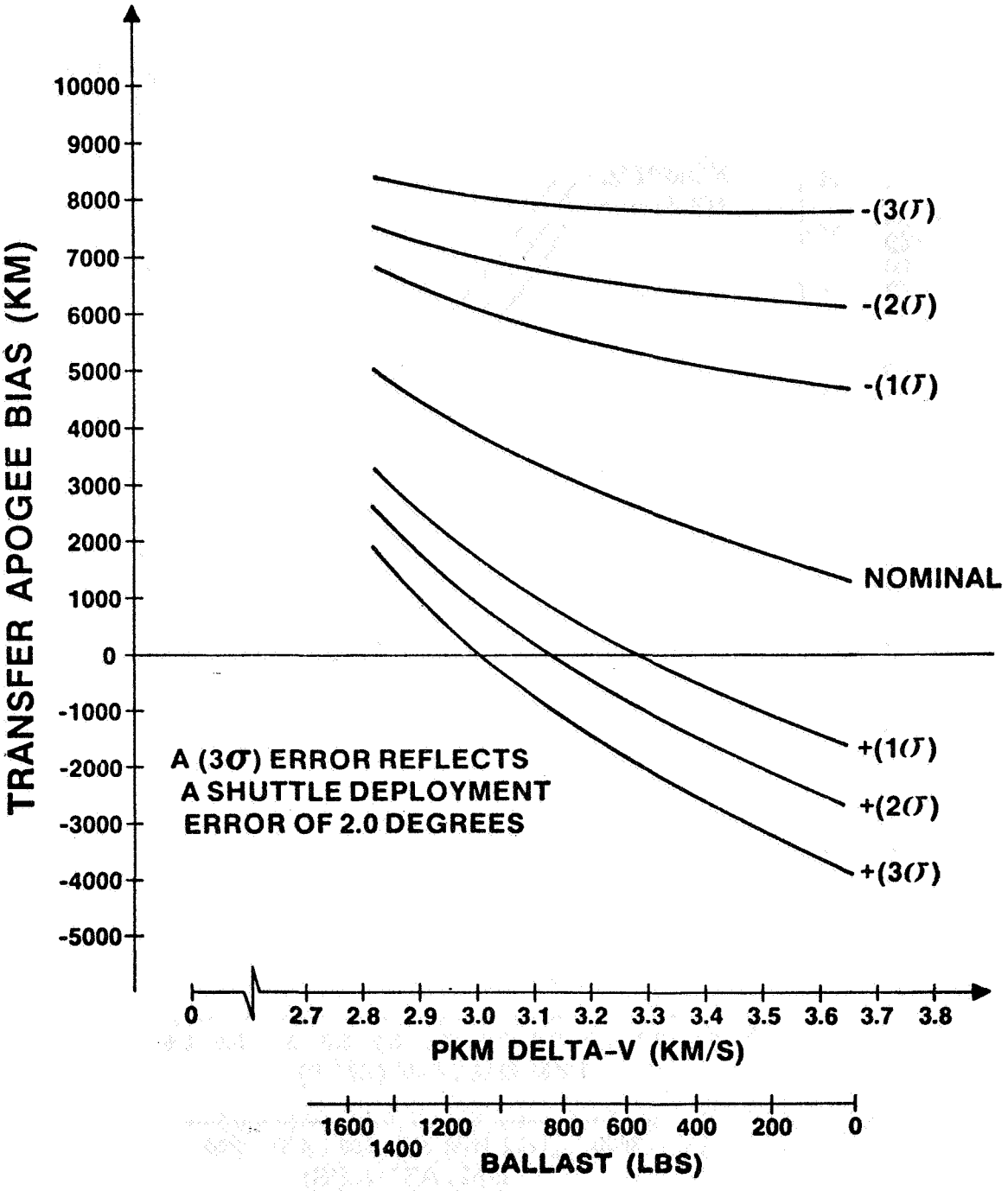

Figure 7. Transfer Apogee Bias vs. PKM Delta-V for GOES-D (SSUS-A)

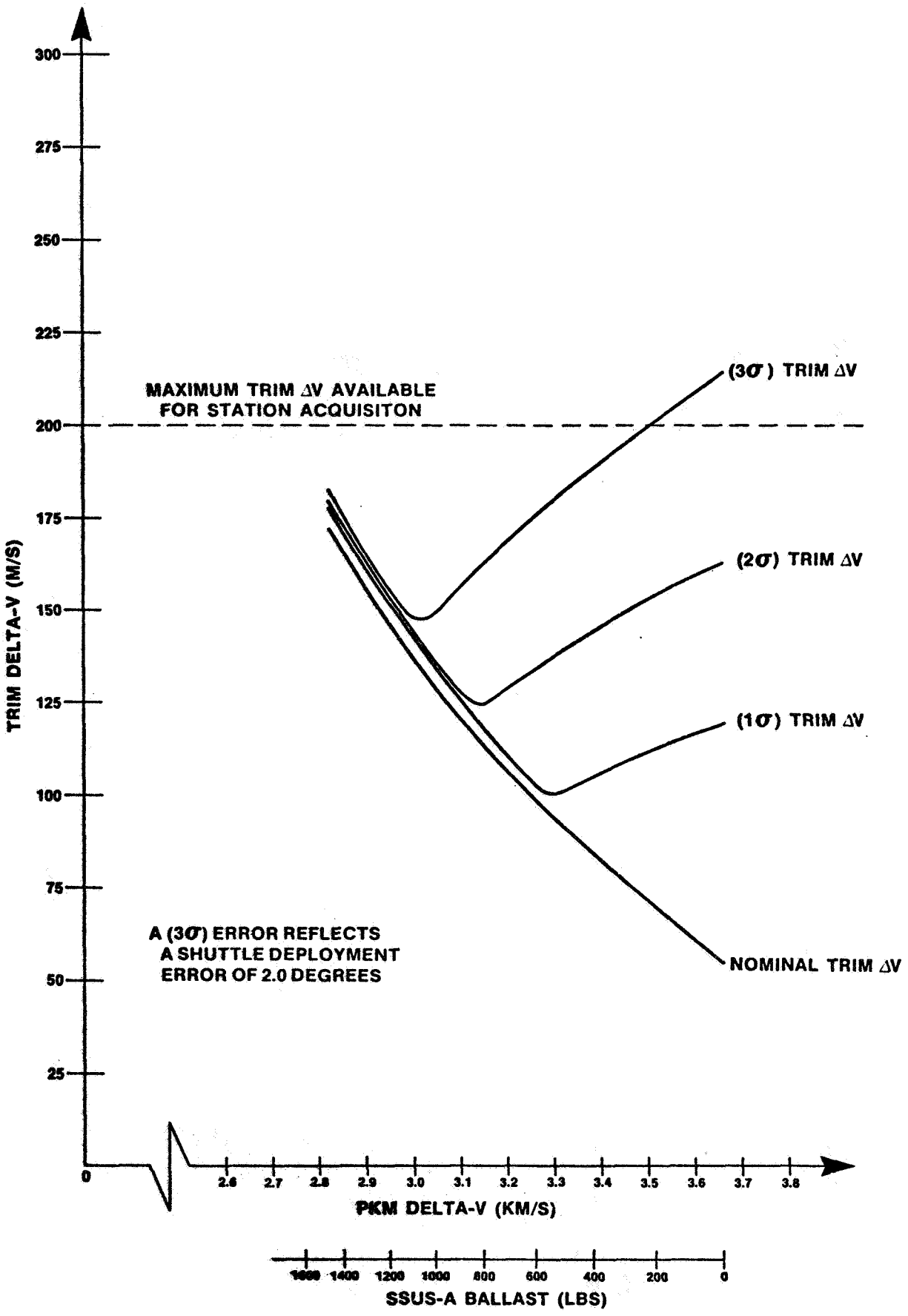

Figure 8. GOES-D Trim Delta-V PKM Delta-V (for SSUS-A)

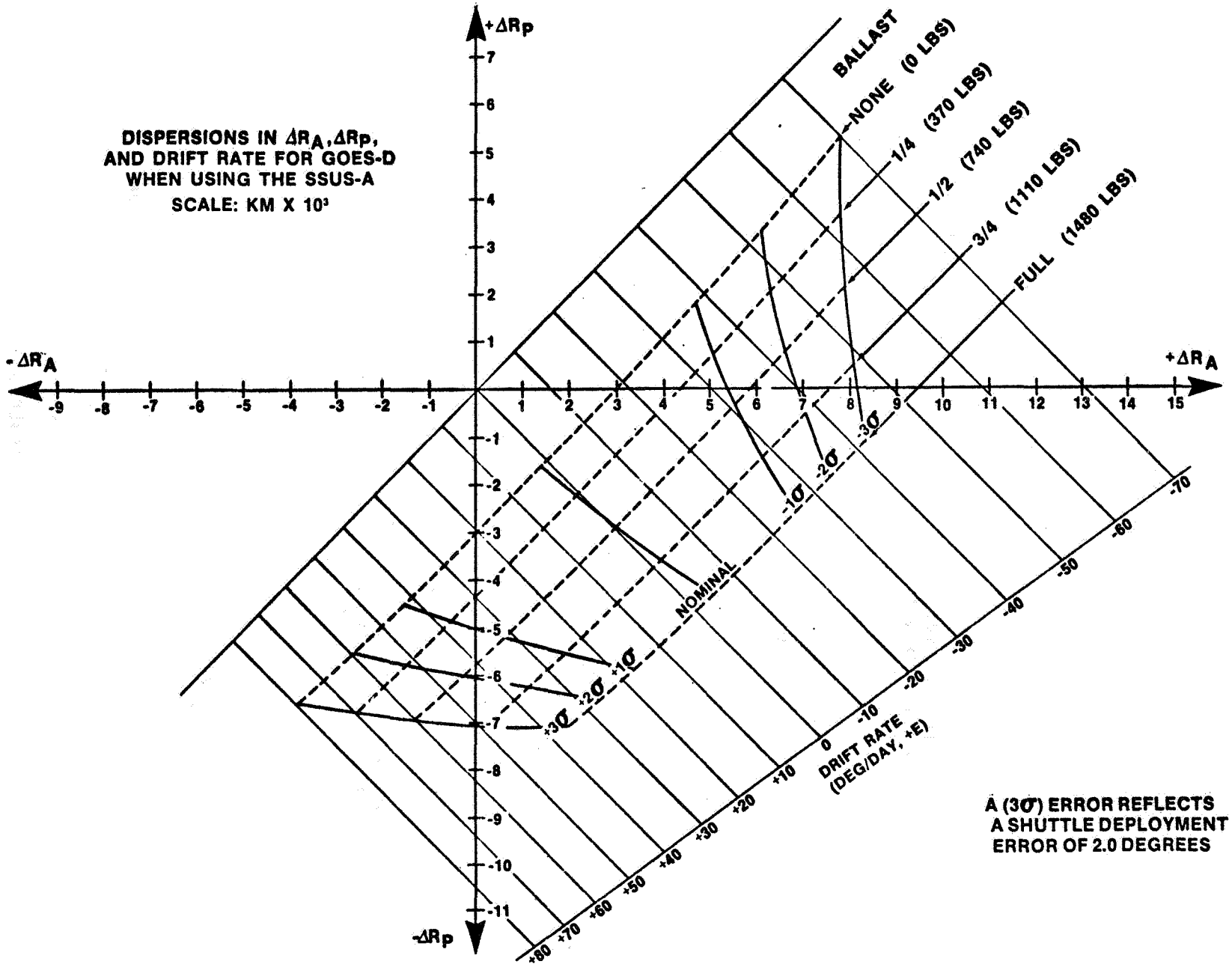
DISPERSIONS IN ΔRA, ΔRP,
AND DRIFT RATE FOR GOES-D
WHEN USING THE SSUS-A
SCALE: KM X 10³
+ΔRP
-ΔRP
-ΔRA
+ΔRA
BALLAST
NONE (0 LBS)
1/4 (370 LBS)
1/2 (740 LBS)
3/4 (1110 LBS)
FULL (1480 LBS)
NOMINAL
±1σ
±2σ
±3σ
DRIFT RATE
(DEG/DAY, +E)
A (3σ) ERROR REFLECTS
A SHUTTLE DEPLOYMENT
ERROR OF 2.0 DEGREES

Figure 9.

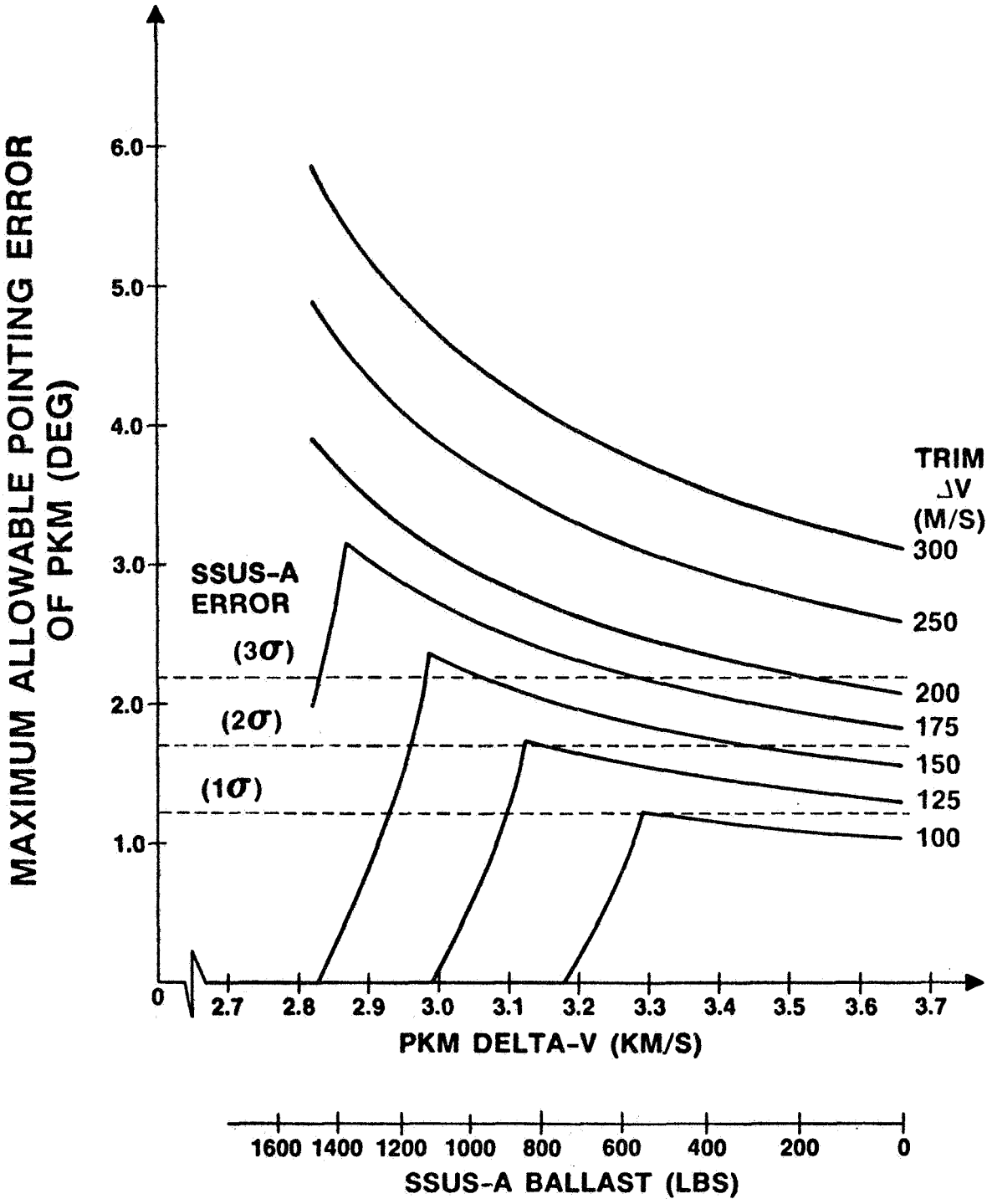

Figure 10. Maximum Allowable Pointing Error of PKM for Various Trim ΔV Budgets vs. PKM Delta-V (SSUS-A)

PRELAUNCH ANALYSIS AND OPERATIONS RESULTS FOR SEASAT-I DEFINITIVE ORBIT COMPUTATIONS

E. Doll

Goddard Space Flight Center

ABSTRACT

Definitive orbital computations for the SEASAT Project are required to be performed in an operational environment with an accuracy of 50 meters along track, 30 meters cross track and 30 meters radial. In order to establish the operations procedures and determine the mathematical modeling required under which the Goddard Trajectory Determination System would function to meet the definitive orbit computations requirements for the SEASAT-I spacecraft, prelaunch analysis was performed. Orbital solutions from the prelaunch analysis using S-band observational tracking data and associated data from the LANDSAT-I and GEOS-III spacecraft which were used to establish the criteria for SEASAT-I definitive orbit computations are presented. Definitive orbital computation results for the SEASAT-I spacecraft utilizing preplanned procedures and mathematical modeling are presented.

SIRIO: ONE YEAR OF STATION KEEPING

F. Palutan and S. Trumpy

Italian National Research Council

ABSTRACT

About one year ago SIRIO was successfully launched and guided to its geostationary target position by a joint team composed of NASA and Italian technicians. The strategy followed in maintaining the station point and the results achieved are here briefly described.

The method used at the Fucino control center for orbit determination is presented. Azimuth and elevation data from SHF antennas located at Fucino and Lario are used as input for the determination. An estimation of the uncertainty of the orbit is given; a comparison is made between determinations performed using the method here described and determinations performed using VHF ranging data. Also, the difference in using data from a single SHF station or two stations is shown.

In the area of attitude determination, a study has been carried out for predicting the spacecraft spin axis precession. The model used is explained and then the agreement between predicted and measured attitude outlined.

SIRIO

One year of station keeping

Franco Palutan - TELESPAZIO - Rome

Stefano Trumpy - CNUCE,Institute of CNR - Pisa

Introduction

The SIRIO project is an important research program sponsored by the Consiglio Nazionale delle Recerche (CNR), the Italian National Research Council, to perform telecommunication experiments on Super High Frequency (SHF) bands (12-18 GHZ) over a two year period.

While the SIRIO satellite was designed and assembled in Italy, CNR contracted with the U.S. National Aeronautics and Space Administration (NASA) to provide the launch vehicle (a 2313 Delta rocket) and the necessary ground assistance to launch and position the satellite in orbit.

SIRIO was launched from Cape Canvaral on August 25, 1977 at 23.50 hours GMT. After spacecraft separation, control was taken over by the MultiSatellite Operation Control Center (MSOCC) at the Goddard Space Flight Center (GSFC) and a joint team of NASA and Italian technicians operated to bring the satellite to the desired station point. After completion of station acquisition maneuvers, the control of the satellite was handed over to Sirio Italian Operation Control Center (SIOCC) located at Fucino, near Rome. This paper briefly describes the experiences gained while maintaining the SIRIO station point during its first year of operational life.

Since SIRIO is Italy's first geostationary spacecraft in orbit, the necessary familiarity with flight control procedures was mainly acquired by the Italian team during the period of cooperation with the NASA. In fact, no relevant new techniques have since been adopted, which differ from those used by the NASA to control geostationary satellites. Consequently, this paper is limited to providing an evaluation of the precision reached in determining the orbit and attitude of the spacecraft and in approaching the target when executing maneuvers, without going into detail concerning the particular techniques used.

There is one exception to this rule: the orbit determination. A description is given of how satisfactory results were achieved using the Fucino SHF antenna pointing data instead of following the procedure based on Very High Frequency (VHF) ranging data, which was used by NASA during the first period of the mission.

Mission Objective

In order to point the on-board SHF antenna on the area of the Baleari Isles in the Mediterranean (optimal sub-antenna point for the SHF experiments), the spacecraft had to be positioned on an equatorial plane with a tolerance of .3 degrees in orbit inclination at a longitude of 15 degrees ± 1 degree W; furthermore the spin axis declination had to be maintained within 1 degree of the negative orbit normal, and, since the satellite is spin stabilized, the spin rate had to be maintained at 90 ± 1 rounds per minute. It was necessary that 12 kg of hydrazine remained at hand-over in order to insure the two year period of operational life.

Hand Over to SIOCC (SIRIO Italian Operation Control Center)

The SIRIO mission evolved in continuously nominal conditions. The final trim maneuver was performed on September 15 with the following results:

- spacecraft longitude = 14.61 degrees
- orbit inclination = .311 degrees
- spin axis declination = - 89.64 degrees
- spin rate = 90.5 rounds per minute
- 24 kg hydrazine left

After testing the spacecraft health status and the complete readiness of the SIOCC for operations, handover was operative on September 29 at 24.00 GMT. At that point the orbit inclination had lowered to below .3 degrees and thus everything was nominal.

GSFC continued orbit determination support via VHF ranging measurements on a biweekly basis until the end of 1977. In parallel, Telespazio began the determinations based on the SHF ground antenna pointing data which, from the beginning of 1978, have been carried on stand alone.

Station Keeping Operative Limits

After handover, it was found convenient to reduce the tolerances of the mission in order to avoid time constraints in performing maneuvers and to insure a more accurate antenna pointing. The actual operative constraints for SIRIO are the following:

- spacecraft longitude = 15 degrees W ± .5 degrees
- orbit inclination = .2 degrees
- spin axis declination = - 89.80 degrees
- spin rate = 90 ± 1 round per minute

With the new constraints, the average period between cycles of maneuvers is about 5 months. Maneuvers are normally planned to occur in a series of two or three different corrections closely linked in time to each other (North-South, East-West and attitude corrections). Since the tolerances are not critical, in order to phase the maneuvers, the spacecraft can be left drifting out of the imposed limits for a short time.

Mission Control Ground Equipment

SIOCC is equipped with a front-end computer utilized for spacecraft telemetry control, spacecraft command, for performing the first level of computations on experimental data, for archiving, etc.. The flight dynamics control tasks are performed by the CNUCE computing systems at Pisa, connected to the SIOCC, via data link, for telemetry data transmission. A joint team from Telespazio and CNUCE is encharged with the spacecraft control planning; Telespazio is responsible for the operations on the spacecraft while CNR is responsible for the mission as a whole.

Orbit History

In fig. 1, the longitude of the spacecraft subsatellite point is shown over a one year period together with the inclinations of the orbital plane. The curve discontinuities clearly show the occurrence of the orbital maneuvers while the attitude corrections have been so small that no practical influence on the orbit can be seen.

Attitude History

Fig. 2 shows the attitude history in a polar diagram; the two attitude corrections and the perturbation caused by the North-South maneuver of May 2 are clearly shown. The diagram can be used to predict attitude in the second year of spacecraft life and to tune the mathematical models at present under study which aim at representing the spin axis precession movement in a trial and error procedure.

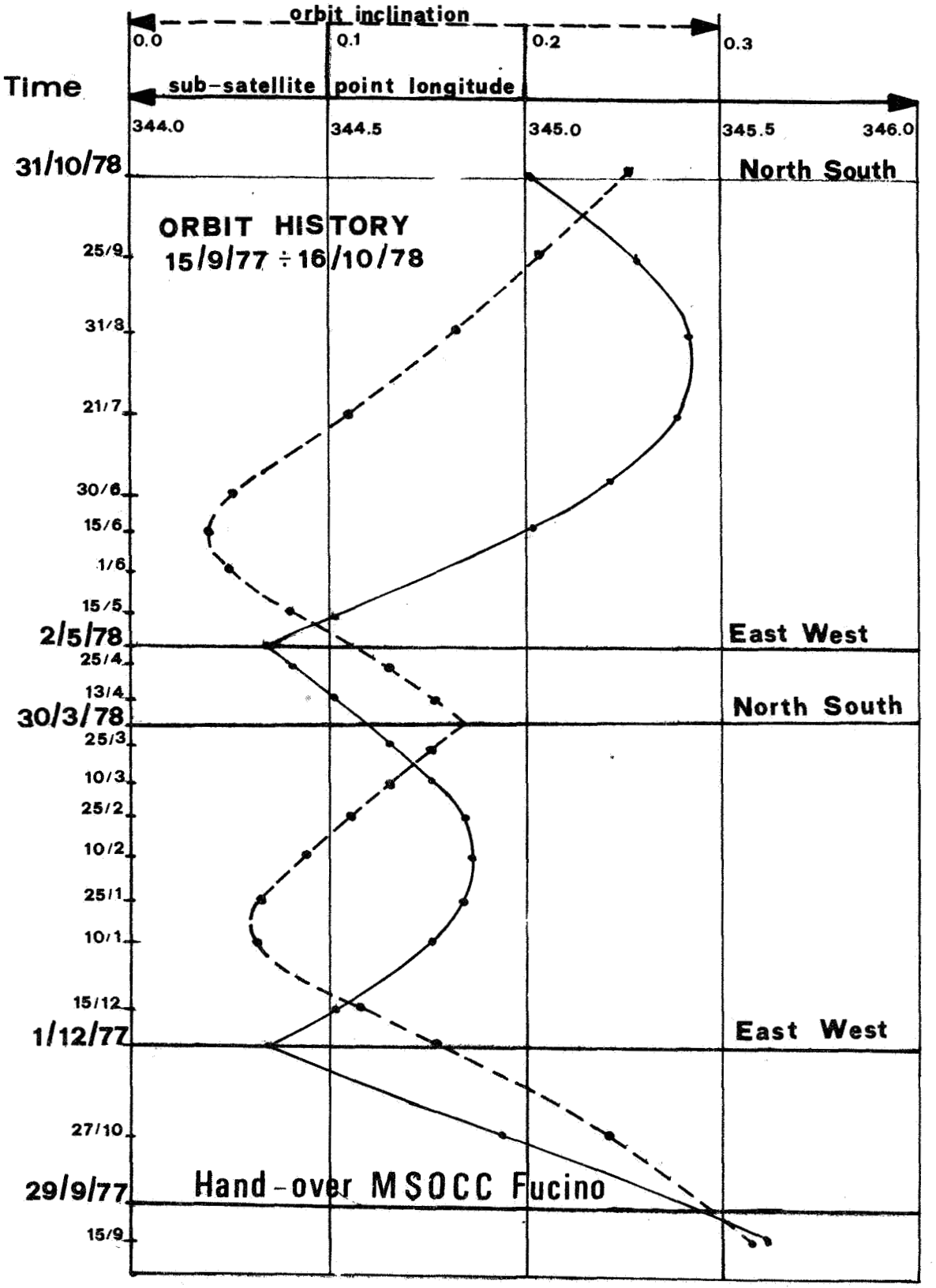
orbit inclination
0.0
0.1
0.2
0.3
Time
sub-satellite point longitude
344.0
344.5
345.0
345.5
346.0
31/10/78
North South
ORBIT HISTORY
15/9/77 ÷ 16/10/78
25/9
31/8
21/7
30/6
15/6
1/6
15/5
2/5/78
East West
25/4
13/4
30/3/78
North South
25/3
10/3
25/2
10/2
25/1
10/1
15/12
1/12/77
East West
27/10
29/9/77
Hand-over MSOCC Fucino
15/9

Figure 1

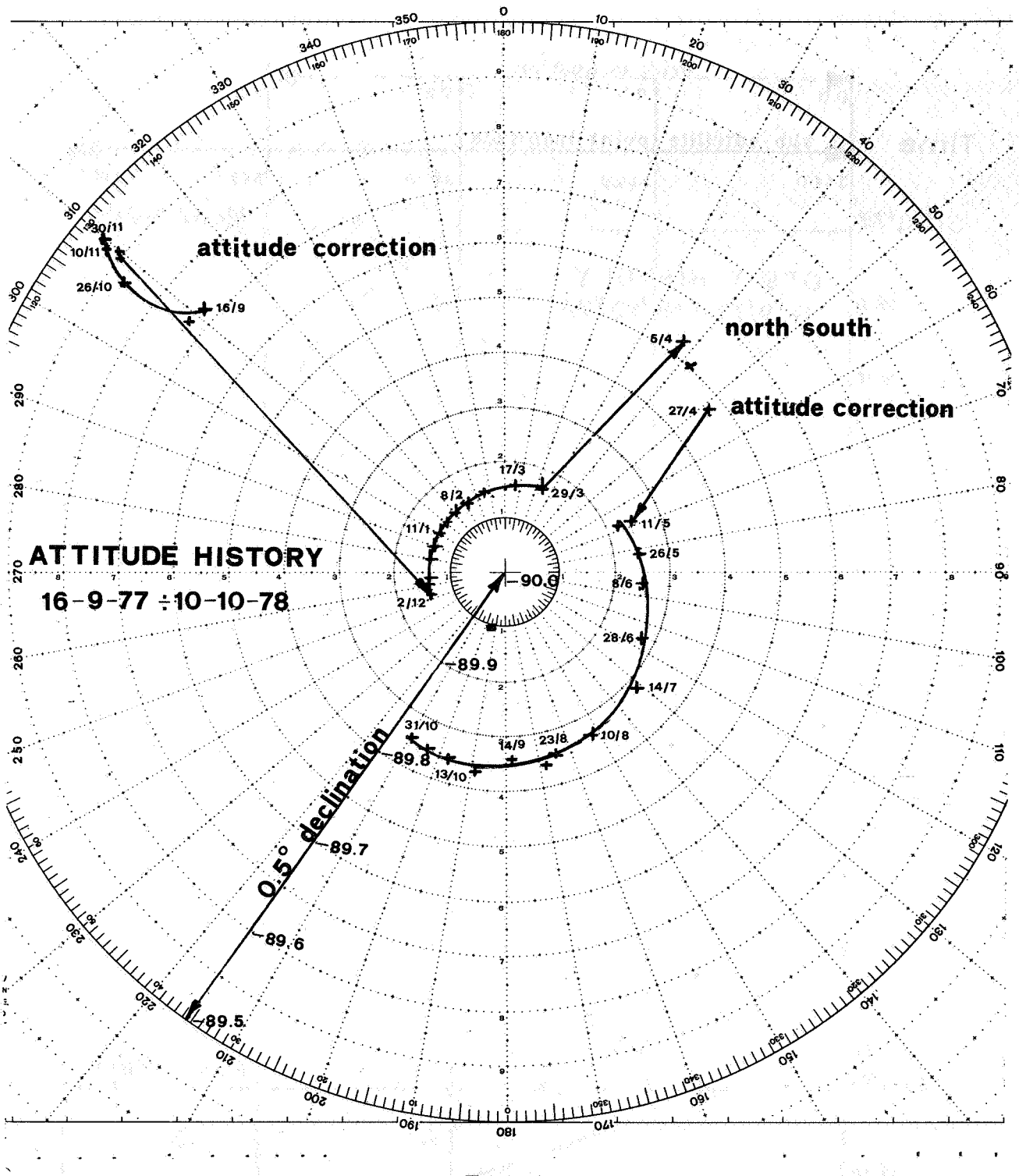
ATTITUDE HISTORY
16-9-77 ÷ 10-10-78
attitude correction
north south
attitude correction
0.5° declination
90.0
89.9
89.8
89.7
89.6
89.5
30/11
10/11
26/10
16/9
5/4
27/4
17/3
29/3
8/2
11/1
2/12
11/5
26/5
8/6
28/6
14/7
10/8
23/8
14/9
31/10
13/10

Figure 2

Maneuvers

In the table included with fig. 3, an outline of the maneuvers performed on the SIRIO satellite is given. In consideration of the fact that the granularity, which can be reached by the satellite auxiliary propulsion system when firing a single pulse is relatively large, the results were always very satisfactory.

DATE	TYPE	JETS	PULSES OR BURNTIME	TARGET	RESULTS
DEC 1 77	E-W	RAD B	12 PULS	15.° LONG ON 03/26/78	15.4°LONG on 03/26/78
DEC 1 77	ATT	AX B	4 PULS	RA = 218° DEC=-89.88°	RA = 255° DEC=-89.93°
MAR 30 78	N-S	AX A+B	110 SEC	INCLIN=.18° NODE=270°	INCLIN=.168° NODE=272.2°
MAY 2 78	E-W	RAD B	11 PULS	INITIAL DRIFT .0125deg dayW FINAL DRIFT .0210deg dayE	FINAL DRIFT .0202deg dayE
MAY 2 78	ATT	AX B	2 PULS	RA=53° DEC=-89.93°	RA=66.50° DEC=-89.88°

Figure 3

Mission situation at Midway point

At midway point in its operational life, SIRIO continues regular transmission of experimental data; no major or chronic failures have occurred either on the SIRIO payload or in the basic spacecraft. All those elements subject to degradation, e.g. batteries, solar pannels, etc., have had a lower degradation rate than expected.

The hydrazine tanks still contain approximately 20.5 kg of fuel; after the North-South maneuver, which is programmed for October 31, we expect to have approximately 18.5 kg left.

As the average yearly fuel consumption necessary to maintain the present station point is approximately 4 kg, we should have enough fuel left to considerably extend the spacecraft life. No final decision has so far been taken but there are already plans for utilizing SIRIO for a number of additional experiments.

Attitude Determination

In the present geostationary position, 250 major frames are selected from a 24 hour period of data for each determination.A least square filter is used to determine the:

- spin axis right ascension
- spin axis declination
- sun angle bias
- sun sensor mounting angle bias
- sun to earth in bias

All the biases are presumed to be constant over the 24 hour period. Earth radius bias cannot be determined in the present satellite position but it has already been determined during the GSFC controlled mission phase.

Two verifications are applicable to validate the solution of the attitude given by the filter. In the first, biases are inserted in two deterministic methods to resolve the attitude frame by frame; this first method resolves the attitude by using sun-angle and sun-to-earth-in data, the second one by using sun-angle and earth-length data. A graphic display then provides the dispersions of these resolved attitudes from the one computed by the filter; the trend of the resolved attitudes over the time span covered by the selected frames gives also an indication of the correctness of the determined biases.

A second verification is made using the attitudes and the biases determined by the filter in order to simulate telemetry data. A graphic comparison between simulated and acquired telemetry data confirms this solution. At the end of this process, the attitude of the satellite is determined in geostationary position with a 3 sigma coning angle of .1 degree.

Orbit Determinations

The Sirio orbit determination method is based on angular observations, supplied by the Fucino SHF telecomunications antenna.

The azimuth and elevation angles are automatically acquired at intervals of one hour. An orbit determination process is statistically significant with a number of observations from 200 to 500, made over a time period from 5 to 10 days. A smaller number of observations makes the estimation process more critical or even impossible, while the use of data from a period of more than 10 days does not really improves the orbit estimation accuracy.

The observations are supplied by the SHF telecommunications antenna, which is a 17 m. paraboloid, working in the 12 and 18 GHZ bands; the beam width at 3 db is

.045 deg, and the digital encoders accuracy is .01 deg. The nominal tracking error, in autotracking mode, is .01 deg (3sigma), and the nominal pointing error (bias) is .01 deg (1sigma) both in azimuth and in elevation.

The mathematical model used in the estimation process takes into account the 5x5 geopotential, and the perturbations due to the sun and the moon; the Cowell numerical integrator is used, with an integration step of 800 sec. The estimation process is based on a differential correction method.

The spacecraft position accuracy (x,y,z) varies from 200 to 500 m (1sigma), and the velocity accuracy ($\dot{x},\dot{y},\dot{z}$) is in the order of 3 cm/sec (1sigma); this corresponds to a longitude uncertainty of 2x10 deg (1sigma) at determination epoch.

The accuracy of the statistical process is quite good, due to the very high quality of angular data supplied by the SHF antenna. The real limitation of the method is caused by the observation biases. A periodic check of the pointing accuracy of the antenna can not be made, for operational reasons; the observation bias, measured before the beginning of the mission, was within the nominal limits (.01deg.), and the a priori value is assumed to be zero.

The orbit accuracy has been tested by an independent source, the NASA determinations performed from September to December 1977. The agreement between the NASA and TELESPAZIO determinations is quite satisfactory; as can be seen from the table of fig 4, the differences in semimajor axis, eccentricity and inclination are very low. The node and perigee arguments and mean anomaly are less accurate; this is due to the very low inclination of the geostationary orbit. Very important, however, is good agreement in the spacecraft right ascension, which is roughly the sum of Ω ,ω,M.

EPOCH: 1977	SEPT. 15, 18.00		OCT. 27, 00.00		DEC. 2. 00.00	
	NASA	TELESPAZIO	NASA	TELESPAZIO	NASA	TELESPAZIO
SEMIMAJOR AXIS (KM)	42165.530	42165.458	42168.584	42168.216	42164.359	42164.117
ECCENTRICITY	$0.348\ 10^{-3}$	$0.321\ 10^{-3}$	$0.261\ 10^{-3}$	$0.259\ 10^{-3}$	$0.215\ 10^{-3}$	$0.202\ 10^{-3}$
INCLINATION (DEG)	0.306	0.309	0.235	0.244	0.161	0.154
ASCENDING NODE (DEG)	250.728	251.140	250.752	249.371	249.363	247.986
ARGUM. OF PERIGEE (DEG)	239.119	239.957	237.562	239.334	234.912	239.754
MEAN ANOMALY (DEG)	120.112	118.883	251.875	251.496	290.806	287.356
SUM OF Ω,ω,M (DEG)	249.959	249.980	20.189	20.201	55.081	55.096

Figure 4

Another independent source of information, which has been used to verify the Sirio orbit determination method, is the optical observation. This is possible twice per year, when the sun declination is equal to the spacecraft declination in an hour angle declination reference system centered at the observer. In this situation the sun light is reflected to the observer by the spacecraft which has his spin axis normal to the equatorial plane. Two optical observations were performed in March and October 1978, using amateur high quality equipment, with an observation error in the order of .003 deg.

The Sirio position has been measured on photographic plates with respect to a star with a known position. The March observation gave a difference between the nominal and the observed positions of .018 deg both in rigth ascension and declination; the October observation gave a difference of .022 deg in rigth ascension and .005 deg in declination. Therefore, main features of the Sirio orbit dtermination method are the following:

- simplicity : the observations acquisition is automatic, with no intervention of the operator, and without any interference with spacecraft operations;

- low cost : no additional equipment is required , other than that used for telecommunications;

- the accuracy is compatible with the requirements of the Sirio mission, in particular, and, in general, with those of the geostationary telecommunications missions;

-this method seems to be applicable for future telecommunications missions, with frequency bands in the 12-14 or 20-30 GHZ range.

References

1. Palutan, F. "The Sirio Control Center at Fucino for the Geostationary Phase of the Mission" Alta Frequenza, April 1978

2. Faconti, G.; Trumpy, S. "The Flight Dynamics System for the Control of the SIRIO spacecraft during its operational life", CNUCE technical report no. 122, Feb. 1977 and annexed to Proceedings of the 17th "Convegno sullo Spazio", Rome, Mar. 1977

3. Letico, V.; Trumpy, S.; Violi, V. "Gestione della missione SIRIO", Proceedings of the 18th "Convegno sullo Spazio",

Rome, Mar. 1978

4. Faconti, G.; Guidotti, P. "Attitude Simulator Program (ASP): User's Manual" CNUCE technical report no. 136 Aug. 1977

5. Bianchini, G. "Strategia e primi risultati sperimentali del controllo orbitale del Sirio", Proceedings of the 18th "Convegno sullo Spazio", Rome, Mar. 1978

6. Di Francescantonio, G; Palutan, F.;Bergamaschi, S. "Determinazione orbitale del Sirio nella fase geostazionaria: metodo di misura e risultati sperimentali" , Proceedings of the 18th "Convegno sullo Spazio", Rome, Mar. 1978

7. De Agostini, A.; Graziani, F. "Determinazione e controllo di assetto del satellite Sirio", Proceedings of the 18th "Convegno sullo spazio", Rome, Mar. 1978

8. Faconti, G.; Trumpy, S. "The Fligth Dynamics System for the Orbit and Attitude Control of the Sirio Spacecraft", Alta Frequenza, Apr. 1978

Acknowledgements

The authors would like to thank their colleagues from NASA and CSC (Computer Science Corporation) for all their collaboration during the pre-launch period in the study and the planning of post-handover spacecraft operations. Their contribution, which was based on a relevant experience in geostationary missions, represented, for us, an essential starting point for our investigations in spacecraft control techniques.
Particular thanks are due to W. Bryant, R. DeFazio and R. Werking from NASA and L. Chen and M. Goorevich from CSC.

AN EFFICIENT APPROACH TO GENERATE ORBITAL ELEMENTS FOR GEOSTATIONARY SATELLITES

D. Phillips

U.S. Department of Commerce/NOAA

ABSTRACT

We describe a software package which generates Keplerian osculating orbital elements for a geostationary satellite by using earth edge and landmark measurements from imagery frames. This package has the advantages of being efficient and compact; it fits into 32 K of a 48 bit machine and execution time is less than two minutes. Furthermore, the approach of only requiring imagery measurements eliminates the laborious procedures necessary to process ranging information from ground stations. Finally, the accuracy of the results of this approach have been roughly equal to two visible pixels RMS. These results compare favorably to results from more elaborate orbit generating packages such as Geodyne at NOAA.

BIBLIOGRAPHIC DATA SHEET

1. Report No.	2. Government Accession No.	3. Recipient's Catalog No.
CP 2082		

4. Title and Subtitle	5. Report Date
Flight Mechanics/Estimation Theory Symposium, October 1978	April 1979
	6. Performing Organization Code: 582
7. Author(s): Arthur J. Fuchs, Editor	8. Performing Organization Report No.: G-7813
9. Performing Organization Name and Address: Goddard Space Flight Center, Greenbelt, Maryland 20771	10. Work Unit No.
	11. Contract or Grant No.
	13. Type of Report and Period Covered
12. Sponsoring Agency Name and Address: National Aeronautics and Space Administration, Washington, D.C. 20546	14. Sponsoring Agency Code

15. Supplementary Notes

16. Abstract

This document is a compilation of papers presented at the Flight Mechanics/Estimation Theory Symposium held October 18-19, 1978, at the Goddard Space Flight Center.

17. Key Words (Selected by Author(s))	18. Distribution Statement
Astrodynamics	STAR Category 13 Unclassified–Unlimited

19. Security Classif. (of this report)	20. Security Classif. (of this page)	21. No. of Pages	22. Price*
Unclassified	Unclassified	371	$11.00

*For sale by the National Technical Information Service, Springfield, Virginia 22151.

GSFC 25-44 (10/77)